Investigation of Interface behaviour on Perovskite Solar Cells



Jacob Tse-Wei Wang

University College

University of Oxford

A thesis submitted for the degree of

Doctor of Philosophy

Trinity, 2016

Acknowledgements

First and foremost, I like to offer my gratitude to my supervisor Prof. Robin Nicholas, for giving me the opportunity to pursue my DPhil study here at Oxford. Under his inspiring guidance, I have learned how a good scientist should be, and been motivated to become one like him. Without his infinite wisdom and patience to guide me through various challenges, this thesis would not be completed in schedule.

I also would like to thank my co-supervisor Prof. Henry Snaith, leading me to conduct research in the field of perovskite solar cells; although he is very busy, but every short discussion always pumping me lots of new ideas in the direction of research. With his boundless enthusiasm in science, I have learned to be passionate and persistent to my research.

Over the four good years in the Clarendon Laboratory, I have had the pleasure to work with the brightest minds in the world, I would like to thank the people in the RJN group, Jack, Beate, Nate, Sharky, Markus, Guilio, and my Carbon buddy Severin, your humour and optimism are the qualities I amazed and look up; though we RJN are a small group, but our bond (Carbon?) make us a great team! And I also like to thank all the people in the Snaith group, including Giles, Konrad, Jiewei, Mingzhen, Nobuya, Alba, Rebecca, Zhiping, Wei, Thomas, Tomas, Mike S., Derek, Bernard, Sam, Amir, Sandeep, Pablo, Golnaz, Pabitra, and Jin for every memorable moment we shared; but particular thanks goes to Clare for helping us tracking Henry down, and people in the office G24, Martina for always looking after us, Kita for supplying the nice sniffing rum, Max for all the fun hacking stuff, David

for the Canadian/French(!?) jokes, Grey for the beers and the kind proof-reading; and of course my master and mentor, James Ball, who lead me into the world of solar cells, and taught me how rigorous the science should be.

In addition, I like to thank the fellow Taiwanese friends at Oxford, especially, Duen-Wei, Bo, Will, Elisabeth, Porky, Po-Hsiang, Fusheng, Terry, Gary, Min-Wen for sharing lots of good laugh and food together, forming the little but cosy society in this remote town far from our home country. Also, without the generous funding from the Swire Educational Trust, I would not be able to have spent my DPhil study at University College. And not to mention meeting all the brilliant people at Univ, especially the Percy Gang, Brendan, Claire, Claas and Charlotte, who are the greatest neighbours and friends in life.

I owe everything to my family for allowing me the freedom to study, Dad, thank you for working so hard and bringing bread back to home, mom, thank you for your limitless care; if I have achieved any little thing, it is because of you two make that happened, and I dedicate this thesis to you; thanks also to my sister, brother, and my parents in law for all of your support and taking my responsibility in the family while we are away. Last but not least, my lovely wife, Molly, thank you for being my lifelong partner and going through my ups and downs together. With your endless support and encouragement, I have been able to explore the world dauntlessly, and I am so looking forward to starting our next great adventure together.

Abstract

Historically, the interfaces and charge transportation layers dictate the performance in heterojunction solar cells. This thesis addresses the interface behaviours and the interfacial layers within perovskite solar cells (PSCs), and provides insights and practicable solutions to facilitate the realisation of efficient PSCs.

To achieve efficient charge collection with interlayer fabricated with low-temperature processes, a graphene-TiO_2 nanocomposite is demonstrated; By investigating the carrier transport, we found the insertion of graphene improved the electron collection efficiency with its high surface area and ballistic carrier conduction properties, and in conjunction with pre-synthesised TiO_2, we have successfully circumvented the need for high-temperature annealing, enabling the whole device to be fabricated at under 150 °C.

While the anomalous hysteresis behaviour which is widely observed in regular PSCs structure is a significant problem, the quest of stable PSCs seems to be answered by the use of inverted PSCs structures. We show a detailed development of inverted PSCs which are deconstructed layer by layer. Numerous approaches have been tailored to improve interfaces, and energy levels between layers, leading to an efficient and hysteresis-free perovskite solar cells.

Lastly, an in-depth study of impurity doping is investigated using Al^{3+}. The doping with small metal ions in the perovskite precursor has been found to influenced the crystallisation and optoelectronic properties of the perovskite crystals. Here, for the first time, the correlation between reduced structural crystal defects is clearly linked to enhanced photovoltaic properties, with the best performance for the lowest electronic disorder in the $CH_3NH_3PbI_3$ crystal.

Publications

1. Wang, J. T.-W., Wang, Z., Pathak, S., Zhang, W., DeQuilettes, D., Wisnivesky,F., Huang, J., Nayak, P., Patel, J., Yusof, H., Vaynzof, Y., Zhu, R., Ramirez, I., Zhang, J., Ducati, C., Grovenor, C., Johnston, M.B., Ginger, D.S., Nicholas, R. J. & Snaith, H. J. Efficient Methylammounium Lead-iodide Perovskite Solar Cells by Metal Ion Doping. Energy & Environmental Science, Accepted Manuscript, 2016.

2. Levine, I., Nayak, P., Wang, J. T.-W., Sakai N., Reenen, S., Mukhopadhyay, S., Snaith, H., Hodes, G. & Cahen, D. Interface-Dependent Ion Migration/Accumulation Controls Hysteresis in $MAPbI_3$ Solar Cells. The Journal of Physical Chemistry, Accepted Manuscript, 2016.

3. Pearson, A. J., Eperon, G.E., Hopkinson, P. E., Habisreutinger, S. E., Wang, J. T.-W., Snaith, H. J. & Greenham, N. C. Oxygen Degradation in Mesoporous $Al_2O_3/CH_3NH_3PbI_{3-x}Cl_x$ Perovskite Solar Cells: Kinetics and Mechanisms. Advanced Energy Materials, Accepted Manuscript, 2016.

4. Galkowski, K., Mitioglu, A., Eperon, G.E., Wang, J. T.-W., Stergiopoulos, T., Stranks, S.D., Snaith, H. J. & Nicholas, R. J. Determination of the exciton binding energy and effective masses for methylammonium and formamidinium lead tri-halide perovskite semiconductors. Energy & Environmental Science, **9**(3), 962-970, 2016.

5. Saliba, M., Wood, S.M., Patel, J.B., Nayak, P.K., Huang, J., Webber, J.A., Wenger, B., Stranks, S.D., Hörantner, M.T., Wang, J. T.-W. and Nicholas, R. J. Structured Organic–Inorganic Perovskite toward a Distributed Feedback Laser. Advanced Materials, **2**8(5) 923–929, 2016.

6. Miyata, A., Mitioglu, A., Plochocka, P., Portugall, O., Wang, J. T.-W., Stranks, S. D. Snaith, H. J. & Nicholas, R. J. Direct Measurement of the Exciton Binding Energy and Effective Masses for Charge carriers in an Organic-Inorganic Tri-halide Perovskite. Nature Physics, **1**1(7), 582–587, 2015.

7. Wojciechowski, K., Leijtens, T., Spirova, S., Schlueter, C., Hoerantner, M., Wang, J. T.-W., Li, C. Z., Jen, A. K.-Y., Lee, T.L. & Snaith, H. J. C60 as an Efficient N-Type Compact Layer in Perovskite Solar Cells. The Journal of Physical Chemistry Letters, **6**(12), 2399-2405, 2016.

8. Snaith, H. J., Abate, A., Ball, J. M., Eperon, G. E., Leijtens, T., Noel, N. K., Wang, J. T.-W.,Wojciechowski, K.,& Zhang, W. Anomalous Hysteresis in Perovskite Solar Cells. The Journal of Physical Chemistry Letters, **5**(9), 1511-1515, 2014.

9. Wang, J. T.-W., Ball, J. M., Barea, E. M., Abate, A., Alexander-Webber, J. A., Huang, J., Saliba, M., Mora-Sero, I., Bisquert, J., Snaith, H. J.& Nicholas, R. J. Low-temperature processed electron collection layers of graphene TiO_2 nanocomposites in thin film perovskite solar cells. Nano letters **1**4(2), 724-730, 2013.

Contents

1 Introduction **1**

1.1 Background and Motivation 1

1.2 Aims of the thesis 3

2 Background **8**

2.1 Semiconductor 9

2.2 Principles of Solar Cells 12

2.2.1 Light absorption and generation of charge 12

2.2.2 Charge Separation 14

2.2.3 Charge Recombination 17

2.2.4 Charge Collection 19

2.3 Characterisation of Solar Cells 20

2.4 Principles of Perovskite Solar Cell Operation 22

2.4.1 Perovskite 22

2.4.2 Structures of Perovskite Solar Cells 24

2.4.3 Charge Carrier Dynamics 27

2.4.4 Operation Mechanism 29

2.5 Interlayers 31

2.5.1 Electron-Transporting Layer (ETL) 33

2.5.2 Hole-Transporting Layer (HTL) 34

2.5.3 Electrodes and Buffer Layers 35

3 Method **45**

3.1 Materials Preparation 45

3.1.1 Methylammonium Lead Mix-Halide Perovskite ($CH_3NH_3PbI_{3-x}Cl_x$) 45

3.1.2 Methylammonium Lead Iodide Perovskite ($CH_3NH_3PbI_3$) 46

3.2 Fabrication of Perovskite Solar cells . . . 46
3.2.1 Mesoporous-Superstructured Solar Cell fabrication . . . 46
3.2.2 Planar Perovskite Solar Cell fabrication . . . 47
3.3 Material Characterization . . . 48
3.3.1 Scanning Electron Microscopy (SEM) . . . 48
3.3.2 Transmission Electron Microscopy (TEM) . . . 48
3.3.3 X-ray Diffraction Measurement . . . 49
3.3.4 Nanoscale Secondary Ion Mass Spectrometry . . . 49
3.3.5 Atomic Force Microscopy (AFM) . . . 50
3.3.6 Inductively Coupled Plasma Optical Emission Spectrometry (ICP-OES) . . . 50
3.3.7 X-ray and Ultra-Violet Photoemission Spectroscopy (XPS and UPS) Measurements . . . 51
3.3.8 Kelvin Probe and Surface Photo Voltage (SPV) . . . 51
3.4 Electrical Characterization . . . 52
3.4.1 Solar Cell Characterization . . . 52
3.4.2 Impedance Spectroscopy . . . 52
3.5 Optical Characterization . . . 53
3.5.1 UV-visible Absorption Spectra . . . 53
3.5.2 Raman Spectroscopy . . . 53
3.5.3 Photoluminescence Spectroscopy . . . 53
3.5.4 Fluorescence Microscopy . . . 54
3.5.5 Incident Photon to Converted Electron Measurement (IPCE) or External Quantum Efficiency (EQE) . . . 54
3.5.6 Fourier Transform Photocurrent Spectroscopy (FTPS) . . . 55

4 Gaphene-TiO_2 Nanocomposites as Electron Collection Layers in Thin Film Perovskite Solar Cells 58
4.1 Context . . . 59
4.2 Introduction . . . 59
4.3 Gaphene-TiO_2 Nanocomposites . . . 62
4.3.1 Graphene Nanoflakes . . . 62
4.3.2 TiO_2 Nanoparticles . . . 64

4.3.3 Nanocomposites . . . 65
4.3.4 The Coverage of TiO_2 Nanoparticles on Graphene . . . 68
4.4 Photovoltaic Behaviour . . . 70
4.4.1 Device Architecture . . . 70
4.4.2 Device Performance . . . 72
4.5 Charge Collection . . . 76
4.5.1 Light Harvesting and Quantum Efficiency . . . 76
4.5.2 Charge Carrier Conductivity . . . 78
4.6 Summary . . . 79

5 Tailoring of Interfacial Layers in The Inverted Perovskite Solar Cells 85
5.1 Context . . . 86
5.2 Introduction . . . 86
5.3 Surface Modification on Transparent Conducting Electrode . . . 88
5.3.1 Surface Potential . . . 90
5.3.2 Work Function Influenced Device Performance . . . 91
5.4 Hole-Transporting Layer and Thickness dependence . . . 94
5.5 Perovskite Layer and Surface Morphology . . . 97
5.5.1 Influence of Precursor Solution Temperature on Micromorphology 97
5.5.2 Morphology Influenced Device Performance . . . 99
5.6 Electron-Transporting Layer and Thickness Dependence . . . 103
5.7 Buffer Layer and Metal Electrode . . . 106
5.8 Hysteresis Behavior Comparison . . . 111
5.9 Open-Circuit Voltage Enhancement by Hole -Transporting Layer Engineering . . . 114
5.9.1 Doping Influenced Device Performance . . . 116
5.9.2 Optical Characterisation on Different Hole-Transporting Materials 120
5.10 Summary . . . 123

6 Metal Ion Doping in the $CH_3NH_3PbI_3$ 135
6.1 Context . . . 136
6.2 Introduction . . . 136

6.3 Characterization of Al^{3+}-doped Perovskite . . . 139
6.3.1 Crystal structure . . . 139
6.3.2 Microstrain . . . 140
6.3.3 Micromorphology and Al detection . . . 142
6.3.4 Impact on Crystallization . . . 147
6.4 Optoelectronic Properties . . . 150
6.4.1 Photoluminescence Behaviour . . . 150
6.4.2 Surface Potential & Trap states . . . 153
6.4.3 Electronic Disorder . . . 155
6.5 Photovoltaic Behaviour . . . 157
6.5.1 Device Architecture . . . 157
6.5.2 Device Performance . . . 157
6.6 Summary . . . 166

7 Conclusion and Outlook **171**
7.1 Conclusion and Outlook . . . 171
7.1.1 Conclusion . . . 171
7.1.2 Outlook . . . 175

Chapter 1

Introduction

1.1 Background and Motivation

As the advance of industrialisation brings benefits, it also comes with a price, the emission of greenhouse gases, such as carbon dioxide (CO_2) and methane (CH_4), which result in global warming, leading to various extreme weather and changes in the ecological systems.[1, 2] Though the burning of fossil fuels accounts for the major greenhouse gas production, the world energy supply and the electricity generation are still strongly reliant on this limited and non-environmental friendly source, see fig. 1.1.

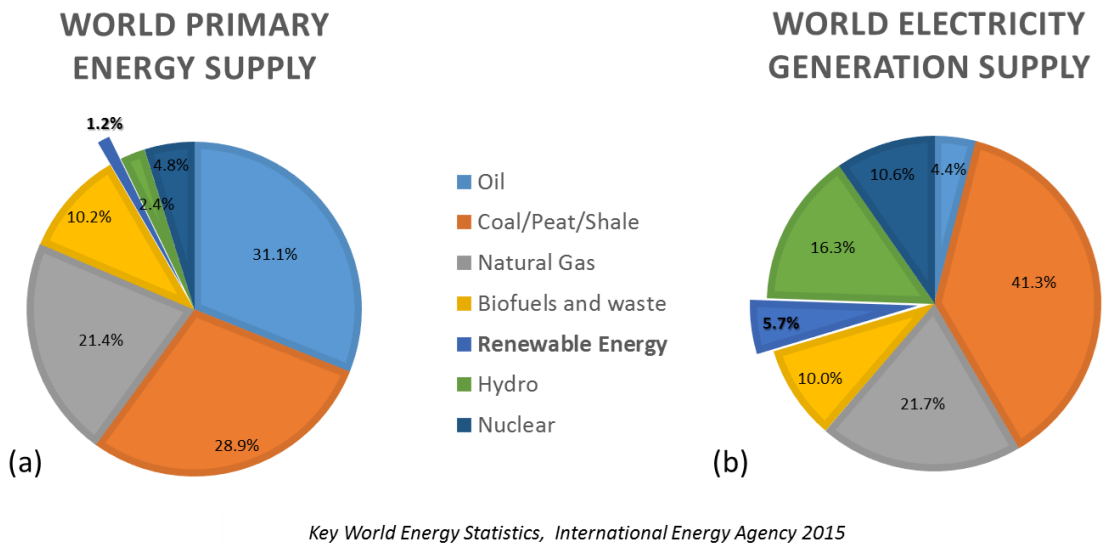


Figure 1.1: The sources of (a) global energy supply and (b) the electricity generation; data retrieved from the Key World Energy Statistics, International Energy Agency, 2015.

Now the world has finally come to a consensus on the Paris agreement of United Nations Framework Convention on Climate Change (UNFCCC), and decided to hold the increase in global average temperature by reducing the emission of greenhouse gases and increasing shares on alternative energy supply sources.[3] Among all the renewable energy sources, solar energy is the most abundant one, about 120,000 terawatts (TW) of solar radiation is ceaselessly provided[4], and to use this enormous energy supply, the most efficient way is via photovoltaic devices (PV). However, to deliver a large fraction of the global energy demand via solar cells will require continued improvements in energy conversion efficiency combined with further reductions in cost. The current mainstream solar cells are made from mono-crystalline silicon, provide a power conversion efficiency (PCE) around 25% in lab-scale record, around 22% for large module efficiency[5, 6]; with over 85% of current PV production using this wafer-based silicon technology, and the remaining 15% is shared between thin-film devices, such as CdTe, GaAs, and CIGS.[7] These inorganic-based solar cells require materials to be processed under high-temperature with high purity control, which employs expensive manufacturing techniques; and the use of scarce elements also increases the production cost. While in recent years, the price of solar has plummeted, with USD$ 1.00 per Watt within reach due to the manufacture learning curve providing large-scale economics.[8] However, to compete with other energy sources, the cost still needs to be reduced further.

Recently, the emergence of perovskite solar cells has attracted lots of attention; with advantages including low-temperature process, low material cost, and compatibility with roll-to-roll processing, make it a very promising candidate to challenge the existing silicon dominance. However, this technology is still rather young; though the first discovery of the organic-inorganic perovskite that can be traced back is 1978, by the German scientist Dieter Webber[9, 10]. But due to a different historical focus, it was only in 2009 that the first solar cell was being reported with a PCE of 3.8% on a sensitised solar cell by Miyasaka and co-workers.[11] With a major leap of PCE to over 10%, achieved by

replacing the liquid electrolyte in the sensitised solar cells with all solid-state transport layers[12], this technology start getting noticed. Within three years, a record-breaking PCE of over 20% has been demonstrated[13]. Now with a flood of research interests, the breakthroughs in this emerging photovoltaics are growing at a fastest speed in the history of solar cells development, achieving the highest efficiency, with the lowest cost solar cells to answer the global energy dilemma does not seem impossible anymore.

1.2 Aims of the thesis

This thesis is building on the discovery of the interfaces of perovskite solar cells (PSCs). As this new type of solar cells are still at an early stage of development, and there is much research that can still be done to improve efficiencies and investigate the fundamental science. To compete with the A-list solar cells on the market, minimising the charge recombination by improving the interface has proven crucial to achieve high performance solar cells; where the calculated Shockley-Queisser limit for PSCs is about is about 31%[14], and the current record-breaking PSCs is about 22% with a fill factor (FF) lower than 80%[15]. In comparison, the GaAs solar cell has a Shockley-Queisser limit around 33%, with the state-of-the-art device showing PCE approaching 30% with a FF close to 87%[5]. As these two materials share similar exceptional optoelectronic properties in terms of bandgap and effective masses[16, 17], this suggests that there are still plenty of space left for PSCs to improve their performance.

In chapter 2, we will first cover the overview of the background knowledge required for this thesis, which includes the basic principles of semiconductors, solar cells, operation principles of perovskite solar cells, and the role of interfacial layers for readers to better understand the following chapters. A detailed description of materials used, fabrication of solar cells, and characterisation techniques will be described in chapter 3.

Evolving from the solid-state dye-sensitised solar cells (ss-DSSC), the fabrication of PSCs shares the similar building blocks, working mechanisms and the use of materials. However, in the regular PSCs, the preparation of the thin TiO_2 electron-transporting layer (ETL) still required to be sintered at a temperature over 500 °C, which is unfavourable for low-cost production, applications on plastic substrates, and fabrication of multi-junction device architectures for even higher efficiencies. In chapter 4, we employ liquid phase exfoliated graphene and hydrothermally synthesised TiO_2 to form a low-temperature processed nanocomposite as ETL, enabling the entire device to be fabricated at temperatures no higher than 150 °C. With synergetic efforts from the pre-synthesised anatase TiO_2 to function as gatekeeper for carrier selection/injection, and graphene to act as a continuous 2D conductive framework to provide superior charge-transportation in the nanocomposites. The resulting regular PSCs was able to compete with the best high-temperature processed PSCs while the work was published. This has generated tremendous interest in this area and shown promise for the industrially preferred application.

Perovskite solar cells are particularly sensitive to the interface and the details of materials applied. In chapter 5, we put particular emphasis on the development of inverted PSCs, which inherited the structure from organic photovoltaics (OPV), which not only have advantages in a fully low-temperature process (less than 100 °C) to be compatible with the roll-to-roll processing, but also eliminate the unwanted anomalous hysteresis behaviour. Although many efforts have been made to improve the regular (n-i-p) architecture to facilitate charge extraction with improved selective contacts and deposition process for further pushing the performance ahead, however, the presence of hysteresis behaviour has cast a shadow with the concerns of stability in the regular PSCs; as has been pointed out, the origin of hysteresis is likely to stem from the unfavourable interfaces within the device. Therefore, it is particularly important to understand the difference between the two structures, and investigate the interface behaviours. Here, a

development of inverted PSCs will be demonstrated, from the cathode to anode, and the influence of energy level alignment on device performance will be studied and discussed. With the careful evaluation on the interface and energy level alignment of the individual components. We will show how various approaches have contributed toward the improved wettability, surface morphology, and better matching energy levels between interfaces, leading to a hysteresis-free perovskite solar cells. Then, we also provide a comprehensive comparison between the fullerene-based regular and inverted structure PSCs. The careful optimisations throughout the entire carrier transport pathways, provide new insights into the future development of interface engineering and show the importance of interlayers for highly efficient and hysteresis-free PSCs.

In traditional thin-film photovoltaic materials processing, the influence of impurity doping has been studied extensively, and has been found to either alter the crystallisation or induce the electronic doping; however, in the perovskite community, this has been largely unexplored. Here, in chapter 6, we demonstrate how the addition of small metal ions as potential dopants has profoundly influenced the quality of the perovskite; not only facilitating the crystallisation process by changing the surface energy of the crystal growth front making it more favourable, but also due to a tendency to segregate at the grain boundaries. The resulting films have shown a two-fold increase in the quantum luminescences efficiency, and a significantly reduced electronic disorder, which means that the recombination at the potential defect sites has been substantially reduced. Moreover, these improved optoelectronic qualities also translate directly to a superior device performance.

Finally, the key findings in this thesis, and the potential development and outlook for the PSCs will be summarised and discussed in chapter 7.

References

[1] Christopher S. Watson, Neil J. White, John A. Church, Matt A. King, Reed J. Burgette, and Benoit Legresy. Unabated global mean sea-level rise over the satellite altimeter era. *Nature Climate Change*, 5(6):565–568, may 2015.

[2] E. M. Fischer and R. Knutti. Anthropogenic contribution to global occurrence of heavy-precipitation and high-temperature extremes. *Nature Climate Change*, 5(6):560–564, apr 2015.

[3] Paris Agreement, FCCC/CP/2015/L.9/Rev.1. *UNFCCC secretariat.*

[4] Oliver Morton. Solar energy: Silicon Valley sunrise. *Nature*, 443(7107):19–22, sep 2006.

[5] Martin A. Green, Keith Emery, Yoshihiro Hishikawa, Wilhelm Warta, and Ewan D. Dunlop. Solar cell efficiency tables (version 47). *Progress in Photovoltaics: Research and Applications*, 24(1):3–11, jan 2016.

[6] Albert Polman, Mark Knight, Erik C Garnett, Bruno Ehrler, and Wim C Sinke. Photovoltaic materials: Present efficiencies and future challenges. *Science (New York, N.Y.)*, 352(6283):aad4424, apr 2016.

[7] Arnulf Jäger-Waldau. PV Status Report 2014. Technical report, European Commission, 2014.

[8] Varun Sivaram and Shayle Kann. Solar power needs a more ambitious cost target. *Nature Energy*, 1(4):16036, 2016.

[9] Dieter Weber. CH3NH3PbX3, a Pb(II)-System with Cubic Perovskite Structure. *Zeitschrift f{ü}r Naturforschung B*, 33b(August 1978):1443–1445, 1978.

[10] Dieter Weber. CH3NH3SnBrxI3-x (x=0-3), a Sn(II)-system with the cubic perovskite structure. *Zeitschrift f{ü}r Naturforschung*, 33b:862–865, 1978.

[11] Akihiro Kojima, Kenjiro Teshima, Yasuo Shirai, and Tsutomu Miyasaka. Organometal Halide Perovskites as Visible-Light Sensitizers for Photovoltaic Cells. *Journal of the American Chemical Society*, 131(17):6050–6051, may 2009.

[12] Michael M. Lee, Joël Teuscher, Tsutomu Miyasaka, Takurou N. Murakami, and Henry J. Snaith. Efficient Hybrid Solar Cells Based on Meso-Superstructured Organometal Halide Perovskites. *Science*, 338(6107):643–647, nov 2012.

[13] Woon Seok Yang, Jun Hong Noh, Nam Joong Jeon, Young Chan Kim, Seungchan Ryu, Jangwon Seo, and Sang Il Seok. High-performance photovoltaic perovskite layers fabricated through intramolecular exchange. *Science*, 348(6240):1234–1237, jun 2015.

[14] Wei E. I. Sha, Xingang Ren, Luzhou Chen, and Wallace C. H. Choy. The efficiency limit of CH3NH3PbI3 perovskite solar cells. *Applied Physics Letters*, 106(22):221104, jun 2015.

[15] Michael Saliba, Taisuke Matsui, Ji-Youn Seo, Konrad Domanski, Juan-Pablo Correa-Baena, Mohammad Khaja Nazeeruddin, Shaik M Zakeeruddin, Wolfgang Tress, Antonio Abate, Anders Hagfeldt, and Michael Grä Tzel. Cesium-containing triple cation perovskite solar cells: improved stability, reproducibility and high efficiency. *Energy Environ. Sci.*, 9(6):1989–1997, mar 2016.

[16] D. A. Broido, L. J. Sham, and I J Sham. Effective masses of hales at GaAs-A1CxaAs heterojunctions. *Physical Review B*, 31(2):888–892, jan 1985.

[17] Atsuhiko Miyata, Anatolie Mitioglu, Paulina Plochocka, Oliver Portugall, Jacob Tse-Wei Wang, Samuel D. Stranks, Henry J. Snaith, and Robin J. Nicholas. Direct measurement of the exciton binding energy and effective masses for charge carriers in organic–inorganic tri-halide perovskites. *Nature Physics*, 11(7):582–587, jun 2015.

Chapter 2

Background

This chapter gives an overview of the background knowledge required for the understanding of this thesis, which includes the basic principles of semiconductor, solar cells, and the operation of perovskite solar cells and its interfacial layers. Note: For more in depth information, please refer to Sze et al.[1], Rosenburg et al.[2], Nelson et al.[3], and Wurfel et al.[4]

2.1 Semiconductor

In this chapter, we will briefly discuss the building block of photovoltaics, the semiconductor, which allows solar cells to convert the light into electricity. In general, materials can be roughly classed into three categories, metals, insulators, and semiconductors. The major difference between these three types of materials is their energy states, also called band gaps (E_G). To understand the flow of charge and potential difference within the band structure, it is essential to determine the Fermi level (E_F) of a material. The Fermi level can be regarded to be a hypothetical energy level being filled up with a 50% chance by electrons for any non-zero temperature, while at absolute zero (zero degree Kelvin), it has an occupancy chance of 100%.[1]

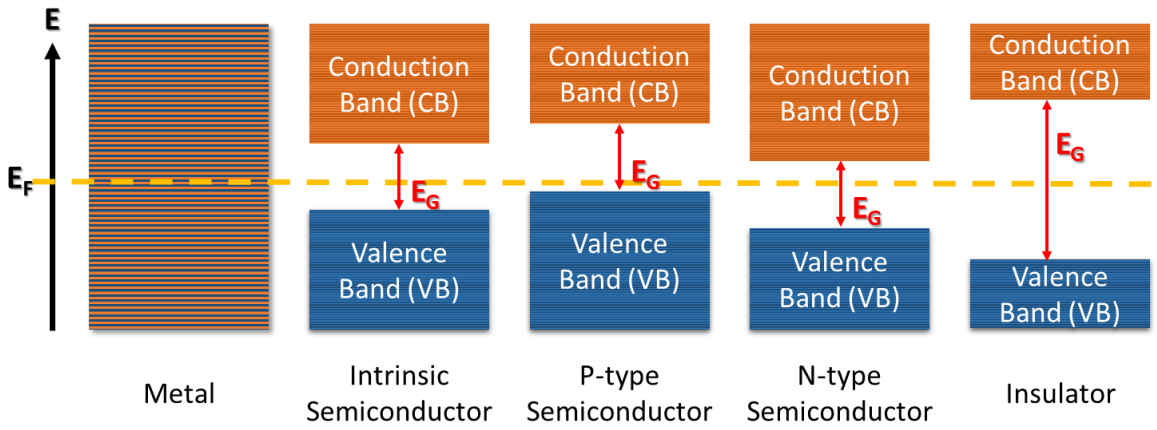


Figure 2.1: Energy band diagrams for metals, insulators, semiconductors, and doped semiconductors illustrating the differences of the forbidden gap (E_G), and their conduction and valence band alignments relative to their Fermi levels(E_F). Blue and orange lines depicts filled states and empty states, respectively.

The energy states, or so-called bands of a material are occupied or not, depending upon whether the original molecular orbitals were occupied. The highest occupied band, which contains the valence electrons, is called the valence band (VB). The lowest unoccupied band is called the conduction band (CB). These two terms are analogue to the terms typically used in describing organic materials, Highest Occupied and Lowest Unoccupied

and Molecular Orbitals (HOMO and LUMO), where the long-range delocalization in the energetic band is not possible.[2]

Metals allow electrons to freely transfer within their continuum of energy states. They either have minuscule band gaps or none, due to the overlap of their valence and conduction bands. Their E_F lies inside at least one band, its position gives us information about the velocities of the electrons which play a part in electrical conduction. Insulators usually have an E_F inside their relative large forbidden gap. This large gap means it is very difficult for electrons in VB to be promoted to the CB, resulting in a fully occupied VB and an empty CB under normal circumstances. Semiconductors, have a conductivity range situated between metals and insulators. However, this does not mean that semiconductors are simply poor conductive metals. Instead, semiconductors are generally insulating without energy excitation or impurity doping. Both of these cases will be discussed below. With the input of stimulus such as light, heat, or an electric field, provides energy to excite a semiconductor's electron from the VB, across the band gap, to the CB. The presence of electrons in the CB also results in an equal number of positive charges (holes) in the VB. If an electron in a metal was raised to higher energy state, it would decay back to its ground state very quickly through the continuum of energy states. While a semiconductor has a different behaviour where the band gap enables the excited electrons to remain in their excited states and to be exploited for further energy conversion.

Doping in semiconductors

As mentioned above, conductivity in semiconductors can be tuned with the aid of doping. Doping is achieved by adding impurities to the intrinsic host material, which frees electrons or holes from them, thus increasing the number of free carriers for conduction. This method of adding electrons or holes to levels near to the conduction or valence

bands, shifts the Fermi level closer to the CB or VB within the material, making the material more conductive (less resistive) for electrons or holes upon doping. Here the conductivity (σ) and resistivity (ρ) in a semiconductor can be described as

$$\sigma = \frac{1}{\rho} = q(\mu_n n + \mu_p p) \tag{2.1.1}$$

Where q is the electronic charge, n is the density of electrons, and p is the density of holes, μ_n and μ_p are the mobilities of the electrons and holes, respectively. In fig. 2.2 we show an illustration of how the typical semiconductor Silicon, can be doped with impurities to make a p-type semiconductor by doping with group III elements like boron, or with group V elements like phosphorus to make an n-type semiconductor.

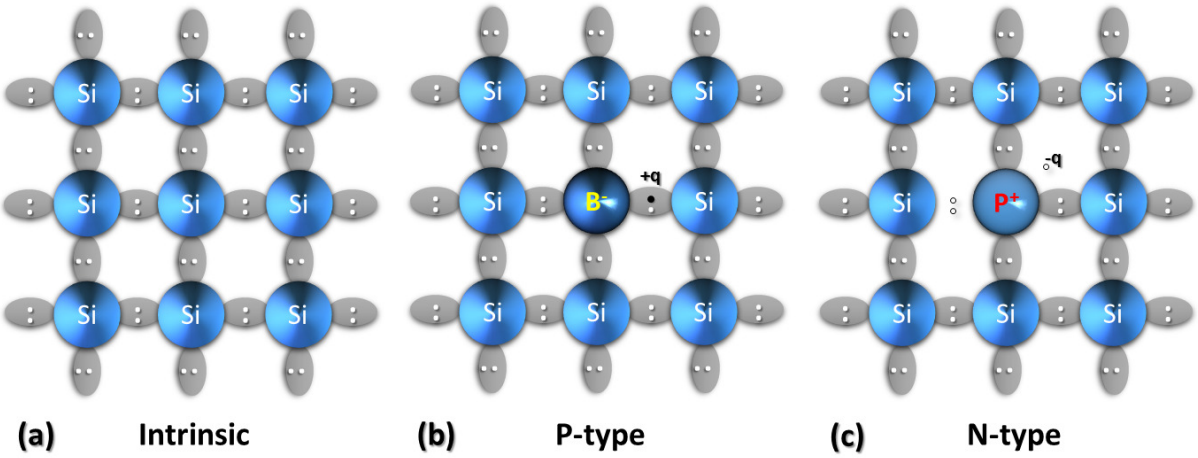


Figure 2.2: Schematic diagram of (a) intrinsic silicon crystal lattice, doped with impurities to produce excess of delocalised or mobile (b) holes (p-type) or (c) electrons (n-type). Note that this is a two-dimensional representation of a three-dimensional material. Each silicon atom has four close neighbouring atoms, and it shares two electrons with each of them forming four covalent bonds.

2.2 Principles of Solar Cells

The first reported photovoltaic effect can be dated back to 1839 by Edmond Becquerel.[5] However, it was not until 1954, that the first practical device was unveiled by Bell Labs, when they presented the simplest solar cell (fig. 2.3), a p-n junction or diode, where two types of semiconductors contact each other. Upon photoexcitation, electrons and holes are collected at opposite ends, thus current is generated. The following sections discuss the different processes taking place here.

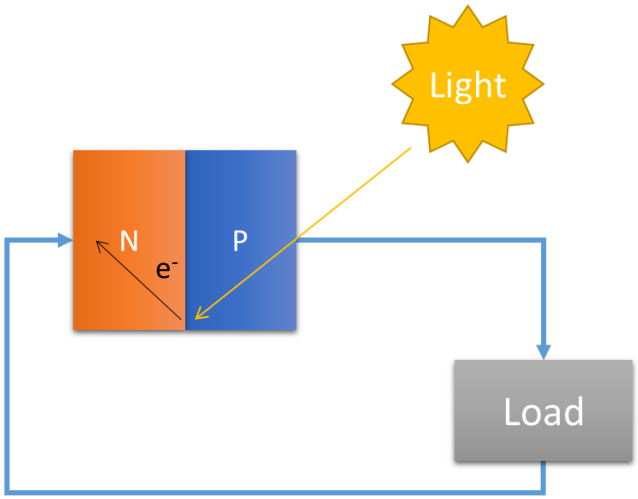


Figure 2.3: Photovoltaic cells require a spatial asymmetry manner to drive the photoexcited charge carriers through external circuit to generate current and voltage.

2.2.1 Light absorption and generation of charge

In fig. 2.4, we show the standard terrestrial solar spectrum (Air Mass 1.5), corresponding to the sun at an elevation angle of 42° with an integrated irradiance of 1000 W/m^2. It is important to note here, that for a photovoltaic material with a particular band gap, only the photons with enough energy to excite electrons across the bandgap can be absorbed. Though the high energy photons are needed to generate electron-hole pair, only the potential energy of the semiconductor's E_g will be gathered, while the excessive

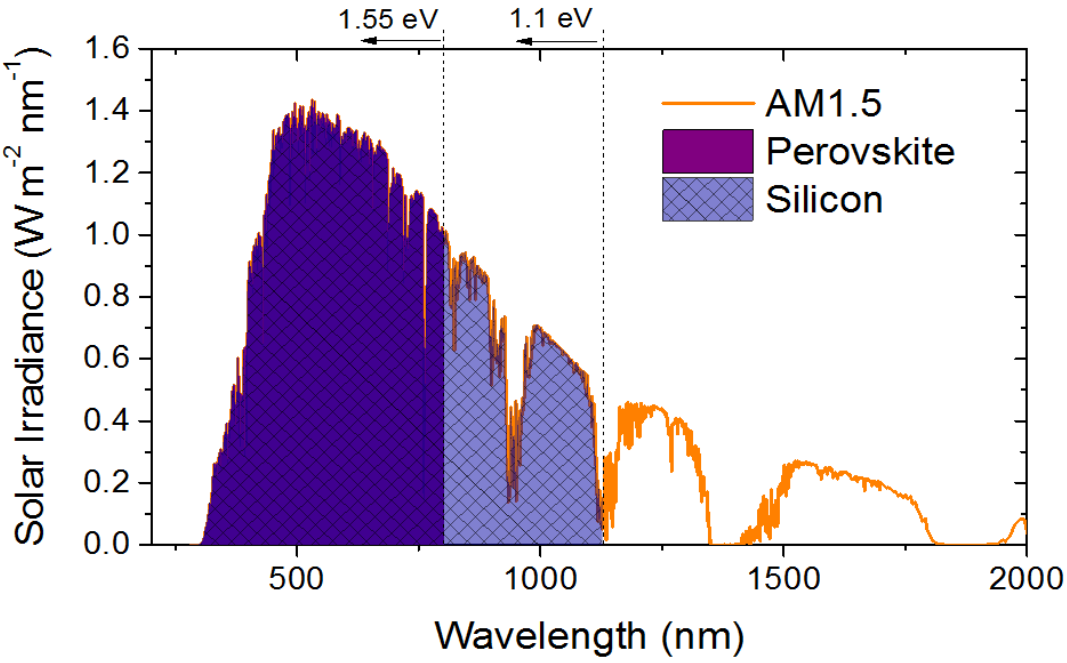


Figure 2.4: AM 1.5 solar spectrum with indication of region can be absorbed by standard crystalline silicon (Eg = 1.1 eV), and $CH_3NH_3PbI_3$ (Eg = 1.55 eV) respectively.

energy in carriers will be quickly lost via thermalisation[3], see fig. 2.5. Thus, it is in our interest to investigate the solar spectrum with respect to the band gap. According to the Shockley-Queisser's theory, the ideal band gap range for a photovoltaic material would be around 1.1-1.4 eV.[6] Crystalline silicon is a material with a bandgap in this range. In fig. 2.4 we indicate where crystalline silicon's (Eg = 1.1 eV) absorption coverage is, and we also show that of $CH_3NH_3PbI_3$ (Eg = 1.55 eV).

Once the photons are absorbed, the created mobile electron hole pairs, are known as excitons (See fig. 2.6). This pair of electrons and holes are attracted to each other due to the Coulomb force, and their binding energy is mainly dominated by the dielectric constant of the material. Excitons can be roughly categorized in two classes, Frenkel excitons (binding energy between 0.1 to 1 eV, typical of organic semiconductors) and Wannier-Mott Excitons (binding energy on the order of 0.01 eV, typical of inorganic

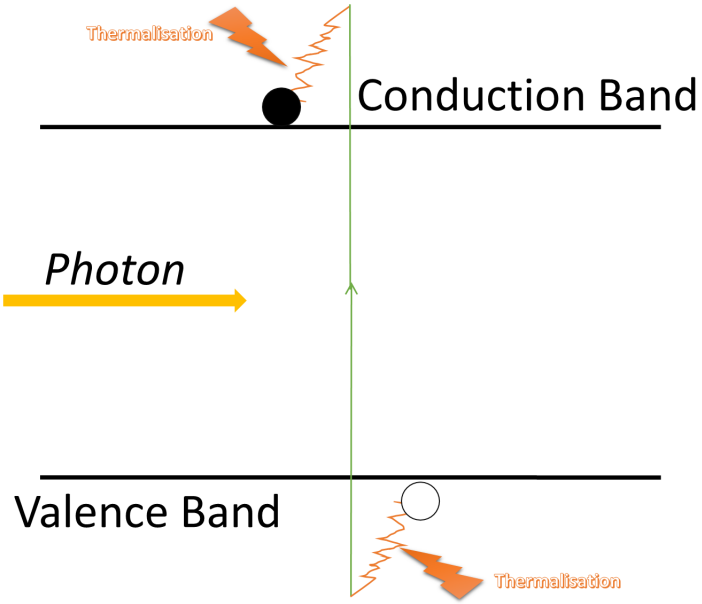


Figure 2.5: Photon absorption in a semiconductor generate electron-hole pair at respected band edge with excessive kinetic energy release by thermalisation.

semiconductors)[7]

2.2.2 Charge Separation

After the generation of electron-hole pairs, it is important to separate the charges before they recombine. As mentioned before, the pair of electrons and holes are attracted to each other with a binding energy due to the Coulomb force. Separating these charges plays a vital role in how photovoltaic devices generate photocurrent (in short circuit condition) and photovoltage (in open circuit condition). A driving force is required to separate the charges, and the most common way is to create a spatial variation in the electronic environment.

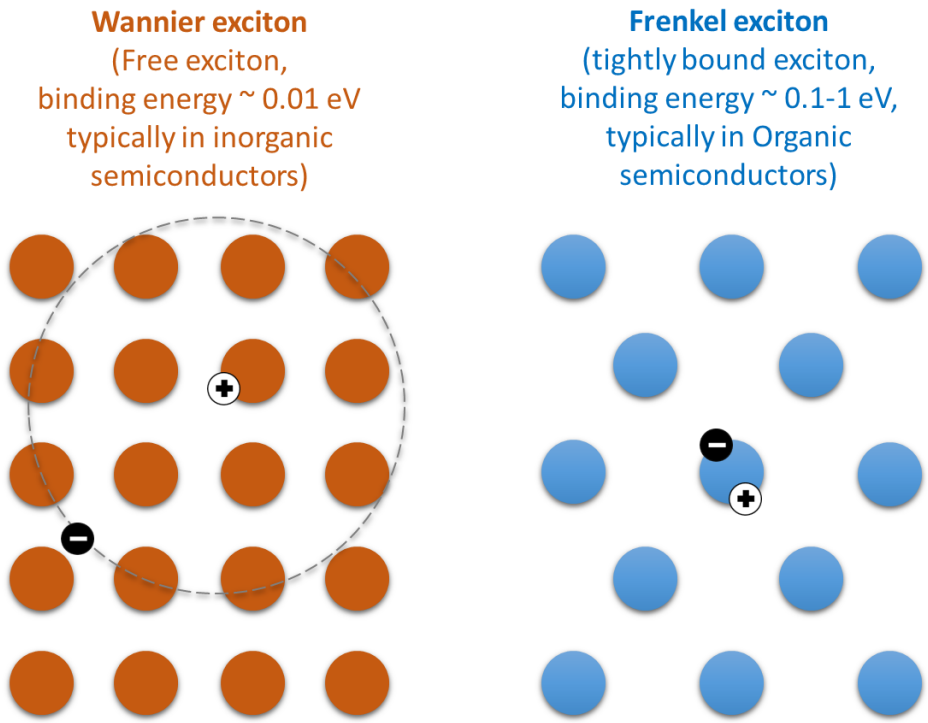


Figure 2.6: Types of excitons exist in semiconductors with different binding energy resulting in different carrier behaviour.

p-n Junction

Taking the aforementioned first practical PV device as an example: the contact between p- and n-type semiconductors, makes their Fermi levels align to the same energy, causing band-bending, and making electrons migrate into the p-type side and holes migrate to the n-type side.[3] The departure of electrons and holes, meanwhile, also leaves positive ions (at n-type) and negative ions (at p-type) behind, this creates an intrinsic built-in electric field called the depletion region, see fig. 2.7. This built-in potential can be calculated by subtracting from the values of bandgap to the difference of Fermi levels with respect to the band edges of doped region.[8] Upon illumination with light, the energy of the incident photons is absorbed by electrons, thus creating mobile electron hole pairs. With the presence of the built-in field to drive the electrons to the left and holes to the right, we realise charge separation and current flow. This happens through

a combination of drift and diffusion of mobile carriers which can be described by the equation below.

$$J_{Light} = q(n\mu_n + p\mu_p)E + q(D_n\frac{d_n}{d_x} + D_p\frac{d_p}{d_x}) \tag{2.2.1}$$

Here, J_{Light} is the photocurrent, μ is carrier mobility, E is the electric field, D is the diffusion coefficient, x is the position along the direction of current flow, n and p are the carrier concentrations for electrons and holes, respectively.

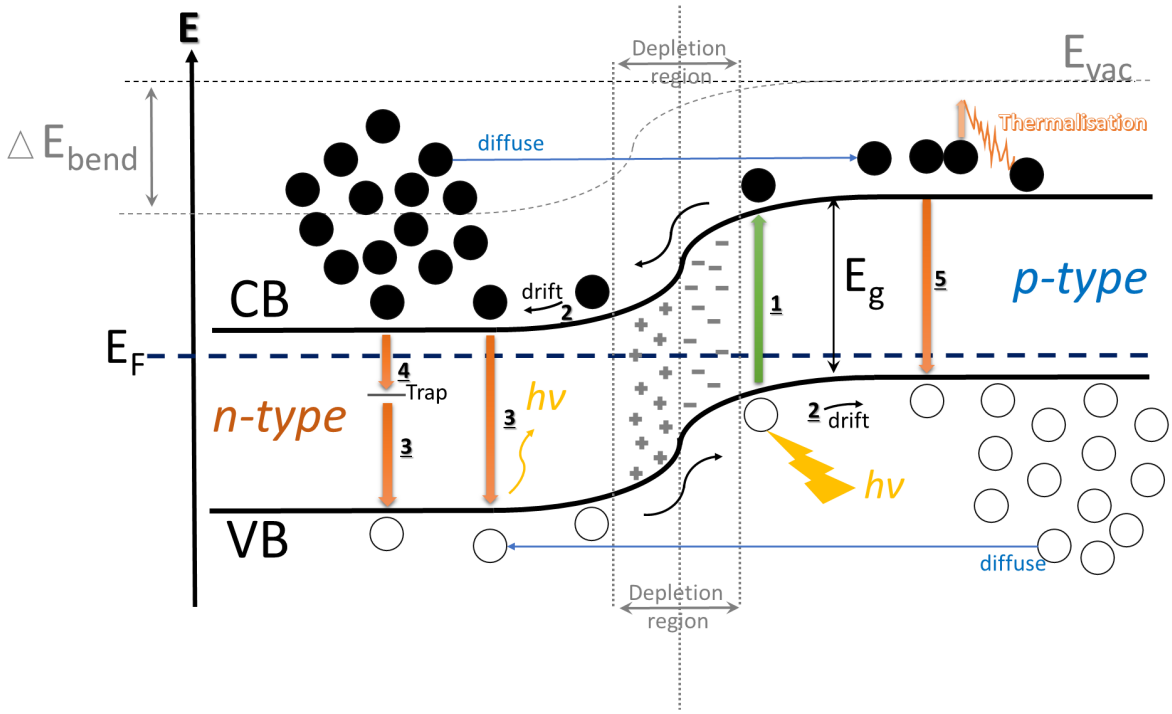


Figure 2.7: Schematic diagram of a p-n junction under illumination with enumerated process. 1, upon illumination, the photo-excited electron and hole pairs appear in CB and VB respectively. 2, the depletion region acts as the built-in field to drive electrons to the n-type side and holes to the p-type side. 3, Radiative recombination of the electron-hole pair (may be followed by the emission of light). 4, Trap-assisted decay. 5, Auger recombination of the electron-hole pair, where the electron-hole pair recombines giving its energy to a neighbouring carrier.

p-i-n Junction

As the name suggests, the p-i-n junction is similar to the p-n junction, but the only difference is with an intrinsic semiconductor inserted between the p and n contacts. The intrinsic layer is left undoped, so when the contacts form, it creates the equivalent built-in electric field as in the p-n junction, but with the insertion of an intrinsic layer, the depletion region is elongated.[1] This is preferable for materials with long wavelength response and shorter diffusion length. Since under long wavelength irradiation, only those electron-hole pairs close to the depletion region will contribute to the photocurrent generation. Therefore, the wider the depletion width, the more useful electron-hole pairs can be generated within the device. But the wide depletion region is not always beneficial; the intrinsic layer is undoped leading to a lower conductivity, which potentially increases the series resistance of the device, so it is only useful for materials with a shorter diffusion length.[4]

2.2.3 Charge Recombination

Once a charge carrier is produced, its lifetime is not unlimited. There is a tendency for carriers to recombine due to the existence of Coulombic force.[2] The length of carrier travels before it recombines is called Diffusion length (L_D), and can be defined as

$$L_D = \sqrt{D\tau} \tag{2.2.2}$$

Where D is the diffusion constant, and can be described as a function of carrier mobility(μ), temperature (T), Boltzmann constant (k_B), and the elementary charge (e):

$$D = \mu k_B T e^{-1} \tag{2.2.3}$$

τ is the carrier lifetime, which defines as the average time it takes for an excess minority carrier to recombine.

Recombination is unlike the generation of carriers, which has one dominant mechanism only, instead, it has several competing pathway.They can be classed into two categories: radiative and non-radiative recombination. Figure 2.7 illustrates three different recombination mechanisms, where the radiative decay (3) demonstrates a band to band charge recombination (bimolecular) accompanied by light emission. Non-radiative recombination shows different behaviours in (4) with trap-assisted recombination (monomolecular) and (5) Auger recombination involving three carriers: when an electron and a hole recombine, the energy is given to a third carrier rather than being dissipated in the form of light or heat.[3]

The overall recombination rate is contributed by three different pathways and is dependent on the charge carrier density (n), hence the total recombination rate (R_{total}) is given by

$$R_{total} = k1 + nk2 + n^2k3 \tag{2.2.4}$$

Where k1, k2 and k3 are representing the monomolecular rate constant, bimolecular rate constant, and Auger rate constant, respectively. While τ is inversely proportional to total recombination rate (R_{total}), hence from equation 2.2.3, we can rewrite the equation 2.2.2 as

$$L_D(n) = \sqrt{\frac{\mu k_B T}{R_{total}(n)e}} \tag{2.2.5}$$

From here, we can describe the carrier diffusion length as a function of carrier mobility and recombination.

2.2.4 Charge Collection

So far, we have discussed the phenomena of absorption, separation, and recombination, now to estimate how much current we can collect, we need to consider two situations in a diode, with and without illumination. The p-n junction create energetic gradient in both cases, therefore, the overall current generated is,

$$J_{Tot} = J_{Light} - J_{Dark}. \tag{2.2.6}$$

When under dark, the built-in field shifts the electrons toward the n-type layer and holes toward the p-type layer. To disable such a current flowing, an external electric field is needed. This applied field is also known as the open-circuit voltage, and the current flowing without electrical load is called the dark current (J_{dark}), which flows in the opposite direction of the photocurrent. Here, it can be written as,

$$J_{Dark}(V) = J_0(e^{qV/mk_BT} - 1) \tag{2.2.7}$$

where J_0 is a constant, k_B is Boltzmann's constant, T is temperature, and m is the ideality factor, ranging between 1 and 2 (when a diode behaves in the ideal scenario, m=1).

While under illumination, the photocurrent (J_{Light}) is a function of the diode's properties (absorption, charge separation, and recombination) over the incident light spectrum, and it can be integrated with the product of External Quantum Efficiency (EQE) and the incident solar spectrum as

$$J_{Light} = q \int EQE(E)\Phi_{AM1.5}(E)d(E) \tag{2.2.8}$$

where EQE represents how efficiently that photon can be absorbed to create the electron-hole pair.

Now to find the total current (J_{Tot}) in an illuminated diode, we can rewrite the equation 2.2.6 as below,

$$J_{Tot} = q \int EQE(E)\Phi_{AM1.5}(E)d(E) - J_0(e^{qv/mk_BT} - 1) \tag{2.2.9}$$

When m=1, this is the total current collection for an ideal diode.[3]

2.3 Characterisation of Solar Cells

From the previous discussion, we can describe the photovoltaic device with simplified equivalent circuit models under different conditions. In fig. 2.8a, we show an ideal diode with a photocurrent source (J_{Light}) in parallel with a diode running the dark current (J_{Dark}) in the opposite direction of J_{Light}. The device under open circuit and short circuit conditions are shown in fig. 2.8b and c. The non-ideal diode circuit having a series resistance (R_{series}) and a shunt resistance (R_{shunt}) describing the possible leakage currents in a real device architecture is shown in fig. 2.8d.

To describe the performance of a solar cell, we use the current density-voltage measurement (J-V) to characterize the device, where a working voltage range bias is applied to the device and the net current generated with and without illumination is measured. In fig. 2.9 we illustrate the typical J-V curves in the light and dark, which are offset by the generated photocurrent (J_{Light}), and a number of indicative parameters which can be extracted from the J-V measurement, such as J_{sc}, V_{oc}, the maximum power point (P_{MPP}), the fill factor (FF), and the most important one, the power conversion efficiency (PCE or η). We have introduced the physical meaning of J_{sc} and V_{oc} in the

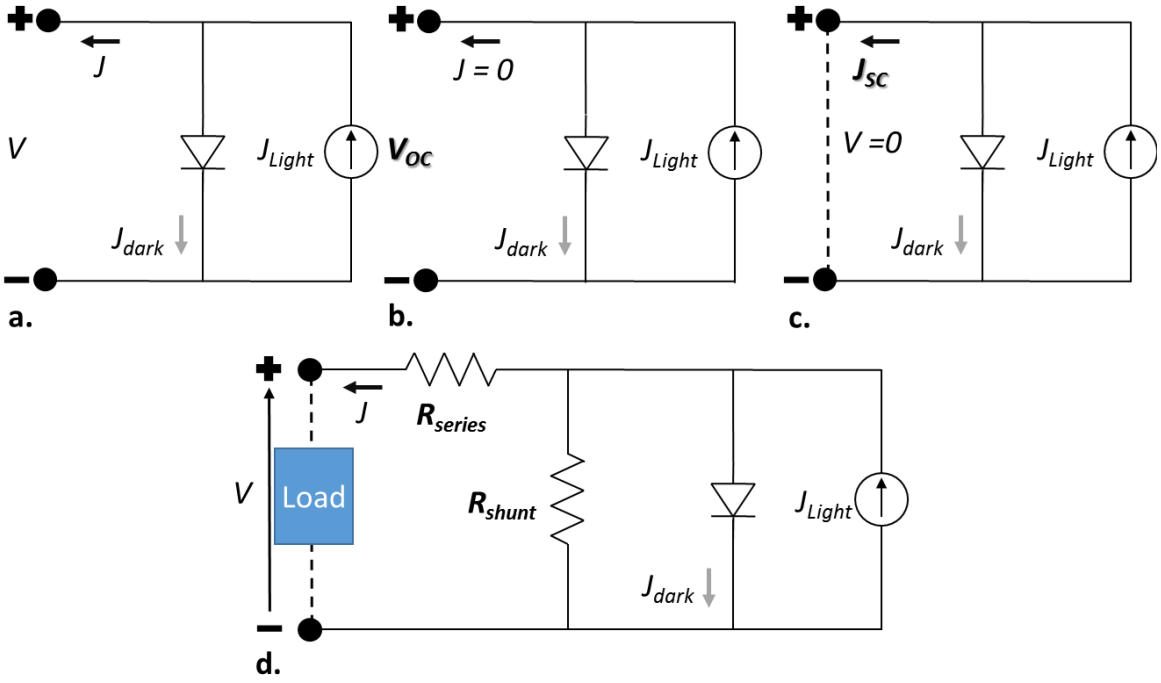


Figure 2.8: The equivalent circuit for photovoltaic devices consists of a photocurrent sources (J_{light}) generated upon illumination in parallel with a diode running the dark current (J_{dark}) showing a, the ideal diode circuit. b, when the electric circuit is isolated, the device is in the open circuit condition and the voltage across the terminals is called the open-circuit voltage (V_{oc}). c, when the circuits are connected without voltage applied, the device is in the short circuit condition, and a current flow between them is known as the short circuit current (J_{sc}). d, the non-ideal diode circuit in real devices, where a shunt resistance (R_{shunt}) and a series resistance (R_{series}) are presented in the circuit model.

previous discussion. We can observe that the intersection between light J-V curve and the x-axis (J=0), represents the V_{oc}, and that with the y-axis(V=0), represents the J_{sc}. The power density is given by P = JV, the P_{MPP} is the point where the product of J and V is maximized(J_M and V_M). Fill factor is a ratio to describe the ideality of the device, and represents the resistive and recombination losses. From the P_{MPP} and the light J-V curve's intersection we can derive the fill factor as

$$FF = \frac{J_M V_M}{J_{sc} V_{oc}} \tag{2.3.1}$$

And we can express the power conversion efficiency in a solar cell as

$$PCE = \frac{J_{sc} V_{oc} FF}{P_{in}} \tag{2.3.2}$$

Where Pin is the power density of incident radiation.

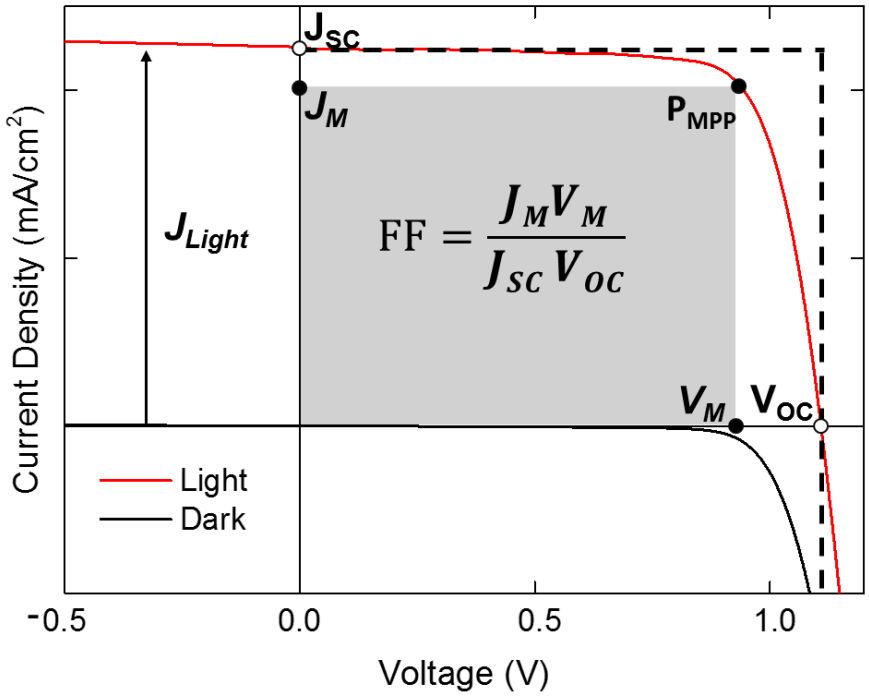


Figure 2.9: The representative light and dark J-V curves, with key parameters shown in the graph.

2.4 Principles of Perovskite Solar Cell Operation

2.4.1 Perovskite

Perovskite is a group of material has crystal structure with a general chemical formula ABX_3, where A and B are two different cations, and X is an anion. See fig. 2.10 for

details. The most common material adopted this structure is calcium titanium oxide ($CaTiO_3$). There are hundreds of materials that share this structure with a myriad of properties. Here we focus on the organic-inorganic halide hybrid perovskite materials, which own the most exceptional optoelectronic properties within the perovskite family.

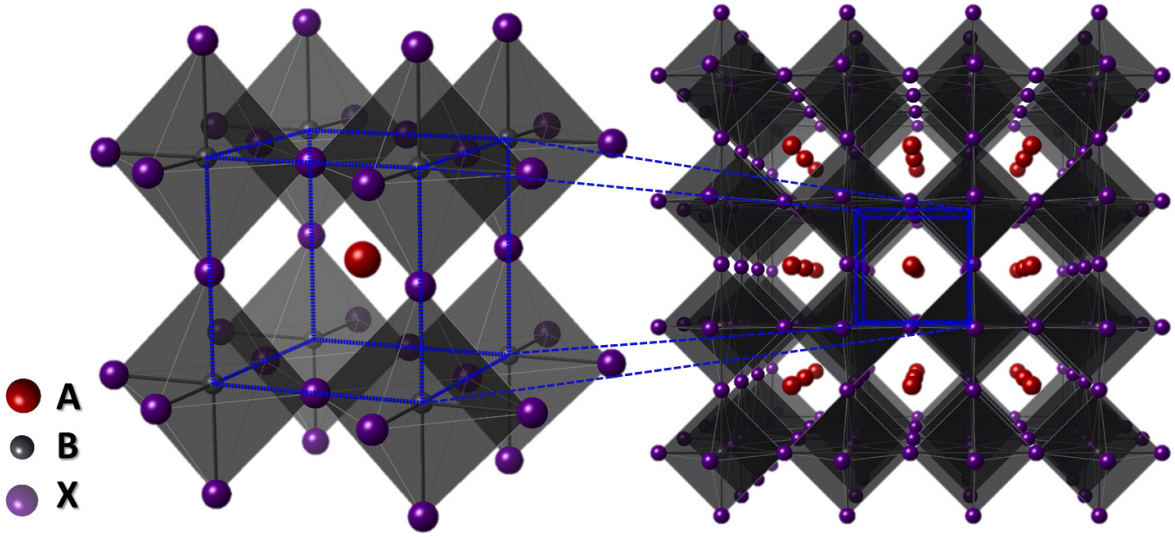


Figure 2.10: A typical 3D perovskite crystal structure in cubic phase, with a 4x4x4 supercell and its unit cell outlined in colour blue, which has a general chemical formula of ABX_3, where A and B are cations, and X as anion.

To evaluate the stability and distortion of the crystal structure and the compatibility of ions within the crystal structure, a tolerance factor (TF) is used, which was proposed by Victor Goldschmidt in 1926 as the equation below.[9]

$$TF = \frac{r_A + r_X}{\sqrt{2}(r_B + r_X)} \tag{2.4.1}$$

Where r_A, r_B, and r_X are representing the ionic radius of A, B, and X ions in an ABX_3 perovskite structure. According to Kieslich et al., if a TF falls between 0.8-1, a stable 3D perovskites can be formed, while if the TF falls outside the range, the 3D perovskite may still be formed, but also likely to result a low dimensional compound (TF>1) or a reduced packing density (TF<0.8) which lead to a perovskite-like structure material.[10] Hence,

with the TF concept as a guidance, various organic-inorganic perovskites have been investigated. In the most common composition of ABX_3, the A site is usually occupied by an organic protonated-amine cation, such as Methylammonium ($CH_3NH_3^+$, MA^+) or Formamidinium ($H_2NCNH_2^+$, FA^+), the B site is generally dominated by a divalent metal ion, such as Pb^{2+} , or Sn^{2+}, while the X site is available to halide anions such as Cl^-, Br^-, and I^-. By mixing ions in different combinations, we can influence properties such as structural stability and optical bandgap. A great deal of research effort has been focused on the methylammonium lead iodide ($CH_3NH_3PbI_3$) perovskite, since it was the first organic-inorganic perovskite being demonstrated with superior photovoltaic performance. With a bandgap of 1.55 eV, it not only has a high absorption coefficient, but also shows advantages in easy solution-based fabrication processing [11, 12]. It has a carrier diffusion lengths over 1 μm [13], and an exciton binding energy of 16 meV [14]. According to the simulations, it can potentially reach a V_{oc} of 1.3 V and a J_{sc} of 26 mA/cm^2, which gives a maximum efficiency of 31%.[15] These extraordinary properties explain why it is at the forefront of the photovoltaic research. In the following sections, we will discuss the operation mechanism and the charge transport layers which enable high-performing perovskite cells.

2.4.2 Structures of Perovskite Solar Cells

DSSC-MSSC

The perovskite was first used as a sensitizer on mesoporous TiO_2 in the liquid-electrolyte dye-sensitized solar cells by Miyasaka and co-workers in 2009.[16] A high V_{oc} of 0.96 V on $CH_3NH_3PbBr_3$, and over 10 mA/cm^2 J_{sc} on $CH_3NH_3PbI_3$ with a good starting PCE of 3.8% was achieved. Two years later, an improvement was made by Park and co-workers via preparing the $CH_3NH_3PbI_3$ perovskite as quantum dots to sensi-

tise the mesoporous TiO_2 and PCE of 6.5% was obtained with the J_{sc} elevated to 16 mA/cm^2.[17] However, $CH_3NH_3PbI_3$ perovskite cannot survive the environment of liquid-electrolyte long enough, as it tends to be dissolved in the iodide-based redox electrolyte. In 2012, almost concurrently, substantial progress was made by replacing the liquid-electrolyte with a solid-state hole transport material (HTM), namely 2,2,7,7-tetrakis-(N,N-di-p-methoxyphenyl amine)9,9-spirobifluorene (spiro-oMeTAD). A 9.7% PCE was reported with $CH_3NH_3PbI_3$ as an absorber on a mesoporous TiO_2 scaffold by Im et al.,[17] while a 10.9% PCE was realised by using $CH_3NH_3PbI_{3-x}Cl_x$ on an Al_2O_3 insulating scaffold by Lee et al., which shows the absence of a meso-TiO_2 layer, with V_{oc} over 1.1 V generated.[11] This important finding in the later work indicates the carriers can transfer freely within the perovskite layer without the need to be sensitised by the meso TiO_2. This opened up a new device architecture in the PSC field, termed as Meso-Superstructured Solar Cells (MSSCs). MSSCs have a structure of FTO\compact TiO_2\Al_2O_3+$CH_3NH_3PbI_3$\Spiro-oMeTad\Au.[11] Since then great effort has been made toward the optimising the film quality, bandgap engineering, interfacial and compositional design which lead to PCE exceeding 20% today.[18, 19, 20, 21, 22]

Planar Structure PSCs

Further structure refinement was done by Ball et al., where the first planar n-i-p structure in PSCs was realised with a simplified architecture of FTO\compact TiO_2(n-type)\$CH_3NH_3PbI_3$(intrinsic)\Spiro-oMeTad(p-type)\Au.[12] In the meanwhile, an important study revealing both hole and electron diffusion lengths exceeding 1μm further corroborated the feasibility of planar junction in PSCs.[13] Subsequently, morphology improvement was made on these thin films via processing control in their deposition techniques[23] and thermal evaporation[24] to achieve full surface coverage and minimise pinholes which pushed the PCE forward to over 15%. A champion record of

19.3% was achieved by employing a yttrium-doped compact TiO_2 in the planar n-i-p PSCs.[25] However, an anomalous hysteresis effect was being commonly found in these cells, showing unstable behaviour of these photovoltaics.[26] Since a planar structure of n-i-p architecture has proved practical, an inverse sequence architecture of p-i-n was also being demonstrated with a PCE of 3.4%, by varying the deposition sequence of transport layer from p-i-n to n-i-p on the transparent electrode, which is termed "inverted structure".[27, 28] Interestingly, in these inverted PSCs, when all the inorganic transporting layers are replaced with organic transporting layers such as conjugated polymers and fullerenes, the aforementioned hysteresis behaviour is either suppressed or disappears, which we will discuss with more details in chapter 5.

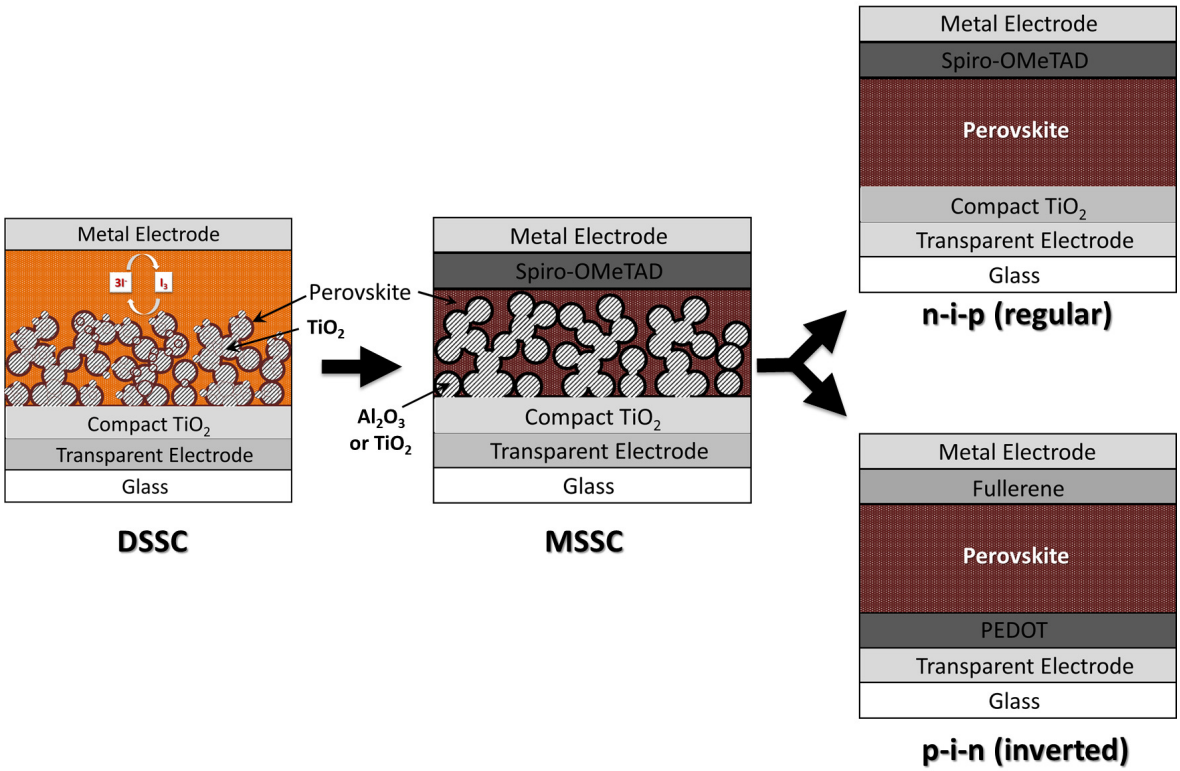


Figure 2.11: Structures evolution of perovskite solar cells, where it evolve from the DSSC to MSSC, follow by planar n-i-p or p-i-n architecture.

2.4.3 Charge Carrier Dynamics

After efficient solar cells were demonstrated[11, 24, 18], tremendous efforts in unveiling the fundamental properties of perovskite have been made. Stranks et al.[13] and Xing et al.[29] almost simultaneously reported an observation of over 100 nm carrier diffusion length (L_D) with $CH_3NH_3PbI_3$ using Time-correlated single-photon counting (TCSPC) technique, yet, a more astonishing result of L_D over 1 μm on $CH_3NH_3PbI_{3-x}Cl_x$ was uncovered by Stranks, when compared to ordinary organic photovoltaics shows two orders of magnitude higher value for the L_D.[13] It is also worth noting here, that a report of a solution-grown $CH_3NH_3PbI_3$ single crystal has recently further advanced the record carrier diffusion length to over 175 μm.[30]

Wehrenfennig et al.[31] using Terahertz spectroscopy (TS), further unveiled the kinetics of carrier recombination. They found a very low monomolecular (trap-assisted) recombination rate (k1) at ~$10^{-6}s^{-1}$, and bimolecular (electron-hole) recombination rate (k2) around 10-10 cm^3s^{-1} which defy the Langevine limit by 4 orders of magnitude, while a Auger (many-body) recombination rate (k3) shows a comparable value of ~10^{-28} cm^6s^{-1} to the strongly confined semiconductors, i.e. quantum dots, whereas Milot et al. later found the value of k3 displays a strong dependence on the structural phase of perovskite across different temperature regimes.[32]

Apart from the exceptionally long diffusion length and the low recombination rate revealed, the charge mobility reported is also quite noteworthy. A Hall effect and resistivity measurement showing an electron mobility of ~66 $cm^2V^{-1}s^{-1}$ was first presented by Stoumpos et al.[33] Later on, Wehrenfennig et al. also demonstrated an effective charge mobility of 8 $cm^2V^{-1}s^{-1}$ for $CH_3NH_3PbI_3$ and 11.6 $cm^2V^{-1}s^{-1}$ for $CH_3NH_3PbI_{3-x}Cl_x$.[31] A value of over 33 $cm^2V^{-1}s^{-1}$ for a evaporated and pin-hole free $CH_3NH_3PbI_{3-x}Cl_x$ was also reported.[34]

In section 2.2.2, we discussed the different types of excitons in semiconductors and their behaviour. The Coulombic force between the electron-hole pair plays a dominant role in a solar cell operation; thus, many investigations have been made to better understand excitons in perovskites, as the quest for a more clear picture of the fundamental properties intensifies. There has been a very wide range of exciton binding enery (2 to 62 meV) reported since early 1990.[35, 36] The first study disclosed a value of 37 meV deriving from the diamagnetic shifts in the magnetoabsorption measurement on a bulk $CH_3NH_3PbI_3$. However, later on, a value of 50 meV was reported using a comparable experiment approach.[36] This is a result of the use of the dielectric constant (ϵ) to evaluate the exciton binding energy (E_b) which was varied as a function of both frequency and temperature.[37] More attempts were made via the temperature dependence of the PL intensity[38, 39], absorption onsets[40, 41], but these are still not giving a conclusive result yet. Recently, Miyata et al. were able to determine the (E_b with a value of 16 meV at 4 K, and few meV at room temperature, with an effective mass of 0.104 me (electron mass) via the direct observation of both 1s and 2s excitonic features, and circumvent the need to evaluate base on the value of ϵ. This finding indicates a free-carrier behaviour (Wannier-Mott model) and the thermal energy at room temperature is enough to dissociate the exciton already.[42]

More recently, a photon recycling effect in perovskite has been reported by Pazos-Outon et al., showing the absorption and reemission of excited carriers occurs many times during the carrier transport within the perovskite by probing the build-up of the internal photon gas and monitoring the propagation of photogenerated luminescence in a thin film $CH_3NH_3PbI_3$. These effects can be further improved by reducing nonradiative decay pathways or using higher fluences, where radiative decay pathways dominate.[43]

In sum, these extraordinary dynamic features can support the exceptional performance observed in perovskite photovoltaics, and lay out the guidelines for more exciting dis-

coveries to be made.

2.4.4 Operation Mechanism

The operation mechanism in PSCs is fairly straightforward, and can be explained in a simplified scenario. Once a photon is absorbed by the perovskite, an electron-hole pair is created, as mentioned in the section 2.2.2, the charge-transporting layers are the prerequisite to separate the pair efficiently. Here, we can briefly list the operation mechanisms of a typical planar perovskite solar cell (consisting of intrinsic, n-type, and p-type layers) as below, which we also illustrate in the fig. 2.12.

1. After photons are absorbed in the perovskite, electrons and holes are excited into CB and VB, respectively.

2. Electrons are injected into the conduction band of the ETM, which has a deep valance band to prevent hole injection.

3. If the ETM has the sub-band gap states, the electron transport may be limited by trapping and de-trapping process.

4. Holes are injected into the valence band of the HTM, which has a high conduction band to prevent electron injection.

5. Hole transport is via a hopping mechanism.

Here, one can see the charge transporting layer, plays a key role in facilitating the current generation. In the next section, we will discuss the interfacial transporting layers in more detail.

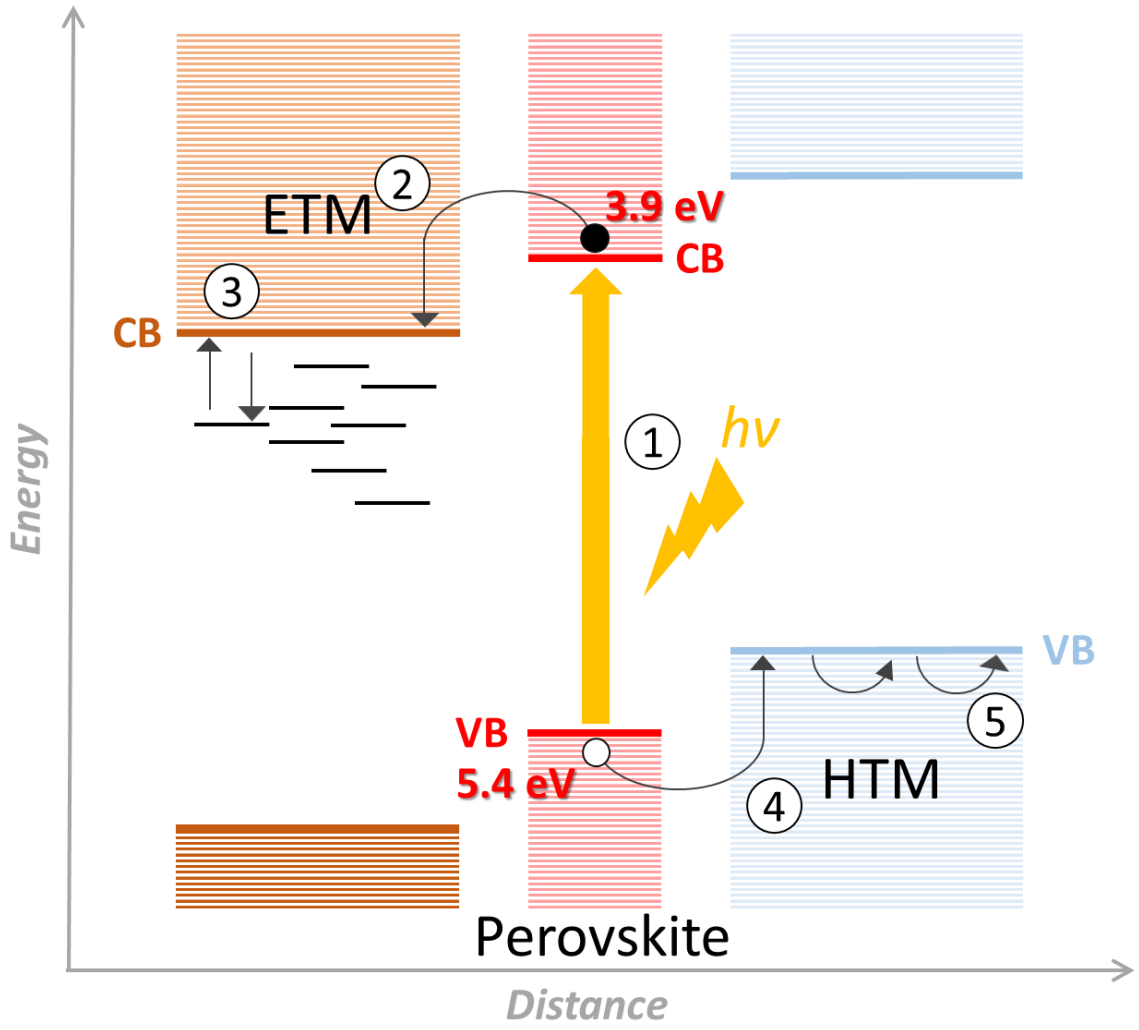


Figure 2.12: The operation mechanism for a perovskite solar cell with energy level diagram and numbering for the key processes for charge generation and trans-portation: 1. Exciton generated by photon absorption; 2. Electron injected into ETM's conduction band; 3. If the ETM has sub-band gap states, the electron transport may be limited by trapping and de-trapping proccesses; 4. Hole injected into HTM; 5. Hole transport via hopping mechanism.

2.5 Interlayers

The interlayers play a significant role in facilitating charge separation. As discussed in the section 2.2.2 and 2.2.3, once the electron-hole pairs are generated, it is critical to separate these charges before they recombine which would lead to a loss of photocurrent. The faster the carriers can be removed from the interface, the better chance to avoid a loss mechanism they have. To achieve the rapid charge extraction from the interface, the insertion of interlayers is essential. Clearly, the function of the interlayers dictate the performance of the solar cells. Since the earliest development of the organic photovoltaics (OPV), the employment of the interlayers was common. Accordingly, tremendous efforts have been made to understand the function of the interfacial layer and drive the OPV device performance forward.[44, 45, 46, 47, 48, 49, 50] Here, the same concepts can be readily applied to the development of efficient PSCs. Energy level alignment is the most vital and the first factor we need to consider when designing a photovoltaic device. Altering the energy level of interfacial layers to match with the band edges of the perovskite can minimise the potential loss. As in a heterojunction photovoltaic device, upon illumination, the generation of electron-hole pairs would disturb the equilibrium of Fermi levels, which split into the electron-quasi-Fermi levels (E_{Fn}) and hole-quasi-Fermi levels (E_{Fp}), respectively, where the difference between E_{Fn} and E_{Fp} determines the V_{oc} of the solar cell.[51] In addition to the enhanced V_{oc}; matching energy levels also lead to an increase in J_{sc} and FF by facilitating carrier extraction and collection with reduced energy barriers. Therefore, altering the energy levels (i.e. chemical doping, stacking of multi-interfacial layers, etc.) of electron-transporting materials (ETM) and hole-transporting materials (HTM) is a popular approach to improve device performance.

The carrier mobility of an interlayer is another important factor that governs the performance of photovoltaics. Since carriers need to be efficiently transported and collected on each side, high mobility is desirable to minimise the possibility of recombination.

Improving interface between layers by employing self-assembled molecules at the interfaces or altering the dipole moment on the surface.[52] has been found to be a useful way to improve the wetting between layers[53]. Promoting the surface morphology and properties at an interface are also efficient methods to boost device performance.

In addition to improve the contacts, avoiding unfavourable contacts can also be beneficial; Chemical reactions between metal/organic layers are found to influence the contact behaviour and lead to "S-shape" J-V curves which affect the V_{oc}, J_{sc}, and FF.[54] An inert buffer layer inserted between metal/organic interfaces has been proven to successfully avoid such undesirable feature and act as an optical spacer to enhance current collection.[55, 48]

From here, the primary function of an interlayer can be summarised as having one or more of the following functions:

1. Form a selective contact for electrons and holes respectively.

2. Facilitate charge extraction and injection by reducing the energy barrier.

3. Modify surface properties/relative polarity for better film formation.

4. Suppress reaction between the metal/organic or organic/organic interface.

5. Act as an optical spacer to increase the photocurrent collection.

Where all roles are related, and simultaneously influence each other.It is therefore critical to understand the operation principles of the interlayers to achieve the maximum performance of the device.

2.5.1 Electron-Transporting Layer (ETL)

The ideal electron-transporting layer should have a LUMO/CB energy level that is compatible with the conduction band of perovskite. Preferably it can also serve as a hole blocking layer to minimise charge recombination, see fig. 2.12. Additionally, minimal absorption spectrum overlap with perovskite, and superior thermal and photochemical stability are also desired qualities of a good ETL. Since the dominant charge carriers in a n-type layer are electrons, the electron conductivity and mobility are vital to the intrinsic electrical properties of the electron transporting materials (ETM), which can be classed into two categories, inorganic metal oxides, and organic molecules. In PSCs, the most common ETM is TiO_2. The first perovskite-based photovoltaic was demonstrated on a DSSC, where the compact TiO_2 and mesoporous TiO_2 both played indispensable role in the electron extraction and collection.[16] The presence of meso-TiO_2 layers in the regular PSCs structure, have been found to influence the hysteresis J-V behaviour.[56] However, drawbacks are also being reported; it has been found that there are substantial numbers of electron trap states existing within the TiO_2 layer varying from 1 eV to just below the CB edge, which are mainly contributed to by defects such as oxygen vacancies, grain boundaries, and poor electrical contact between TiO_2 particles (will be discussed in chapter 4 with more details).[57, 58] Additionally, a critical instability has been identified from the photo-induced desorption of surface-adsorbed oxygen on TiO_2 which causes severe degradation of solar cells over its long-term operation.[59] As a result, replacement of metal oxides sharing similar energy alignment with TiO_2 are being sought, such as ZnO[60], SnO_2[61], and WO_x[62], or the hybrid composites, such as TiO_2-SAM[63], TiO_2-graphene[64] or WO_x-TiO_2[65]. These all may be good candidate materials for an ETL. On the other hand, organic-based ETMs have also emerged as potential candidate in the quest for a better ETL. Fullerene molecules, PCBM, first debuted in the inverted architecture of PSCs, where it inherits the structure from the OPV, are showing

comparable performance to the regular structure with negligible hysteresis.[66, 28, 67] Pure fullerene (C60)[68] and its derivatives are also being reported, such as ICBA[66], $PC_{71}BM$[69], and IPH[70], where they boast an adjustable work function to align their energy level with perovskite via chemical synthesis, and faster charge extraction properties (high mobility or conductivity via doping) than the normal metal oxides, allowing them achieve efficient electron transportation.

2.5.2 Hole-Transporting Layer (HTL)

As with the ETL, the HTL, plays the same important role in extracting and transporting carriers, but for holes. It concurrently serves as an electron blocking layer to suppress radiative recombination. Typical HTL materials are usually formed by organics, due to their flexibility of manipulation and preparation and also because it is relatively straightforward to modify the properties of hole-transporting materials (HTM) via chemical synthesis. These HTMs share some of the same requirements as the ETMs have: close energy level alignments (HTM's HOMO to the VB of perovskite), high carrier mobility, few trap states, and uniform morphology at the interface.

Evolving from the ssDSSCs, the first solid-state HTM being that was applied to the PSCs was the small organic molecule, Spiro-OMeTAD. It showed a PCE of 9%[71]. It is still the most widely used HTM for PSCs. Recently, Saliba et al. have demonstrated the impressive PCE of 21% based on the triple cation (Cs/FA/MA) lead perovskite in a regular structure with Spiro-OMeTAD as the HTM.[72]

Though Spiro-OMeTAD is still among one of the best HTMs, the requirement for additional dopants (Li-TFSI, tbp) and its oxygen-induced doping, make it difficult to control and time-consuming.[73]

The synthesis of Spiro-OMeTAD involves multi-step reactions and several purification

processes which lead to a high fabrication cost, thus limiting its large-scale commercial viability.[74] Therefore, scientists have been searching to find an alternative to replace Spiro-OMeTAD. In the quest for the ideal HTM, various types of materials have been proposed, including organic molecules[75],conducting polymers[27, 28, 76], carbon nanotubes[77, 78], and inorganic materials.[28, 66, 79, 80] Poly(tertiary arylamine) (PTAA) by far is the best performing contestant and have demonstrated a PCE exceeding 20%.[22]

It is worth noting here, that in a regular structure, a thicker(>100 nm) HTL is required to reach full coverage on top of the perovskite layer to prevent short circuits, but in the inverted structure, only a thin layer (<100 nm) of HTM is required. However, layers that are too thick would also result in higher R_{series}, therefore, it is critical to balance between the hole-conductivity and the shunt resistance with optimum HTL thickness to obtain the best device performance.

2.5.3 Electrodes and Buffer Layers

A typical solar cell design usually makes use of a transparent electrode in the front and a metal electrode at the back to collect the photogenerated current. An ideal electrode is desired to have qualities including low sheet resistance, high chemical stability, low cost, and a matching energy level respect to its collecting carriers. For a transparent electrode, the high transparency is the prerequisite. The most common transparent electrode is Fluorine doped Tin Oxide (FTO), given its robustness for high-temperature fabrication and chemical inertness, it is a very suitable anode for the preparation of n-type compact and mesoporous TiO_2 layer in the regular structure of PSCs. While in the inverted structure, Indium tin oxide (ITO) is more widely used as a cathode, given its high conductivity and transparency. With its higher work function, it is more preferable for the p-i-n architecture. However, the inclusion of the rare element Indium makes

ITO relatively expensive. Nevertheless, it is still being widely adopted by community and industry due to its virtues. For metal electrodes, the noble elements of Ag and Au are widely used as the cathode in the regular structure of PSCs, for their matching energy levels and easily accessible deposition method (eveaporation). While for inverted structure, a combination of a thin buffer layer (i.e. LiF or small organic molecules) and a dual metal layer consisting of a lower work function metal (i.e., Ca, Ba) with Al or Ag is widely used as the anode to facilitate electron injection/collection.[27, 70, 81] However, it is reported that a degraded interface was observed in the ambient environment between the perovskite layer and metal electrodes including silver and aluminium.[82] As for gold, it is widely recognised for its superior chemical inertness compared to silver and aluminium, but with a mild degradation still being reported.[83] These degradation behaviours have been attributed to the presence of high moisture or heat induced chemical reaction between the perovskite and the metals.[84]

References

[1] Simon M. Sze and Kwok K. Ng. *Physics of Semiconductor Devices*, volume 3. John Wiley & Sons, 2006.

[2] H. M. Rosenberg. *The Solid State: An Introduction to the Physics of Solid State Materials.* Oxford University Press, 1995.

[3] Jenny Nelson. *The Physics of Solar Cells.* Imperial College Press, may 2003.

[4] Peter Würfel and Uli Würfel. *Physics of Solar Cells: From Basic Principles to Advanced Concepts.* John Wiley & Sons, 2009.

[5] AE Becquerel. On electric effects under the influence of solar radiation. *CR Acad. Sci*, 9(711-4), 1839.

[6] Solar Spectral Irradiance: Air Mass 1.5, 1999.

[7] Martin Pope and Charles E. Swenberg. *Electronic Processes in Organic Crystals and Polymers.* Oxford University Press, 1999.

[8] K. Taretto, U. Rau, and J. H. Werner. Method to extract diffusion length from solar cell parameters—Application to polycrystalline silicon. *Journal of Applied Physics*, 93(9):5447, 2003.

[9] V. M. Goldschmidt. Die Gesetze der Krystallochemie. *Die Naturwissenschaften*, 14(21):477–485, may 1926.

[10] Gregor Kieslich, Shijing Sun, and Anthony K. Cheetham. An extended Tolerance Factor approach for organic–inorganic perovskites. *Chem. Sci.*, 6(6):3430–3433, may 2015.

[11] Michael M. Lee, Joël Teuscher, Tsutomu Miyasaka, Takurou N. Murakami, and Henry J. Snaith. Efficient Hybrid Solar Cells Based on Meso-Superstructured Organometal Halide Perovskites. *Science*, 338(6107):643–647, nov 2012.

[12] James M. Ball, Michael M. Lee, Andrew Hey, and Henry J. Snaith. Low-temperature processed meso-superstructured to thin-film perovskite solar cells. *Energy & Environmental Science*, 6(6):1739, 2013.

[13] Samuel D Stranks, Giles E Eperon, Giulia Grancini, Christopher Menelaou, Marcelo J P Alcocer, Tomas Leijtens, Laura M Herz, Annamaria Petrozza, and Henry J Snaith. Electron-hole diffusion lengths exceeding 1 micrometer in an organometal trihalide perovskite absorber. *Science (New York, N.Y.)*, 342(6156):341–344, oct 2013.

[14] Atsuhiko Miyata, Anatolie Mitioglu, Paulina Plochocka, Oliver Portugall, Jacob Tse-Wei Wang, Samuel D. Stranks, Henry J. Snaith, and Robin J. Nicholas. Direct measurement of the exciton binding energy and effective masses for charge carriers in organic–inorganic tri-halide perovskites. *Nature Physics*, 11(7):582–587, jun 2015.

[15] Wei E. I. Sha, Xingang Ren, Luzhou Chen, and Wallace C. H. Choy. The efficiency limit of CH3NH3PbI3 perovskite solar cells. *Applied Physics Letters*, 106(22):221104, jun 2015.

[16] Akihiro Kojima, Kenjiro Teshima, Yasuo Shirai, and Tsutomu Miyasaka. Organometal Halide Perovskites as Visible-Light Sensitizers for Photovoltaic Cells. *Journal of the American Chemical Society*, 131(17):6050–6051, may 2009.

[17] Jeong-Hyeok Im, Chang-Ryul Lee, Jin-Wook Lee, Sang-Won Park, and Nam-Gyu Park. 6.5% Efficient Perovskite Quantum-Dot-Sensitized Solar Cell. *Nanoscale*, 3(10):4088, oct 2011.

[18] Julian Burschka, Norman Pellet, Soo-Jin Moon, Robin Humphry-Baker, Peng Gao, Mohammad K Nazeeruddin, and Michael Grätzel. Sequential deposition as a route to high-performance perovskite-sensitized solar cells. *Nature*, 499(7458):316–319, jul 2013.

[19] Jeong-Hyeok Im, In-Hyuk Jang, Norman Pellet, Michael Grätzel, and Nam-Gyu Park. Growth of CH3NH3PbI3 cuboids with controlled size for high-efficiency perovskite solar cells. *Nature nanotechnology*, 9:927–932, aug 2014.

[20] Nam Joong Jeon, Jun Hong Noh, Young Chan Kim, Woon Seok Yang, Seungchan Ryu, and Sang Il Seok. Solvent engineering for high-performance inorganic-organic hybrid perovskite solar cells. *Nature Materials*, 13:1–7, 2014.

[21] Nam Joong Jeon, Jun Hong Noh, Woon Seok Yang, Young Chan Kim, Seungchan Ryu, Jangwon Seo, and Sang Il Seok. Compositional engineering of perovskite materials for high-performance solar cells. *Nature*, 517:476–480, jan 2015.

[22] Woon Seok Yang, Jun Hong Noh, Nam Joong Jeon, Young Chan Kim, Seungchan Ryu, Jangwon Seo, and Sang Il Seok. High-performance photovoltaic perovskite layers fabricated through intramolecular exchange. *Science*, 348(6240):1234–1237, jun 2015.

[23] Giles E. Eperon, Victor M. Burlakov, Pablo Docampo, Alain Goriely, and Henry J. Snaith. Morphological control for high performance, solution-processed planar heterojunction perovskite solar cells. *Advanced Functional Materials*, 24(1):151–157, sep 2014.

[24] Mingzhen Liu, Michael B Johnston, and Henry J Snaith. Efficient planar heterojunction perovskite solar cells by vapour deposition. *Nature*, 501(7467):395–398, sep 2013.

[25] H Zhou, Q Chen, G Li, S Luo, T.-b. Song, H.-S. Duan, Z Hong, J You, Y Liu, and Y Yang. Interface engineering of highly efficient perovskite solar cells. *Science*, 345(6196):542–546, jul 2014.

[26] Henry J. Snaith, Antonio Abate, James M. Ball, Giles E. Eperon, Tomas Leijtens, Nakita K. Noel, Samuel D. Stranks, Jacob Tse Wei Wang, Konrad Wojciechowski, and Wei Zhang. Anomalous hysteresis in perovskite solar cells. *Journal of Physical Chemistry Letters*, 5(9):1511–1515, mar 2014.

[27] Jun Yuan Jeng, Yi Fang Chiang, Mu Huan Lee, Shin Rung Peng, Tzung Fang Guo, Peter Chen, and Ten Chin Wen. CH3NH3PbI3 perovskite/fullerene planar-heterojunction hybrid solar cells. *Advanced Materials*, 25(27):3727–3732, jul 2013.

[28] Pablo Docampo, James M Ball, Mariam Darwich, Giles E Eperon, and Henry J Snaith. Efficient organometal trihalide perovskite planar-heterojunction solar cells on flexible polymer substrates. *Nature communications*, 4:2761, jan 2013.

[29] Guichuan Xing, Nripan Mathews, Shuangyong Sun, Swee Sien Lim, Yeng Ming Lam, Michael Grätzel, Subodh Mhaisalkar, and Tze Chien Sum. Long-range balanced electron- and hole-transport lengths in organic-inorganic CH3NH3PbI3. *Science*, 342(6156):344–347, oct 2013.

[30] Hua Dong, Zhaoxin Wu, Bin Xia, Jun Xi, Fang Yuan, Shuya Ning, Lixin Xiao, and Xun Hou. Modified deposition process of electron transport layer for efficient inverted planar perovskite solar cells. *Chem. Commun.*, apr 2015.

[31] Christian Wehrenfennig, Giles E. Eperon, Michael B. Johnston, Henry J. Snaith, and Laura M. Herz. High charge carrier mobilities and lifetimes in organolead trihalide perovskites. *Advanced Materials*, 26(10):1584–1589, mar 2014.

[32] Rebecca L Milot, Giles E Eperon, Henry J Snaith, Michael B Johnston, and Laura M Herz. Temperature-Dependent Charge-Carrier Dynamics in CH3NH3PbI3 Perovskite Thin Films. *Advanced Functional Materials*, 25(39):6218–6227, sep 2015.

[33] Constantinos C Stoumpos, Christos D Malliakas, and Mercouri G Kanatzidis. Semiconducting Tin and Lead Iodide Perovskites with Organic Cations: Phase Transitions, High Mobilities, and Near-Infrared Photoluminescent Properties. *Inorganic Chemistry*, 52(15):9019–9038, aug 2013.

[34] Christian Wehrenfennig, Mingzhen Liu, Henry J. Snaith, Michael B. Johnston, and Laura M. Herz. Charge-carrier dynamics in vapour-deposited films of the organolead halide perovskite CH3NH3PbI3xClx. *Energy & Environmental Science*, 7(7):2269, jun 2014.

[35] M Hirasawa, T Ishihara, T Goto, K Uchida, and N Miura. Magnetoabsorption of the lowest exciton in perovskite-type compound (CH3NH3)PbI3. *Physica B: Condensed Matter*, 201(July–August):427–430, 1994.

[36] K Tanaka, T Takahashi, T Ban, T Kondo, K Uchida, and N Miura. Comparative Study in the Excitons in Lead- Halide based Perovskite-type Crystals CH3NH3PbBr3 CH3NH3PbI3. *Solid State Communications*, 127(9-10):619–623, sep 2003.

[37] Laura M Herz. Charge-Carrier Dynamics in Organic-Inorganic Metal Halide Perovskites. *Annual review of physical chemistry*, feb 2016.

[38] Shuangyong Sun, Teddy Salim, Nripan Mathews, Martial Duchamp, Chris Boothroyd, Guichuan Xing, Tze Chien Sum, and Yeng Ming Lam. The origin of high efficiency in low-temperature solution-processable bilayer organometal halide hybrid solar cells. *Energy {&} Environmental Science*, 7(1):399, 2014.

[39] Tom J. Savenije, Carlito S. Ponseca, Lucas Kunneman, Mohamed Abdellah, Kaibo Zheng, Yuxi Tian, Qiushi Zhu, Sophie E. Canton, Ivan G. Scheblykin, Tonu Pullerits, Arkady Yartsev, and Villy Sundström. Thermally activated exciton dissociation and recombination control the carrier dynamics in organometal halide perovskite. *Journal of Physical Chemistry Letters*, 5(13):2189–2194, jun 2014.

[40] Valerio D'Innocenzo, Giulia Grancini, Marcelo J P Alcocer, Ajay Ram Srimath Kandada, Samuel D Stranks, Michael M Lee, Guglielmo Lanzani, Henry J Snaith, and Annamaria Petrozza. Excitons versus free charges in organo-lead tri-halide perovskites. *Nature communications*, 5:3586, apr 2014.

[41] Jacky Even, Laurent Pedesseau, and Claudine Katan. Analysis of multivalley and multibandgap absorption and enhancement of free carriers related to exciton screening in hybrid perovskites. *Journal of Physical Chemistry C*, 118(22):11566–11572, may 2014.

[42] Atsuhiko Miyata, Anatolie Mitioglu, Paulina Plochocka, Oliver Portugall, Jacob Tse-Wei Wang, Samuel D. Stranks, Henry J. Snaith, and Robin J. Nicholas. Direct measurement of the exciton binding energy and effective masses for charge carriers in organic–inorganic tri-halide perovskites. *Nature Physics*, 11:582–587, 2015.

[43] L. M. Pazos-Outon, M. Szumilo, R. Lamboll, J. M. Richter, M. Crespo-Quesada, M. Abdi-Jalebi, H. J. Beeson, M. Vru ini , M. Alsari, H. J. Snaith, B. Ehrler, R. H. Friend, and F. Deschler. Photon recycling in lead iodide perovskite solar cells. *Science*, 351(6280):1430–1433, mar 2016.

[44] Y. Hirose, A. Kahn, V. Aristov, P. Soukiassian, V. Bulovic, and S. R. Forrest. Chemistry and electronic properties of metal-organic semiconductor interfaces: Al, Ti, In, Sn, Ag, and Au on PTCDA. *Physical Review B*, 54(19):13748–13758, nov 1996.

[45] Hisao Ishii, Kiyoshi Sugiyama, Eisuke Ito, and Kazuhiko Seki. Energy Level Alignment and Interfacial Electronic Structures at Organic/Metal and Organic/Organic Interfaces. *Advanced Materials*, 11(8):605–625, jun 1999.

[46] P. Peumans, V. Bulovic, and S. R. Forrest. Efficient photon harvesting at high optical intensities in ultrathin organic double-heterostructure photovoltaic diodes. *Applied Physics Letters*, 76(19):2650, may 2000.

[47] V. D. Mihailetchi, P. W. M. Blom, J. C. Hummelen, and M. T. Rispens. Cathode dependence of the open-circuit voltage of polymer:fullerene bulk heterojunction solar cells. *Journal of Applied Physics*, 94(10):6849, oct 2003.

[48] M. Vogel, S. Doka, Ch. Breyer, M. Ch. Lux-Steiner, and K. Fostiropoulos. On the function of a bathocuproine buffer layer in organic photovoltaic cells. *Applied Physics Letters*, 89(16):163501, oct 2006.

[49] Li-Min Chen, Zheng Xu, Ziruo Hong, and Yang Yang. Interface investigation and engineering – achieving high performance polymer photovoltaic devices. *Journal of Materials Chemistry*, 20(13):2575, mar 2010.

[50] Roland Steim, F. René Kogler, and Christoph J. Brabec. Interface materials for organic solar cells. *Journal of Materials Chemistry*, 20(13):2499, mar 2010.

[51] Boyuan Qi and Jizheng Wang. Open-circuit voltage in organic solar cells. *Journal of Materials Chemistry*, 22(46):24315, nov 2012.

[52] S. Khodabakhsh, B. M. Sanderson, J. Nelson, and T. S. Jones. Using Self-Assembling Dipole Molecules to Improve Charge Collection in Molecular Solar Cells. *Advanced Functional Materials*, 16(1):95–100, jan 2006.

[53] Mariano Campoy-Quiles, Toby Ferenczi, Tiziano Agostinelli, Pablo G. Etchegoin, Youngkyoo Kim, Thomas D. Anthopoulos, Paul N. Stavrinou, Donal D. C. Bradley, and Jenny Nelson. Morphology evolution via self-organization and lateral and vertical diffusion in polymer:fullerene solar cell blends. *Nature Materials*, 7(2):158–164, jan 2008.

[54] Ankit Kumar, Srinivas Sista, and Yang Yang. Dipole induced anomalous S-shape I-V curves in polymer solar cells. *Journal of Applied Physics*, 105(9):094512, may 2009.

[55] J.Y. Kim, S.H. Kim, H.-H. Lee, K. Lee, W. Ma, X. Gong, and A.J. Heeger. New Architecture for High-Efficiency Polymer Photovoltaic Cells Using Solution-Based Titanium Oxide as an Optical Spacer. *Advanced Materials*, 18(5):572–576, mar 2006.

[56] Hui-Seon Kim and Nam-Gyu Park. Parameters Affecting I-V Hysteresis of CH3NH3PbI3 Perovskite Solar Cells: Effects of Perovskite Crystal Size and Mesoporous TiO2 Layer. *The journal of physical chemistry letters*, 5(17):2927–34, sep 2014.

[57] Juan Bisquert. Hopping Transport of Electrons in Dye-Sensitized Solar Cells. *The Journal of Physical Chemistry C*, 111(46):17163–17168, nov 2007.

[58] Anders Hagfeldt, Gerrit Boschloo, Licheng Sun, Lars Kloo, and Henrik Pettersson. Dye-Sensitized Solar Cells. *Chemical Reviews*, 110(11):6595–6663, 2010.

[59] Tomas Leijtens, Giles E Eperon, Sandeep Pathak, Antonio Abate, Michael M Lee, and Henry J Snaith. Overcoming ultraviolet light instability of sensitized TiO with meso-superstructured organometal tri-halide perovskite solar cells. *Nature communications*, 4:2885, jan 2013.

[60] Dianyi Liu and Timothy L. Kelly. Perovskite solar cells with a planar heterojunction structure prepared using room-temperature solution processing techniques. *Nature Photonics*, 8(2):133–138, dec 2013.

[61] Weijun Ke, Guojia Fang, Qin Liu, Liangbin Xiong, Pingli Qin, Hong Tao, Jing Wang, Hongwei Lei, Borui Li, Jiawei Wan, Guang Yang, and Yanfa Yan. Low-Temperature Solution Processed Tin Oxide as an Alternative Electron Transporting Layer for Efficient Perovskite Solar Cells. *Journal of the American Chemical Society*, may 2015.

[62] Kai Wang, Yantao Shi, Qingshun Dong, Yu Li, Shufeng Wang, Xufeng Yu, Mengyao Wu, and Tingli Ma. Low Temperature and Solution Processed Amorphous WOX as Electron Selective Layer for Perovskite Solar Cells. *The Journal of Physical Chemistry Letters*, 6:755–759, feb 2015.

[63] Konrad Wojciechowski, Samuel D Stranks, Antonio Abate, Golnaz Sadoughi, Aditya Sadhanala, Nikos Kopidakis, Garry Rumbles, Chang-Zhi Li, Richard H Friend, Alex K-Y Jen, and Henry J Snaith. Heterojunction modification for highly efficient organic-inorganic perovskite solar cells. *ACS nano*, 8(12):12701–9, dec 2014.

[64] Jacob Tse-Wei Wang, James M. Ball, Eva M. Barea, Antonio Abate, Jack A. Alexander-Webber, Jian Huang, Michael Saliba, Ivan Mora-Sero, Juan Bisquert, Henry J. Snaith, and Robin J. Nicholas. Low-temperature processed electron collection layers of graphene/TiO2 nanocomposites in thin film perovskite solar cells. *Nano letters*, (2):724–30, feb.

[65] Kai Wang, Yantao Shi, Bo Li, Liang Zhao, Wei Wang, Xiangyuan Wang, Xiaogong Bai, Shufeng Wang, Ce Hao, and Tingli Ma. Amorphous Inorganic Electron-Selective Layers for Efficient Perovskite Solar Cells: Feasible Strategy Towards Room-Temperature Fabrication. *Advanced materials (Deerfield Beach, Fla.)*, 28(9):1891–7, mar 2016.

[66] Jun Yuan Jeng, Kuo Cheng Chen, Tsung Yu Chiang, Pei Ying Lin, Tzung Da Tsai, Yun Chorng Chang, Tzung Fang Guo, Peter Chen, Ten Chin Wen, and Yao Jane Hsu. Nickel oxide electrode interlayer in CH3NH3PbI 3 perovskite/PCBM planar-heterojunction hybrid solar cells. *Advanced Materials*, 26(24):4107–4113, mar 2014.

[67] Yuchuan Shao, Zhengguo Xiao, Cheng Bi, Yongbo Yuan, and Jinsong Huang. Origin and elimination of photocurrent hysteresis by fullerene passivation in CH3NH3PbI3 planar heterojunction solar cells. *Nature Communications*, 5:5784, dec 2014.

[68] Konrad Wojciechowski, Tomas Leijtens, Svetlana Siprova, Christoph Schlueter, Maximilian T Hörantner, Jacob Tse-Wei Wang, Chang-Zhi Li, Alex K-Y Jen, Tien-Lin Lee, and Henry J Snaith. C60 as an Efficient n-Type Compact Layer in Perovskite Solar Cells. *The journal of physical chemistry letters*, 6(12):2399–405, jun 2015.

[69] Chien-Hung Chiang, Zong-Liang Tseng, and Chun-Guey Wu. Planar heterojunction perovskite/PC 71 BM solar cells with enhanced open-circuit voltage via a (2/1)-step spin-coating process. *J. Mater. Chem. A*, 2(38):15897–15903, jul 2014.

[70] Lidón Gil-Escrig, Cristina Momblona, Michele Sessolo, and Henk J. Bolink. Fullerene imposed high open-circuit voltage in efficient perovskite based solar cells. *J. Mater. Chem. A*, 4(10):3667–3672, mar 2016.

[71] Hui-Seon Kim, Chang-Ryul Lee, Jeong-Hyeok Im, Ki-Beom Lee, Thomas Moehl, Arianna Marchioro, Soo-Jin Moon, Robin Humphry-Baker, Jun-Ho Yum, Jacques E Moser, Michael Grätzel, and Nam-Gyu Park. Lead iodide perovskite sensitized all-solid-state submicron thin film mesoscopic solar cell with efficiency exceeding 9{%}. *Scientific reports*, 2:591, jan 2012.

[72] Michael Saliba, Taisuke Matsui, Ji-Youn Seo, Konrad Domanski, Juan-Pablo Correa-Baena, Nazeeruddin Mohammad K., Shaik M Zakeeruddin, Wolfgang Tress, Antonio Abate, Anders Hagfeldt, and Michael Grätzel. Cesium-containing Triple Cation Perovskite Solar Cells: Improved Stability, Reproducibility and High Efficiency. *Energy Environ. Sci.*, mar 2016.

[73] Ute B Cappel, Torben Daeneke, and Udo Bach. Oxygen-induced doping of spiro-MeOTAD in solid-state dye-sensitized solar cells and its impact on device performance. *Nano letters*, 12(9):4925–31, sep 2012.

[74] Kai Zhang, Ling Wang, Yanliang Liang, Siqi Yang, Jing Liang, Fangyi Cheng, and Jun Chen. A thermally and electrochemically stable organic hole-transporting material with an adamantane central core and triarylamine moieties. *Synthetic Metals*, 162(5-6):490–496, apr 2012.

[75] Nam Joong Jeon, Jaemin Lee, Jun Hong Noh, Mohammad Khaja Nazeeruddin, Michael Grätzel, and Sang Il Seok. Efficient inorganic-organic hybrid perovskite solar cells based on pyrene arylamine derivatives as hole-transporting materials. *Journal of the American Chemical Society*, 135(51):19087–90, dec 2013.

[76] Jin Hyuck Heo, Sang Hyuk Im, Jun Hong Noh, Tarak N. Mandal, Choong-Sun Lim, Jeong Ah Chang, Yong Hui Lee, Hi-jung Kim, Arpita Sarkar, Md. K. Nazeeruddin, Michael Grätzel, and Sang Il Seok. Efficient inorganic–organic hybrid heterojunction solar cells containing perovskite compound and polymeric hole conductors. *Nature Photonics*, 7(6):486–491, may 2013.

[77] Severin N Habisreutinger, Tomas Leijtens, Giles E Eperon, Samuel D Stranks, Robin J Nicholas, and Henry J Snaith. Carbon Nanotube/Polymer Composites as a Highly Stable Hole Collection Layer in Perovskite Solar Cells. *Nano letters*, 14(10):5561–5568, 2014.

[78] Severin N. Habisreutinger, Tomas Leijtens, Giles E. Eperon, Samuel David Stranks, Robin J. Nicholas, and Henry J. Snaith. Enhanced Hole Extraction in Perovskite Solar Cells Through Carbon Nanotubes. *The Journal of Physical Chemistry Letters*, 5(23):4207–4212, nov 2014.

[79] Chuantian Zuo and Liming Ding. Solution-Processed Cu2O and CuO as Hole Transport Materials for Efficient Perovskite Solar Cells. *Small (Weinheim an der Bergstrasse, Germany)*, 11(41):5528–32, nov 2015.

[80] Senyun Ye, Weihai Sun, Yunlong Li, Weibo Yan, Haitao Peng, Zuqiang Bian, Zhiwei Liu, and Chunhui Huang. CuSCN-based inverted planar perovskite solar cell with an average PCE of 15.6%. *Nano Letters*, 15(6):3723–3728, may 2015.

[81] Jangwon Seo, Sangman Park, Young Chan Kim, Nam Joong Jeon, Jun Hong Noh, Sung Cheol Yoon, Sang Il Seok, and Perovskite Solar Cells. Benefits of very thin PCBM and LiF layers for solution-processed p-i-n perovskite solar cells. *Energy Environ. Sci.*, 7:2642–2646, jun 2014.

[82] Yuichi Kato, Luis K. Ono, Michael V. Lee, Shenghao Wang, Sonia R. Raga, and Yabing Qi. Silver Iodide Formation in Methyl Ammonium Lead Iodide Perovskite Solar Cells with Silver Top Electrodes. *Advanced Materials Interfaces*, 2(13):1500195, sep 2015.

[83] Antonio Guerrero, Jingbi You, Clara Aranda, Yong Soo Kang, Germà Garcia-Belmonte, Huanping Zhou, Juan Bisquert, and Yang Yang. Interfacial Degradation of Planar Lead Halide Perovskite Solar Cells. *ACS nano*, 10(1):218–24, jan 2016.

[84] Tomas Leijtens, Giles E. Eperon, Nakita K. Noel, Severin N. Habisreutinger, Annamaria Petrozza, and Henry J. Snaith. Stability of Metal Halide Perovskite Solar Cells. *Advanced Energy Materials*, 5(20):1500963, sep 2015.

Chapter 3

Method

3.1 Materials Preparation

3.1.1 Methylammonium Lead Mix-Halide Perovskite ($\mathbf{CH_3NH_3PbI_{3-x}Cl_x}$)

MAI was prepared by mixing methylamine solution (CH_3NH_2, 33 wt% in absolute ethanol) with hydroiodic acid (HI, 57 wt% in water) with excess methylamine under nitrogen atmosphere in ethanol at room temperature. A white colored powder of MAI can be derived by using a rotary evaporator to facilitate the MAI recrystallization.

To prepare $CH_3NH_3PbI_{3-x}Cl_x$ precursor solutions, Methylammonium iodide (MAI) and lead chloride ($PbCl_2$) were mixed at a 3:1 molar ratio, then dissolved in anhydrous N,N-Dimethylformamide with final concentrations of 40 wt% to produce a mixed halide $CH_3NH_3PbI_{3-x}Cl_x$ perovskite precursor solution.

To form the film of $CH_3NH_3PbI_{3-x}Cl_x$ perovskite, the precursor solution was spin-coated on a cleaned substrate in a nitrogen-filled glovebox at 2000 rpm for 45 seconds, then allowed to dry at room temperature for 30 minutes. It was then annealed on a hotplate in the following sequence, 90°C for 2 hours, 100°C for 20 minutes, then at 120 °C for 20 minutes in the nitrogen-filled glovebox as previously reported by Lee et al.[1]

3.1.2 Methylammonium Lead Iodide Perovskite ($CH_3NH_3PbI_3$)

The methylammonium lead iodide ($CH_3NH_3PbI_3$) precursor solution was prepared by mixing methylammonium iodide (Dyesol) and lead acetate trihydrate (Aldrich) at a 3:1 molar ratio, then dissolved in anhydrous N,N-Dimethylformamide with final concentrations of 30 wt% with the addition of hypophosphorous acid (3 μl/ml).

To form the film of $CH_3NH_3PbI_3$ perovskite, the precursor solution was spin-coated on a cleaned substrate in a nitrogen-filled glovebox at 2000rpm for 45 seconds, then allowed to dry at room temperature for 10 minutes. It was then annealed on a hotplate t 100°C for 10 minutes as previously reported by Zhang et al.[2, 3]

3.2 Fabrication of Perovskite Solar cells

3.2.1 Mesoporous-Superstructured Solar Cell fabrication

Devices were fabricated on fluorine doped tin oxide (FTO) coated glass substrates (Pilkington, 7 Ω/sq). Firstly, the anode contact pattern was defined by etching the FTO with 2M HCl and zinc powder. Substrates were then cleaned sequentially in hellmanex, acetone, and isopropanol. Then perform O_2 plasma treatment for 10 minutes. A $\sim$50 nm of electron-transporting layer (ETL) was deposited with either TiO_2 or Gaphene-TiO_2 on top of the cleaned FTO. A compact TiO_2 ETL layer was deposited by spin-coating (2000 rpm for 60 seconds) a precursor solution consist of titanium isopropoxide (350 μl), ethanol (2.5 ml), and 2M HCl (35 μl), then annealed at 500°C for 30 minutes (ramping from room temperature in 45 minutes). The low-temperature processed Gaphene-TiO_2 ETL was deposited by spin-coating the dispersion at 2000 rpm for 60s, and heated at

150 °C for 60 min. The mesostructured layer was deposited by spin-coating a colloidal dispersion of Al_2O_3 solution at 2500 rpm for 60 seconds and annealed at 150 °C for 30 minutes. Then the perovskite layer was deposited by the aforementioned method. The hole-transporting layer (HTL) was then deposited via spin-coating an 8.5 wt% Spiro-OMeTAD in chlorobenzene solution with tert-butylpyridine (tBP) and lithium bis(trifluoromethanesulfonyl)imide (Li-TFSI) added. Finally, devices were completed with evaporation of 80 nm Au or Ag contact electrodes through a shadow mask.

3.2.2 Planar Perovskite Solar Cell fabrication

N-I-P Architecture (Regular Structure)

Devices were fabricated on fluorine doped tin oxide (FTO) coated glass substrates (Pilkington, 7 Ω/sq). Firstly, the anode contact pattern was defined by etching the FTO with 2M HCl and zinc powder. Substrates were then cleaned sequentially in hellmanex, acetone, and isopropanol. Then perform O_2 plasma treatment for 10 minutes. A ∼50 nm compact TiO_2 ETL layer was deposited by spin-coating (2000rpm for 60 seconds) a precursor solution consisting of titanium isopropoxide (350 μl), ethanol (2.5 ml), and 2M HCl (35 μl), then annealed at 500°C for 30 minutes (ramping from room temperature in 45 minutes). Then the perovskite layer was deposited by the aforementioned method. The hole-transport layer (HTL) was then deposited via spin-coating a 7 wt% Spiro-OMeTAD in chlorobenzene solution with tBP and Li-TFSI added. Finally, devices were completed with evaporation of 80 nm Au or Ag contact electrodes through a shadow mask.

P-I-N architecture (Inverted Structure)

The inverted devices here were fabricated on cleaned fluorine doped tin oxide (FTO) coated glass serving as the transparent electrode. Firstly, the cathode contact pattern was defined by etching the FTO with 2M HCl and zinc powder. We then deposited the hole transport layer (HTL) of ∼20 nm thickness by spin-coating a solution of F4-TCNQ-doped poly-TPD. Then the perovskite layer was prepared by spin-coating at 2000 rpm for 45 seconds from as-prepared precursor solution, drying 10 min on the bench in the glovebox, followed by annealing at 100°C for 5 minutes. A n-type collection layers, PCBM (dissolved in DCB, 2 wt%) was spincoated on top of the perovskite at 1000 rpm for 30 seconds. Followed by the deposition of a thin (∼5 nm) buffer layer of bathocuproine (BCP, 0.5 mg/ml in IPA) by spinning at 6000 rpm for 20 seconds. Finally, devices were completed by thermal evaporation of 70 nm of silver contacts.

3.3 Material Characterization

3.3.1 Scanning Electron Microscopy (SEM)

The morphologies of the perovskites were investigated using a scanning electron microscopy (SEM) (Hitachi S-4300) at an accelerating voltage of 5 kV after platinum coating samples prepared on glass substrates.

3.3.2 Transmission Electron Microscopy (TEM)

The preparation of a cross-sectional lamellar specimen was carried out on a FEI Helios dual beam FEG SEM/FIB microscope, fitted with an Omniprobe micromanipulator for in-situ lift-out. The sample preparation was performed following a standard FIB in-situ

lift-out technique,1 and the thinning step of the lamellar specimen was performed with decreasing beam current to reduce sample damage and improve sputtering of the material. The cross-sectional specimen was analyzed through high angle annular dark field STEM (HAADF-STEM), using a Fischione detector on a FEI Tecnai Orisis TEM/STEM equipped with a field-assisted thermionic emitter gun, operating at 200 kV.[4] This experiment was performed via collaboration at the Department of Materials Science and Metallurgy, University of Cambridge.

3.3.3 X-ray Diffraction Measurement

Diffraction patterns were obtained from samples of perovskite deposited on FTO glass using an X-ray diffractometer (Panalytical X'Pert Pro) with a conventional 1.8kW sealed X-ray tube source, using a Cu target, and a vertical circle theta:theta goniometer with a radius of 240 mm.

3.3.4 Nanoscale Secondary Ion Mass Spectrometry

A CAMECA NanoSIMS 50 instrument was used to acquire chemical distributions with spatial resolution better than ∼100 nm. The instrument uses a 16 keV primary ^{133}Cs+ beam to bombard the sample surface and collects and analyses selected secondary negative ions. For this experiment, c.a. 300 nm perovskite films were prepared on silicon wafer surfaces. $^{27}Al^{16}O^-$ secondary ions were collected to show the distribution of aluminium in the perovskite layer using a to achieve good lateral resolution, and the secondary electron image from the same location. This data is D1 = 3 or 4 aperture presented over areas of 8 by 8 μm containing 256 by 256 pixels, and was collected without preliminary $^{133}Cs^+$ implantation to avoid sputtering away the thin samples. A series of up to 30 sequential images were recorded at the same location to effectively depth

profile the sample down to the silicon substrate, and to allow us to locate the centre of the perovskite film from the secondary electron images where the polycrystalline grain structure can be clearly identified. The images were processed using OpenMIMS software (MIMS, Harvard University; www.nrims.harvard.edu). This experiment was performed via collaboration at the Department of Materials, University of Oxford.

3.3.5 Atomic Force Microscopy (AFM)

AFM images were in non-contact mode with perovskite samples prepared on the FTO substrate using a ThermoMicroscopes AutoProbe M5 housed in an acoustic isolation enclosure, with a scan rate of 0.3 Hz and 256 x 256 pixels. We used Aluminum coated antimony doped Si tips (Bruker), which have typical tip radii of 8 nm, resonant frequencies of 75 kHz, and stiffness of 3 N/m.

3.3.6 Inductively Coupled Plasma Optical Emission Spectrometry (ICP-OES)

A SPECTROBLUE SOP system (Ametek Inc) was utilized for the trace Al^{3+} doping level analysis. Basically, multi-element calibration standard solutions were prepared by diluting the commercial standard solution (100 μg/L, GNM-M33198-2013) with 2% nitric acid in deionized water, giving the final concentrations of 0, 0.05, 0.1, 0.2, 0.5, 1, 2, 5 and 10 μg/L. The ICP-OES analysis was then performed on these calibration standards to obtain the reference peak intensities for Al (167.078 nm) and Pb (220.353 nm). Calibration curves (R2=0.999) were then generated based on these reference peak intensities. After that, the control and the 0.15 mol% Al^{3+}-doped films were first dissolved in 2% HNO_3 solution and then tested by ICP-OES system to obtain the Al and Pb signal intensities. By comparing the signal intensities to the calibration standard curves,

the contents of Al and Pb could be determined with an error of ±2%, which mainly induced by preparing the standard reference solution. This experiment was performed via collaboration at School of Physics, Institute of Modern Optics, Peking University.

3.3.7 X-ray and Ultra-Violet Photoemission Spectroscopy (XPS and UPS) Measurements

Samples for photoemission spectroscopy measurements were transferred to the ultrahigh vacuum chamber (ESCALAB 250Xi) for XPS/UPS measurements. XPS measurements were carried out using a XR6 monochromated Al Kα source (hν = 1486.6 eV) and pass energy of 20 eV. UPS measurements were performed using a He discharge lamp (hν = 21.2 eV) and pass energy of 2 eV. This experiment was performed via collaboration at Centre for Advanced Materials, Universität Heidelberg.

3.3.8 Kelvin Probe and Surface Photo Voltage (SPV)

Vibrating Kelvin Probe (probe diameter = 2 mm, KP Technology, UK) was used to determine the surface potential. All the measurements were done at ambient condition. Calibration of the kelvin probe was done by a freshly cleaved highly ordered pyrolytic graphite surface which has known work function of 4.65 eV.[5] For SPV measurement, a quartz tungsten halogen lamp was used as a light source and the sample was illuminated from the air interface using an optical fiber coupled to the light source. The intensity was varied linearly by controlling the power supplied to the lamp. The maximum power density on the sample surface was 1 mW/cm^2.

3.4 Electrical Characterization

3.4.1 Solar Cell Characterization

The current-voltage characteristics of the solar cells were measured under AM1.5 light at 100 mW/cm^2 generated using an ABET Class AAB sun 2000 simulator calibrated using a National Renewable Energy Laboratories (NREL) calibrated KG5 filtered silicon reference cell. The mismatch factor, determining the accuracy of the solar spectrum, was calculated to be $\sim\pm1\%$ between 400 to 1100 nm. All devices were masked with a 0.0965 cm^2 metal aperture to define the active area and to eliminate edge effects and avoid unwanted contributions to charge collection from a wider area than the device.[6] The light intensity was checked every time at the beginning of measurement by a calibrated reference diode. JV curves were recorded with a Keithley 2400 sourcemeter at a scan rate of 0.38 V/s. The Maximum power point voltage was determined from the JV scans and current measured holding at this voltage for the stabilised power output scans.

3.4.2 Impedance Spectroscopy

Impedance Spectra were recorded using an FRA-equipped PGSTAT-30 from Autolab, at forward bias, applying a 20 mV AC sinusoidal signal over the constant applied bias with the frequency ranging between 1 MHz and 0.01 Hz. Impedance Spectroscopy measurements were performed under 1 sun illumination (AM 1.5 G, 100 mW/cm^2) with an ABET Class Sun 2000 solar simulator, followed the work of Kim et al.[7] This experiment was performed via collaboration at Institute of Advanced Materials, Universitat Jaume I.

3.5 Optical Characterization

3.5.1 UV-visible Absorption Spectra

For the absorbance analysis,]the perovskite films were deposited on cleaned glasses and measured on a Varian Carry 300 Bio (Agilent Technologies). To minimize any potential errors, at least three samples were checked and the average of all spectra presented.

3.5.2 Raman Spectroscopy

Raman spectroscopy was performed at room temperature with a Horiba spectrometer using a probe laser at a wavelength of 514 nm with in-house built optical lens array integrated with a monochromator.

3.5.3 Photoluminescence Spectroscopy

Perovskite samples were prepared on glass and coated with an inert polymer poly(methylmethacrylate), PMMA. PL spectra were acquired following previous report[8] using a time-resolved single photon-counting set-up (FluoTime 300, PicoQuant). Samples were photoexcited using a 507-nm laser head (LDH-P-C-510, PicoQuant) with pulse duration of 117 ps, fluence of 30 nJ/cm^2 per pulse and a repetition rate of 1 MHz. Photolumninscense Quantum Efficiency (PLQE), Steady-state photoluminescence quantum efficiency values were determined using a 532 nm CW laser excitation source (Suwtech LDC-800) to illuminate a sample in an integrating sphere (Oriel Instruments 70682NS), and the laser scatter and PL were collected using a fiber-coupled detector (Ocean Optics MayaPro). The spectral response of the fiber-coupled detector setup was calibrated using a spectral irradiance standard (Oriel Instruments 63358). PLQE calculations were

carried out using a homemade established technique.[9]

3.5.4 Fluorescence Microscopy

Optical microscopy and spectroscopy were performed using a custom sample scanning confocal microscope built around a Nikon TE-2000 inverted microscope fitted with an infinity corrected 50x dry objective (Nikon L Plan, NA 0.7, CC 0-1.2). We measured the point spread function of our systems to be ∼350 nm FWHM. A 470 nm pulsed diode laser (PDL-800 LDH-P-C-470B, 70 ps pulse width), fluence of ∼30 nJ/cm^2 per pulse was used for excitation with repetition rate of 40 MHz for collecting fluorescence images. The emission was filtered through a 50/50 dichroic beamsplitter and a 700 nm longpass filter. Photoluminescence from the sample was directed to a Micro Photon Devices (MPD) PDM Series single photon avalanche photodiode with a 50 μm active area. The sample stage was controlled using a piezo controller (Physik Instrumente E-710). For fluorescence images, the pixel step size was set to 100 nm with a pixel dwell time (integration time) of 50 ms. This experiment was performed via collaboration with the Department Chemistry at the University of Washington.

3.5.5 Incident Photon to Converted Electron Measurement (IPCE) or External Quantum Efficiency (EQE)

Incident photon to converted electron measurements where performed using a modified Bruker Vertex 80 Fourier Transform Infrared spectrometer, coupled to a transimpedance amplifier (Stanford Research SR570). All devices were measured in short circuit configuration under illumination of AM1.5 light at 100 mW/cm^2. EQE values were calibrated using a National Renewable Energy Laboratories (NREL) calibrated silicon reference cell with a known EQE spectrum.

3.5.6 Fourier Transform Photocurrent Spectroscopy (FTPS)

Urbach energies were determined by performing EQE measurements as described above, except with the AM1.5 light source replaced by a tungsten halogen lamp that was filtered with RG715 and KG3 filters. The low energy tail of the measured EQE onset was then fitted using the expression

$$\eta(h\nu) = \eta_0 e^{(h\nu - E_0)}/E_U \tag{3.5.1}$$

where $\eta(h\nu)$ is the EQE spectrum, $h\nu$ is the photon energy, and E_U is the Urbach energy. In an approximation, a shallow slope in the rise in the external quantum efficiency (EQE) below the band gap indicates a large density of sub band gap states, and in contrast a steep rise in the EQE below the band gap indicates a lower density of sub band gap states. We can quantify this steepness, by fitting the exponential rise in the EQE spectra below the band gap, known as the Urbach tail, to derive the Urbach energy (E_U).[10, 11] Weighting factors: A nonlinear regression was performed using MATLAB to extract the Urbach energy from the EQE data. Robust fitting was performed using a bisquared (Tukey's biweight) weighting function. The errors in the Urbach energy based on this fitting procedure represent a 95% confidence limits. This FTPS experiment was performed via collaboration with Prof. Michael Johnston, Department of Physics, University of Oxford.

References

[1] Michael M. Lee, Joël Teuscher, Tsutomu Miyasaka, Takurou N. Murakami, and Henry J. Snaith. Efficient Hybrid Solar Cells Based on Meso-Superstructured Organometal Halide Perovskites. *Science*, 338(6107):643–647, nov 2012.

[2] Wei Zhang, Michael Saliba, David T. Moore, Sandeep K. Pathak, Maximilian T. Hörantner, Thomas Stergiopoulos, Samuel D. Stranks, Giles E. Eperon, Jack A. Alexander-Webber, Antonio Abate, Aditya Sadhanala, Shuhua Yao, Yulin Chen, Richard H. Friend, Lara A. Estroff, Ulrich Wiesner, and Henry J. Snaith. Ultrasmooth organic–inorganic perovskite thin-film formation and crystallization for efficient planar heterojunction solar cells. *Nature Communications*, 6:6142, jan 2015.

[3] Wei Zhang, Sandeep Pathak, Nobuya Sakai, Thomas Stergiopoulos, Pabitra K. Nayak, Nakita K. Noel, Amir A. Haghighirad, Victor M. Burlakov, Dane W. DeQuilettes, Aditya Sadhanala, Wenzhe Li, Liduo Wang, David S. Ginger, Richard H. Friend, and Henry J. Snaith. Enhanced optoelectronic quality of perovskite thin films with hypophosphorous acid for planar heterojunction solar cells. *Nature Communications*, 6:10030, nov 2015.

[4] R M Langford and M Rogers. In situ lift-out: steps to improve yield and a comparison with other FIB TEM sample preparation techniques. *Micron (Oxford, England : 1993)*, 39(8):1325–30, dec 2008.

[5] P. G. Schroeder, C. B. France, B. A. Parkinson, and R. Schlaf. Orbital alignment at p-sexiphenyl and coronene/layered materials interfaces measured with photoemission spectroscopy. *Journal of Applied Physics*, 91(11):9095, may 2002.

[6] Henry J Snaith. How should you measure your excitonic solar cells? *Energy & Environmental Science*, 5(4):6513, 2012.

[7] Hui-Seon Kim, Ivan Mora-Sero, Victoria Gonzalez-Pedro, Francisco Fabregat-Santiago, Emilio J Juarez-Perez, Nam-Gyu Park, and Juan Bisquert. Mechanism of carrier accumulation in perovskite thin-absorber solar cells. *Nature communications*, 4:2242, jan 2013.

[8] Samuel D Stranks, Giles E Eperon, Giulia Grancini, Christopher Menelaou, Marcelo J P Alcocer, Tomas Leijtens, Laura M Herz, Annamaria Petrozza, and Henry J Snaith. Electron-hole diffusion lengths exceeding 1 micrometer in an organometal trihalide perovskite absorber. *Science (New York, N.Y.)*, 342(6156):341–344, oct 2013.

[9] John C. de Mello, H. Felix Wittmann, and Richard H. Friend. An improved experimental determination of external photoluminescence quantum efficiency. *Advanced Materials*, 9(3):230–232, mar 1997.

[10] Stefaan De Wolf, Jakub Holovsky, Soo-Jin Moon, Philipp Löper, Bjoern Niesen, Martin Ledinsky, Franz-Josef Haug, Jun-Ho Yum, and Christophe Ballif. Organometallic Halide Perovskites: Sharp Optical Absorption Edge and Its Relation to Photovoltaic Performance. *The Journal of Physical Chemistry Letters*, 5(6):1035–1039, mar 2014.

[11] Aditya Sadhanala, Felix Deschler, Tudor H Thomas, Siân E. Dutton, Karl C Goedel, Fabian Cornelius Hanusch, May Ling Lai, Ullrich Steiner, Thomas Bein, Pablo Docampo, David Cahen, and Richard H. Friend. Preparation of Single Phase Films of CH3NH3Pb(I1-xBrx)3 with Sharp Optical Band Edges. *The Journal of Physical Chemistry Letters*, 5(15):2501–2505, jul 2014.

Chapter 4

Gaphene-TiO_2 Nanocomposites as Electron Collection Layers in Thin Film Perovskite Solar Cells

The work in this chapter has been adapted and reproduced in part with permission from: Jacob Tse-Wei Wang, James M. Ball, Eva M. Barea, Antonio Abate, Jack-Alexander Webber, Jian Huang, Michael Saliba, Ivan Mora-Sero, Juan Bisquert, Henry J. Snaith & Robin J. Nicholas , *Nano Letters*, 14, 2, (2014) 724-730 [1]. Copyright 2014 American Chemical Society.



4.1 Context

The highest efficiencies to-date in perovskite solar cells have been achieved in a mesoporous structure with a thin electron collection layer that requires sintering over 450 °C. This is unfavourable for low-cost production, applications on plastic substrates, and multi-junction device architectures. Here in this chapter, we report a low-cost, solution-based deposition procedure utilizing nanocomposites of graphene and TiO_2 nanoparticles as the electron collection layers in perovskite solar cells. The graphene nanoflakes provide exceptional charge-collection in the nanocomposites, also enable the entire device to be fabricated at temperatures not higher than 150 °C. These solar cells for the first instance demonstrate the all-low temperature procedure with photovoltaic performance up to 15.6%. This work demonstrates that graphene/metal oxide nanocomposites have the potential to contribute significantly toward the development of low-cost solar cells with superior performance.

4.2 Introduction

Thin-film photovoltaics aim to reduce the cost per unit energy of electricity generated from sunlight compared to conventional silicon solar cells. Several approaches have been developed for solar cells such as amorphous and nanocrystalline Si,[2] inorganic compound semiconductors,[3, 4] quantum dot solar cells (QDSCs),[5] dye-sensitized solar cells (DSSCs),[6] organic solar cells (OSCs),[7] and now perovskite solar cells (PSCs).[8] In particular, solid-state perovskite-based solar cells have risen to the forefront of emerging PV research.[8, 9, 10, 11, 12, 13] Evolving from DSSCs, MSSCs have demonstrated remarkably high power conversion efficiency of over 20%, broad light absorption, and open-circuit voltages (V_{oc}) of over 1.1 V, by employing an organic-inorganic halide perovskite, $CH_3NH_3PbI_{3-x}Cl_x$, as the absorber, coated upon the surface of a mesoporous

alumina scaffold. Perovskite absorbers are also desirable by virtue of being easy to solution-process at low-temperature using low-cost materials and do not rely on the use of elements in limited supply, unstable solvents such as hydrazine, and high-temperature annealing. In the most efficient thin-film solar cells, electron-collection layers also play a vital role by facilitating selective charge collection. For most commercial thin film solar cells, CdS is used for this purpose, however it significantly contributes to parasitic absorption in the solar cell and additionally contains non-desirable Cd.[14] Metal oxide materials such as TiO_2 , ZnO are widely used in most studies on emerging technologies since they can prevent shunting and leakage currents under reverse bias.[15] But such materials still require high temperature processing to increase their crystallinity and achieve suitably high charge carrier mobility.[16] Similarly this still remains a challenge for MSSCs, as high-temperature sintering of the n-type TiO_2 electron-selective contact is still important for high performance. High-temperature sintering has several drawbacks because it results in a higher cost, slower production, and it limits the applications to solid, temperature resilient substrates, preventing its use with plastic and malleable metal foils, and in addition multijunction device architectures.[17] Replacing the sintered TiO_2 compact layers should make the perovskite solar technology as versatile in its deployment as organic photovoltaics. Several approaches have been reported in order to achieve comparable electronic properties for the n-type collection layers in other solar technologies, such as atomic layer deposition (ALD), high-pressure pressing, chemical sintering, sol-gel, and electrodeposition.[18, 19, 20, 21, 22] Up to now, these alternative methods have not yet achieved an equivalent performance to the conventional high-temperature process, due to crack formation in the film, poor adhesion to the substrate, unfavorable crystallinity of TiO_2, and a lack of good connectivity between particles.[23, 24] Meanwhile, advances in graphene research have led to numerous fundamental breakthroughs. In this atom-thick two-dimensional (2D) material charge-carriers mimic relativistic particles with zero mass[25], which endow it with remarkably

high charge mobility and electronic conductivity.[26, 27, 28] It has not only been identified as one of the strongest materials[29], but is also equipped with unique properties ranging from superior thermal conductivity, and high optical transmittance.[30, 31, 32] Therefore, it has aroused interest in applications for graphene-based nanocomposites including photovoltaics, photocatalysis, nanoelectronics, sensors, etc.[33, 34, 35, 36, 37] In particular, in graphene-TiO_2 nanocomposites, exploiting the benefits of high conductivity and better electrical contacts of graphene and graphene like materials to electron transport has been proposed.[38, 39, 40, 41] To date, only reduced graphene oxide (RGO) has been used instead of pristine graphene, which requires the use of toxic hydrazine vapor, and high-temperature annealing above 400 °C under an inert gas atmosphere to transform Graphene Oxide (GO) into RGO.[41] RGO is much easier to disperse in solvents and can give mono-layer RGO in large quantities in comparison to GO, since RGO chemically functionalized groups of oxides provide better solvent solubility and dispersion. However, large populations of defects still remain after the reduction, which seriously degrade the electronic properties.[42, 43] Much higher quality graphene can be produced by Liquid-Phase Exfoliation (LPE) of graphite powders using organic solvents as developed by Hernandez et al.[44] and O'Neill et al.[45] When compared to the other high quality graphene production methods such as Chemical Vapor Deposition (CVD), Molecular Beam Epitaxy (MBE), and growth on SiC;[46] LPE with organic solvents is quick and low-cost making it an industrially scalable method. Thus, via this technique, we can envisage having enhanced graphene nanocomposites applied to a range of applications.

4.3 Gaphene-TiO_2 Nanocomposites

Here we develop a low temperature processed nanocomposites of pristine graphene nanoflakes and anatase-TiO_2 nanoparticles, and employ it as the electron selective contact in PSCs. We observe reduced series resistance and unexpectedly reduced recombination losses with the low temperature composite. The resulting sub 150 °C processed PSCs exhibit up to 15.6% power conversion efficiency. Slightly higher than the previously high temperature sintered devices due to the superior properties of the Gaphene-TiO_2 nanocomposites. To gain a better insight into the intrinsic properties of the starting materials, we performed detailed characterizations of graphene, TiO_2 , and their nanocomposites.

4.3.1 Graphene Nanoflakes

We produced graphene from graphite flakes by Liquid Phase Exfoliation (LPE) with isopropanol as the dispersant, under sonication for up to 70 h. The detailed synthetic procedure has been described elsewhere. In general, Graphene was exfoliated following O'Neil's work.[45] Initially the graphite powder was sieved through a 0.5 mm mesh to remove the large agglomerate particles, followed by dispersion in the isopropanol at an initial concentration of 0.5 mg/ml. After sequential sonication and centrifugation, the graphene was finally dispersed in an isopropanol solution at a concentration of 3.0 μg/ml. A detailed description of the dispersion process has been described in the literature elsewhere.[44] Sonication was performed in an ultrasonic bath (Branson 1510E-MT) and with a sonic tip (MSE Soniprep 150). The concentration of the graphene dispersion was defined by absorbance measurements at 660 nm via the Beer-Lambert law A =αcl, where A is absorbance, α is the absorption coefficient as 3620 L/g*m,[44] c is solution concentration, and l is the optical path length.

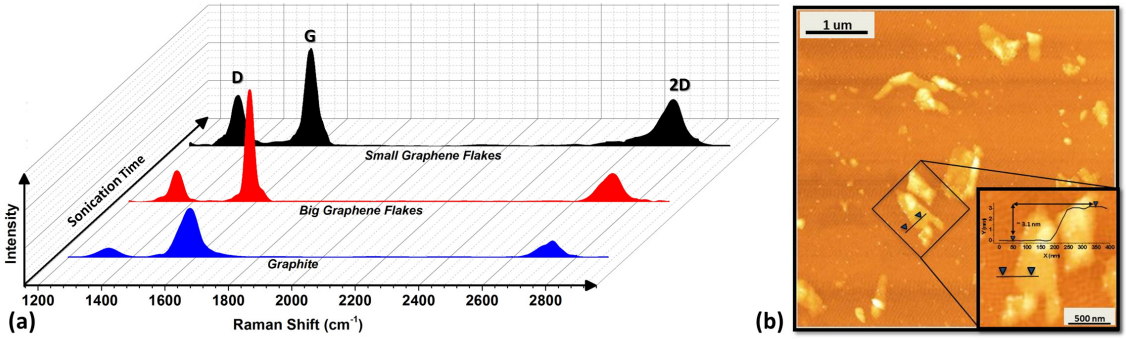


Figure 4.1: (a) Raman spectra of starting graphite flakes and its exfoliated graphene deposited on the SiO_2 substrate with increasing sonication time. (b) AFM image of exfoliated graphene scanned with 5 um x 5 um size, and enlargement of the graphene flakes and its height profile of the lines shown in the inset figure.

We performed Raman spectroscopy and Atomic Force Microscopy (AFM) to probe the graphene film quality and the number of graphene layers in each flake. The samples were prepared on SiO_2 substrates by drop casting the graphene solution and heating on a hot plate at 100°C. Fig. 4.1a shows the Raman spectrum for samples with decreasing flake size, controlled by increasing sonication time. Raman spectra give unique peaks for graphite materials. The two most prominent peaks are the G band ($\sim$1580 cm^{-1}) and the 2D band ($\sim$2700 cm^{-1}) as expected. We observe a difference in the contribution to the 2D band's shape from multiple peaks between exfoliated graphene flakes and starting graphite, suggesting our prepared samples are few-layer graphene.[47] In addition, we observed increased intensity for the peaks of the D band ($\sim$1350 cm^{-1}), progressing from the graphite flakes toward graphene. The reason for the appearance of the D band is that exfoliating graphite into graphene produces progressively smaller flakes with increasing sonication time. We see that the intensity ratio of the D and G peaks I_D/I_G increases from graphite (I_D/I_G= 0.14) as it is converted into graphene flakes (I_D/I_G= 0.3), then increases further (I_D/I_G= 0.52) during continuous sonication. O'Neill et al., following the same technique, found that this was caused by a variation in flake size.[45] They suggest that liquid phase exfoliation of graphene causes the flake size to decrease

and therefore the area/perimeter ratio to decrease, increasing the contribution of flake edges to the Raman spectrum. Because the D band not only represents the defects of graphene, but also the edges, more exposed edges increases the I_D/I_G ratio.[47] The AFM image of exfoliated graphene flakes in fig. 4.1b allows us to have an approximate overview of the graphene morphology and its number of layers. It can be seen that the graphene flakes are distributed randomly over the substrate. The dimension of flakes varies between 0.1-1 μm. We also performed cross-sectional analysis of the graphene flakes, where we show a representative flake with a height of $\sim$3.1 nm in the inset to Fig. 4.1 b. We thus estimate that we have sheets of approximately 5 layers of graphene.[48] As reported in the literature, solution deposition of a graphene film onto SiO_2 can cause aggregation of the flakes. Therefore, although we observe very few monolayer flakes in our sample on SiO_2, this may give an overestimate of number of layers in the graphene flakes in our final nanocomposites films. Our Raman and AFM characterization are in good agreement with previous work, indicating high quality graphene synthesis without introducing significant defects via oxidation, and as prepared graphene is comparable to defect-free graphene.[44, 45]

4.3.2 TiO_2 Nanoparticles

We prepared anatase TiO_2 nanoparticles following a hydrothermal method as below.

The anatase-TiO_2 nanoparticles were synthesized by a hydrothermal method. 11.72 g of titanium (IV) isopropoxide (Sigma Aldrich, product number 377996) was mixed with 2.4 g of acetic acid and stirred at room temperature for 15 min. This was followed by adding 58 ml deionized water and stirring for 60 min with a magnetic stirrer at 2000 rpm. Next, 0.8 ml Nitric Acid (HNO_3, 70%) was added to the solution, which was heated to 80 °C and stirred for a further 2 hrs. 75 ml deionized water was then added, before transferring all of the solution to Teflon cups in an autoclave held at 250 °C for 14 hours.

After cooling to room temperature, 0.48 ml HNO_3 was added, followed by centrifugation at 7000 rpm and rinsing with water three times. Centrifugation and rinsing was repeated twice more before a final rinse in the absolute ethanol (Fluka, product number 02860) to obtain a final dispersion concentration of 56 mg/ml in ethanol.

The TiO_2 nanoparticles were approximately 25 nm in diameter, and were blended with the graphene dispersion afterward.

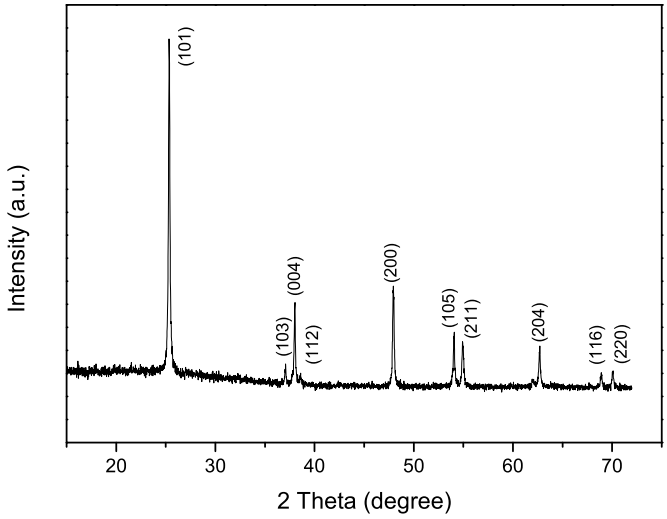


Figure 4.2: X-ray diffraction spectra of as synthesized TiO_2 nanoparticles.

We initially investigated the properties of the as synthesized TiO_2 nanoparticles with X-ray diffractometer. The Fig. 4.2 shows the X-ray diffraction spectra of as synthesized anatase-TiO_2 nanoparticle. All patterns index to the titania with peaks are corresponding to the anatase phase in the JCPDS, card No: 21-1272.

4.3.3 Nanocomposites

For the preparation of Gaphene-TiO_2 nanocomposites, the required wt% graphene content in the nanocomposite was fabricated from adding an appropriate volume of the

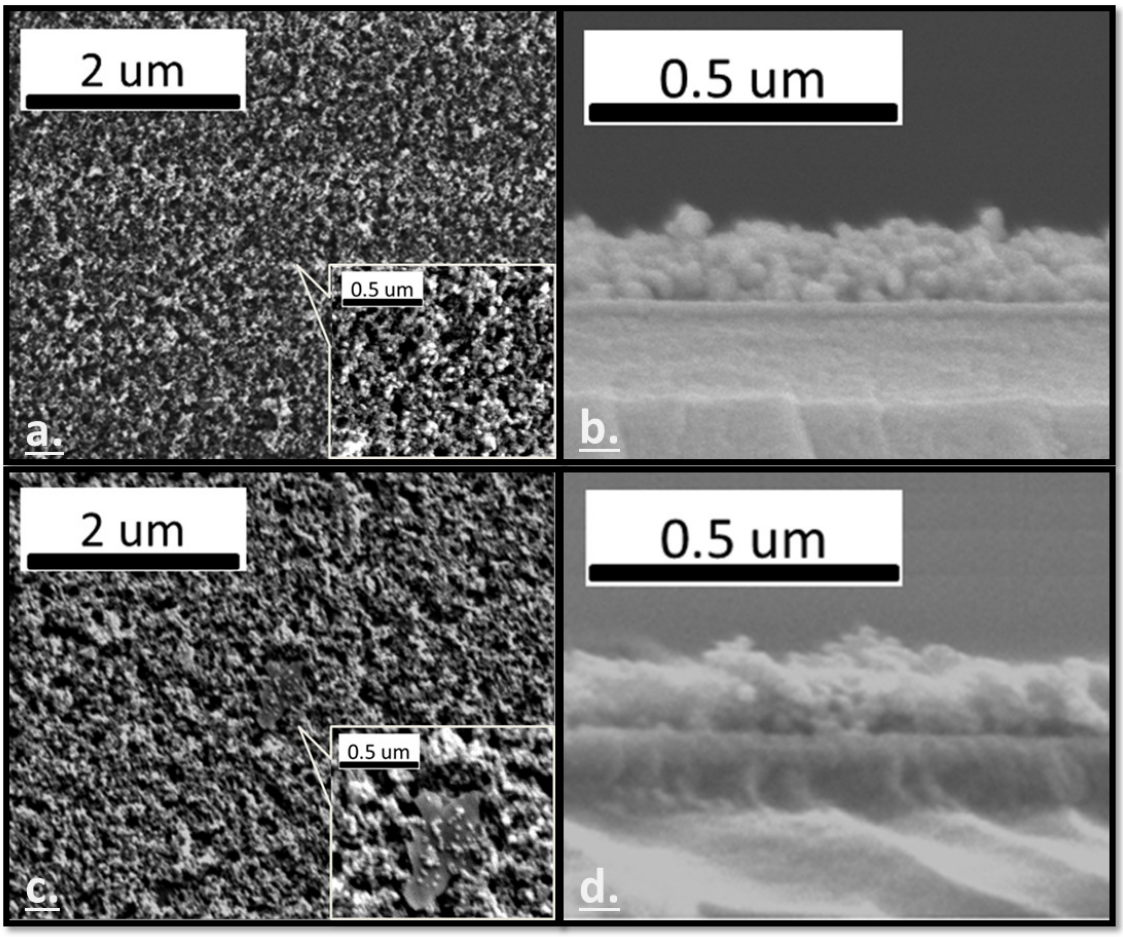


Figure 4.3: SEM images of (a) TiO_2 nanoparticles only electron collection layer with enlargement micrographs in the inset, and (b) its cross-section. (c) Gaphene-TiO_2 nanocomposite as electron collection layer with enlargement micrographs in the inset, and (d), its cross-section.

graphene in isopropanol dispersion into 0.75 ml of the TiO_2 nanoparticles dispersion. Then it was stirred and put in the ultrasonic bath for approximately 20 min to disperse the graphene and allow TiO_2 nanoparticles to anchor onto the graphene nanoflakes.

We show in fig. 4.3 with detailed comparison between SEM micrographs of layers consisting of TiO_2 nanoparticles only, and Gaphene-TiO_2 nanocomposites prepared on glass microscope slides. in fig 4.3c, we show the exposed surface of the nanocomposite highlighting TiO_2 nanoparticles anchored upon a graphene nanoflake. With graphene's remarkable conductivity it may serve as a highway for electron transportation and collection. In fig. 4.4. (a) to (f) we further demonstrated the AFM images of electron-selective

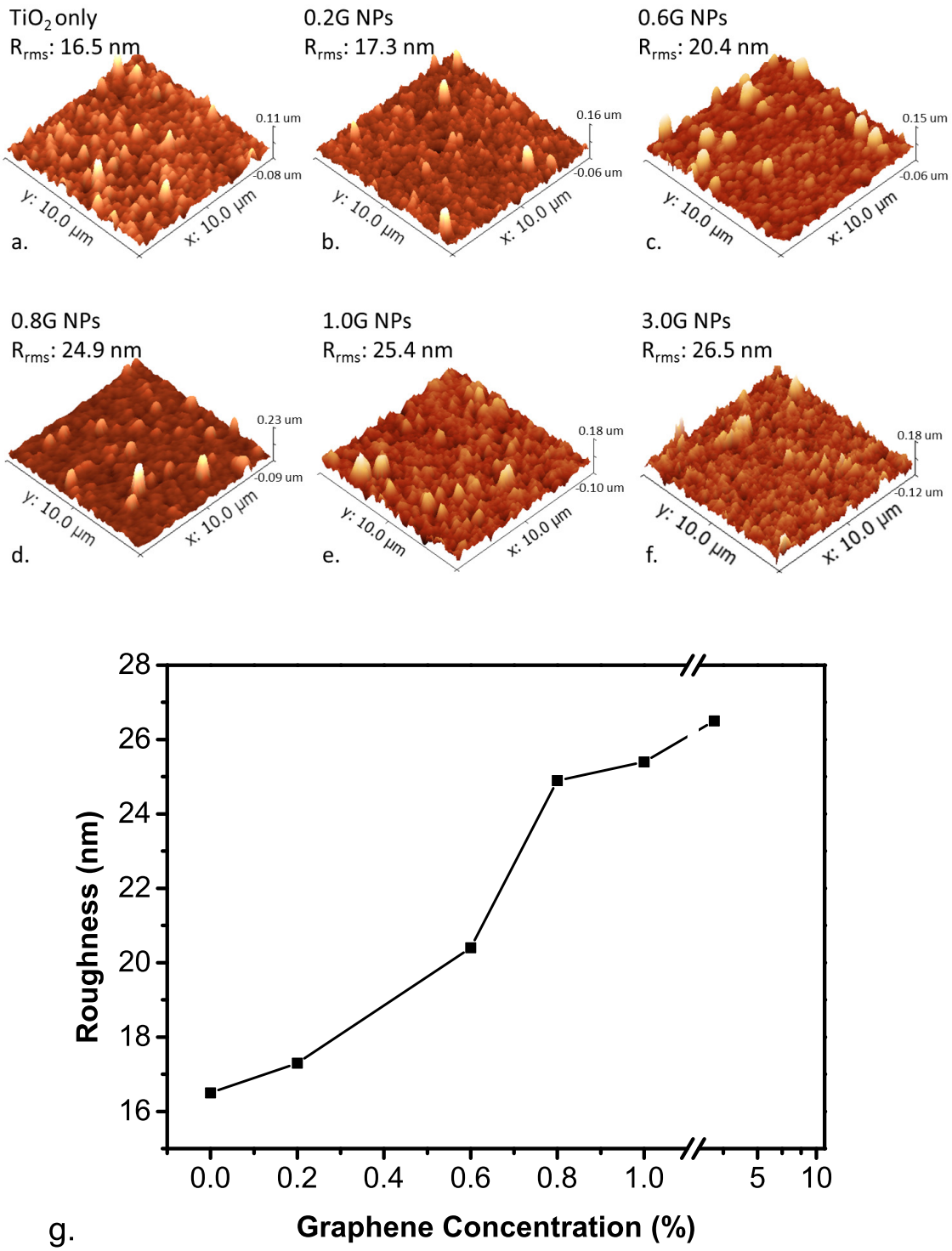


Figure 4.4: AFM images of (a) TiO_2 nanoparticles only electron-transporting layer, and (b) to (f) Gaphene-TiO_2 nanocomposite as electron-transporting layer with different graphene loading respective to the TiO_2 weight percent, and their roughness summarized in (g).

layers with their R_{rms} depicted in fig. 4.4 (g).

4.3.4 The Coverage of TiO_2 Nanoparticles on Graphene

Graphene is known to have a high specific surface area (2630 m^2/g).[49] Here we estimate the TiO_2 nanoparticles coverage on graphene as below. The best ratio of Gaphene-TiO_2 nanocomposite in this study is 0.6 wt%, if we assume there is 6 mg graphene in the suspended solution, we have 1 g of TiO_2 in the solution. Total surface area of 6 mg graphene: 0.006 g x 2630 m^2/g =15.78 m^2; Total volume of 1g TiO_2 nanoparticles: 1 g/4.23g/cm^3 (TiO_2 density) = 0.236 cm^3 = 2.36E-7 m^3. Typical TiO_2 nanoparticle Diameter: 25 nm (from SEM). Volume of 25 nm TiO_2 nanoparticle: 4/3 πr^3 = 4/3 $\pi(12.5E-9m)^3$ = 8.18E-24 m^3; Total number of 1g TiO_2 nanoparticles = Total volume of 1g TiO_2 nanoparticles/ Volume of 25nm TiO_2 nanoparticle = 2.36E-7 m^3 / 8.18E-24 m^3 = 2.89E+16. Area of a TiO_2 nanoparticle with close packing arrangement: $\sqrt{3}/2$ x (Diameter of nanoparticle)^2 = 5.41E-16. Total area covered by 1g TiO_2 = Area of a TiO_2 nanoparticle with close packing arrangement x Total particles number of 1g TiO_2 nanoparticles = 5.41E-16 x 2.89E+16 m^2 = 15.63 m^2. Therefore, the coverage of TiO_2 nanoparticles on graphene is total area covered by 1g TiO_2 with closed packing/total surface area of 6 mg graphene = 15.63 m^2/ 15.78 m^2 $\approx$ 99%. Then, we can summarize the calculations above with the equation 4.3.1 below, which allows us to plot the TiO_2/graphene coverage ratio in fig. 4.5, as a function of graphene/TiO_2 mass ratio. Where S = TiO_2 /graphene coverage ratio, ρ = TiO_2 density, r = nanoparticle radius, y = graphene surface area/mass, x = graphene/TiO_2 mass ratio.

$$S = \frac{3}{4\rho ryx * 0.9069} \tag{4.3.1}$$

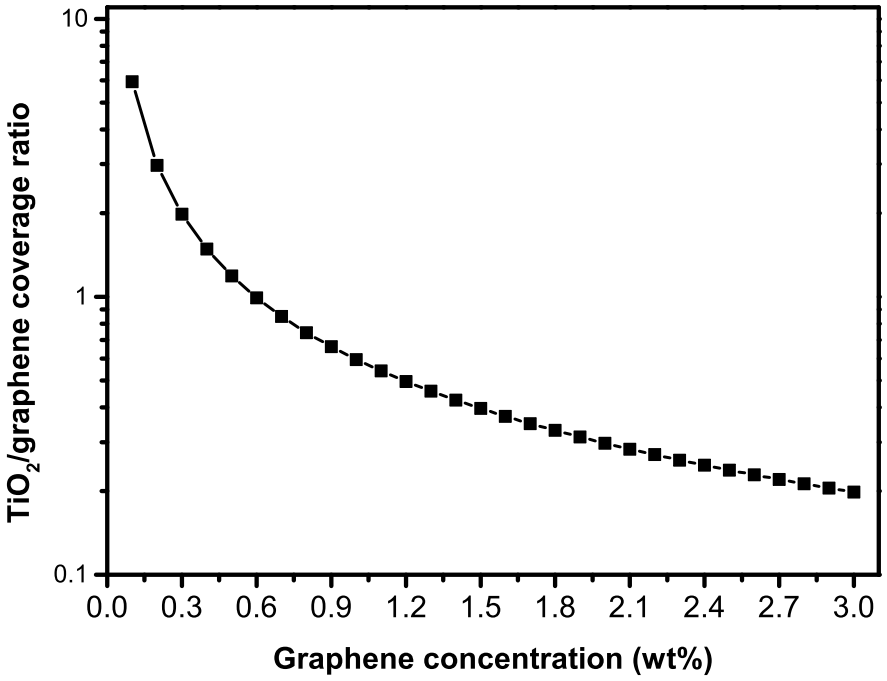


Figure 4.5: TiO_2/graphene coverage ratio with graphene concentration.

4.4 Photovoltaic Behaviour

4.4.1 Device Architecture

Apart from the high-temperature processing limitation, another key issue in performance of the PSCs at present is the minimization of the series resistance. The compact n-type TiO_2 charge collection layers may significantly contribute to series resistance, as has been previously observed in solid-state DSSCs and planar heterojunction perovskite solar cells.[50] Following the characterization of the nanocomposite materials, we investigate the performance of Gaphene-TiO_2 nanocomposites as ETL. We fabricated a series of solar cells with a varying content of graphene flakes in the composite to assess its impact. We show the full device architecture in a color-enhanced cross-sectional scanning electron microscopy image and a schematic illustration of the device architecture along with an energy level diagram in Fig. 4.6. All the devices here were fabricated on cleaned fluorine doped tin oxide (FTO) coated glass serving as the transparent electrode and substrate. We deposit the n-type collection layer of 100 nm thickness by spin-coating from an isopropanol solution of a blend of graphene and TiO_2. We note that upon careful sonication before spin-coating, we produce a dense and well-distributed nanocomposite, with graphene acting as a continuous 2D conductive framework, allowing TiO_2 nanoparticles to anchor onto the graphene nanoflakes (See fig. 4.3 c for TiO_2 nanoparticles coverage on graphene). Following deposition of a 400 nm Al_2O_3 nanoparticle mesostructure from an isopropanol solution, $CH_3NH_3PbI_{3-x}Cl_x$ perovskite was deposited by spin-coating its precursor solution in DMF onto a warmed substrate, resulting in an infiltration of the perovskite within the mesostructure with the addition of a capping layer (around 350 nm). The main difference between the devices studied here and those reported by Ball et al.[11] is the additional capping layers of perovskite which results from coating upon a warm substrate. Then we deposited Spiro-OMeTAD as the hole-transporting layer

(HTL). Finally, devices were completed by thermal evaporation of gold contacts.

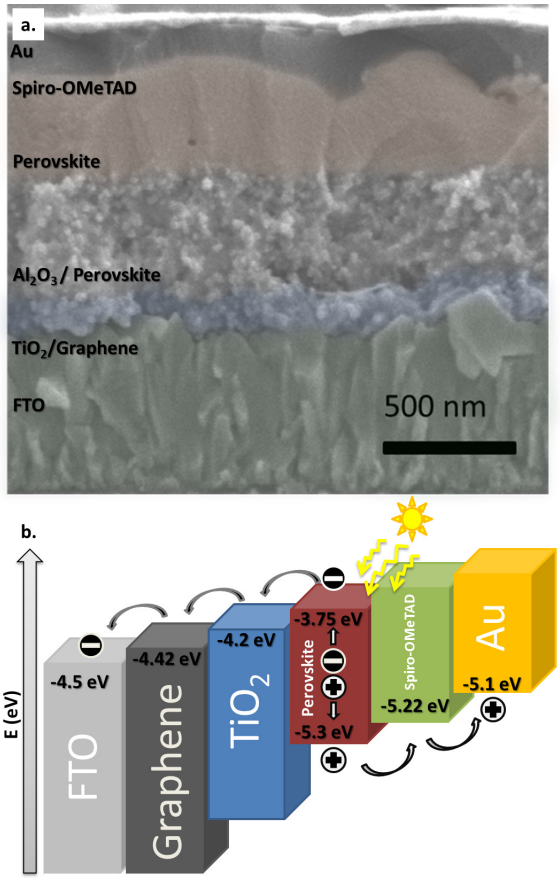


Figure 4.6: (a) Cross-sectional SEM micrographs with color-enhanced and annotated cross-section showing a general schematic of the solar cell architecture. (b) Schematic illustration of energy levels of the materials used in this study. We note that these are the energy levels of the individual materials, and upon contact within the solar cell there is likely to be a considerable relative shift.[51] We also note that the graphene and TiO_2 are blended into a single composite layer and not layered as depicted in the energy level diagram.

4.4.2 Device Performance

In order to optimize the devices, we varied the content of graphene in the Gaphene-TiO_2 composite. The mean solar cell performance parameters for a batch of 83 devices, extracted from current-voltage curves measured under simulated AM 1.5, 106.5 mW/cm^2 sunlight are shown in fig. 4.7. We can see a clear trend of device enhancement by the introduction of graphene. Starting from the neat TiO_2 nanoparticles (NPs only), the average short-circuit current density (J_{sc}) and fill factor (FF) are around 13 mA/cm^2 and 0.56, respectively. With increasing graphene concentration in the electron collection layer, both the J_{sc} and FF increase up to average values of around 18.5 mA/cm^2 and 0.7, respectively, peaking at 0.6 wt%, followed by a decrease with further increases of graphene content. However, in contrast to the J_{sc} and FF, the average open circuit voltage (V_{oc}) only increased slightly with graphene's addition to the TiO_2, with an average V_{oc} of around 1 V up to 0.8 wt%. V_{oc} begins to decrease as the graphene concentration increases over 0.8 wt%, probably due to bare graphene contacting the perovskite directly, resulting in a less selective electrode, i.e. recombination directly between the electrons in the graphene and holes in the perovskite. This is consistent with our estimate in the fig. 4.5 that the optimum graphene content of 0.6 wt% corresponds to just over 1 monolayer coverage of the graphene by TiO_2 nanoparticles. Hence, the power conversion efficiency (PCE), $\eta = J_{sc}{*}V_{oc}{*}P_{in}$ where P_{in} is incident solar irradiance, peaks with an average PCE value around 12.4%.

In fig. 4.8, we show the current density-voltage (J-V) curves of the best performing cells of each series, including cells with only neat TiO_2 , neat graphene, high-temperature sintered TiO_2 , and no n-type charge collection layer at all (just FTO). As can be seen in the J-V curves and the summarized performance parameters in Table 1, devices without any electron collection layer in the device architecture have inferior performance, but they do work. One of the main losses for the perovskite device coated directly upon the

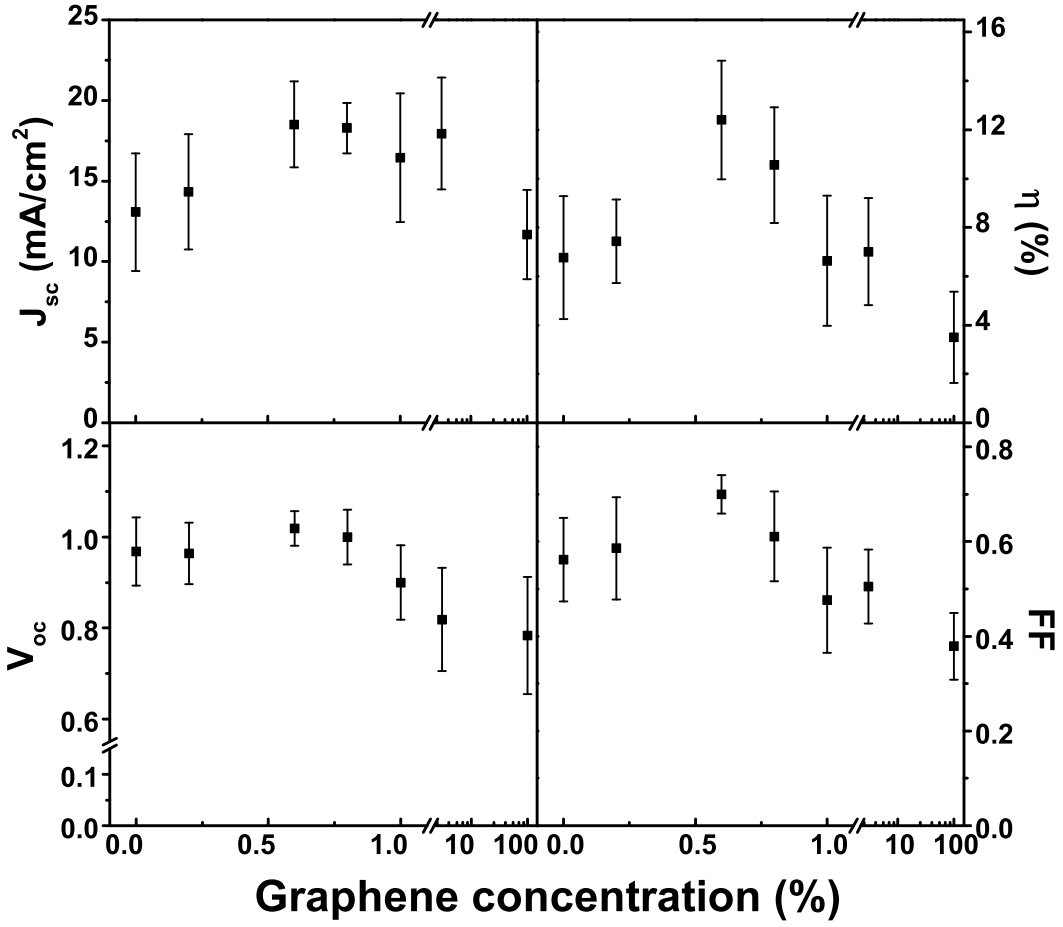


Figure 4.7: Graphene-concentration dependence in the nanocomposites of the parameters extracted from a single batch current-voltage measurements of solar cells under simulated AM 1.5, 106.5 mW/cm^2 irradiance.

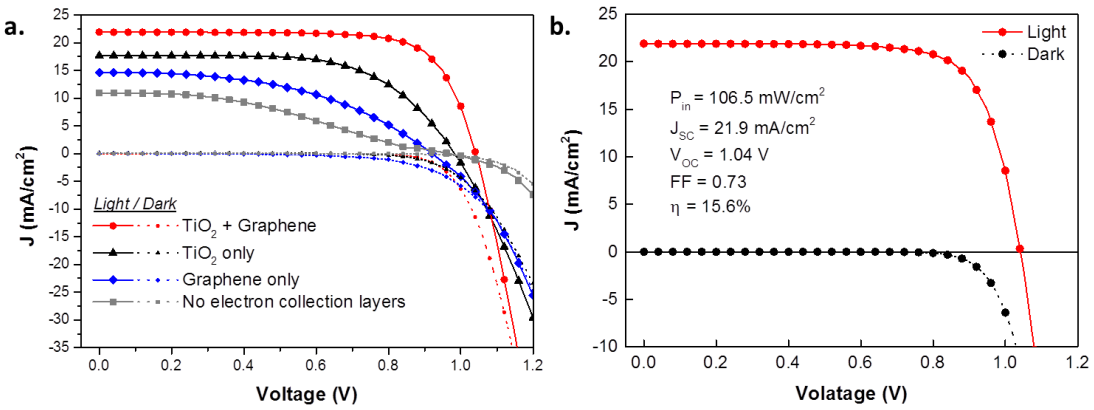


Figure 4.8: (a) Current-Voltage characteristics of different electron collection layers under simulated AM 1.5, 100 mW/cm^2 solar irradiation (solid line), and in the dark (dotted line). (b) the best performing (η=15.6%) solar cell based on a Gaphene-TiO_2 nanocomposites under simulated AM 1.5, 106.5 mW/cm^2 solar irradiation (solid line), and in the dark (dotted line), which processed at temperatures not exceeding 150°C. Solar cell performance parameters are given in the inset.

FTO conducting glass is fill factor, presumably due to an unfavorable electronic contact forming at the FTO perovskite interface. The electron collection layers with either neat graphene or low temperature processed TiO_2 nanoparticles show an improvement to J_{sc} and FF over the devices fabricated directly on FTO. We see further enhancement when we combine the graphene and TiO_2 nanoparticles together as a nanocomposites. The most efficient low-temperature processed PSCs based on a Gaphene-TiO_2 nanocomposite electron collection layer, exhibits a short-circuit photocurrent of 21.9 mA/cm^2, open-circuit voltage of 1.05 V, and a very high fill factor of 0.73 yielding a power conversion

Table 4.1: Best performance of Photovoltaics based on different electron collection layer in this study under simulated AM 1.5, 106.5 mW/cm^2 solar irradiation.

Sample	J_{sc} (mA/cm^2)	V_{oc} (V)	FF	PCE (%)	Rs (Ohm*cm^2)
Gaphene-TiO_2	21.9	1.04	0.73	15.6	4.3
TiO_2 only	17.7	1.00	0.61	10.0	10.1
Graphene only	14.6	0.90	0.48	5.9	20.3
No electron collection layer	10.8	0.95	0.37	3.7	79.1
High-temperature sintered TiO_2	21.4	1.00	0.70	14.1	5.9

efficiency of 15.6%, (under 106.5 $mWcm^{-2}$) which was the best reported low-temperature solution-processed solar cell matching the highest reported efficiency of perovskite-based solar cells fabricated at either high temperature or by vapor deposition while we unveiled this result.[12] In addition, to the best of our knowledge, before this result published, the best performing solar cells incorporating graphene as a contact to crystalline Si, remained at a power conversion efficiency of 14.5%,[52] hence our work here also set a milestone for the photovoltaic applications of graphene. In fig. 4.9, we show histograms of the solar cell performance parameters for the best devices, highlighting their reproducibility.

Enhancements in the efficiency can be attributed to the improved V_{oc}, J_{sc}, and FF, and may stem from beneficial factors resulting from synergetic effects between graphene and TiO_2 nanoparticles. As graphene has a work function between that of FTO and the TiO_2 conduction band, it may reduce the formation of energy barriers at the material interfaces and therefore behave as a better electron collector than with TiO_2 alone.[53] Secondly, the superior charge mobility of graphene, may provide improved electrical conductivity of the layer. From the very high fill factor, it is clear that the Gaphene-TiO_2 composite reduces the series resistance as compared to neat TiO_2 or even the conventional sintered TiO_2 ETL. We can quantify the series resistance in the solar cell from the reciprocal value of the linear slope of the J-V curves near the open-circuit voltage. We observe a decrease in the series resistance (R_{series}) to only 4 Ω cm^{-2}, as listed in the Table 4.1. This reduced series resistance has a striking impact upon the device FF.[54]

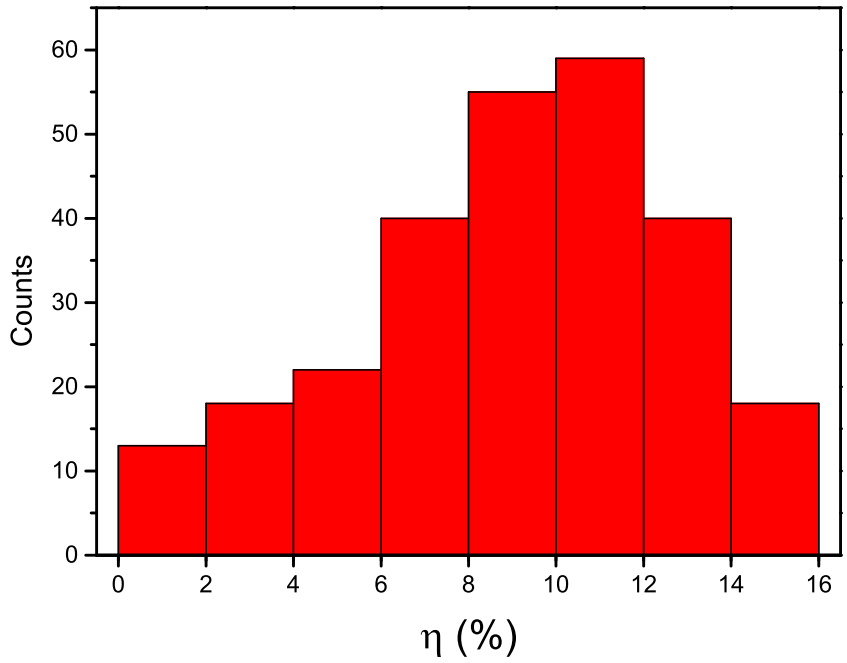


Figure 4.9: Histogram of device efficiencies from 265 unique devices fabricated with 0.6 wt% Gaphene-TiO_2 nanocomposites, as the most efficient device architecture explored in the present report.

4.5 Charge Collection

4.5.1 Light Harvesting and Quantum Efficiency

The variation in J_{sc} with graphene concentration can be due to variations in the amount of light absorbed by the active layer, the charge-collection efficiency (η_{cc}) and the charge-separation efficiency (η_{sep}). The internal quantum efficiency (IQE) is given by IQE = η_{cc}*η_{sep}. To account for variation in the light absorption in the active layer as a function of graphene concentration, the LHE (proportion of light incident on the cell which gets absorbed by the active layer) was measured. The LHE spectra of the active layer measured on complete devices incorporating a low-temperature Gaphene-TiO_2 nanocomposite are shown in fig. 4.10a. Further detailed discussion can be found in the

previous literature.[11] An example of cumulative light extinction through the device layers with 0.6 wt% Gaphene-TiO_2 nanocomposites as an electron collection layer is shown in fig. 4.10b. The different composition of Gaphene-TiO_2 nanocomposites and its internal quantum efficiency are given in fig. 4.10c which was calculated by integration over the absorption spectrum. In fig. 4.10d, we also show the transmittance spectra of the different composition of Gaphene-TiO_2 nanocomposites with glass slide as reference substrate. We conclude therefore that the changes in the photocurrent density between the samples are not due to changes in the total light absorbed in the perovskite layers.

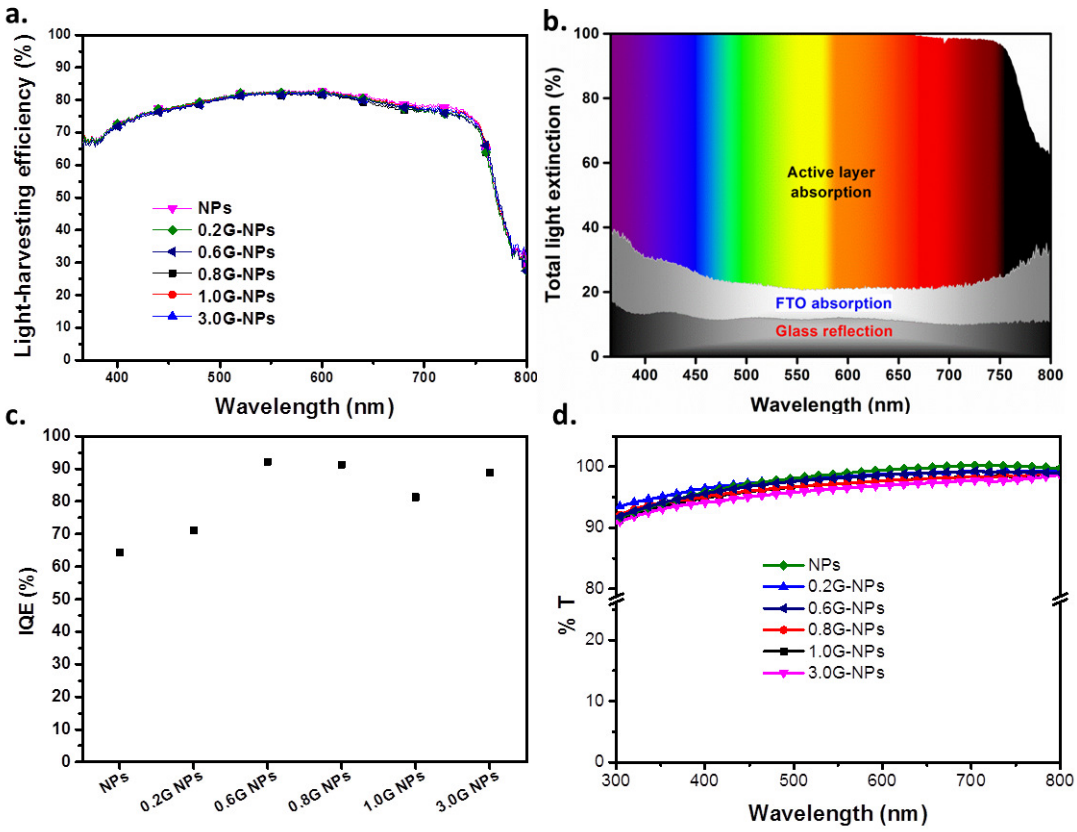


Figure 4.10: (a) Light-harvesting efficiency spectra of complete devices incorporating with different graphene-concentration in the electron collection layer. (b) Cumulative light extinction and (c), internal quantum efficiency in the low-temperature process Gaphene-TiO_2 perovskite solar cells. (d) Transmittance spectra of different graphene-concentration as electron collection layers on glass slides.

4.5.2 Charge Carrier Conductivity

In order to further investigate the role of graphene addition to the observed enhanced solar cell performance, we performed Impedance Spectroscopy (IS) characterization on solar cells under working cell conditions (1 sun illumination). In previous works, the methodology and analysis of the Impedance spectroscopy is described in detail.[55, 56] From these measurements we can extract the series resistance in the device, R_{series}, and the recombination resistance, R_{rec}. The R_{rec} explicitly relates to the component of resistance under forward bias due to electron and hole recombination within the solar cell. Our results are shown in Fig. 4.11, where we observed that the addition of graphene reduces the series resistance in the cell, consistent with that extracted from the JV curves. This is consistent with an increase of the conductivity of the n-type collection layers or to a reduction in a contact resistance, either at the Perovskite/n-type layer, or n-type layers/FTO interface. The reduction in R_{series} in the devices is consistent with the JV curves and explains the increase in FF and efficiency. A second factor leading to improved performance is the recombination resistance, R_{rec}, which we show to increase with the Gaphene-TiO_2 composite in Fig. 4.11b. We would envisage that the highly conductive graphene should introduce new recombination centres, and indeed the lower photocurrent in the graphene only devices is consistent with this. However, if the graphene flakes are fully coated with TiO_2 nanoparticles, then there should be no, or limited direct contact between the graphene and the perovskite. Previously it has been observed that TiO_2 nanoparticles will undergo efficient electron transfer to Graphene.[41] Hence we postulate that in the Gaphene-TiO_2 composite, most of the electron density will reside on the graphene, and the ensuing "depleted" TiO_2 contacting the perovskite will have a lower recombination rate with the holes in the perovskite, due to the reduced electron density in the TiO_2 , thus contributing to the increase in the photocurrent under working conditions.

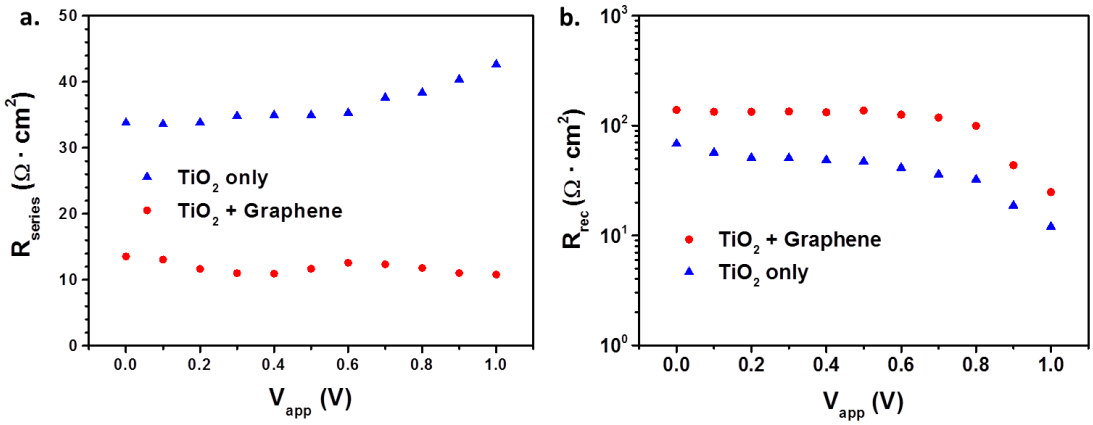


Figure 4.11: (a) Light-harvesting efficiency spectra of complete devices incorporating with different graphene-concentration in the electron collection layer. (b) Cumulative light extinction and (c), internal quantum efficiency in the low-temperature process Gaphene-TiO_2 perovskite solar cells. (d) Transmittance spectra of different graphene-concentration as electron collection layers on glass slides.

4.6 Summary

In this chapter, we have demonstrated the successful combination of two emerging materials, graphene and hybrid organic-inorganic trihalide perovskites, in solar cells. By exploiting nanocomposites of high quality graphene flakes and pre-synthesized TiO_2 nanoparticles in perovskite solar cells as a low-temperature processed electron collection layer, we have achieved a remarkable power conversion efficiency of 15.6%. This was the best recorded efficiency for low-temperature processed solar cells, and matched the highest reported efficiency of high-temperature processed perovskite solar cells while this study is published. This work also set a milestone for incorporation of graphene in solar cells. This finding indicates that high efficiency solar cells may no longer need a high-temperature sintering process for TiO_2 as the electron collection layer. By combining with the fast printing deposition methods, the Gaphene-TiO_2 nanocomposite is ready to be compatible with reel-to-reel process and meet the needs of large scale industrial manufacture on a range of substrates and multi-layer architectures.

References

[1] Jacob Tse-Wei Wang, James M. Ball, Eva M. Barea, Antonio Abate, Jack A. Alexander-Webber, Jian Huang, Michael Saliba, Ivan Mora-Sero, Juan Bisquert, Henry J. Snaith, and Robin J. Nicholas. Low-temperature processed electron collection layers of graphene/TiO2 nanocomposites in thin film perovskite solar cells. *Nano letters*, 14(2):724–30, feb 2014.

[2] M A Green, K Emery, Y Hishikawa, W Warta, and E D Dunlop. Solar cell efficiency tables (version 41). *Progress in Photovoltaics*, 21(1):1–11, 2013.

[3] P Jackson, D Hariskos, E Lotter, S Paetel, R Wuerz, R Menner, W Wischmann, and M Powalla. New world record efficiency for Cu(In,Ga)Se-2 thin-film solar cells beyond 20%. *Progress in Photovoltaics*, 19(7):894–897, 2011.

[4] J Britt and C Ferekides. THIN-FILM CDS/CDTE SOLAR-CELL WITH 15.8-PERCENT EFFICIENCY. *Applied Physics Letters*, 62(22):2851–2852, 1993.

[5] A J Nozik. Quantum dot solar cells. *Physica E-Low-Dimensional Systems & Nanostructures*, 14(1-2):115–120, 2002.

[6] B Oregan and M Gratzel. A LOW-COST, HIGH-EFFICIENCY SOLAR-CELL BASED ON DYE-SENSITIZED COLLOIDAL TIO2 FILMS. *Nature*, 353(6346):737–740, 1991.

[7] G Yu, J Gao, J C Hummelen, F Wudl, and A J Heeger. POLYMER PHOTOVOLTAIC CELLS - ENHANCED EFFICIENCIES VIA A NETWORK OF INTERNAL DONOR-ACCEPTOR HETEROJUNCTIONS. *Science*, 270(5243):1789–1791, 1995.

[8] Michael M. Lee, Joël Teuscher, Tsutomu Miyasaka, Takurou N. Murakami, and Henry J. Snaith. Efficient Hybrid Solar Cells Based on Meso-Superstructured Organometal Halide Perovskites. *Science*, 338(6107):643–647, nov 2012.

[9] Dal-Ho Kim and Jea-Gun Park. Polymer photovoltaic cell embedded with p-type single walled carbon nanotubes fabricated by spray process. *Nanotechnology*, 23(32):325401, aug 2012.

[10] Jun Hong Noh, Sang Hyuk Im, Jin Hyuck Heo, Tarak N Mandal, and Sang Il Seok. Chemical management for colorful, efficient, and stable inorganic-organic hybrid nanostructured solar cells. *Nano Letters*, 13(4):1764–1769, apr 2013.

[11] James M. Ball, Michael M. Lee, Andrew Hey, and Henry J. Snaith. Low-temperature processed meso-superstructured to thin-film perovskite solar cells. *Energy & Environmental Science*, 6(6):1739–1743, 2013.

[12] Julian Burschka, Norman Pellet, Soo-Jin Moon, Robin Humphry-Baker, Peng Gao, Mohammad K Nazeeruddin, and Michael Grätzel. Sequential deposition as a route to high-performance perovskite-sensitized solar cells. *Nature*, 499(7458):316–319, jul 2013.

[13] Henry J. Snaith. Perovskites: The Emergence of a New Era for Low-Cost, High-Efficiency Solar Cells. *The Journal of Physical Chemistry Letters*, 4(21):3623–3630, nov 2013.

[14] Michael Graetzel, René a J Janssen, David B Mitzi, and Edward H Sargent. Materials interface engineering for solution-processed photovoltaics. *Nature*, 488(7411):304–312, aug 2012.

[15] V Thavasi, V Renugopalakrishnan, R Jose, and S Ramakrishna. Controlled electron injection and transport at materials interfaces in dye sensitized solar cells. *Materials Science & Engineering R-Reports*, 63(3):81–99, 2009.

[16] B S Ong, C S Li, Y N Li, Y L Wu, and R Loutfy. Stable, solution-processed, high-mobility ZnO thin-film transistors. *Journal of the American Chemical Society*, 129(10):2750–2751, 2007.

[17] Z M Beiley and M D McGehee. Modeling low cost hybrid tandem photovoltaics with the potential for efficiencies exceeding 20%. *Energy & Environmental Science*, 5(11):9173–9179, 2012.

[18] David Muñoz-Rojas, Haiyan Sun, Diana C. Iza, Jonas Weickert, Li Chen, Haiyan Wang, Lukas Schmidt-Mende, and Judith L. MacManus-Driscoll. High-speed atmospheric atomic layer deposition of ultra thin amorphous TiO 2 blocking layers at 100 C for inverted bulk heterojunction solar cells. *Progress in Photovoltaics: Research and Applications*, 21:393–400, apr 2013.

[19] M Durr, A Schmid, M Obermaier, S Rosselli, A Yasuda, and G Nelles. Low-temperature fabrication of dye-sensitized solar cells by transfer of composite porous layers. *Nature Materials*, 4(8):607–611, 2005.

[20] X L Hu, G S Li, and J C Yu. Design, Fabrication, and Modification of Nanostructured Semiconductor Materials for Environmental and Energy Applications. *Langmuir*, 26(5):3031–3039, 2010.

[21] H C Weerasinghe, P M Sirimanne, G V Franks, G P Simon, and Y B Cheng. Low temperature chemically sintered nano-crystalline TiO2 electrodes for flexible dye-sensitized solar cells. *Journal of Photochemistry and Photobiology a-Chemistry*, 213(1):30–36, 2010.

[22] J W Gong, J Liang, and K Sumathy. Review on dye-sensitized solar cells (DSSCs): Fundamental concepts and novel materials. *Renewable & Sustainable Energy Reviews*, 16(8):5848–5860, 2012.

[23] N G Park, J van de Lagemaat, and A J Frank. Comparison of dye-sensitized rutile- and anatase-based TiO2 solar cells. *Journal of Physical Chemistry B*, 104(38):8989–8994, 2000.

[24] H C Weerasinghe, F Z Huang, and Y B Cheng. Fabrication of flexible dye sensitized solar cells on plastic substrates. *Nano Energy*, 2(2):174–189, 2013.

[25] S Ito, N L C Ha, G Rothenberger, P Liska, P Comte, S M Zakeeruddin, P Pechy, M K Nazeeruddin, and M Gratzel. High-efficiency (7.2%) flexible dye-sensitized solar cells with Ti-metal substrate for nanocrystalline-TiO2 photoanode. *Chemical Communications*, (38):4004–4006, 2006.

[26] J H Chen, C Jang, S D Xiao, M Ishigami, and M S Fuhrer. Intrinsic and extrinsic performance limits of graphene devices on SiO2. *Nature Nanotechnology*, 3(4):206–209, 2008.

[27] A K Geim and K S Novoselov. The rise of graphene. *Nature materials*, 6(3):183–191, 2007.

[28] S. V. Morozov, K. S. Novoselov, M. I. Katsnelson, F. Schedin, D. C. Elias, J. A. Jaszczak, and A. K. Geim. Giant Intrinsic Carrier Mobilities in Graphene and Its Bilayer. *Physical Review Letters*, 100(1):016602, jan 2008.

[29] C Lee, X D Wei, J W Kysar, and J Hone. Measurement of the elastic properties and intrinsic strength of monolayer graphene. *Science*, 321(5887):385–388, 2008.

[30] Tao Chen, Longbin Qiu, Zhenbo Cai, Feng Gong, Zhibin Yang, Zhongsheng Wang, and Huisheng Peng. Intertwined aligned carbon nanotube fiber based dye-sensitized solar cells. *Nano Letters*, 12(5):2568–2572, may 2012.

[31] A A Balandin, S Ghosh, W Z Bao, I Calizo, D Teweldebrhan, F Miao, and C N Lau. Superior thermal conductivity of single-layer graphene. *Nano Letters*, 8(3):902–907, 2008.

[32] R R Nair, P Blake, A N Grigorenko, K S Novoselov, T J Booth, T Stauber, N M R Peres, and A K Geim. Fine Structure Constant Defines Visual Transparency of Graphene. *Science*, 320(5881):1308, 2008.

[33] Haiying He, Peter Zapol, and Larry A Curtiss. Computational screening of dopants for photocatalytic two-electron reduction of CO2 on anatase (101) surfaces. *Energy {&} Environmental Science*, 5(3):6196–6205, 2012.

[34] X Huang, Z Y Zeng, Z X Fan, J Q Liu, and H Zhang. Graphene-Based Electrodes. *Advanced Materials*, 24(45):5979–6004, 2012.

[35] X Huang, X Y Qi, F Boey, and H Zhang. Graphene-based composites. *Chemical Society Reviews*, 41(2):666–686, 2012.

[36] Zongyou Yin, Jixin Zhu, Qiyuan He, Xiehong Cao, Chaoliang Tan, Hongyu Chen, Qingyu Yan, and Hua Zhang. Graphene-Based Materials for Solar Cell Applications. *Advanced Energy Materials*, 4(1):1300574, jan 2014.

[37] S X Wu, Q Y He, C L Tan, Y D Wang, and H Zhang. Graphene-Based Electrochemical Sensors. *Small*, 9(8):1160–1172, 2013.

[38] Yanhui Zhang, Zi-Rong Tang, Xianzhi Fu, and Yi-Jun Xu. Engineering the Unique 2D Mat of Graphene to Achieve Graphene-TiO2 Nanocomposite for Photocatalytic Selective Transformation: What Advantage does Graphene Have over Its Forebear Carbon Nanotube? *Acs Nano*, 5(9):7426–7435, 2011.

[39] C Z Zhu, S J Guo, P Wang, L Xing, Y X Fang, Y M Zhai, and S J Dong. One-pot, water-phase approach to high-quality graphene/TiO2 composite nanosheets. *Chemical Communications*, 46(38):7148–7150, 2010.

[40] Y Y Liang, H L Wang, H S Casalongue, Z Chen, and H J Dai. TiO2 Nanocrystals Grown on Graphene as Advanced Photocatalytic Hybrid Materials. *Nano Research*, 3(10):701–705, 2010.

[41] N L Yang, J Zhai, D Wang, Y S Chen, and L Jiang. Two-Dimensional Graphene Bridges Enhanced Photoinduced Charge Transport in Dye-Sensitized Solar Cells. *Acs Nano*, 4(2):887–894, 2010.

[42] A Pron, P Gawrys, M Zagorska, D Djurado, and R Demadrille. Electroactive materials for organic electronics: preparation strategies, structural aspects and characterization techniques. *Chemical Society Reviews*, 39(7):2577–2632, 2010.

[43] J N Coleman. Liquid Exfoliation of Defect-Free Graphene. *Accounts of Chemical Research*, 46(1):14–22, 2013.

[44] Y Hernandez, V Nicolosi, M Lotya, F M Blighe, Z Y Sun, S De, I T McGovern, B Holland, M Byrne, Y K Gun'ko, J J Boland, P Niraj, G Duesberg, S Krishnamurthy, R Goodhue, J Hutchison, V Scardaci, A C Ferrari, and J N Coleman. High-yield production of graphene by liquid-phase exfoliation of graphite. *Nature Nanotechnology*, 3(9):563–568, 2008.

[45] A O'Neill, U Khan, P N Nirmalraj, J Boland, and J N Coleman. Graphene Dispersion and Exfoliation in Low Boiling Point Solvents. *Journal of Physical Chemistry C*, 115(13):5422–5428, 2011.

[46] F Bonaccorso, A Lombardo, T Hasan, Z P Sun, L Colombo, and A C Ferrari. Production and processing of graphene and 2d crystals. *Materials Today*, 15(12):564–589, 2012.

[47] A C Ferrari, J C Meyer, V Scardaci, C Casiraghi, M Lazzeri, F Mauri, S Piscanec, D Jiang, K S Novoselov, S Roth, and A K Geim. Raman spectrum of graphene and graphene layers. *Physical Review Letters*, 97(18), 2006.

[48] K S Novoselov, A K Geim, S V Morozov, D Jiang, Y Zhang, S V Dubonos, I V Grigorieva, and A A Firsov. Electric field effect in atomically thin carbon films. *Science*, 306(5696):666–669, 2004.

[49] F. Bonaccorso, L. Colombo, G. Yu, M. Stoller, V. Tozzini, A. C. Ferrari, R. S. Ruoff, and V. Pellegrini. Graphene, related two-dimensional crystals, and hybrid systems for energy conversion and storage. *Science*, 347(6217):1246501, jan 2015.

[50] Mingzhen Liu, Michael B Johnston, and Henry J Snaith. Efficient planar heterojunction perovskite solar cells by vapour deposition. *Nature*, 501(7467):395–398, sep 2013.

[51] X Wang, L J Zhi, and K Mullen. Transparent, conductive graphene electrodes for dye-sensitized solar cells. *Nano Letters*, 8(1):323–327, 2008.

[52] E Z Shi, H B Li, L Yang, L H Zhang, Z Li, P X Li, Y Y Shang, S T Wu, X M Li, J Q Wei, K L Wang, H W Zhu, D H Wu, Y Fang, and A Y Cao. Colloidal Antireflection

Coating Improves Graphene-Silicon Solar Cells. *Nano Letters*, 13(4):1776–1781, 2013.

[53] H J Snaith and M Gratzel. The role of a "Schottky barrier" at an electron-collection electrode in solid-state dye-sensitized solar cells. *Advanced Materials*, 18(14):1910–1914, 2006.

[54] Jenny Nelson. *The Physics of Solar Cells*. Imperial College Press, may 2003.

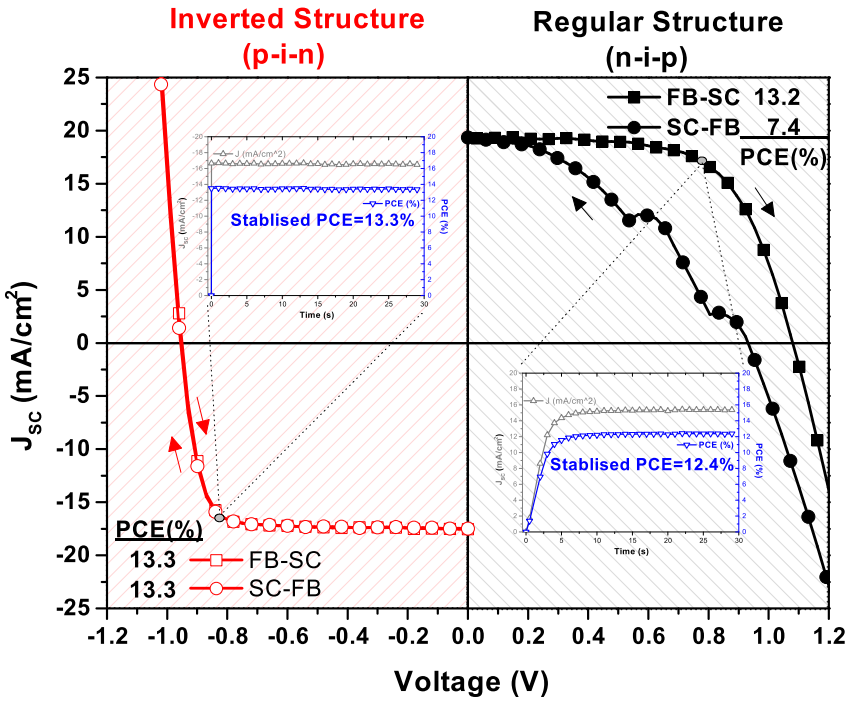
[55] Hui-Seon Kim, Ivan Mora-Sero, Victoria Gonzalez-Pedro, Francisco Fabregat-Santiago, Emilio J Juarez-Perez, Nam-Gyu Park, and Juan Bisquert. Mechanism of carrier accumulation in perovskite thin-absorber solar cells. *Nature communications*, 4:2242, jan 2013.

[56] Hui-Seon Kim, Jin-Wook Lee, Natalia Yantara, Pablo P Boix, Sneha a Kulkarni, Subodh G Mhaisalkar, Michael Grätzel, and Nam-Gyu Park. High Efficiency Solid State Sensitized Solar Cell Based on Submicrometer Rutile TiO2 Nanorod and CH3NH3PbI3 Perovskite Sensitizer. *Nano Letters*, may 2013.

Chapter 5

Tailoring of Interfacial Layers in The Inverted Perovskite Solar Cells

The work in this chapter has been adapted and reproduced in part with permission from: Jacob Tse-Wei Wang, Henry J. Snaith, and Robin Nicholas, Interface Engineering on Inverted Perovskite Solar Cells, *manuscript in preparation.*



5.1 Context

Organic-inorganic halide perovskites have generated tremendous interest over the past few years. Many efforts have been made to improve the regular (n-i-p) architecture in facilitating charge extraction with improved selective contacts and deposition processes to further push the performance ahead. However, an anomalous hysteresis behaviour is widely observed in the regular structure, much worse than for the inverted (p-i-n) architecture. It has been pointed out, the cause of hysteresis is very likely to stem from unfavourable interfaces within the device. Therefore, it is important to understand the difference, and investigate the role of the interfaces in the two structures, so as to push up the device performance. In this chapter, a development of inverted PSCs will be demonstrated, and the influence of energy level alignment on device performance will be studied and discussed.

5.2 Introduction

The architecture of the PSCs can be mainly categorised into two types by the sequence of selective contacts being deposited, designated as "p-i-n" and "n-i-p" configuration. (Note that, n, p, and i stand for n-type, p-type selective contacts, and i for the intrinsic perovskite layer, respectively) Between these two architectures on PSCs, early efforts were first made on the n-i-p mesoporous architecture configuration as the PSCs were evolving from the structure of solid-state dye-sensitised solar cells (ssDSSCs)[1, 2]. Ball et al. later discovered the feasibility of pure planar heterojunction (PHJ) n-i-p structure, but compared to the meso-structure solar cells (MSSCs), the planar structure was still showing inferior performance due to poor film coverage[3]. Nonetheless, substantial improvement was demonstrated by Liu et al., using thermal evaporation deposition to achieve uniform perovskite coverage and realise a power conversion efficiency (PCE) over

15% on PHJ structure[4]. Stranks et al. showed the carrier diffusion length could be over 1 μm further proving the practicability of PHJ structure.[5] Now, PSCs with n-i-p architecture has shown performance on a par with a conventional Si-based solar cell, but a thin layer of meso TiO_2's presence is still required and an anomalous hysteresis in the current-voltage (J-V) curves is still widely observed in the regular n-i-p configuration[6, 7]. Lately, efforts have been made to identify the origin of the anomalous hysteresis, and evidence shows hysteresis effect in PSCs are predominantly influenced by; a) nature of the electronic contact between the perovskite and the p- and n-type contact materials, b) existence of a large defect density within or near the surface of the perovskite material, and c) excess and labile ions, such as interstitial defects (iodide or methylammonium) present in the perovskite film.[8, 9]

Meanwhile, the emergence of the inverted p-i-n configuration has shifted the focus of PSCs development, where the structure was inherited from the organic photovoltaics (OPV)[10, 11], deploying mainly organic-based contacts on both selective electrodes showing comparable performance to n-i-p structures but without any hysteresis behaviour [12]. Apart from the absence of hysteresis behaviour, the inverted PSCs also benefit from other advantages from the OPV, such as low-temperature processing, flexibility, an adjustable work function and charge extraction properties in the organic-based interfacial layers via chemical synthesis or chemical doping imposed properties. Consequently, this architecture has attracted a lot of attention. It is well known that the interfacial layers play a crucial role in assisting charge separation and injection. The faster the carriers can be removed from the interface, the better chance to avoid a loss mechanism. Thus, to achieve fast charge extraction, it is essential to have optimised charge-transporting pathways with good interfaces throughout all layers in the solar cells. Therefore, in the quest for highly efficient PSCs, it is important to investigate the merits of inverted PSCs, so as to push the performance further forward. In this chapter, the individual components from cathode to anode, forming a working inverted PSCs will

be studied. And the influence of the energy level alignment on device performance will be evaluated and discussed.

5.3 Surface Modification on Transparent Conducting Electrode

The most commonly used transparent electrode in the PSCs is Fluorine-doped Tin Oxide (FTO), with its robustness for high-temperature fabrication and chemical inertness, and is less expensive compared to Indium-doped Tin Oxide (ITO), which make it widely adopted as the transparent conducting electrode in the optoelectronic community.[13] FTO is known to have a work function of $\sim$ 4.4 eV[14], hence is commonly used as an anode to collect the electrons. However, Docampo et al. reported the first inverted PSCs with FTO as a cathode to facilitate hole injection and collection[10]. These applications normally require a cathode with a work function (Φ) between 4.7-5.0 eV for efficient device operation, which makes FTO's energy level incompatible with hole collection, whereas the use of an ITO electrode ($\Phi \approx$ 4.8 eV) would be more appropriate.[11, 15] But in the interest of pursuing a cheap alternative to the ITO electrode, here, we try to adopt the FTO as the transparent electrode, in an inverted architecture of Al/TiO_x/PCBM/$CH_3NH_3PbI_{3-x}Cl_x$/PEDOT:PSS/FTO structure[10]. However, a barely working device with huge hysteresis is observed, seen fig. 5.1. As the work function of the standard PEDOT:PSS (AI 4083) employed is 5.1-5.2 eV[16, 17]; it is believed a largely mismatched energy level difference ($\sim$ 0.7-0.8 eV) is presented at the interface, which acts as a Schottky barrier between the FTO and PEDOT:PSS to cause the apparent decrease in the device performance[18, 19], and the presence of amorphous metal oxide (TiO_x) may be the origin of the huge hysteresis[20, 21] with UV-degradation likely to happen[22]. Therefore, in the following sections, the structure

of Ag/BCP/PCBM/$CH_3NH_3PbI_{3-x}Cl_x$/PEDOT:PSS/FTO will be adopted to have a more systematic study unless further notice provide.

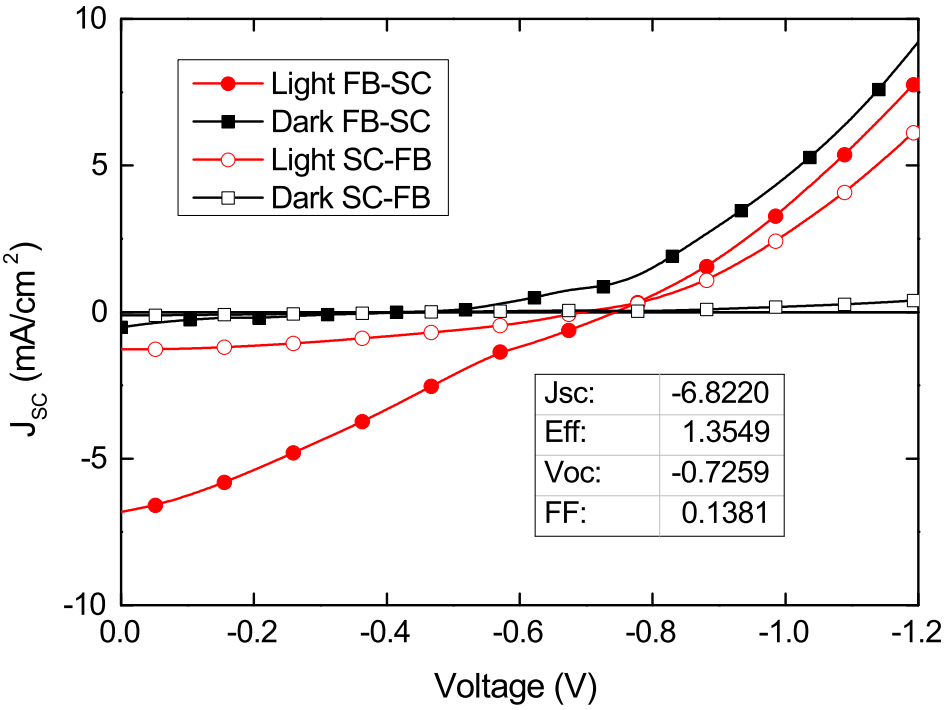


Figure 5.1: The inverted PSCs employed the structure of Al/TiO_x/PCBM/$CH_3NH_3PbI_{3-x}Cl_x$/PEDOT:PSS/FTO showing poor performance with huge hysteresis.

The general strategy to minimise an interfacial barrier at a junction is to adjust the work function at the interface. Surface modification is a commonly used method to alter the work function for such an issue. There are several approaches which have been employed on the metal-oxide electrode to achieve the desired energy level alignment with the hole-transporting materials (HTMs), including the Oxygen-plasma treatment[23], UV-ozone irradiation[24], and acid/base treatment[25, 26]. These post-treatments have been shown to effectively remove the organic contaminants on the surface of the transparent electrode, increase the hydrophilicity and wettability by introducing hydroxide functional groups on the surface, and increase the work function, thus leading to several benefits

for hole-injection/collection[23, 27] Among these methods, Piranha treatment is one of the standard recipes in the RCA clean, which Werner Kern developed while working for RCA in 1965[28], and comprises of a 3:1 mixture of sulphuric acid (H_2SO_4) with hydrogen peroxide (H_2O_2), which has a powerful ability to remove most of the organic matter. This is due to its nature as strong oxidising agent to hydroxylate most of the surfaces and make them very hydrophilic, and hence is used very frequently in the microelectronic industry. However, for the ITO substrate, it is reported the aggressive nature of Piranha solution will dissolve ITO due to the presence of Indium, hence, it is always avoided and not many studies of its use have been reported.[29] Here, we introduced the piranha treatment for the FTO, and compared this with bare-FTO (general cleaning process is applied to all the substrates prior to the treatment (with/without), which involved Hellmanex cleaning, ultrasonic acetone bath, and DI water rinsing). As has been pointed out by Armstrong et al., with the Piranha treatment, a higher concentration of hydroxide species would be produced on the surface of the oxide than by O_2-Plasma.[29] The work function of the treated surface is likely to be changed, as the surface potential is very sensitive to the polarity, morphology, and chemical state of the electrode surface.[30, 27].

5.3.1 Surface Potential

Using a Kelvin probe measurement (see Chapter 3 for experiment setup) on the FTO substrates, and we found an increase of work function from $\sim$ 4.4 eV (with bare-FTO) to $\sim$ 4.7 eV (with Piranha treated-FTO). To illustrate the energetic differences with and without the treatment applied on the FTO. We show in the fig. 5.2a and b, where the Fermi level reaches equilibrium between the two contacts, results in a final interfacial energy level alignment difference. In fig. 5.2b., we can see the modified transparent electrode has a work function that is closer to the Fermi level (E_F) of PEDOT:PSS, and a reduced hole-tranporting barrier (Φ_h'). This observation shows a good agreement

with previous reports on the other metal oxide surfaces[30, 31, 32], which also indicate a better hole collection/injection at the interface, and may further lead to an improved current injection efficiency in the device.

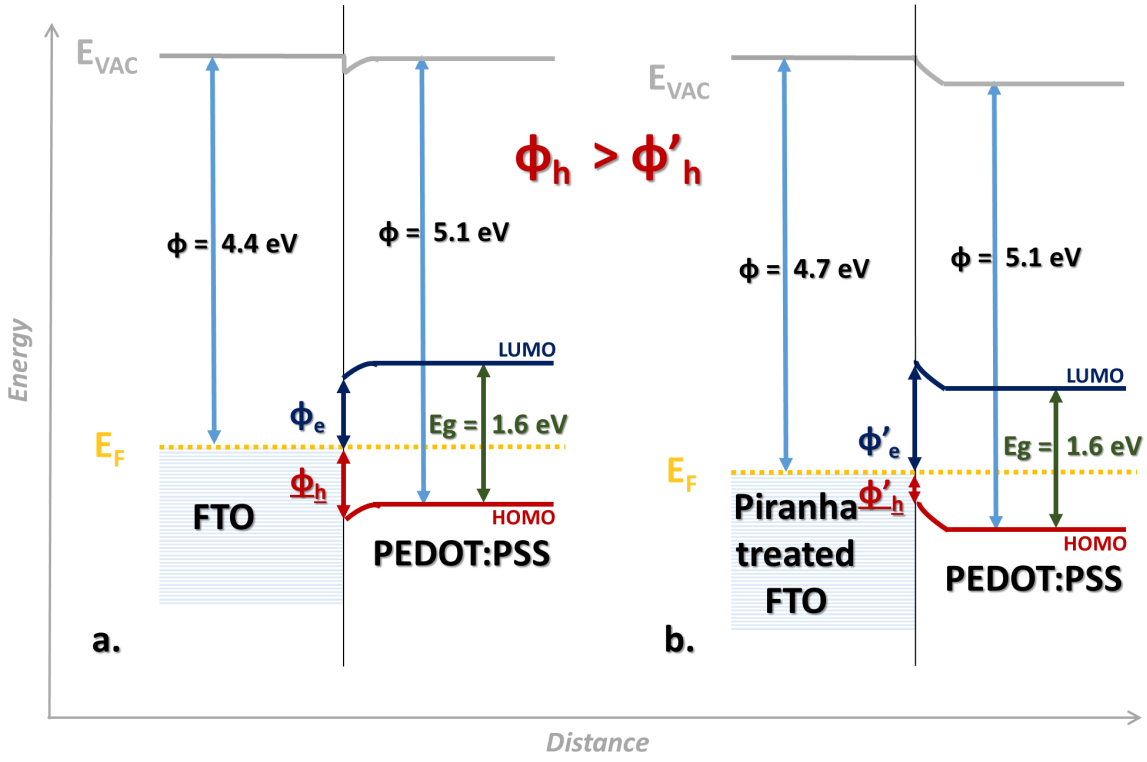


Figure 5.2: Schematic illustration of (a) the bare-FTO surface and PEDOT:PSS interface, and (b) the Piranha-treated FTO surface and PEDOT:PSS interface, with their corresponding energy level shifts indicated and showing the hole barrier (Φ_h) after the treatment (Φ'_h) being reduced.

5.3.2 Work Function Influenced Device Performance

In order to confirm the effect of the surface treatment, we use the treated substrates in the inverted PSCs (Ag/BCP/PCBM/$CH_3NH_3PbI_{3-x}Cl_x$/PEDOT:PSS/FTO). In fig. 5.3 and Table 5.1, we show the mean solar cell performance parameters for a batch of solar cells with different surface treatment, extracted from J-V curves measured under simulated AM 1.5, 100 mW/cm^2 sunlight. We can see a clear enhancement in device performance with the introduction of surface modification. For devices fabricated from

the bare-FTO, the average short-circuit current density (J_{sc}) and FF are around -7.1 mA/cm^2 and 0.21, respectively, showing a poor charge transport behaviour. With the surface treatment by Piranha solution, both the J_{sc} and FF increase up to average values of -15.6 mA/cm^2 and 0.58, respectively, and we also observe that the average open-circuit voltage (V_{oc}) shows a small improvement, increasing from -0.86 V to -0.89 V. As a result, the power conversion efficiency (PCE) substantially improves from less than 1% to around 8%. The dramatic enhancement, can be attributed primarily to the better matching of the energy levels, as the reduced hole-transporting barrier can link to the improved current density here, where we see a similar observation to Li et al., when an acid treatment was applied to an ITO surface.[19] It is worth noting here, that the typical O_2-plasma treatment also shows an overall PCE enhancement compared to the bare-FTO, however, all the average performance parameters are still lower than the Piranha-treated devices.

Table 5.1: Mean solar cell performance parameters with different surface treatment on FTO under simulated AM 1.5, 100 mW/cm^2 solar irradiation

Sample	Jsc(mA/cm^2)	Voc(V)	FF	PCE(%)
Bare-FTO	-7.1±7.4	-0.90±0.02	0.20±0.11	0.9±0.9
Plasma Treatment	-12.2±3.0	-0.82±0.09	0.45±0.14	4.7±2.4
Pirahna Treatment	-15.6±3.3	-0.09±0.10	0.60±0.06	8.3±2.7

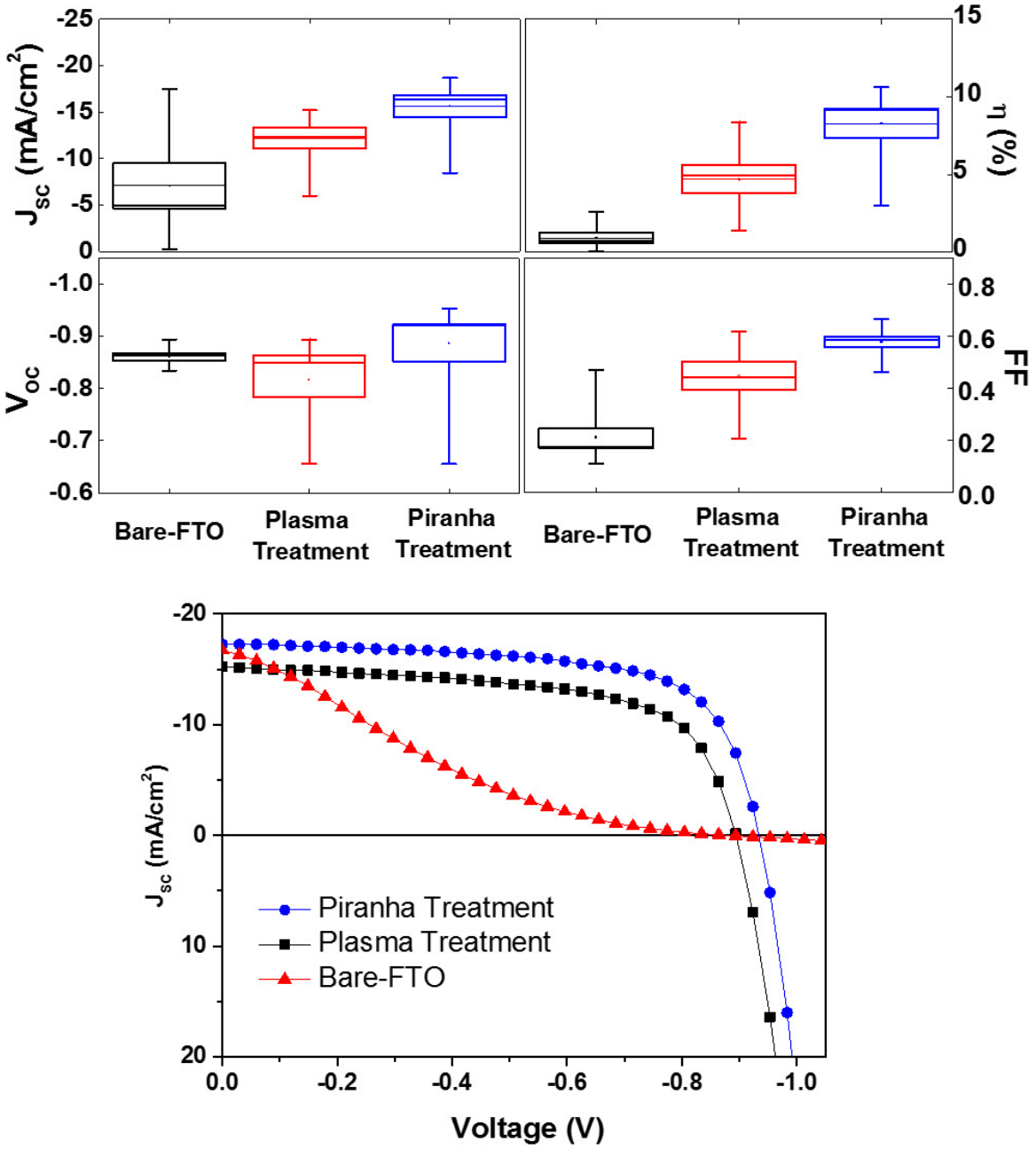


Figure 5.3: Devices performance characteristics with different surface treatment of under simulated AM 1.5, 100 mW/cm^2 irradiance in air. (a) Device performance parameters extracted from a batch of current-voltage measurements. (b) The current density-voltage curves of the best devices in the batch.

5.4 Hole-Transporting Layer and Thickness dependence

Among the various conducting polymers, poly(3,4-ethylenedioxythiophene):poly(styrenesulfonate) (PEDOT:PSS) is the most widely used hole-transporting material (HTM), owing to its efficient hole-selectivity accompanied by high transparency, good thermal stability, and the flexibility in deposition methods with its water-soluble nature; which make it very appealing for photovoltaic applications.[33] In addition to these practical benefits, it has also been successfully commercialised by many companies, with large-scale manufacture leading to economically viability.[34] From the previous section, we have found the Piranha treatment leads to improved surface properties on FTO, here in this section, we report the study of PEDOT:PSS on the Piranha-treated FTO and its thickness impact on the photovoltaic performance.

In fig. 5.4a, we show the best-performing current density-voltage (J-V) curves of devices with different PEDOT:PSS thickness varied by spinning speed, extracted from a batch of solar cells measured under simulated AM 1.5, 100 mW/cm^2 sunlight, where a clear J_{sc} enhancement can be seen, which increases from 16 mA/cm^2 (4500 rpm) to over 19 mA/cm^2 (6500 rpm). Here, the concentration of the HTL was kept unchanged by using the stock-solution (AI 4083) as received. The corresponding statistical distributions also show the same increase, which can be found in fig. 5.4b and Table 5.2. The changed HTL thickness was found to have a significant impact on device performance, especially J_{sc} and FF. Starting from 4500 rpm, the average short-circuit current density and fill factor (FF) are around -14.6 mA/cm^2 and 0.53, respectively. With decreasing PEDOT:PSS thickness in the HTL, both the J_{sc} and FF increase up to average values of around -16.4 mA/cm^2 and 0.61, respectively, peaking at 6500 rpm, followed by a decrease with further decreasing thickness. However, in contrast to the J_{sc} and FF, the average open circuit

voltages (V_{oc}) remain more or less the same with an average V_{oc} of around -0.94 V. Hence, the power conversion efficiency (PCE), peaks with an average PCE value around 10.2%. The J_{sc} and FF enhancement can be simply explained by the reduction of series resistance in the device, and can be further attributed to the improved hole-transporting efficiency within the solar cells, which share the same observation as shown by Kim et al.[35]

Table 5.2: Mean solar cell performance parameters with different thickness of PEDOT:PSS varied by spinning speed, under simulated AM 1.5, 100 mW/cm^2 solar irradiation.

Spinning Speed of PEDOT:PSS (rpm)	Jsc(mA/cm^2)	Voc(V)	FF	PCE(%)
4500	-14.6±2.0	-0.92±0.04	0.53±0.10	7.3±2.1
5000	-15.1±2.8	-0.81±0.28	0.5±0.15	6.9±3.8
5500	-16.8±1.5	-0.91±0.11	0.6±0.12	9.3±2.7
6000	-16.3±3.5	-0.88±0.19	0.61±0.14	9.4±3.8
6500	-16.2±6.1	-0.94±0.1	0.61±0.17	10.2±3.7
7000	-15.3±5.8	-0.92±0.04	0.63±0.14	9.4±4.0
7500	-15.5±1.7	-0.92±0.07	0.58±0.10	8.4±2.3

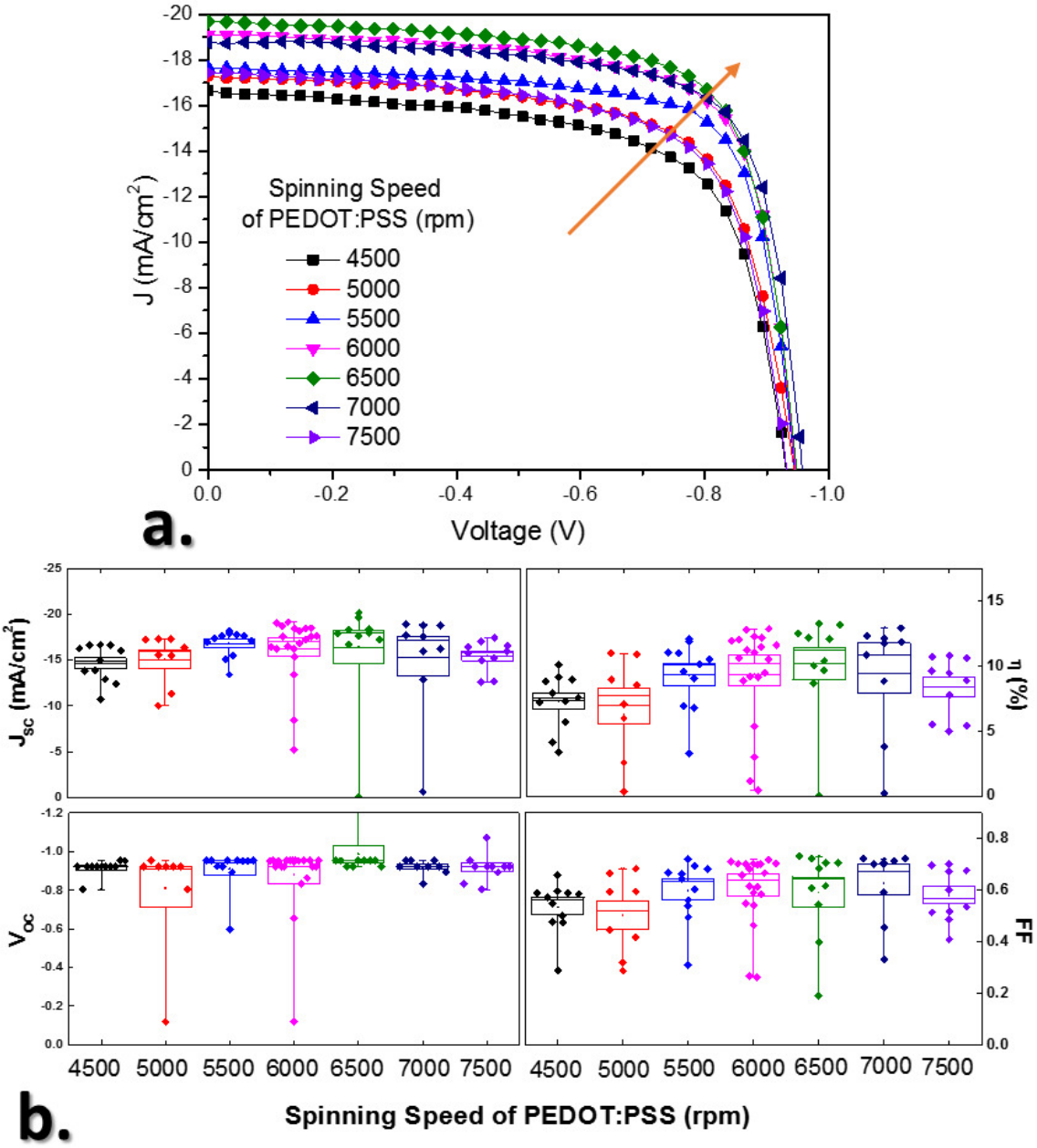


Figure 5.4: Device performance characteristics with different HTL thickness under simulated AM 1.5, 100 mW/cm^2 irradiance in air. (a) Device performance parameters extracted from a batch of current-voltage measurements. (b) The current density-voltage curves of the best devices in the batch.

5.5 Perovskite Layer and Surface Morphology

One of the many virtues of organic-inorganic perovskite is its easily implemented solution-processing properties, leading to the lowest-cost production for thin-film solar cells.[1, 3, 36] Spin-coating is one of the most accessible and reproducible methods for lab-scale research. Organic-inorganic perovskite thin-film deposition has been developed successfully with the assistance of a mesoporous scaffold[1, 2]. However, as reported by Burlakov et al. the uniform formation of single step solution-processed thin-film perovskite without a mesoporous scaffold can be difficult.[37]

5.5.1 Influence of Precursor Solution Temperature on Micro-morphology

Here, we fabricate the perovskite layer following the work of Eperon et al.[36], where they control the perovskite surface morphology on TiO_2 by varying the annealing temperature and time on the spin-coated film. However, due to the different surface properties of the underlying layer (metal oxide vs. polymer), the optimised recipe for deposition on TiO_2 does not apply on the PEDOT:PSS here directly, and results in an incomplete surface coverage with lots of voids on the HTL, see fig. 5.5a., where a room-temperature ($\sim$ 20 °C) $CH_3NH_3PbI_{3-x}Cl_x$ precursor solution was applied on the PEDOT:PSS, following the optimised recipe from Eperon et al.[36] The formation of voids in the absorption layer has been regarded as an unfavourable in PHJ devices, as it not only enables shunting paths, but also causes reduced light absorption, which eventually degrades the device performance. Accordingly, numerous efforts have been made to reduce them in thin-film perovskite formation, such as two-step sequential deposition[38], interdiffusion deposition[39], solvent engineering[40], and hot-substrate casting[41]. Inspired by these thin-film engineering studies and the hints on the importance of solvent vaporisation. We

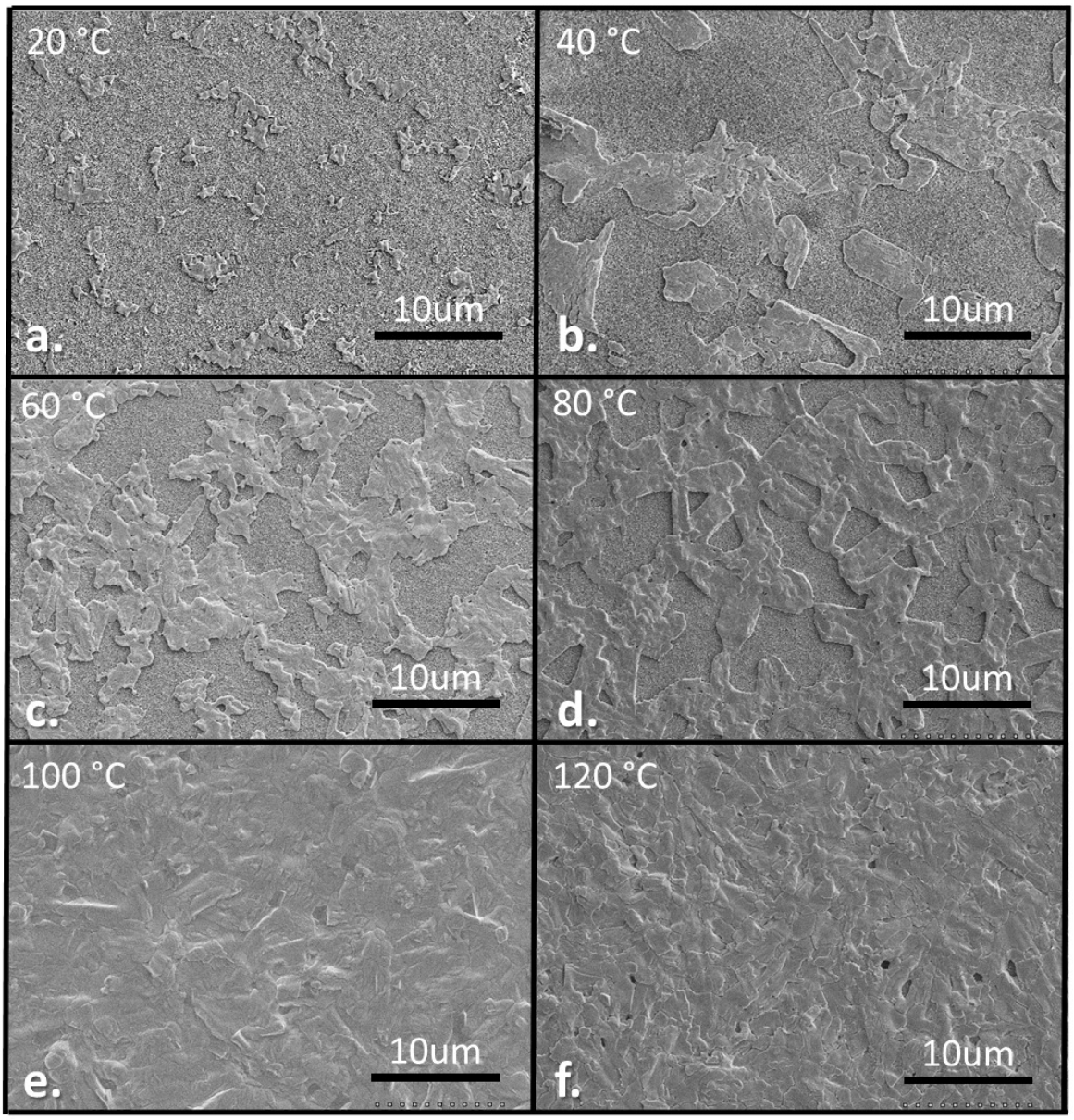


Figure 5.5: SEM images of perovskite films formed on PEDOT:PSS under different hot-solution casting temperature.

introduced a hot-precursor solution casting technique to improve the $CH_3NH_3PbI_{3-x}Cl_x$ film formation, where a better temperature control can be achieved by avoiding the cooling which occurs during substrate transfer. This gives a more reproducible process than can be achieved by hot-substrate casting. A range of temperatures from 20 °C (room-temperature, non-heated) to 120 °C were applied by the hot-plate in intervals of 20 °C to the vial containing the $CH_3NH_3PbI_{3-x}Cl_x$ precursor with lid-closed. Once the designated-temperature is reached, a 100 μl precursor solution is pipetted from the vial and dynamically spincoated on the substrate immediately.

In fig. 5.5 a-f, we show the top surface SEM micrographs of the perovskite formed at different hot-solution casting temperatures. Due to the temperature-influenced solvent vaporisation rate and the as-cast film wetting properties on the PEDOT, the perovskite surface morphology shows the appearance of islands at room temperature deposition, while as we start increasing the precursor solution casting temperature, we can see the islands are starting to merge with increasing temperature, and display a nearly complete coverage at 100 °C solution-casting temperature with voids (dark holes) beginning to appear at the highest temperature.

5.5.2 Morphology Influenced Device Performance

Knowing the hot-solution casting effects on the perovskite surface morphology, we then fabricated inverted PSCs with same parameters. The mean solar cell performance parameters with hot-solution casting at different temperatures are shown in the Table. 5.3 and its corresponding current-voltage curves and statistic distribution are presented in fig. 5.6. The changed perovskite morphology was found to have a notable influence in all aspects of device performance. Where short-circuit current densities were raised from an average 2 mA/cm^2 to over 17 mA/cm^2, fill factors (FF) were increased from 0.5 to nearly 0.7, and the V_{oc} increased from 0.73 V to over 0.9 V, between room-temperature

and 100 °C solution casting temperature. However, following the peak performance at 100°C there is a fall off, presumably due to the appearance of the pin-holes at higher casting temperatures, and both the J_{sc} and FF are starting to decrease. As a result, the peak power conversion efficiency (PCE), gives an average PCE value around 10.6% for 100 °C casting temperature. The enhanced device performance may be attributed to the improved interface and surface morphology observed, where it is likely to avoid the pin-hole induced shunting paths which reduce the recombination rate, and potentially increase the light absorption by a more uniform morphology with minimised light reflection.

Table 5.3: Mean solar cell performance parameters with hot-solution casting at different temperature, under simulated AM 1.5, 100 mW/cm^2 solar irradiation.

Hot-solution casting temperature (°C)	Jsc(mA/cm^2)	Voc(V)	FF	PCE(%)
20	-11.9±1.9	-0.73±0.11	0.5±0.12	4.5±1.9
40	-12.6±2.9	-0.73±0.13	0.51±0.07	4.9±2.1
60	-13.4±2.8	-0.89±0.10	0.54±0.12	6.6±2.4
80	-15.8±1.4	-0.88±0.03	0.53±0.07	7.5±1.5
100	-17.6±1.5	-0.89±0.01	0.70±0.03	10.9±1.3
120	-15.6±2.7	-0.91±0.02	0.6±0.08	8.6±2.2

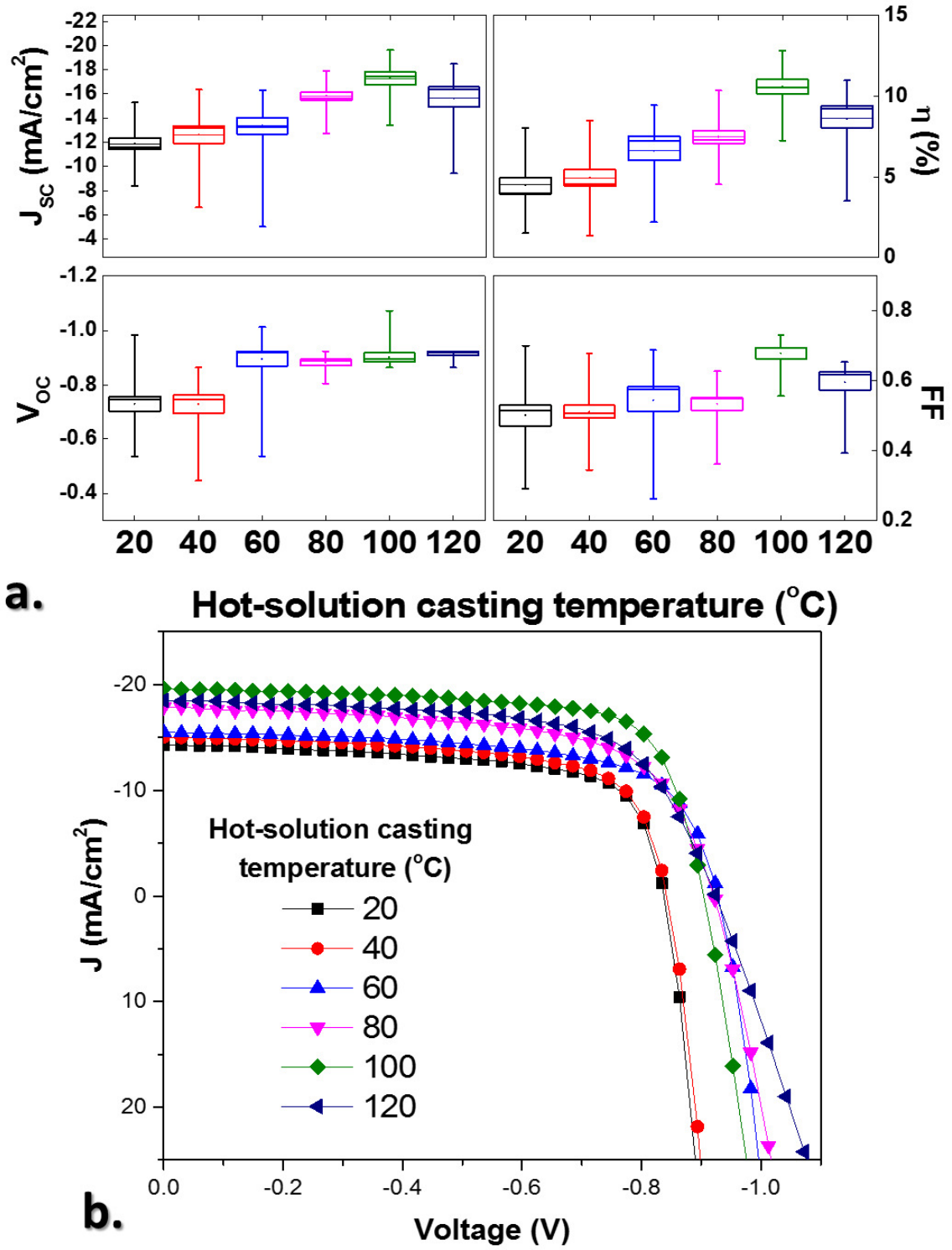


Figure 5.6: Devices performance characteristics with hot-solution casting at different temperature under simulated AM 1.5, 100 mW/cm^2 irradiance in air. (a) Device performance parameters extracted from a batch of current-voltage measurements. (b) The current density-voltage curves of the best devices in the batch.

To confirm whether the increased J_{sc} and the overall device performance is also coming from the increased light absorption, we performed UV-vis absorption measurements on the perovskite films with different hot-solution casting temperatures. In fig. 5.7 we show the UV-vis spectra, where it exhibits the same trend as observed in the device performance and SEM surface coverage, as the maximum absorption was attained at the 100 °C hot-solution casting perovskite film.

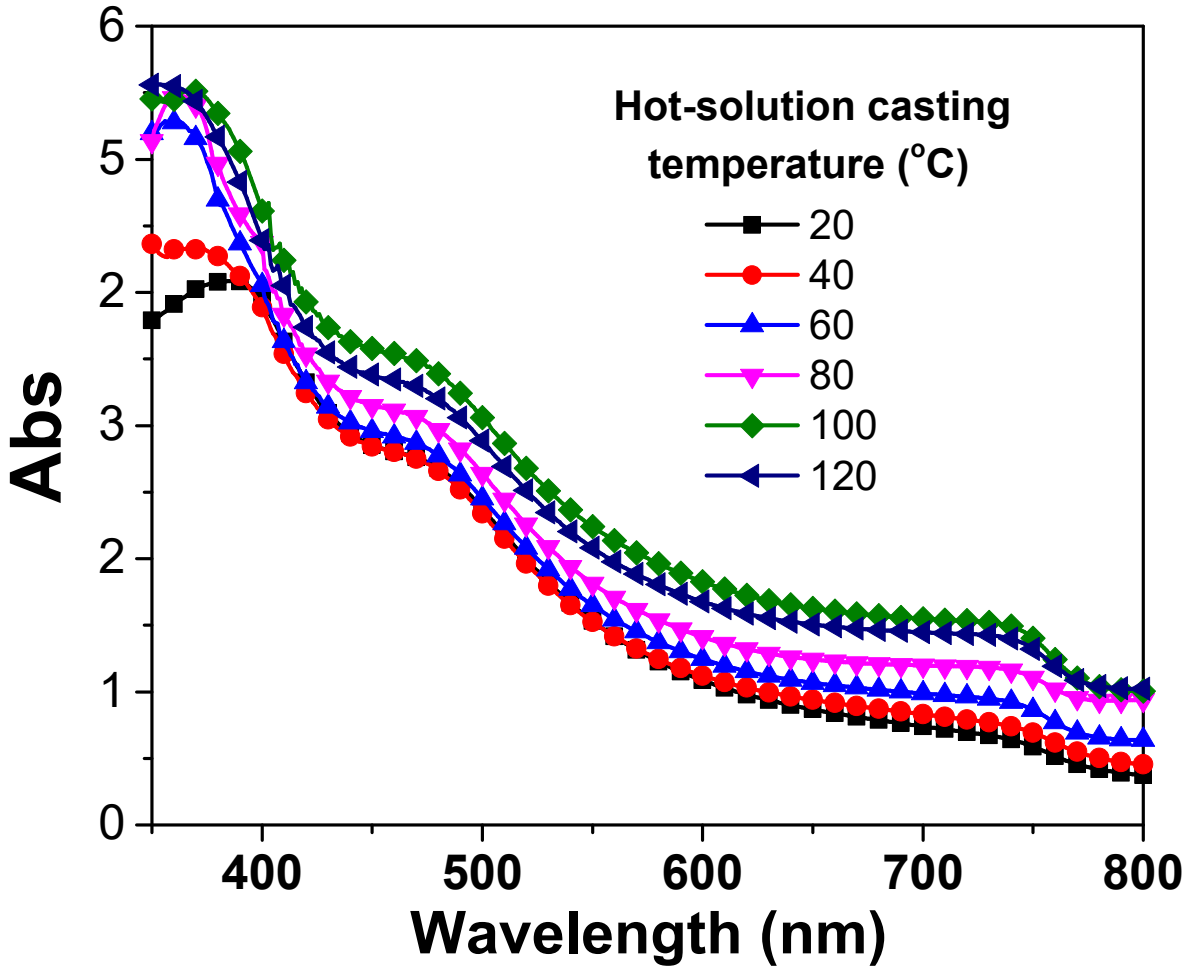


Figure 5.7: The UV-vis absorption spectra of perovskite films formed on PEDOT:PSS under different hot-solution casting temperature.

5.6 Electron-Transporting Layer and Thickness Dependence

Not only playing a dominant role in organic photovoltaics (OPV), the fullerene-based materials are also proving vital in efforts to facilitate electron-transport in the PSCs.[11, 12, 42] Among all the fullerene derivatives, [6,6]-Phenyl C61 butyric acid methyl ester (PCBM) is the most widely used electron-transporting material (ETM) for inverted PSCs, where owing to its ester functional group it can be easily dissolved in most of polar solvents (i.e. Chlorobenzene (CB), 1,2-Dichlorobenzene (oDCB)), thus making it favourable for solution-processing. In addition, PCBM also has a LUMO level compatible with the conduction band of the perovskites, leading to a small electron transport barrier, therefore making it an ideal ETM.[43]

As has been pointed out by Yin et al., the undercoordinated Pb^{2+} and I^{-} are likely to be present at the surface of perovskite, which may act as defects and traps for carriers.[44] Hence, it is important to remove these charge transfer barriers by means of passivation. Recent studies have also shown that the presence of a fullerene layer, in either regular or inverted PSCs architecture, can successfully suppress the anomalous hysteresis behaviour, which may be correlated to these surface defects.[12, 21, 45]

Here, we apply the PCBM on top of our modified perovskite layer, and follow the work of Shao et al. [12], upon the annealing of PCBM layer, they showed the surface defects are being efficiently passivated via the infiltration of the PCBM molecule into the perovskite layer. However, due to the different surface roughness of the perovskite thin-film, we performed the optimisation of the PCBM thickness by varying its concentration in the CB, ranging from 20 to 50 mg/ml.

In fig. 5.8a, we show the average performance parameter extracted from the current

density-voltage (J-V) curves of a batch devices measured under simulated AM 1.5, 100 mW/cm^2 sunlight with different PCBM thickness. A clear trend of performance improvement can be found with the increasing concentration of PCBM in the CB, which leads to an increasing thickness forming on top of the perovskite. Here, a maximum average PCE of 10.4±2.0 % can be attained with the 40 mg/ml PCBM concentration, which can be linked to the enhanced J_{sc} and V_{oc}. This improvement may be explained by a better coverage with the concentration of 40 mg/ml PCBM applied, resulting in a smaller device series resistance and higher shunting resistance. However, once the ETL thickness exceeds the optimum, an increased series resistance is observed, hence a reduced device performance is found in the 50 mg/ml device. In fig. 5.8b. we further show the best performing devices in the batch, which show the same distribution with the maximum PCE peaking at 40 mg/ml. While compared with a thinner ETL sample (20 mg/ml), the main enhancement is coming from the J_{sc} and FF. Detailed device performance parameters are summarised in the Table. 5.4.

Table 5.4: Mean solar cell performance parameters with different thickness of PCBM varied by concentration, under simulated AM 1.5, 100 mW/cm^2 solar irradiation.

Concentration of PCBM (mg/ml)	Jsc(mA/cm^2)	Voc(V)	FF	PCE(%)
20	-14.7±3.0	-0.89±0.06	0.59±0.06	8.0±2.5
30	-16.3±2.1	-0.92±0.02	0.63±0.06	9.6±1.8
40	-17.9±0.6	-0.91±0.05	0.63±0.1	10.4±2.0
50	-16.7±1.4	-0.92±0.02	0.60±0.1	9.3±1.9

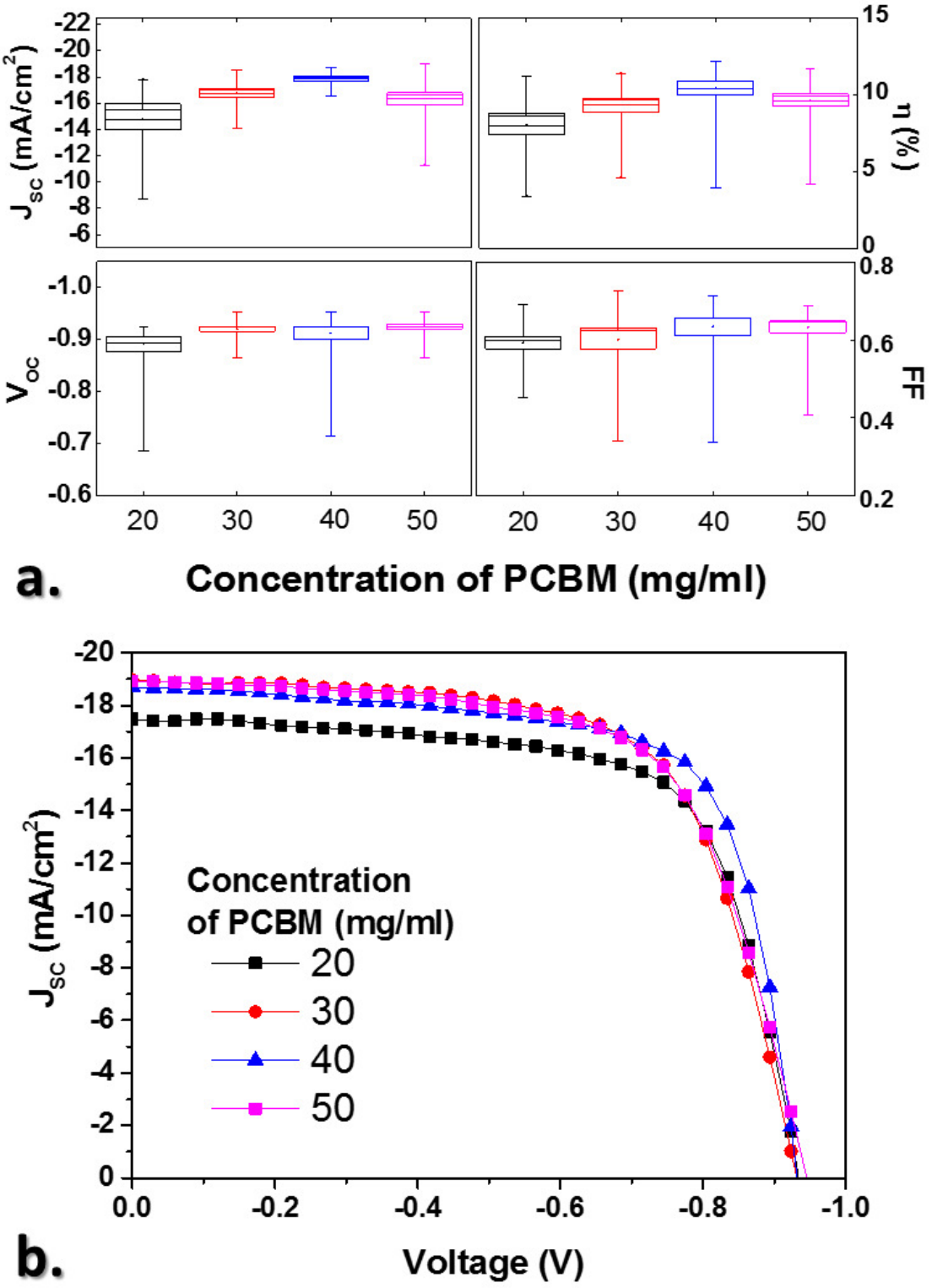


Figure 5.8: Devices performance characteristics with different thickness of PCBM varied by concentration under simulated AM 1.5, 100 mW/cm^2 irradiance in air. (a) Device performance parameters extracted from a batch of current-voltage measurements. (b) The current density-voltage curves of the best devices in the batch.

5.7 Buffer Layer and Metal Electrode

In general, the performance of a perovskite solar cell, and of any heterojunction solar cell, is affected by the nature of the buffer layers and electrodes, which play an indispensable part in the device efficiency.

In the regular structure of PSCs, the noble elements Ag and Au are widely used as the cathode due to their matching energy levels and easily accessible deposition methods; whereas, for inverted structures, a combination of a thin buffer layer and a dual metal layer consist of lower work function metal (i.e., Ca, Ba) with Al or Ag are widely used as the anode to facilitate electron injection/collection.[11, 46, 47]

The role of buffer layers here is specifically referring to the interlayer between the metal anode and ETL, where the presence of a buffer layer can prevent the diffusion of metal ions towards the ETL, and avoid any unfavourable reactions which can occur between the metal and organic layers, which are likely to influence the device performance.[48, 49] Accordingly, the use of buffer layers is widely adopted in the field of OPV, where both organic- and inorganic-based materials have been exploited and studied extensively, such as lithium fluoride (LiF), cesium carbonate (Cs_2CO_3), molybdenum trioxide (MoO_3), sodium chloride (NaCl), bathophenanthroline (BPhen), or bathocuproine (BCP).[50, 51, 52, 53, 54, 55].

One of the critical factors governing the quality of these buffer layers, is their energy level offsets at the interface, where a wide bandgap with low injection barrier for electrons and high injection barrier for holes is preferred. LiF is the most commonly used buffer layer with low work function metal electrodes (Al, Ag, etc.), and has been shown to promote the efficiency in OPV and PSCs devices by reducing the energetic barrier by the generation of a dipole moment at the ETL/metal interface.[50] However, the use of LiF, required an intensive effort and strict control of the thickness, as the deposition of

the inorganic-based buffer layer can only be achieved by thermal or sputter deposition in UHV conditions; also, the maximum thickness for the LiF is typically only around 15 Å.[56] Compared with the inorganic-based buffer layers, the main advantage of organic-based buffer layers could be their rather flexible thickness control ($\sim$ 10 nm) and the availability of both solution-deposition and vacuum-deposition methods.[55] BCP is one of the most commonly used buffer layers in OPV, due to its wide bandgap providing superior hole-blocking and electron-transport.[51] Moreover, the use of BCP has also been demonstrated in PSCs by thermal deposition with decent device performance being achieved.[57, 58, 59] However, thus far, the deposition of BCP on PSCs is still limited to the thermal deposition method, whereas solution-based deposition is rare, as the reported solution-deposition of BCP for OPV deivces uses chlorobenzene (CB)[55], which happens to be the same solvent used for the most common ETL (PCBM), thus a dissolution of ETL is likely to happen. While a methanol-dissolved BCP on PSCs has been reported on the PSCs[60], the use of a polar solvent with small molecular size like methanol could also decompose the perovskite films, thus raising concerns of compatibility and reproducibility.[61]

Here, we explore the solution-based deposition of BCP by the use of an orthogonal solvent, isopropanol (IPA), which may have a limited solubility with BCP at room temperature (less than 2 mg/ml), but enough thickness (less than 10 nm) for working devices can still be attained by spin-coating without the risk of damaging underlying layers. This also represents the first orthogonal solution-deposition buffer layer, which enables the inverted PSCs devices to be processed under ambient conditions. In fig. 5.9a, we show the comparison of current-density curves under simulated AM 1.5, 100 mW/cm^2 sunlight with the introduction of BCP on the inverted PSCs. A remarkable improvement can be found with a concentration of 1 mg/ml applied in a device without the buffer layer. The enhancement can be mainly attributed to the dual increase in the FF and J_{sc}, while the V_{oc} remained almost constant. It is worth noting here; that the

devices were taken out of the inert atmosphere to make contact with the bottom FTO electrode before the metal electrode deposition due to the constraints of the equipment set up (The evaporator is not installed within the glovebox). Thus, an "S-shaped" J-V curve is observed on the devices without buffer layer, which indicates an unfavourable interface and poor energy level alignment.[62, 63, 56] Once a thin-layer of BCP is applied (0.5 mg/ml), the S-shape behaviour disappears. On varying the thickness of BCP with different concentration from 0.5 to 1.5 mg/ml, only small changes were seen in the shape of the J-V curves, but the average value of FF and J_{sc} are increased from 0.62 and -16.3 mA/cm^2 (0.5 mg/ml) to 0.67 and -17.6 mA/cm^2 (1.0mg/ml), respectively. This may be due to incomplete coverage at the lowest concentration applied. Hence, the highest average PCE value around 11.3% is obtained at 1 mg/ml. The corresponding statistical distribution can be found in the in fig. 5.9b, and its average performance factors are summarised in Table. 5.5.

Table 5.5: Mean solar cell performance parameters with different thickness of BCP varied by concentration, under simulated AM 1.5, 100 mW/cm^2 solar irradiation.

Concentration of BCP (mg/ml)	Jsc(mA/cm^2)	Voc(V)	FF	PCE(%)
0	-12.9±2.0	-0.91±0.02	0.26±0.03	3.0±0.6
0.5	-16.3±1.6	-0.9±0.02	0.62±0.04	9.0±1.0
1	-17.6±1.6	-0.92±0.12	0.67±0.16	11.3±3.6
1.5	-17.2±1.1	-0.93±0.08	0.58±0.12	9.5±2.4

In principle, the BCP has a LUMO level less than 3.0 eV[64, 65], thus the electron transport across the BCP layer is dominated by tunneling, where it occurs through the states below the LUMO level of the BCP, see fig. 5.10.[66, 65] However, only a relatively thin layer of BCP would be beneficial, as the electric field strength is inversely proportional to the thickness of the buffer layer[66], therefore thick buffer (over 1 mg/ml) layers would result in fewer electrons tunneling into the anode; consequently, an inferior device performance with reduced FF and J_{sc} is observed in the sample of 1.5 mg/ml.

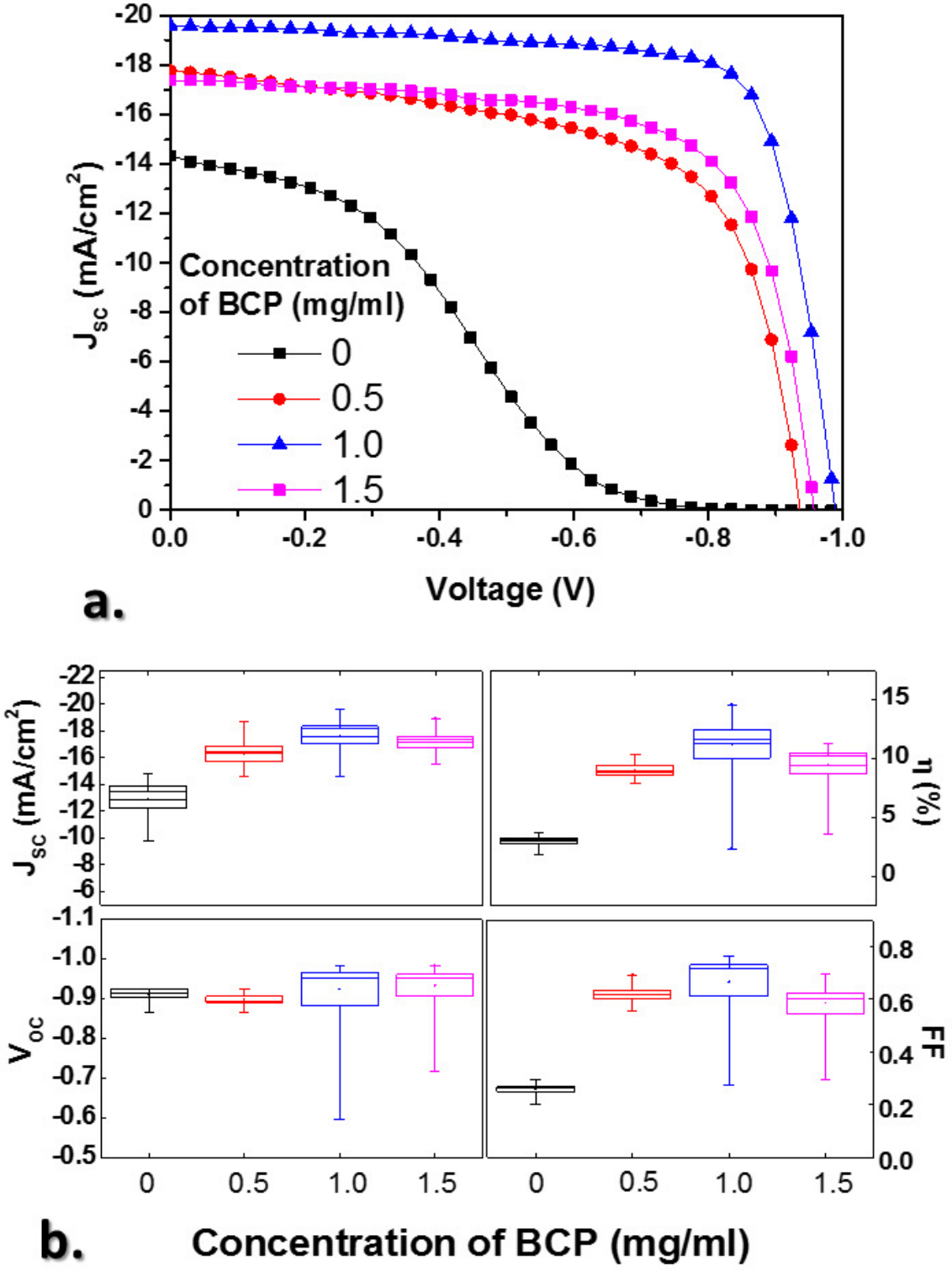


Figure 5.9: Device performance characteristics with different thickness of PCBM varied by concentration under simulated AM 1.5, 100 mW/cm^2 irradiance in air. (a) The current density-voltage curves of the best devices in the batch. (b) Device performance parameters extracted from a batch of current-voltage measurements.

Here, the improvement in the performance can be explained by the contribution of enhanced ETL/metal interface, where the insertion of the BCP layer, may be preventing the unfavourable reactions between the metal and organic layers and avoiding the fragile PCBM from being damaged during metal deposition. More importantly, the deep HOMO level ($6.4 \sim 7.0\ eV$) is blocking the hole injection from the valance band of the perovskite ($\sim 5.4\ eV$), thus effectively reducing the recombination of electron-hole pairs, and increasing the electron collection rate. In addition, a further contribution to the increase in J_{sc} may be attributed to the redistribution of the light intensity in the device,[67] where BCP is believed to act as an optical spacer, thus increasing the absorption and leading to a superior J_{sc}. In total, these enhanced behaviours show good agreement with the previous reports [68, 69] in OPV, and now with the careful optimisation here, an over three-fold boost in the average PCE on the inverted PSCs is obtained.

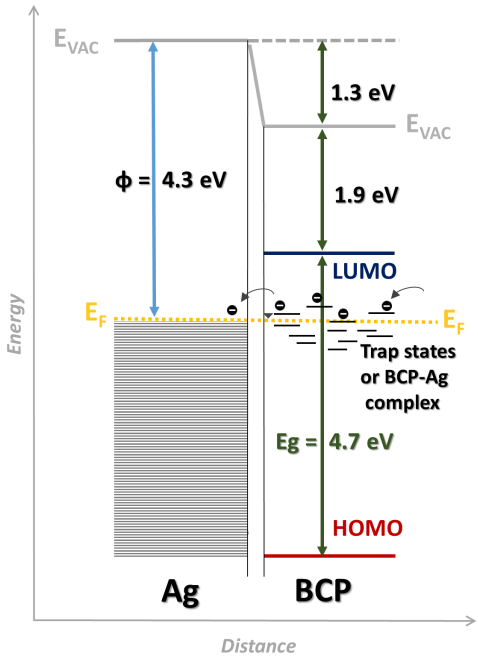


Figure 5.10: Energy level diagrams of the interface between Ag and BCP proposed by Yoshida et al.[65]

5.8 Hysteresis Behavior Comparison

Perovskite solar cells have attracted lots of attention with their exceptional photovoltaic performance since 2012.[1, 2] Though it is important to keep pushing the device performance forward, the fundamental characteristics of the perovskites should not be neglected. One of the challenges which remain unresolved and needs the most attention, is the anomalous hysteresis behaviour appearing during the current-voltage sweeping measurement.[6] Several theories have been proposed to explain the hysteresis behaviour, and the most plausible ones include: (1) interface charge accumulation due to trapping and de-trapping processes[6, 8, 70], and (2) ion (MA^+/ I^-) migration under illumination or applied bias.[8, 70, 71, 72, 73, 74] While the anomalous hysteresis effect is commonly observed in the regular (n-i-p) architecture[6, 75, 20], yet when the same $CH_3NH_3PbI_3$ perovskite is deposited in a reverse architecture, namely the inverted (p-i-n) structure, the hysteresis is claimed to be eliminated.[12, 76, 77]

The disappearance of the hysteresis effect in the inverted architecture compared to the regular structure, is believed to be due to the difference in their n-type contacts[12, 76], where the TiO_2 is widely adopted in the regular structure, whereas the fullerene or its derivatives were used in the inverted structure instead[11, 78, 79]. Shao et al. first proposed that the fullerene molecules are likely to diffuse into grain boundaries and passivate the defects, which are thought to be responsible for the hysteresis[12]; later, Xu et al. further performed DFT simulations to calculate the interaction between fullerene molecules and intrinsic defects, which show that suppressed ion migration could be induced by the introduction of fullerene molecules[80].

With lots of evidence presented and pointing toward the important role of fullerene molecules, in this section, we used the inverted architecture (Ag/BCP/PCBM/ $CH_3NH_3PbI_{3-x}Cl_x$/PEDOT:PSS/FTO) developed in the previous section, compared

with the regular structure (Ag/Spiro-OMeTAD/$CH_3NH_3PbI_{3-x}Cl_x$/C60/FTO), where fullerene molecules are applied as electron-transporting layers in both architectures, see fig. 5.11 for detailed device architecture.

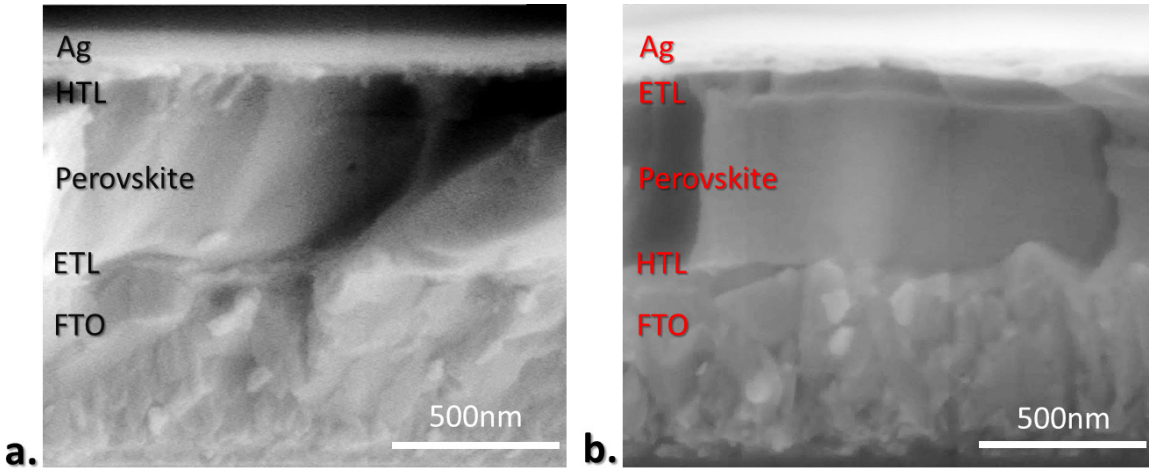


Figure 5.11: Cross-sectional SEM micrographs with annotated layers specified showing (a) the regular structure comprises of Ag/Spiro-OMeTAD/$CH_3NH_3PbI_{3-x}Cl_x$/C60/FTO, and (b) inverted structure comprises of Ag/BCP/PCBM/$CH_3NH_3PbI_{3-x}Cl_x$/PEDOT:PSS/FTO.

In fig. 5.12a, we show the current density-voltage measurement for the regular and inverted structure devices. While both devices include a fullerene-based electron-transport layer, a significant hysteresis behaviour can be observed with the regular structure, where the decrease in the V_{oc} and FF are most pronounced under different sweep directions; When measured from forward bias toward the short-circuit(FB-SC) direction, the V_{oc} and FF were 1.07 V and 0.64, respectively, yet reversing the direction from short-circuit toward forward bias (SC-FB), both V_{oc} and FF fall to 0.92 V and 0.41, respectively; though the J_{sc} remain the same in both directions. The reduced V_{oc} and FF have led to a decrease in PCE from 13.2% to 7.4%. In contrast, the inverted devices appear to have hysteresis-free J-V curves in both sweep directions, with all parameters maintaining more less the same value. To have a better understanding of the two structures, we performed stabilised power output measurements by holding the device at its maximum power point, which can demonstrate the "steady-state" efficiency and reveal a picture

closer to its practical performance.[6]

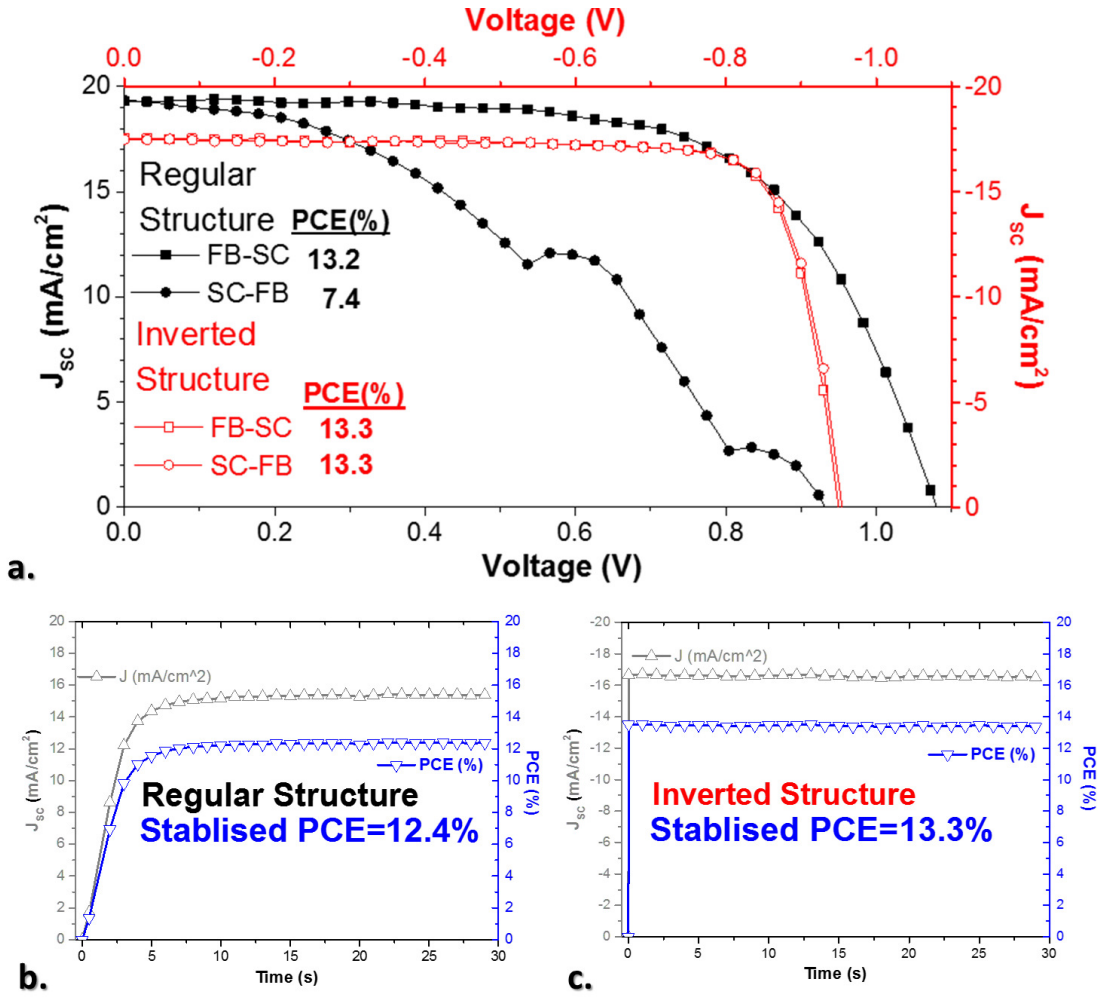


Figure 5.12: (a)The current density-Voltage measurement showing the regular and inverted devices both comprise of a fullerene-based electron-transporting layer; (b) and (c) their stabilised power output measurement under the maximum power points obtained in the J-V scan.

In fig. 5.12b, we show the stabilised photocurrent and PCE for the regular structure, where a slowly increasing photo-response is observed, which may be correlated to the trap filling process[12], and a slightly lower stabilised PCE of 12.4%. In comparison, the inverted structure shows a much faster response time as the photocurrent responds as soon as the illumination starts, with an equivalent stabilised PCE of 13.3% measured from the J-V scan, which indicates either a more efficient trap passivation or the ion migration is suppressed in the inverted structure.

From here, the comparison between the regular and inverted structures suggests that even in the presence of fullerene molecules with the same perovskite applied, the hysteresis effect is still much more pronounced in the regular structure with an inferior stabilised PCE; whereas, the inverted devices show stable performance in all aspects. This may be explained by either a better interface which passivates the trap states resulting from the different deposition sequence or alternatively by the different HTMs applied (Spiro-OMeTAd vs. PEDOT:PSS) or in combination of the two. Though more detailed studies are needed to unveil the mechanisms behind this behaviour, the current results have provided new insights by showing the first side-by-side comparison of fullerene-based devices, which suggest the elimination of the hysteresis effect may be not completely dominated by the fullerene layers, but a synergetic interaction between the two selective contacts is likely to be required.

5.9 Open-Circuit Voltage Enhancement by Hole - Transporting Layer Engineering

In general, the open circuit voltage (V_{oc}) of solar cells is determined by the bandgap of the materials used. But in heterojunction solar cells, like OPV and PSCs, the V_{oc} is affected by the contacts and electrodes applied, which result in the splitting of the quasi-Fermi level, and the difference between the band edges of the light absorbing materials with respect to the ionisation potential and electron affinity of the interfacial layer would decide the V_{oc} .[81]

Follow this reasoning, the applied interfacial layers either side of the light absorbing materials, should have energy levels as close as possible with respect to the band edges where the electrons/holes are collected. Previously, we have demonstrated inverted PSCs based on PEDOT:PSS as the HTL with a PCE close to 15%. However, the intrinsic proper-

ties of PEDOT:PSS have raised some concerns, as its acidic nature would be likely to corrode the ITO electrode, and its hygroscopicity would absorb water molecules leading to a degradation of the perovskite.[82] Moreover, as the valance band of $CH_3NH_3PbI_3$ is around 5.4 eV, PEDOT:PSS has a HOMO level around 5.1 eV[16, 17], leading to an energetic difference around 0.3 eV, this causes a relatively small V_{oc} to be observed at around 0.9 V in these inverted PSCs[11, 10, 39]; compared to the regular structure where a V_{oc} of over 1.1 V is regularly found with Spiro-OMeTAD, which possesses a higher HOMO level around 5.3 eV[1, 3, 83].

In this regard, lots of new hole transporting materials (HTMs) have been investigated as alternatives for PEDOT:PSS in the inverted PSCs, where both organic- and inorganic-based HTMs are proposed including, PTAA[84], PCDTBT[85], Poly-TPD[86], NiO[87], CuSCN[88], and V_2O_5[89]. Among these materials, Poly-TPD and NiO both have a HOMO level at 5.4 eV[90], which matches the valance band of $CH_3NH_3PbI_3$ and $CH_3NH_3PbI_{3-x}Cl_x$, and thus is expected to be able to achieve a higher V_{oc}, compared to the PEDOT:PSS device, see fig. 5.13.

In the NiO system, a V_{oc} over 1.1 V has been demonstrated[91], but a simultaneous decrease was observed in J_{sc}, even with the use of copper doping. This reduced J_{sc} behaviour may link to the presence of trap states observed in the metal oxides[92, 93]. On the other hand, Malinkiewicz et al. first used Poly-TPD with PEDOT:PSS to form bilayer HTLs in inverted PSCs, where a V_{oc} of 1.05 and a decent PCE of 12% were demonstrated.[86]. Later, Zhao et al. used Poly-TPD solely as the HTL in inverted PSCs with an impressive V_{oc} of 1.1 V and a PCE of 15% achieved[94]. However, these Poly-TPD devices still suffer from a lower FF (less than 70%) due to the resistive nature of Poly-TPD when compared to devices with PEDOT:PSS as HTL, where a FF close to 80% are being commonly observed.[39, 79, 58, 95] Therefore, an improvement of the intrinsic conductivity is needed for good performance in Poly-TPD based HTL. Here,

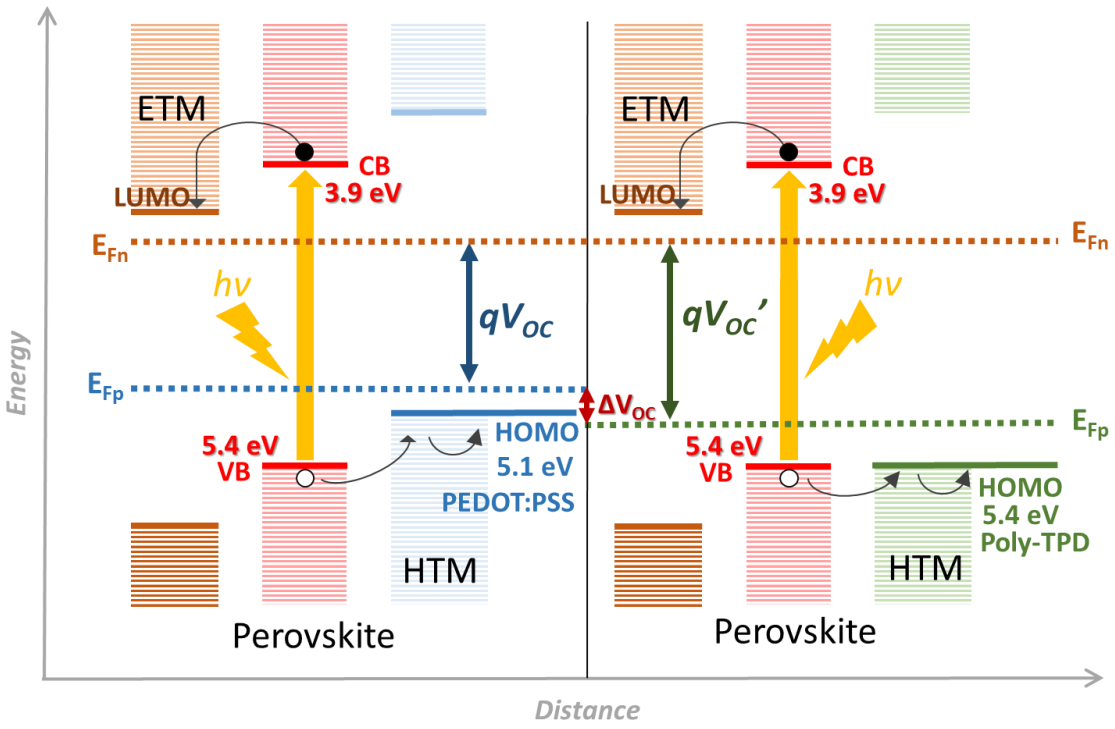


Figure 5.13: Schematic energy level diagrams showing the possible difference of V_{oc} resulted by different HTMs applied on the perovskite.

inspired by the works of doping-induced enhancement on HTMs like Spiro-OMeTAD, NiO, and PTAA[96, 92, 84], we introduced the single-dopant 2,2'-(perfluoronaphthalene-2,6-diylidene)dimalononitrile (F6-TCNNQ) mixed HTL, which has been reported to have a higher molecular weight than the commonly used 2,3,5,6-Tetrafluoro-7,7,8,8-tetracyanoquinodimethane(F4-TCNQ) but with similar doping strength, and thus can prevent dopant diffusion within the device layers during operation and provide a better control, making it an ideal p-dopant for the HTMs.[97, 98]

5.9.1 Doping Influenced Device Performance

To evaluate the influence of F6-TCNNQ doping on the Poly-TPD, we varied the doping concentration of F6-TCNNQ/Poly-TPD ranging from 0-25 wt% (respect to the solid content of Poly-TPD in the toluene) on the piranha treated substrates, then fabricated

the inverted PSCs following previous methods with the architecture of Ag/BCP/PCBM/ $CH_3NH_3PbI_{3-x}Cl_x$/HTM/FTO. For a better comparison, we also prepared the HTL with PEDOT:PSS. It is noted here, the thickness of the HTLs has been kept around 50 nm by controlling the concentration and spinning speed of HTMs applied; also, we do not add any other surfactants or dopants to the Poly-TPD other than the solvent toluene and F6-TCNNQ.

The mean solar cell performance parameters extracted from a batch of current-voltage measurements under simulated AM 1.5, 100 mW/cm^2 sunlight are shown in fig 5.14a., and the corresponding performance factors are summarised in Table. 5.6.

Table 5.6: Mean solar cell performance parameters with different doping ratio of the F6-TCNNQ/PolyTPD (wt%) under simulated AM 1.5, 100 mW/cm^2 solar irradiation

F6-TCNNQ/ PolyTPD (wt%)	**Jsc(mA/cm^2)**	**Voc(V)**	**FF**	**PCE(%)**
0	-19.1±0.9	-0.84±0.27	0.44±0.14	7.8±4.2
5	-19.2±0.4	-1.02±0.01	0.47±0.11	9.3±2.2
10	-20.0±0.6	-1.03±0.02	0.63±0.11	13.1±2.7
15	-20.0±1.0	-1.05±0.02	0.70±0.03	14.7±1.2
20	-19.7±1.4	-1.02±0.03	0.62±0.13	12.6±3.3
25	-20.8±0.8	-0.95±0.07	0.52±0.16	10.6±3.8
PEDOT	-18.5±1.0	-0.94±0.03	0.63±0.09	11.1±2.2

We can see a clear trend of device enhancement with the introduction of F6-TCNNQ. Starting from the intrinsic Poly-TPD (non-doped), the average fill factor (FF) and V_{oc} are around 0.44 and 0.84, respectively. With increasing F6-TCNNQ doping concentration in Poly-TPD, both the FF and V_{oc} increase up to average values of around 0.7 V and 1.05 V, respectively, peaking at 15 wt%, then followed by a decrease with further increases of F6-TCNNQ content. Comparing with the PEDOT:PSS-based devices, the best F6-TCNNQ/Poly-TPD devices show an increase of average V_{oc} by up to 0.11 V, this substantial improvement can be explained by the better energy level alignment between the perovskite and the F6-TCNNQ-doped Poly-TPD. The intrinsic Poly-TPD seem to show inferior performance in every aspect, which can be attributed to the poor contact

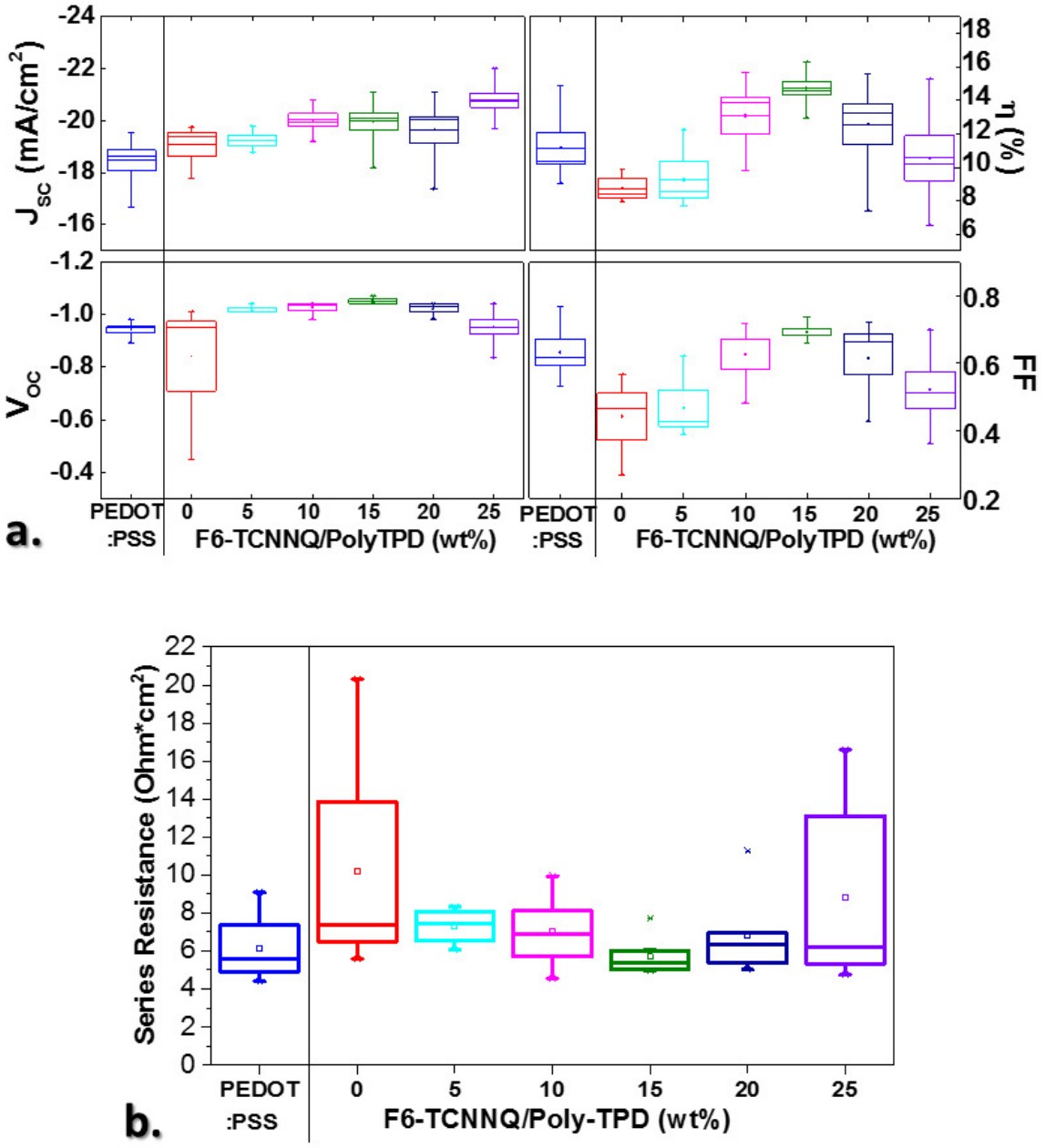


Figure 5.14: Devices performance characteristics with different HTMs applied in the inverted PSCs, under simulated AM 1.5, 100 mW/cm^2 irradiance in air. (a) Device performance parameters extracted from a batch of current-voltage measurements. (b) Series resistance of different HTMs used in this study including, PEDOT:PSS, Poly-TPD, and F6-TCNNQ/Poly-TPD with different doping concentration.

between the perovskite layer and the Poly-TPD, as the surface wetting of the intrinsic Poly-TPD is not favourable with the perovskite precursor solution and resulted in a poor coverage on the HTL, see the fig. 5.15. However, after the addition of F6-TCNNQ, the surface wetting becomes much better giving better coverage of the perovskite, thus providing a better interface between HTL and perovskite, which can also explain the slightly increased J_{sc} observed.



Figure 5.15: Photos of perovskite deposition on top of different HTMs with FTO glass (2.8 cm x 2.8 cm) (a) PEDOT:PSS (b) Poly-TPD (c)F6-TCNNQ/Poly-TPD.

To understand the improved FF observed in the F6-TCNNQ/Poly-TPD devices, we analysed the series resistance (R_{series}) derived from the slope of J-V curves. As shown in Table. 5.7., the device with intrinsic Poly-TPD as HTM has an average R_{series} of 10.2 Ωcm^2 with large standard deviation, possibly due to the inhomogeneous film coverage as shown in the fig. 5.15b. Whereas, with increasing doping concentration of F6-TCNNQ, the average R_{series} starts to reduce down to 5.7 Ωcm^2 at 15 wt%; and this decreasing trend of R_{series} can be correlated to the increased FF, as the primary contribution of the F6-TCNNQ has been reported to effectively increase the hole conductivity.[98] Nonetheless, further increase of the doping concentration, starts to cause an increase of R_{series} together with an enlarged distribution. The aggregation of F6-TCNNQ may be the reason behind this, which has previously been found in the F4-TCNQ-doped

polymer system.[99, 100, 84]

Table 5.7: Mean series resistance derived from the slope of J-V curves with PEDOT:PSS and different doping ratio of the F6-TCNNQ/Poly-TPD (wt%)

F6-TCNNQ /Poly-TPD (wt%)	0	5	10	15	20	25	**PEDOT :PSS**
$\mathbf{R}_{series}(\Omega cm^2)$	10.2±6.8	7.3±1.0	7.0±2.0	5.7±0.9	6.8±2.1	8.8±4.7	6.1±1.8

In fig. 5.16a., we show the current density-voltage (J-V) curves of the best performing cells of three different HTMs in the batch, including cells with PEDOT:PSS, Poly-TPD, and F6-TCNNQ/Poly-TPD. For the PEDOT:PSS devices, a reasonable J_{sc} and FF are achieved, but an inferior V_{oc} is observed when compared to the Poly-TPD based devices; however, a serious loss of FF is found in the intrinsic Poly-TPD devices, presumably due to the poor contact explained above. Comparing with the PEDOT:PSS, the F6-TCNNQ/Poly-TPD devices show major enhancement in both V_{oc} and J_{sc}. Here, the most efficient inverted PSCs use F6-TCNNQ/Poly-TPD as HTL, exhibit short-circuit photocurrent of 21 mA/cm^2, open circuit voltage of 1.05 V, and a good fill factor of 0.74 yielding a power conversion efficiency of 16.3%.

5.9.2 Optical Characterisation on Different Hole-Transporting Materials

To investigate whether the improved short-circuit current in the F6-TCNNQ/Poly-TPD is coming from the increased absorption in the perovskite, we measured the external quantum efficiency (EQE) and the transmission spectra of the corresponding HTMs. In fig. 5.17a. the F6-TCNNQ/Poly-TPD devices display a good EQE across the spectrum, showing a good agreement with the J-V measurement. While the PEDOT:PSS devices show an EQE peaking around 500nm; the intrinsic Poly-TPD devices behave poorly with an EQE value peaking around 700 nm, which may be explained by the unfavourable

interface and its resulting poor charge collection.

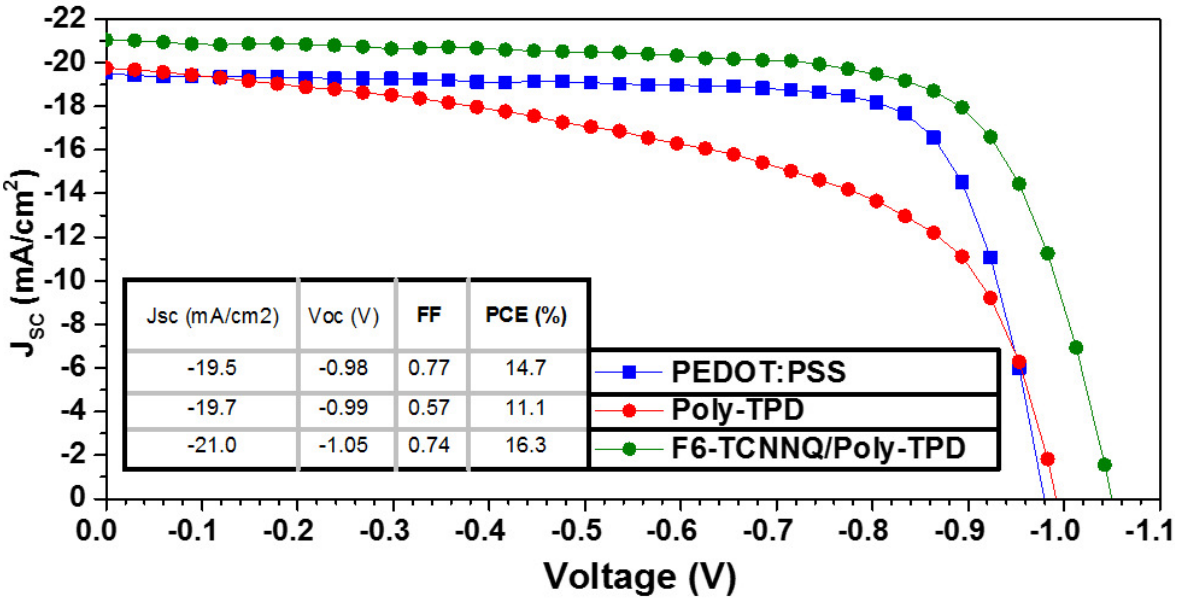


Figure 5.16: The current density-voltage curves of the best devices in a batch with different HTMs applied.

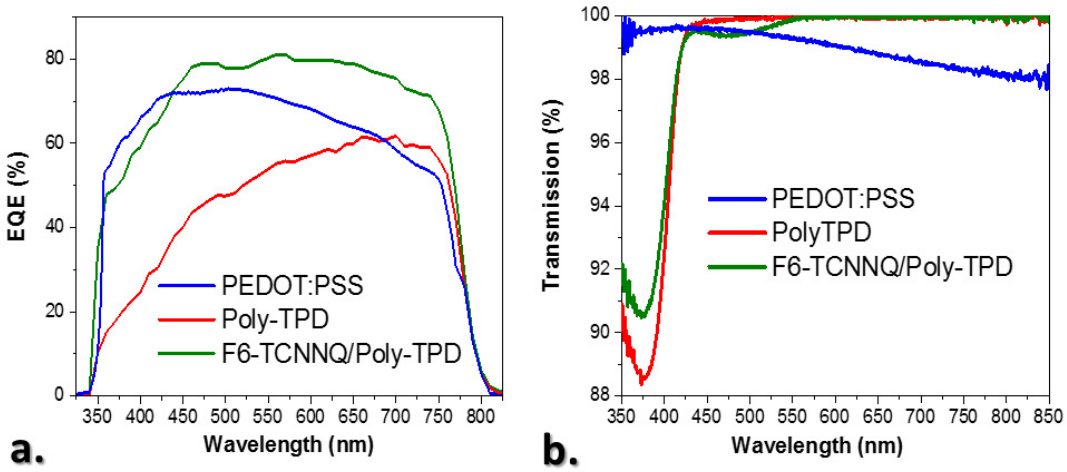


Figure 5.17: The three different HTMs applied in this study with (a) The EQE spectra of the devices (b)Transmission spectra of different HTMs on the glass substrates.

To further unravel the enhanced device performance observed in the F6-TCNNQ/Poly-TPD devices, we performed the photoluminescence (PL) measurements, which has become an efficient method to evaluate the compatibility of the interfacial layers with

perovskite.[10] To probe how the different HTMs influence the hole extraction/collection rate, we deposit a perovskite layer on top of each HTMs with PMMA covered on the top to prevent any unnecessary degradation occur during the measurement.

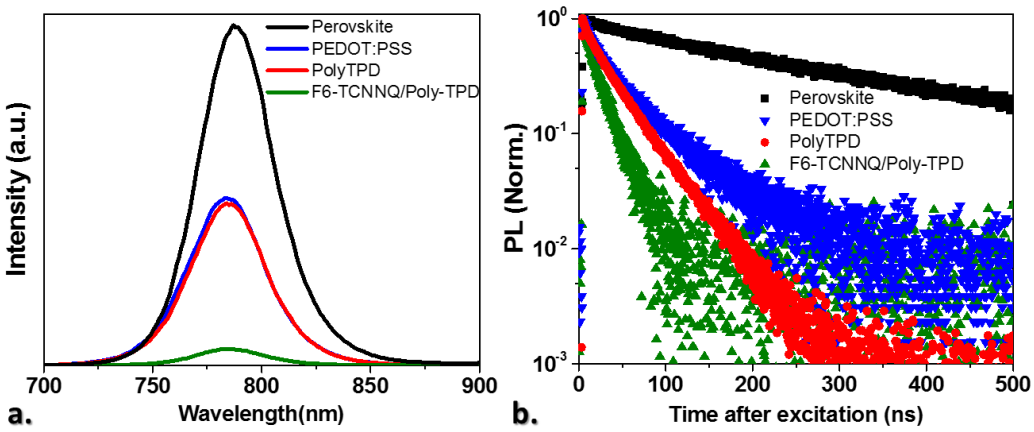


Figure 5.18: Photoluminescence spectroscopy of different HTMs deposited on glass substrate with perovskite on top. a) steady-state spectra (300 mW/cm^2, 507 nm), b) time-resolved photoluminescence decay after excitation at 507 nm with pulsed (2 MHz) and a fluence of 30 nJ/cm^2/pulse.

In fig. 5.18a, we can see the perovskite showing typical emission around 780 nm in the steady-state PL spectra. With the different HTMs applied, the PL of the perovskite is being quenched, where PEDOT:PSS and Poly-TPD, show similarly quenched emission, while with the introduction of F6-TCNNQ in the Poly-TPD, it exhibits significantly higher quenching rates than the intrinsic Poly-TPD, presumably due to the improved hole-transporting property via doping. We further used time-resolved PL spectroscopy to measure the PL decay, and extracted the corresponding average lifetime $<\tau>$ following the work of Stranks et al.[5] Here, the pristine perovskite demonstrates a $<\tau>$ around 300 ns, with the HTMs applied, the photo-generated carriers are being quenched, where the F6-TCNNQ/Poly-TPD sample displays the best quenching ability with a two-fold reduction of $<\tau>$ to less than 20 ns compared to the PEDOT:PSS and intrinsic Poly-TPD, which both have a $<\tau>$ around 40 ns. This fast quenched PL life time, suggests that the F6-TCNNQ/Poly-TPD has a better hole collection/extraction ability, presum-

ably due to the addition of F6-TCNNQ contributing to an enhanced hole conductivity and mobility.[98, 97]

In summary, we have demonstrated improved performance of the perovskite solar cells employing Poly-TPD as a hole-transporting layer. The introduction of F6-TCNNQ, not only improves the surface wetting to give a much better interface, but also reduces the series resistance within the HTLs. In addition, we also reported steady-state PL and time-resolved PL measurements showing the F6-TCNNQ/Poly-TPD can be a promising HTL with its superior hole collection/extraction ability, which suggests the carriers can be removed efficiently from the interface before recombination happens, thus leading to an improved device performance. The best inverted PSCs consist of F6-TCNNQ/Poly-TPD, demonstrating an increased V_{oc} by up to 0.11 V compared to the PEDOT:PSS devices, due to a better matching energy level between the HOMO of Poly-TPD and the conduction band of the perovskite; moreover, the doping of F6-TCNNQ improves the conductivity of the HTLs, thus preventing the J_{sc} or FF being sacrificed in the devices. Therefore, this part of study shows an effective way to improve the properties of hole-transporting layers via energy level engineering, and paves the way for the highly efficient perovskite solar cells.

5.10 Summary

In this chapter, a development of inverted perovskite solar cells with interface engineering from cathode to anode has been demonstrated. With a careful evaluation of the interface of individual components and energy level alignment, device performance has been examined. We shown various approaches including piranha treatment, hot-solution casting, and the insertion of an orthogonal solution-based thin buffer layer, which have all contributed toward the improved wettability, surface morphology, and the better

matching of energy levels between interfaces, leading to hysteresis-free perovskite solar cells. Compared with the regular structure employing fullerene as ETL, we found the existence of hysteresis may not be removed completely by the insertion of fullerene, but by a synergistic interaction between selective contacts which emphasize the importance of interface and interlayers. Finally, we demonstrated an increase in V_{oc} by up to 0.11 V compared to the PEDOT:PSS devices. By exploiting the F6-TCNNQ/Poly-TPD as HTL, not only to improve the surface wetting for a much better interface, but also to increase hole-conductivity, a much better HTM can be achieved. The careful optimisations throughout the entire carrier pathways have facilitated charge transportation, minimised unfavourable recombination, and enabled efficient and hysteresis-free inverted perovskite solar cells to be demonstrated.

References

[1] Michael M. Lee, Joël Teuscher, Tsutomu Miyasaka, Takurou N. Murakami, and Henry J. Snaith. Efficient Hybrid Solar Cells Based on Meso-Superstructured Organometal Halide Perovskites. *Science*, 338(6107):643–647, nov 2012.

[2] Hui-Seon Kim, Chang-Ryul Lee, Jeong-Hyeok Im, Ki-Beom Lee, Thomas Moehl, Arianna Marchioro, Soo-Jin Moon, Robin Humphry-Baker, Jun-Ho Yum, Jacques E Moser, Michael Grätzel, and Nam-Gyu Park. Lead iodide perovskite sensitized all-solid-state submicron thin film mesoscopic solar cell with efficiency exceeding 9%. *Scientific reports*, 2:591, jan 2012.

[3] James M. Ball, Michael M. Lee, Andrew Hey, and Henry J. Snaith. Low-temperature processed meso-superstructured to thin-film perovskite solar cells. *Energy & Environmental Science*, 6(6):1739–1743, 2013.

[4] Mingzhen Liu, Michael B Johnston, and Henry J Snaith. Efficient planar heterojunction perovskite solar cells by vapour deposition. *Nature*, 501(7467):395–398, sep 2013.

[5] Samuel D Stranks, Giles E Eperon, Giulia Grancini, Christopher Menelaou, Marcelo J P Alcocer, Tomas Leijtens, Laura M Herz, Annamaria Petrozza, and Henry J Snaith. Electron-hole diffusion lengths exceeding 1 micrometer in an organometal trihalide perovskite absorber. *Science (New York, N.Y.)*, 342(6156):341–344, oct 2013.

[6] Henry J. Snaith, Antonio Abate, James M. Ball, Giles E. Eperon, Tomas Leijtens, Nakita K. Noel, Samuel D. Stranks, Jacob Tse-Wei Wei Wang, Konrad Wojciechowski, and Wei Zhang. Anomalous hysteresis in perovskite solar cells. *Journal of Physical Chemistry Letters*, 5(9):1511–1515, may 2014.

[7] Michael Saliba, Taisuke Matsui, Ji-Youn Seo, Konrad Domanski, Juan-Pablo Correa-Baena, Mohammad Khaja Nazeeruddin, Shaik M Zakeeruddin, Wolfgang Tress, Antonio Abate, Anders Hagfeldt, and Michael Grä Tzel. Cesium-containing triple cation perovskite solar cells: improved stability, reproducibility and high efficiency. *Energy Environ. Sci.*, 9(6):1989–1997, mar 2016.

[8] Stephan van Reenen, Martijn Kemerink, and Henry J. Snaith. Modeling Anomalous Hysteresis in Perovskite Solar Cells. *The Journal of Physical Chemistry Letters*, 6(19):3808–3814, sep 2015.

[9] Michele De Bastiani, Giorgio Dell'Erba, Marina Gandini, Valerio D'Innocenzo, Stefanie Neutzner, Ajay Ram Srimath Kandada, Giulia Grancini, Maddalena Binda, Mirko Prato, James M. Ball, Mario Caironi, and Annamaria Petrozza. Ion Migration and the Role of Preconditioning Cycles in the Stabilization of the

J - V Characteristics of Inverted Hybrid Perovskite Solar Cells. *Advanced Energy Materials*, page 1501453, oct 2015.

[10] Pablo Docampo, James M Ball, Mariam Darwich, Giles E Eperon, and Henry J Snaith. Efficient organometal trihalide perovskite planar-heterojunction solar cells on flexible polymer substrates. *Nature communications*, 4:2761, jan 2013.

[11] Jun Yuan Jeng, Yi Fang Chiang, Mu Huan Lee, Shin Rung Peng, Tzung Fang Guo, Peter Chen, and Ten Chin Wen. CH3NH3PbI3 perovskite/fullerene planar-heterojunction hybrid solar cells. *Advanced Materials*, 25(27):3727–3732, jul 2013.

[12] Yuchuan Shao, Zhengguo Xiao, Cheng Bi, Yongbo Yuan, and Jinsong Huang. Origin and elimination of photocurrent hysteresis by fullerene passivation in CH3NH3PbI3 planar heterojunction solar cells. *Nature Communications*, 5:5784, dec 2014.

[13] Qiquan Qiao, James Beck, Ryan Lumpkin, Jake Pretko, and James T Mcleskey. A comparison of fluorine tin oxide and indium tin oxide as the transparent electrode for P3OT/TiO2 solar cells. *Solar Energy Materials and Solar Cells*, 90(7-8):1034–1040, may 2006.

[14] Annica Andersson, Nicklas Johansson, Per Bröms, Nu Yu, Donald Lupo, and William R. Salaneck. Fluorine Tin Oxide as an Alternative to Indium Tin Oxide in Polymer LEDs. *Advanced Materials*, 10(11):859–863, aug 1998.

[15] R Schlaf, H Murata, and Z.H Kafafi. Work function measurements on indium tin oxide films. *Journal of Electron Spectroscopy and Related Phenomena*, 120(1-3):149–154, oct 2001.

[16] N. Koch, A. Kahn, J. Ghijsen, J.-J. Pireaux, J. Schwartz, R. L. Johnson, and A. Elschner. Conjugated organic molecules on metal versus polymer electrodes: Demonstration of a key energy level alignment mechanism. *Applied Physics Letters*, 82(1):70, dec 2003.

[17] Jaehyung Hwang, Fabrice Amy, and Antoine Kahn. Spectroscopic study on sputtered PEDOT·PSS: Role of surface PSS layer. *Organic Electronics*, 7(5):387–396, oct 2006.

[18] H.J. Snaith and M. Grätzel. The Role of a "Schottky Barrier" at an Electron-Collection Electrode in Solid-State Dye-Sensitized Solar Cells. *Advanced Materials*, 18(14):1910–1914, jul 2006.

[19] Aiyuan Li, Riming Nie, Xianyu Deng, Huaixin Wei, Shizhao Zheng, Yanqing Li, Jianxin Tang, and King Young Wong. Highly efficient inverted organic solar cells using amino acid modified indium tin oxide as cathode. *Applied Physics Letters*, 104(12), 2014.

[20] Ye Zhang, Mingzhen Liu, Giles E. Eperon, Tomas C. Leijtens, David McMeekin, Michael Saliba, Wei Zhang, Michele de Bastiani, Annamaria Petrozza, Laura M. Herz, Michael B. Johnston, Hong Lin, and Henry J. Snaith. Charge selective contacts, mobile ions and anomalous hysteresis in organic–inorganic perovskite solar cells. *Mater. Horiz.*, 2(3):315–322, 2015.

[21] Konrad Wojciechowski, Tomas Leijtens, Svetlana Siprova, Christoph Schlueter, Maximilian T Hörantner, Jacob Tse-Wei Wang, Chang-Zhi Li, Alex K-Y Jen, Tien-Lin Lee, and Henry J Snaith. C60 as an Efficient n-Type Compact Layer in Perovskite Solar Cells. *The journal of physical chemistry letters*, 6(12):2399–2405, jun 2015.

[22] Tomas Leijtens, Giles E Eperon, Sandeep Pathak, Antonio Abate, Michael M Lee, and Henry J Snaith. Overcoming ultraviolet light instability of sensitized TiO with meso-superstructured organometal tri-halide perovskite solar cells. *Nature communications*, 4:2885, jan 2013.

[23] Dan Lu, Ying Wu, Jianhua Guo, Guang Lu, Yue Wang, and Jiacong Shen. Surface treatment of indium tin oxide by oxygen-plasma for organic light-emitting diodes. *Materials Science and Engineering: B*, 97(2):141–144, jan 2003.

[24] Y. Fukushi, H. Kominami, Y. Nakanishi, and Y. Hatanaka. Effect of ITO surface state to the aging characteristics of thin film OLED. *Applied Surface Science*, 244(1-4):537–540, may 2005.

[25] Zhong Zhi You. Combined AFM, XPS, and contact angle studies on treated indium–tin-oxide films for organic light-emitting devices. *Materials Letters*, 61(18):3809–3814, jul 2007.

[26] S. Gardonio, L. Gregoratti, D. Scaini, C. Castellarin-Cudia, P. Dudin, P. Melpignano, V. Biondo, R. Zamboni, S. Caria, and M. Kiskinova. Characterization of indium tin oxide surfaces after KOH and HCl treatments. *Organic Electronics*, 9(2):253–261, apr 2008.

[27] R.F. Bianchi, A.J.F. Carvalho, M.A. Pereira-da Silva, D.T. Balogh, and R.M. Faria. Characterization of indium-tin-oxide films treated by different procedures: effect of treatment time in aqua regia solution. *Materials Science and Engineering: C*, 24(5):595–599, nov 2004.

[28] Werner Kern. The Evolution of Silicon Wafer Cleaning Technology. *Journal of The Electrochemical Society*, 137(6):1887, jun 1990.

[29] Neal R Armstrong, Chet Carter, Carrie Donley, Adam Simmonds, Paul Lee, Michael Brumbach, Bernard Kippelen, Benoit Domercq, and Seunghyup Yoo. Interface modification of ITO thin films: organic photovoltaic cells. *Thin Solid Films*, 445(2):342–352, dec 2003.

[30] John A. Chaney, Sharon E. Koh, Charles S. Dulcey, and Pehr E. Pehrsson. Surface chemistry of carbon removal from indium tin oxide by base and plasma treatment, with implications on hydroxyl termination. *Applied Surface Science*, 218(1-4):258–266, 2003.

[31] F Nuesch, L J Rothberg, E W Forsythe, Quoc Toan Le, and Yongli Gao. A photoelectron spectroscopy study on the indium tin oxide treatment by acids and bases. *Applied Physics Letters*, 74(1999):880–882, 1999.

[32] Dongguen Shin, Jeihyun Lee, Soohyung Park, Junkyeong Jeong, Ki Won Seo, Hyo Joong Kim, Han Ki Kim, Min Jun Choi, Kwun Bum Chung, and Yeonjin

Yi. Interfacial energy level alignments between low-band-gap polymer PTB7 and indium zinc oxide anode. *Applied Physics Express*, 8(9):5–9, 2015.

[33] Kuan Sun, Shupeng Zhang, Pengcheng Li, Yijie Xia, Xiang Zhang, Donghe Du, Furkan Halis Isikgor, and Jianyong Ouyang. Review on application of PEDOTs and PEDOT:PSS in energy conversion and storage devices. *Journal of Materials Science: Materials in Electronics*, 26(7):4438–4462, mar 2015.

[34] Hui Shi, Congcong Liu, Qinglin Jiang, and Jingkun Xu. Effective Approaches to Improve the Electrical Conductivity of PEDOT:PSS: A Review. *Advanced Electronic Materials*, 1(4):1500017, apr 2015.

[35] Youngkyoo Kim, Amy M. Ballantyne, Jenny Nelson, and Donal D.C. Bradley. Effects of thickness and thermal annealing of the PEDOT:PSS layer on the performance of polymer solar cells. *Organic Electronics*, 10(1):205–209, feb 2009.

[36] Giles E. Eperon, Victor M. Burlakov, Pablo Docampo, Alain Goriely, and Henry J. Snaith. Morphological Control for High Performance, Solution-Processed Planar Heterojunction Perovskite Solar Cells. *Advanced Functional Materials*, 24(1):151–157, jan 2014.

[37] V. M. Burlakov, G. E. Eperon, H. J. Snaith, S. J. Chapman, and A. Goriely. Controlling coverage of solution cast materials with unfavourable surface interactions. *Applied Physics Letters*, 104(9):091602, mar 2014.

[38] Julian Burschka, Norman Pellet, Soo-Jin Moon, Robin Humphry-Baker, Peng Gao, Mohammad K Nazeeruddin, and Michael Grätzel. Sequential deposition as a route to high-performance perovskite-sensitized solar cells. *Nature*, 499(7458):316–319, jul 2013.

[39] Zhengguo Xiao, Cheng Bi, Yuchuan Shao, Qingfeng Dong, Qi Wang, Yongbo Yuan, Chenggong Wang, Yongli Gao, and Jinsong Huang. Efficient, high yield perovskite photovoltaic devices grown by interdiffusion of solution-processed precursor stacking layers. *Energy Environ. Sci.*, 7(8):2619, 2014.

[40] Nam Joong Jeon, Jun Hong Noh, Young Chan Kim, Woon Seok Yang, Seungchan Ryu, and Sang Il Seok. Solvent engineering for high-performance inorganic-organic hybrid perovskite solar cells. *Nature materials*, 13(July):1–7, 2014.

[41] Wanyi Nie, Hsinhan Tsai, Reza Asadpour, Jean-christophe Blancon, Amanda J Neukirch, Gautam Gupta, Jared J Crochet, Manish Chhowalla, Sergei Tretiak, Muhammad A Alam, Hsing-lin Wang, and Aditya D Mohite. High-efficiency solution-processed perovskite solar cells with millimeter-scale grains. *Science*, 347(November):522–525, 2015.

[42] Konrad Wojciechowski, Samuel D Stranks, Antonio Abate, Golnaz Sadoughi, Aditya Sadhanala, Nikos Kopidakis, Garry Rumbles, Chang-Zhi Li, Richard H Friend, Alex K-Y Jen, and Henry J Snaith. Heterojunction modification for highly efficient organic-inorganic perovskite solar cells. *ACS nano*, 8(12):12701–9, dec 2014.

[43] Po-Wei Liang, Chu-Chen Chueh, Spencer T. Williams, and Alex K.-Y. Jen. Roles of Fullerene-Based Interlayers in Enhancing the Performance of Organometal Perovskite Thin-Film Solar Cells. *Advanced Energy Materials*, 5(10):1402321, 2015.

[44] Wan-Jian Yin, Tingting Shi, and Yanfa Yan. Unusual defect physics in CH3NH3PbI3 perovskite solar cell absorber. *Applied Physics Letters*, 104(6):063903, feb 2014.

[45] Jixian Xu, Andrei Buin, Alexander H. Ip, Wei Li, Oleksandr Voznyy, Riccardo Comin, Mingjian Yuan, Seokmin Jeon, Zhijun Ning, Jeffrey J. McDowell, Pongsakorn Kanjanaboos, Jon-Paul Sun, Xinzheng Lan, Li Na Quan, Dong Ha Kim, Ian G. Hill, Peter Maksymovych, and Edward H. Sargent. Perovskite–fullerene hybrid materials suppress hysteresis in planar diodes. *Nature Communications*, 6:7081, may 2015.

[46] Jangwon Seo, Sangman Park, Young Chan Kim, Nam Joong Jeon, Jun Hong Noh, Sung Cheol Yoon, Sang Il Seok, and Perovskite Solar Cells. Benefits of very thin PCBM and LiF layers for solution-processed p-i-n perovskite solar cells. *Energy Environ. Sci.*, 7:2642–2646, jun 2014.

[47] Lidón Gil-Escrig, Cristina Momblona, Michele Sessolo, and Henk J. Bolink. Fullerene imposed high open-circuit voltage in efficient perovskite based solar cells. *J. Mater. Chem. A*, 4(10):3667–3672, mar 2016.

[48] Kouji Suemori, Masaaki Yokoyama, and Masahiro Hiramoto. Electrical shorting of organic photovoltaic films resulting from metal migration. *Journal of Applied Physics*, 99(3):036109, feb 2006.

[49] S. T. Lee, Z. Q. Gao, and L. S. Hung. Metal diffusion from electrodes in organic light-emitting diodes. *Applied Physics Letters*, 75(10):1404, sep 1999.

[50] Christoph J. Brabec, Sean E. Shaheen, Christoph Winder, N. Serdar Sariciftci, and Patrick Denk. Effect of LiF/metal electrodes on the performance of plastic solar cells. *Applied Physics Letters*, 80(7):1288, feb 2002.

[51] M. Vogel, S. Doka, Ch. Breyer, M. Ch. Lux-Steiner, and K. Fostiropoulos. On the function of a bathocuproine buffer layer in organic photovoltaic cells. *Applied Physics Letters*, 89(16):163501, oct 2006.

[52] J. Huang, Z. Xu, and Y. Yang. Low-Work-Function Surface Formed by Solution-Processed and Thermally Deposited Nanoscale Layers of Cesium Carbonate. *Advanced Functional Materials*, 17(12):1966–1973, aug 2007.

[53] Xiaoxia Jiang, Hao Xu, Ligong Yang, Minmin Shi, Mang Wang, and Hongzheng Chen. Effect of CsF interlayer on the performance of polymer bulk heterojunction solar cells. *Solar Energy Materials and Solar Cells*, 93(5):650–653, may 2009.

[54] Felix Nickel, Manuel Reinhard, Zhenhao Zhang, Andreas Putz, Siegfried Kettlitz, Uli Lemmer, and Alexander Colsmann. Solution processed sodium chloride interlayers for efficient electron extraction from polymer solar cells. *Applied Physics Letters*, 101(5):053309, aug 2012.

[55] Teng Xiao, Fadzai Fungura, Min Cai, James W. Anderegg, Joseph Shinar, and Ruth Shinar. Improved efficiency and stability of inverted polymer solar cells with a solution-processed BPhen interlayer and polystyrene beads. *Organic Electronics*, 14(10):2555–2563, oct 2013.

[56] Riccardo Po, Chiara Carbonera, Andrea Bernardi, and Nadia Camaioni. The role of buffer layers in polymer solar cells. *Energy & Environmental Science*, 4(2):285, 2011.

[57] Qi Wang, Yuchuan Shao, Qingfeng Dong, Zhengguo Xiao, Yongbo Yuan, and Jinsong Huang. Large fill-factor bilayer iodine perovskite solar cells fabricated by a low-temperature solution-process. *Energy {&} Environmental Science*, 7(7):2359, 2014.

[58] Zhengguo Xiao, Qingfeng Dong, Cheng Bi, Yuchuan Shao, Yongbo Yuan, and Jinsong Huang. Solvent annealing of perovskite-induced crystal growth for photovoltaic-device efficiency enhancement. *Advanced materials (Deerfield Beach, Fla.)*, 26(37):6503–9, oct 2014.

[59] Jun-Seok Yeo, Rira Kang, Sehyun Lee, Ye-Jin Jeon, NoSoung Myoung, Chang-Lyoul Lee, Dong-Yu Kim, Jin-Mun Yun, You-Hyun Seo, Seok-Soon Kim, and Seok-In Na. Highly Efficient and Stable Planar Perovskite Solar Cells with Reduced Graphene Oxide Nanosheets as Electrode Interlayer. *Nano Energy*, 12:96–104, 2014.

[60] Wei Chen, Yongzhen Wu, Jian Liu, Chuanjiang Qin, Xudong Yang, Ashraful Islam, Yi-Bing Cheng, and Liyuan Han. Hybrid interfacial layer leads to solid performance improvement of inverted perovskite solar cells. *Energy & Environmental Science*, 8(2):629–640, 2015.

[61] Qifan Xue, Zhicheng Hu, Jiang Liu, Jiahui Lin, Chen Sun, Ziming Chen, Chunhui Duan, Jing Wang, Cheng Liao, Woon Ming Lau, Fei Huang, Hin-Lap Yip, and Yong Cao. Highly efficient fullerene/perovskite planar heterojunction solar cells via cathode modification with an amino-functionalized polymer interlayer. *J. Mater. Chem. A*, 2(46):19598–19603, oct 2014.

[62] M. Vogel, S. Doka, Ch Breyer, M. Ch Lux-Steiner, and K. Fostiropoulos. On the function of a bathocuproine buffer layer in organic photovoltaic cells. *Applied Physics Letters*, 89(16), 2006.

[63] Ankit Kumar, Srinivas Sista, and Yang Yang. Dipole induced anomalous S-shape I-V curves in polymer solar cells. *Journal of Applied Physics*, 105(9):094512, may 2009.

[64] Ian G. Hill and Antoine Kahn. Organic semiconductor heterointerfaces containing bathocuproine. *Journal of Applied Physics*, 86(4):2116, 1999.

[65] Hiroyuki Yoshida. Electron Transport in Bathocuproine Interlayer in Organic Semiconductor Devices. *The Journal of Physical Chemistry C*, 119(43):24459–24464, oct 2015.

[66] Xi-Cun Gao, Hong Cao, Chun-Hui Huang, Biao-Guo Li, K. Ibrahim, Feng-Qin Liu, and Shigeo Umitani. Electroluminescence from both a light-emitting layer

and hole transport layer: spectral evidence for charge carrier tunneling injection. *Chemical Physics Letters*, 297(5-6):530–536, dec 1998.

[67] P. Peumans, V. Bulovic, and S. R. Forrest. Efficient photon harvesting at high optical intensities in ultrathin organic double-heterostructure photovoltaic diodes. *Applied Physics Letters*, 76(19):2650, may 2000.

[68] Ankit Kumar, Srinivas Sista, and Yang Yang. Dipole induced anomalous S-shape I-V curves in polymer solar cells. *Journal of Applied Physics*, 105(9), 2009.

[69] T. Sakurai, S. Toyoshima, and K. Akimoto. Role of electrode buffer layers in organic solar cells. In *2013 International Renewable and Sustainable Energy Conference (IRSEC)*, pages 46–48. IEEE, mar 2013.

[70] W. Tress, N. Marinova, T. Moehl, S. M. Zakeeruddin, Mohammad Khaja Nazeeruddin, and M. Grätzel. Understanding the rate-dependent J–V hysteresis, slow time component, and aging in CH 3 NH 3 PbI 3 perovskite solar cells: the role of a compensated electric field. *Energy Environ. Sci.*, 8(3):995–1004, jan 2015.

[71] Christopher Eames, Jarvist M Frost, Piers R F Barnes, Brian C O'Regan, Aron Walsh, and M Saiful Islam. Ionic transport in hybrid lead iodide perovskite solar cells. *Nature Communications*, 6:7497, jun 2015.

[72] Tae-Youl Yang, Giuliano Gregori, Norman Pellet, Michael Grätzel, and Joachim Maier. Significance of ion conduction in a organic-inorganic lead-iodide-based perovskite photosensitizer. *Angewandte Chemie International Edition*, 54(27):7905–7910, may 2015.

[73] Dane W DeQuiletttes, Wei Zhang, Victor M Burlakov, Daniel J Graham, Tomas Leijtens, Anna Osherov, Henry J Snaith, David S Ginger, and Samuel D Stranks. Photo-induced halide redistribution in organic–inorganic perovskite films. 7(May):11683, 2016.

[74] Yongbo Yuan and Jinsong Huang. Ion Migration in Organometal Trihalide Perovskite and Its Impact on Photovoltaic Efficiency and Stability. *Accounts of chemical research*, jan 2016.

[75] Luis K. Ono, Sonia R. Raga, Shenghao Wang, Yuichi Kato, and Yabing Qi. Temperature-dependent hysteresis effects in perovskite-based solar cells. *J. Mater. Chem. A*, 3(17):9074–9080, oct 2014.

[76] Chun-Guey Wu, Chien-Hung Chiang, Zong-Liang Tseng, Nazeeruddin Mohammad K., Anders Hagfeldt, and Michael Grätzel. High efficiency stable inverted perovskite solar cells without current hysteresis. *Energy Environ. Sci.*, jul 2015.

[77] Neeti Tripathi, Masatoshi Yanagida, Yasuhiro Shirai, Takuya Masuda, Liyuan Han, and Kenjiro Miyano. Hysteresis-free and highly stable perovskite solar cells produced via a chlorine-mediated interdiffusion method. *J. Mater. Chem. A*, 3(22):12081–12088, 2015.

[78] Yi-Fang Chiang, Jun-Yuan Jeng, Mu-Huan Lee, Shin-Rung Peng, Peter Chen, Tzung-Fang Guo, Ten-Chin Wen, Yao-Jane Hsu, and Ching-Ming Hsu. High voltage and efficient bilayer heterojunction solar cells based on an organic-inorganic

hybrid perovskite absorber with a low-cost flexible substrate. *Physical chemistry chemical physics : PCCP*, 16(13):6033–6040, mar 2014.

[79] Chien-Hung Chiang, Zong-Liang Tseng, and Chun-Guey Wu. Planar heterojunction perovskite/PC 71 BM solar cells with enhanced open-circuit voltage via a (2/1)-step spin-coating process. *J. Mater. Chem. A*, 2(38):15897–15903, jul 2014.

[80] Jixian Xu, Andrei Buin, Alexander H. Ip, Wei Li, Oleksandr Voznyy, Riccardo Comin, Mingjian Yuan, Seokmin Jeon, Zhijun Ning, Jeffrey J. McDowell, Pongsakorn Kanjanaboos, Jon-Paul Sun, Xinzheng Lan, Li Na Quan, Dong Ha Kim, Ian G. Hill, Peter Maksymovych, and Edward H. Sargent. Perovskite–fullerene hybrid materials suppress hysteresis in planar diodes. *Nature Communications*, 6(May):7081, 2015.

[81] Roland Steim, F. René Kogler, and Christoph J. Brabec. Interface materials for organic solar cells. *Journal of Materials Chemistry*, 20(13):2499, mar 2010.

[82] Mikkel Jørgensen, Kion Norrman, Suren a. Gevorgyan, Thomas Tromholt, Birgitta Andreasen, and Frederik C Krebs. Stability of polymer solar cells. *Advanced Materials*, 24(5):580–612, 2012.

[83] Jacob Tse-Wei Wang, James M. Ball, Eva M. Barea, Antonio Abate, Jack A. Alexander-Webber, Jian Huang, Michael Saliba, Ivan Mora-Sero, Juan Bisquert, Henry J. Snaith, and Robin J. Nicholas. Low-temperature processed electron collection layers of graphene/TiO2 nanocomposites in thin film perovskite solar cells. *Nano letters*, 14(2):724–30, feb 2014.

[84] Qi Wang, Cheng Bi, and Jinsong Huang. Doped hole transport layer for efficiency enhancement in planar heterojunction organolead trihalide perovskite solar cells. *Nano Energy*, 15:275–280, jul 2015.

[85] Qianqian Lin, Ardalan Armin, Ravi Chandra Raju Nagiri, Paul L. Burn, and Paul Meredith. Electro-optics of perovskite solar cells. *Nature Photonics*, 9(2):106–112, dec 2015.

[86] Olga Malinkiewicz, Aswani Yella, Yong Hui Lee, Guillermo Minguez Mínguez Espallargas, Michael Graetzel, Mohammad K Nazeeruddin, and Henk J Bolink. Perovskite solar cells employing organic charge-transport layers. *Nature Photonics*, 8(2):128–132, dec 2013.

[87] Jun Yuan Jeng, Kuo Cheng Chen, Tsung Yu Chiang, Pei Ying Lin, Tzung Da Tsai, Yun Chorng Chang, Tzung Fang Guo, Peter Chen, Ten Chin Wen, and Yao Jane Hsu. Nickel oxide electrode interlayer in CH3NH3PbI 3 perovskite/PCBM planar-heterojunction hybrid solar cells. *Advanced Materials*, 26(24):4107–4113, mar 2014.

[88] Anand S. Subbiah, Ansuman Halder, Soham Ghosh, Neha Mahuli, Gary Hodes, and Shaibal K. Sarkar. Inorganic hole conducting layers for perovskite-based solar cells. *Journal of Physical Chemistry Letters*, 5(10):1748–1753, may 2014.

[89] Chun Xian Guo, Kuan Sun, Jianyong Ouyang, and Xianmao Lu. Layered V2O5/PEDOT Nanowires and Ultrathin Nanobelts Fabricated with a Silk Reelinglike Process. *Chemistry of Materials*, 27(16):5813–5819, aug 2015.

[90] Weibo Yan, Senyun Ye, Yunlong Li, Weihai Sun, Haixia Rao, Zhiwei Liu, Zuqiang Bian, and Chunhui Huang. Hole-Transporting Materials in Inverted Planar Perovskite Solar Cells. *Advanced Energy Materials*, may 2016.

[91] Jin Cui, Fanping Meng, Hua Zhang, Kun Cao, Huailiang Yuan, Yibing Cheng, Feng Huang, and Mingkui Wang. CH3NH3PbI3-Based Planar Solar Cells with Magnetron-Sputtered Nickel Oxide. 6(24):22862–22870, 2014.

[92] Jong H Kim, Po-wei Liang, Spencer T Williams, Namchul Cho, Chu-chen Chueh, Micah S Glaz, David S Ginger, and Alex K Jen. High-Performance and Environmentally Stable Planar Heterojunction Perovskite Solar Cells Based on a Solution-Processed Copper-Doped Nickel Oxide Hole-Transporting Layer. *Advanced Materials*, 27(4):695–701, nov 2014.

[93] Song Chen, Jesse R. Manders, Sai-Wing Tsang, and Franky So. Metal oxides for interface engineering in polymer solar cells. *Journal of Materials Chemistry*, 22(46):24202, 2012.

[94] Dewei Zhao, Michael Sexton, Hye-Yun Park, George Baure, Juan C. Nino, and Franky So. High-Efficiency Solution-Processed Planar Perovskite Solar Cells with a Polymer Hole Transport Layer. *Advanced Energy Materials*, 5(6):1401855, mar 2015.

[95] Po-Wei Liang, Chien-Yi Yi Liao, Chu-Chen Chen Chueh, Fan Zuo, Spencer T. Williams, Xu-Kai Kai Xin, Jiangjen Lin, and Alex K-Y Y Jen. Additive enhanced crystallization of solution-processed perovskite for highly efficient planar-heterojunction solar cells. *Advanced Materials*, 26(22):3748–3754, mar 2014.

[96] Antonio Abate, Tomas Leijtens, Sandeep Pathak, Joël Teuscher, Roberto Avolio, Maria E. Errico, James Kirkpatrik, James M. Ball, Pablo Docampo, Ian McPherson, and Henry J. Snaith. Lithium salts as "redox active" p-type dopants for organic semiconductors and their impact in solid-state dye-sensitized solar cells. *Physical Chemistry Chemical Physics*, 15(7):2572, 2013.

[97] Bj ouml rn L uuml Ssem, Max L Tietze, Hans Kleemann, Christoph Ho szlig Bach, Johann W Bartha, Alexander Zakhidov, and Karl Leo. Doped organic transistors operating in the inversion and depletion regime. *Nature Communications*, 4:1–6, 2013.

[98] Phillip K Koech, Asanga B Padmaperuma, Liang Wang, James S Swensen, Evgueni Polikarpov, Jens T Darsell, James E Rainbolt, and Daniel J Gaspar. Synthesis and Application of 1,3,4,5,7,8-Hexafluorotetracyanonaphthoquinodimethane (F6-TNAP): A Conductivity Dopant for Organic Light-Emitting Devices. *Chemistry of Materials*, 22(13):3926–3932, 2010.

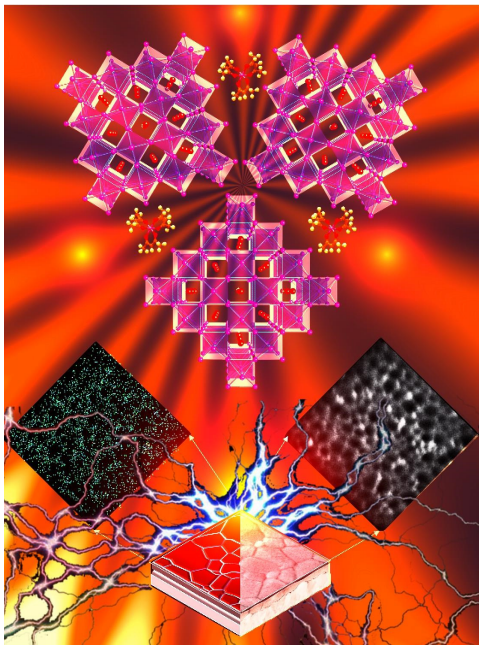
[99] Patrick Pingel, Lingyun Zhu, Kue Surk Park, Jorn-Oliver Vogel, Silvia Janietz, Eung-Gun Kim, Jurgen P. Rabe, Jean-Luc Bredas, and Norbert Koch. Charge-Transfer Localization in Molecularly Doped Thiophene-Based Donor Polymers. *The Journal of Physical Chemistry Letters*, 1(13):2037–2041, jul 2010.

[100] Felix Deschler, Daniel Riedel, Andras Deák, Bernhard Ecker, Elizabeth von Hauff, and Enrico Da Como. Imaging of morphological changes and phase segregation in doped polymeric semiconductors. *Synthetic Metals*, 199:381–387, 2015.

Chapter 6

Metal Ion Doping in the $CH_3NH_3PbI_3$

The work in this chapter has been adapted and reproduced in part with permission from: Jacob Tse-Wei Wang, Zhiping Wang, Sandeep Pathak, Wei Zhang, Dane W. deQuilettes, Florencia Wisnivesky, Jian Huang, Pabitra Nayak, Jay Patel, Hanis Yusof, Yana Vaynzof, Rui Zhu, Ivan Ramirez, Jin Zhang, Caterina Ducati, Chris Grovenor, Michael B. Johnston, David S. Ginger, Robin J. Nicholas & Henry J. Snaith, Efficient Perovskite Solar Cells by Metal Ion Doping, *under review at Energy & Environmental Sciences.*



6.1 Context

Realizing the theoretical limiting power conversion efficiency (PCE) in perovskite solar cells requires a better understanding and control over the fundamental loss processes occurring in the bulk of the perovskite layer and at the internal semiconductor interfaces in devices. One of the main challenges is to eliminate the presence of charge recombination centres throughout the film which have been observed to be most densely located at regions near the grain boundaries. Here, we introduce aluminium acetylacetonate to the perovskite precursor solution, which improves the crystal quality by reducing the microstrain in the polycrystalline film. At the same time, we achieve a reduction in the non-radiative recombination rate, a remarkable improvement in the photoluminescence quantum efficiency (PLQE) and a reduction in the electronic disorder deduced from an Urbach energy of only 12.6 meV in complete devices. As a result, we demonstrate a power-conversion efficiency (PCE) of 19.1% with negligible hysteresis in planar heterojunction solar cells comprising all organic p and n-type charge collection layers. Our work shows that an additional level of control of perovskite thin film quality is possible via impurity cation doping, and further demonstrates the continuing importance of improving the electronic quality of the perovskite absorber and the nature of the heterojunctions to further improve the solar cell performance.

6.2 Introduction

Driven by improvements in the quality of organic-inorganic lead halide perovskites (i.e. $CH_3NH_3PbI_3$) thin films, perovskite solar cells have achieved a series of efficiency breakthroughs since 2009.[1, 2, 3, 4] Starting from structures based on small nanocrystals embellishing the surface of a mesoporous TiO_2 scaffold in 2009, the published highest power conversion efficiency of 21.1% has been achieved in a device architecture which

comprises both a thin layer of mesoporous TiO_2 and a thick solid perovskite absorber layer with micrometre size crystalline domains and a high level of uniformity.[5] In addition, there has been much work on the simplified "planar heterojunction" architecture, where a solid perovskite absorber layer is sandwiched between negative (n) and positive (p) type charge collection layers.[2, 6] One commonality of all this work, is that enhanced crystalline quality and the macroscopic uniformity of the solid perovskite thin films are key parameters which have led to improved device performance. However, there is still much confusion over many factors such as the role and impact of boundaries between the polycrystalline domains, the requirement or not to move towards single crystalline materials, the nature and role of electronic defects in the perovskite absorbers, and the impact of the charge collection layers upon loss processes in the perovskite solar cells.

One specific area which has had some attention is the precise nature of electronic defects in the perovskite films. Yan et al. have used theoretical calculations to propose that many of the defects, such as I or Pb vacancies, will result in states very close to or within the continuum of states in the conduction and valance bands; therefore only having a minor negative electronic impact upon the solar cells.[7] However, Agiorgousis et al. have revealed that there is strong covalency between the Pb cations and I anions in the perovskite plane, which may result in the existence of intrinsic defects, such as undercoordinated Pb dimers and I trimers, which could generate sites within the band gap and serve as charge recombination centres during solar cell operation.[8]

Previously, post treatment of the perovskite films with Lewis bases, such as pyridine, has been shown to enhance the charge carrier lifetime, suggesting that pyridine can passivate surface recombination sites[9], which are possibly under-coordinated Pb sites.[10] However, these sorts of post growth treatments are challenging to control in a reproducible manner, and it is not clear if they are genuinely passivating the defect sites, or simply enabling the perovskite crystal surface to reconstruct in a more favourable

manner with fewer crystal surface defects.[9] On the other hand, incorporation of an impurity "dopant" into the precursor solution itself could provide a more robust way to produce a perovskite film with traps passivated throughout the bulk, or indeed influence the crystallization process in such a way as to minimize the number of defects which result in electronic traps in the first place.[11] Recently, Sargent and coworkers have shown that addition of Phenyl-C61-butyric acid methyl ester (PCBM) directly into the perovskite precursor solution allows PCBM to sit at the grain boundaries of the processed perovskite films, leading to a certain degree of passivation of the trap states at the grain boundaries, and suppression of hysteresis in the n-i-p planar heterojunction device architecture.[12] In addition, PCBM is a very good electron acceptor for use as the n-type charge collection material in perovskite solar cells, hence its role may be two-fold when mixed into the perovskite solution.[13] However, a major challenge to achieving reproducible device performance with this route is the poor solubility and significant phase segregation of PCBM within the perovskite precursor solution.[12]

Here, we investigate the impact of "doping" to the perovskite, $CH_3NH_3PbI_3$ ($MAPbI_3$), with Al^{3+}, a higher valence ion than Pb^{2+}. By introducing a Lewis acid-base coordination complex, $Al(C_5H_7O_2)_3$, aluminium acetylacetonate (Al-$acac_3$), directly into the perovskite precursor solution, which contains lead acetate trihydrate ($PbAc_2$*($3H_2O$)) and methyl ammonium iodide (MAI).[14] Al^{3+} ions have a much smaller ionic radii than Pb^{2+} (53.5 pm vs 119 pm) hence we do not expect to observe substitutional doping within the crystal.[15] However, by careful optimisation of the Al^{3+} ion concentration in the perovskite precursor solution, we dramatically enhance the PLQE of the crystalized perovskite films, which increases to 35% from only 15% for the non-doped (control) films when measured at $\sim$ 10 suns irradiance, which we infer to be due to a reduction in the density of electronic defects. By incorporating these "Al^{3+}-doped" films into "inverted" p-i-n perovskite solar cells, we achieve a measured current-density voltage PCE of 19.1% and a stabilized power output of 18.2%.

6.3 Characterization of Al^{3+}-doped Perovskite

To deposit Al^{3+}-doped $CH_3NH_3PbI_3$ perovskite films, we first prepared a $CH_3NH_3PbI_3$ precursor solution by mixing MAI and ($PbAc_2.(3H_2O)$) at a 3:1 molar ratio in dimethylformamide (DMF), with the addition of hypophosphorous acid, as previously reported by Zhang et al.[11] In order to study the impact of doping concentration on the perovskite, we added varying concentrations (from 0.075 to 1.5 mol% of the Al^{3+}/Pb^{2+} ratio) of Al-$acac_3$ into the as prepared $CH_3NH_3PbI_3$ precursor solutions and fabricated a series of perovskite films. We note that, in this manuscript we will refer to the Al-$acac_3$ addition as "Al^{3+}-doping". We will show evidence towards the end of this chapter that it is indeed the addition of aluminum ions, and not the organic counter ions, which is important for the improvements which we will present.

6.3.1 Crystal structure

We first evaluate if there is any impact of Al^{3+} doping upon the crystallisation process and the final crystal structure of the resulting perovskite films. In fig. 6.1a we show the X-ray diffraction (XRD) spectra for a series of films made with a range of Al^{3+} doping concentrations up to 1.5 mol%. All the perovskite films crystallise in a typical tetragonal crystal (I4/mcm, NO. 140) structure as reported previously.[1] As the doping levels increase up to 0.15 mol%, the intensities of the dominant perovskite (110) and (220) peaks substantially increase with increasing doping concentration, and there is a significant decrease in peak widths (see fig. 6.1c) but no measurable shift in the position of the (110) and (220) diffraction peaks. These results suggest that the (hh0) planes become increasingly aligned in the presence of the Al^{3+} dopant. As the doping level rises to 0.3 mol% concentration, the (110) peak intensity continues to increase, but the peak begins to broaden and shift in position with respect to the control sample. However,

upon further increase in doping concentration, the peak intensity begins to decrease and the peak widths continue to broaden.

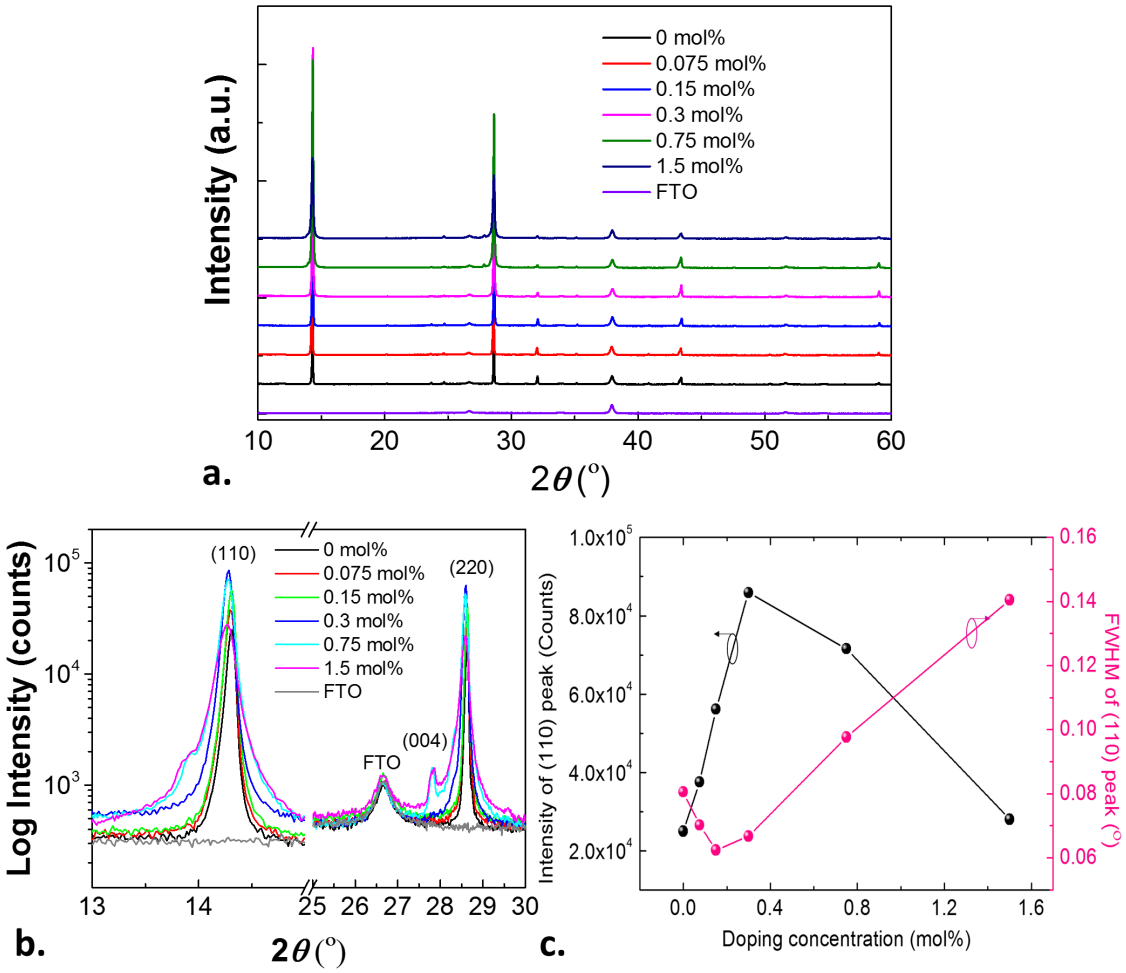


Figure 6.1: (a) X-ray diffraction patterns analysis of perovskite with different Al^{3+} doping concentration, (b) its enlargement in log scale, and (c) the intensity and FWHM variations of (110) peak with different Al^{3+} doping concentrations.

6.3.2 Microstrain

Broadening and shifts in the XRD peak can be caused by either a reduction in the grain size (Scherrer broadening) and/or non-uniform strain (microstrain). We note that Scherrer broadening will only be significant when the grains are in the range of or less than 100 nm, and as we will discuss later we do not expect this to be a significant

contribution here. Strain is the relative change in size of an object with respect to its ideal size (or size before experiencing an external force). The microstrain in a crystalline material is a result of small fluctuations in the lattice spacing, induced by crystal imperfections/structural defects including dislocations, vacancies, stacking faults, interstitials, twinning, and grain boundaries.[16, 17, 18] for scattering of light of wavelength , nλ = 2dsinθ, it is clear that small fluctuations in d (i.e. Δd) will result in small fluctuations, or broadening, in θ when measuring the X-ray diffraction from the material. We quantify the extent of microstrain in our perovskite films by analysing the peak broadening in the diffraction patterns according to the modified Williamson-Hall method.[17, 19] The effective observed peak broadening (Δd_{obs}) determined from the XRD peak width broadening, is a convoluted function of the Gaussian full width half maximum broadening in the 2θ scan due to the instrument response (Δd_{ins}), the grain size (Δd_{size}) and the microstrain (Δd_{ε}). These can be de-convoluted from the observed broadening, via,

$$\Delta d_{obs}^2 = \Delta d_{\varepsilon}^2 + \Delta d_{ins}^2 + \Delta d_{size}^2 \tag{6.3.1}$$

where the unit-less microstrain ε is defined as $\varepsilon = (\Delta d_{\varepsilon}/\mathrm{d})$, where d is the mean d-spacing. Since the perovskite thin films have grains on the order of many hundreds of nm to microns, it is likely that the size effect induced peak width broadening can be neglected, hence if $\Delta d_{size}{}^2 \ll \Delta d_{obs}{}^2$ [19] and we can write,

$$(\Delta d_{obs}^2 - \Delta d_{ins}^2)^{1/2} \approx \varepsilon d. \tag{6.3.2}$$

Therefore, the slope of (Δd_{obs}^2 - Δd_{ins}^2)$^{1/2}$ versus d, gives the magnitude of the microstrain, ε , in the film.

Here we observe in fig. 6.2 that introduction of small amounts of Al^{3+} dopant (< 0.3

mol%) decreases the microstrain. A minimum microstrain of 5.2×10^{-3} is achieved at 0.15 mol%, which is 30% lower than the control film. We note that this is equivalent to d-spacing fluctuations of the order of 0.5%. This suggests that the introduction of a small amount of Al^{3+} dopant reduces the density of crystal defects. Additionally, the (110) XRD peak significantly increases in intensity, consistent with the presence of Al^{3+} enhancing the orientation in the growth of perovskite domains along the [110] direction.[20]

If the Al^{3+} ions partially substitute Pb^{2+} ion sites, we would expect the perovskite lattice to be severely distorted due to the much smaller Al^{3+} ionic radii as compared to the Pb^{2+} ion, which would induce a shift in d.[21] Following this reasoning, the unvarying (hh0) peak position and decreased microstrain imply at the doping level of 0.15%, the Al^{3+} dopants are unlikely to be incorporated within the perovskite crystal lattice. When the doping concentration increases to 0.3 mol%, we observe an increase in microstrain, which continues to increase monotonically with the increasing doping concentration.

6.3.3 Micromorphology and Al detection

In fig. 6.3 we show top-view SEM images of the perovskite samples with different doping concentrations of Al^{3+} . We do not observe any noticeable differences in morphology or apparent grain size in the perovskite films up to doping levels of 0.3 mol%, compared to the control sample. This is consistent with our postulation that the narrowing of the (hh0) diffraction peaks with the doping concentration from zero to 0.15 mol% is not due to crystal size effects.

Morphologically, it appears that the perovskite films can tolerate the addition of Al^{3+} ions to the precursor solution up to around 0.3 mol%, before any negative impact upon the morphology occurs. The disappearance of the polycrystalline grains in the SEM

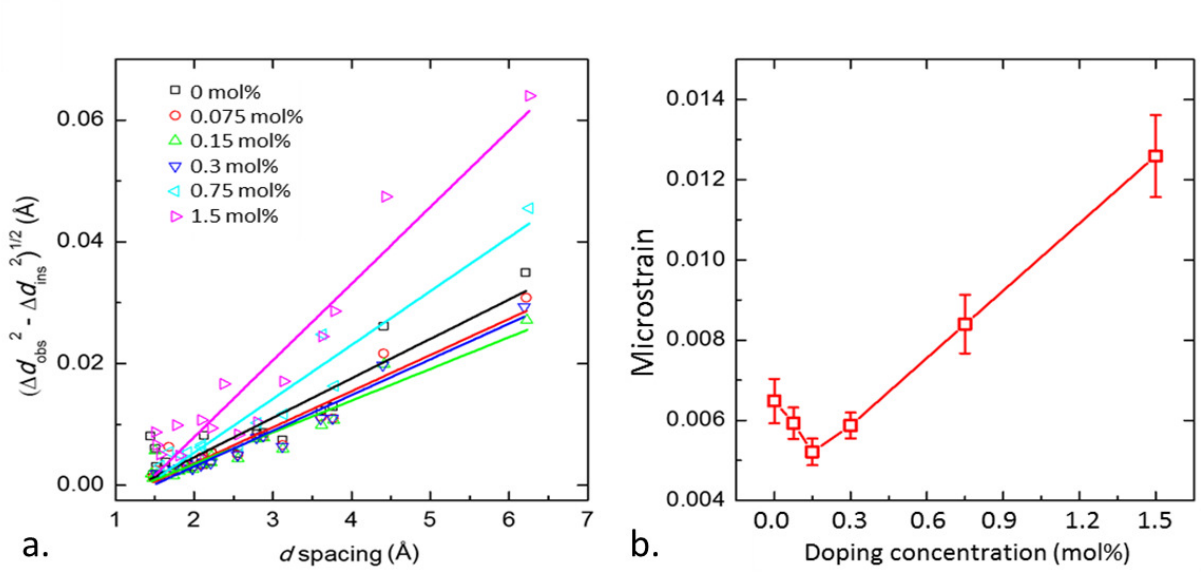


Figure 6.2: Characterizations of Al^{3+}-doped perovskite samples with (a) A modified Williamson-Hall plot of $(\Delta d_{obs}{}^2 - \Delta d_{ins}{}^2)^{1/2}$ versus d spacing extracted from the corresponding diffraction profiles shown in fig. 6.1. The slopes of the solid lines from linear fits indicate the extents of microstrain at different doping concentrations. (b) Calculated microstrain of samples with different Al^{3+} doping concentration from XRD patterns (The error bars for each concentration in the plot b, are determined from the fits in a).

images, with Al^{3+} concentrations at or above 0.75 mol%, is consistent with these films having much smaller polycrystalline domains, which are not clearly discernible in the SEM image. We also note that the XRD patterns for the films with over 0.3 mol% doping, which we have shown in fig. 6.1, are strongly perturbed, indicating a limit to the concentration of Al^{3+} which the perovskite films can tolerate.

To probe whether Al ions remains in the annealed films, we performed inductively coupled plasma optical emission spectrometry (ICP-OES). The detection limits of ICP-OES typically range from parts per million (ppm) to parts per billion (ppb).[22] For the sample with 0.15 mol% Al^{3+} doping (the calculated Al/Pb is 2.6:1000), we determine a molar ratio of Al/Pb of 1.2:1000 from the ICP-OES analysis, which confirms the presence of Al^{3+} in the doped film, only at a slightly lower concentration than in the starting solution. On the contrary, for the control film we determine an Al/Pb molar ratio of 0.016:1000, which is almost negligible, as expected. We further validated this finding

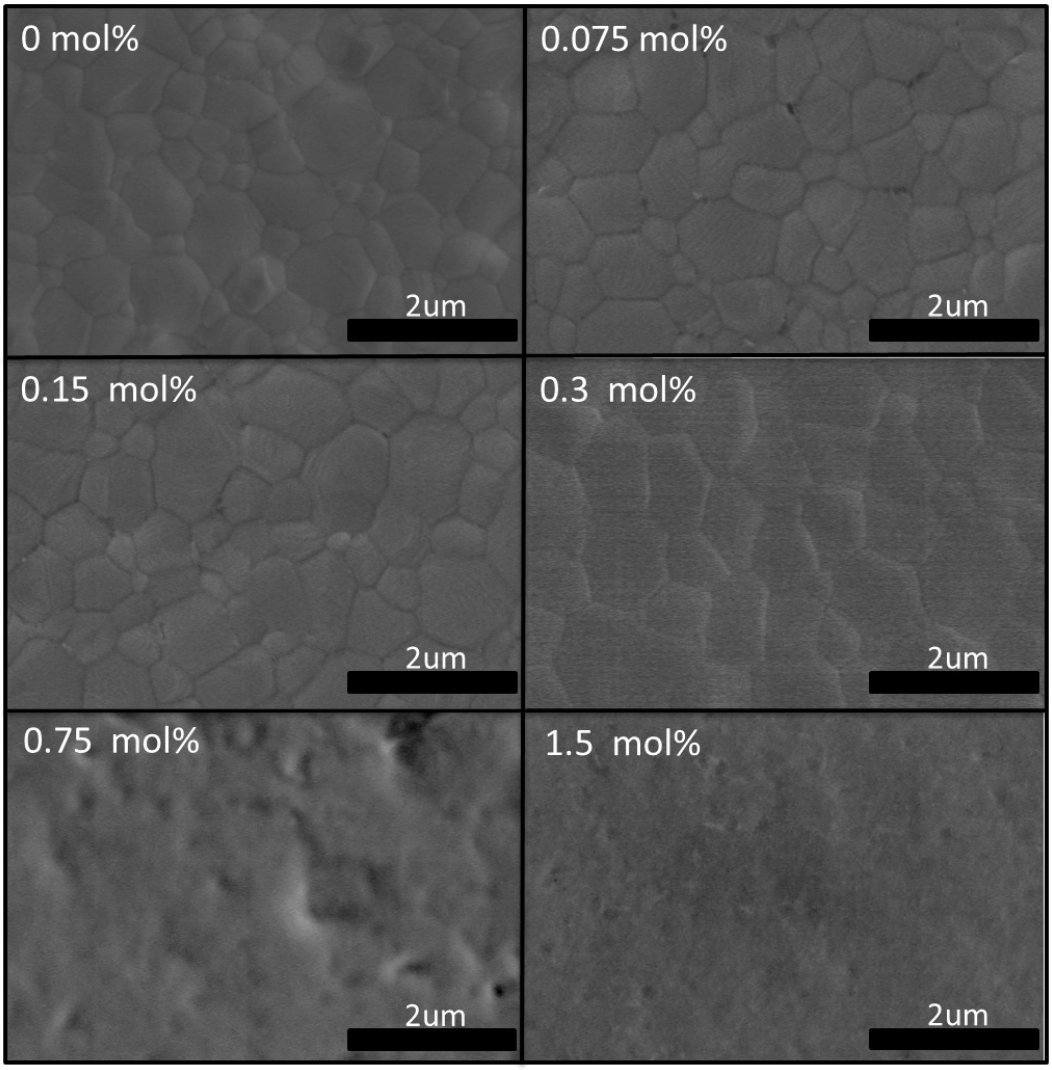


Figure 6.3: Top view scanning electron microscope (SEM) of Al^{3+}-doped perovskite samples with different doping concentrations.

for higher concentration solutions (>0.3 mol%) using X-ray photoelectron spectroscopy (XPS), the results of which we show in fig. 6.4. Due to the closely spaced spin-orbit components for Al 2p ($\Delta = \sim 0.5$ eV), we observe a single peak at a binding energy of $\sim$ 77 eV. This high binding energy is in agreement with a +3 oxidation state of Al, as observed previously for Al_2O_3[23] and AlF_3[24]. However, we could not detect the presence of Al^{3+} below 0.3 mol%, due to the concentration falling below the detection level of the instrument.[25]

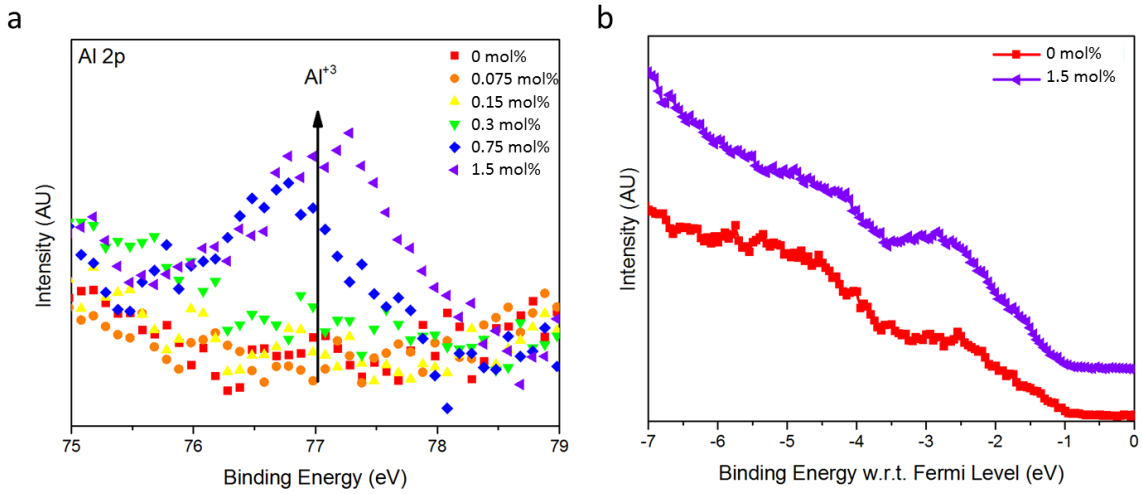


Figure 6.4: X-ray photoemission spectroscopy (XPS) spectra of Al 2p region of control and Al^{3+}-doped perovskite films.

To further investigate the location and distribution of the Al^{3+} ions within the perovskite film, we employed nanoscale secondary ion mass spectrometry (NanoSIMS) to perform elemental mapping for the doping level of 0.15 mol%. The NanoSIMS system uses a 16 KeV primary $^{133}Cs^{+}$ beam to bombard the perovskite film surface, and then collects and analyzes the Al signal as a negative ion which is commonly detected as AlO^{-} (the oxygen is captured from the sample surface or the vacuum system) In fig. 6.5 we show the secondary electron microscopy images overlaid with the elemental map for Al. In the secondary electron image the darker regions are regions of thicker films, which we therefore interpret as being the centre of grains, and the lighter regions are the thinner regions which we therefore interpret to be the grain boundaries. Although the Al signal is apparent everywhere in the film, it is most strongly concentrated near the brighter regions of the secondary electron microscopy image, indicative of increased Al concentration near the grain boundaries.This is consistent with the Al^{3+} ions being predominantly expelled to the perovskite surface and grain boundaries during crystallisation

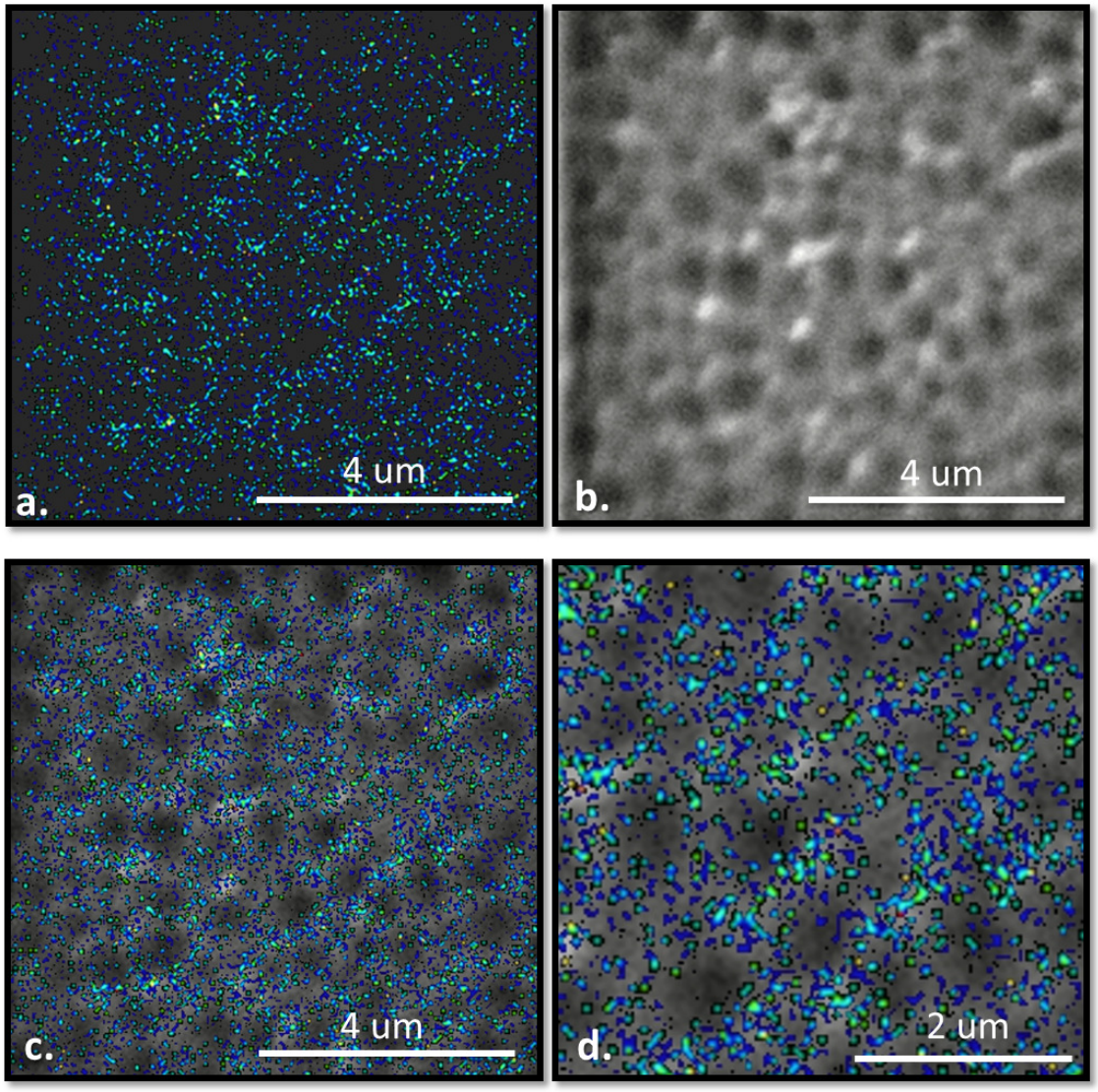


Figure 6.5: (a)NanoSIMS images showing the AlO^- ions mapping of Al^{3+}-doped (0.15 mol%) perovskite and (b) their secondary electron image at the same location.

6.3.4 Impact on Crystallization

Considering all the evidence we have presented above, it appears that the presence of a small amount of Al^{3+} in the perovskite growth solution results in better crystallisation with resultantly fewer crystal defects, as we infer from the reduced microstrain. However, beyond an optimum level of addition of Al^{3+}, the crystallization is strongly perturbed resulting in increased levels of defects. At low Al^{3+} doping concentrations, the Al^{3+} ions appear not to be incorporated into the perovskite lattice, but predominantly expelled to the surface and grain boundaries. The precise mechanism by which the crystallisation is enhanced with a small quantity of Al^{3+} doping is difficult to determine. However, based on our investigation above, we describe our postulated mechanism here: The presence of impurity ions is known to influence crystallisation of materials since the earliest investigations of crystal growth.[26] Impurity ions can either slow down crystallisation by adsorbing to crystal surfaces and sterically inhibiting growth, or the impurity ions can accelerate crystal growth by changing the surface energy of the crystal growth front making it more favourable for accelerated crystallization.[27, 28, 29] In the low concentration regime (below 0.3mol% Al^{3+}) we infer that the Al^{3+} is facilitating enhanced crystallization, and specifically the growth of (hh0) crystal planes, resulting in more orientated crystalline domains. In fig. 6.6, we show a schematic diagram of the proposed perovskite growth mode and influence of the Al^{3+} doping. We also illustrate crystal defects which could potentially exist at the edges of the perovskite crystal surface in the form of terraces, and indicate how the Al^{3+} doping can reduce the prevalence via the selective enhancement of growth of these terraces.

In order to visualize how the Al^{3+} doping has influenced the as-crystalized films, we performed atomic force microscopy (AFM) measurements on our samples. We show these images in the bottom row of fig. 6.6, and plot histograms for the distribution in heights from the images. The lower regions correspond to the troughs at the boundary

of the grains, and the higher regions correspond to the top most surfaces of the grains. For the control sample we observe a symmetric, approximately Gaussian distribution of heights, indicating that the surface of the perovskite film is continuously undulating over the measured length-scale, with no specific preferred height. We estimate a half-width at half-maximum (HWHM) height distribution of 33 nm. This level of undulation is almost identical to the underlying FTO substrate, which we determine a HWHM height distribution of 34 nm, which we show in the fig. 6.7 Thus the control perovskite film does not appear to planarize the FTO.

In contrast, for the optimum (0.15 mol%) doped perovskite sample, the height distribution becomes asymmetric with a background undulation of the same extent, but with an additional distribution with a much narrower HWHM of ∼16nm on the top-most region of the films. This indicates that the top of the grains are much flatter in the Al^{3+} doped samples than in the control samples. The height distribution for the 1.5 mol% Al^{3+} doped sample significantly changes, but still shows a relatively narrow distribution on the top surface and a long tail indicating a relatively flat film, but now with the presence of pinholes. Since the crystal morphology of the 1.5 mol% sample has changed considerably, we cannot compare this directly to the other two compositions. These observations further corroborate that, with low levels of Al^{3+} doping, the perovskite crystalline growth is indeed enhanced and preferentially selects certain planes, while in addition the reduced roughness of the surface of the grains is consistent with a reduction in terrace/step-like defects on the crystal surface.

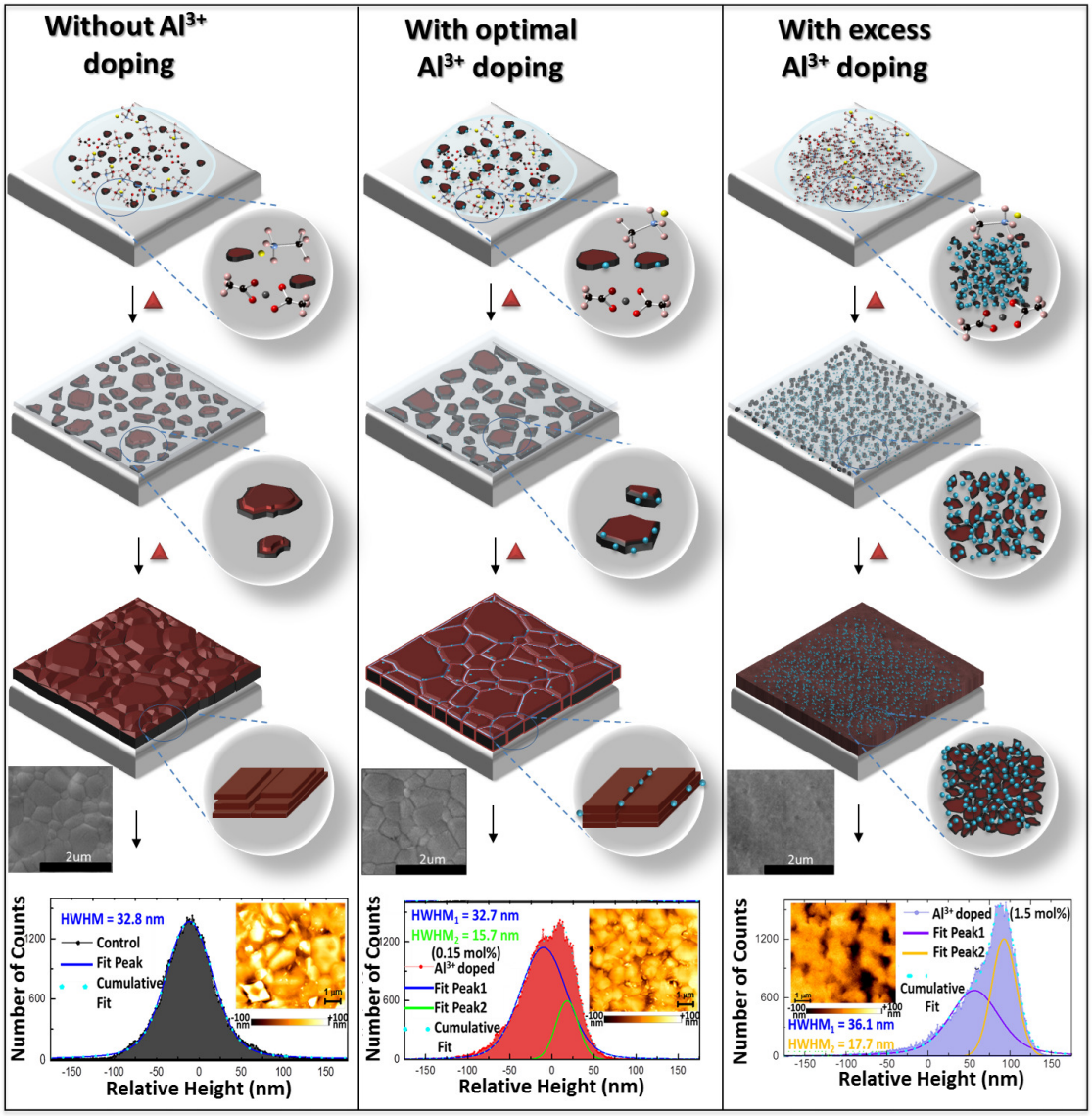


Figure 6.6: Schematic diagram of the proposed perovskite polycrystalline thin film growth and influence of the Al^{3+} doping with illustrated C, N, H, O, I, Pb, and Al atoms are indicated by the color of black, blue, pink, red, grey, and cyan respectively; And histograms of the surface topography and the images (insets) from AFM measurements of different samples. Best fits for the histograms are obtained using one and two Voigt distributions, respectively for the control and the optimized sample. The individual distribution components with their HWHM, and the cumulative fits are labelled as in the figure.

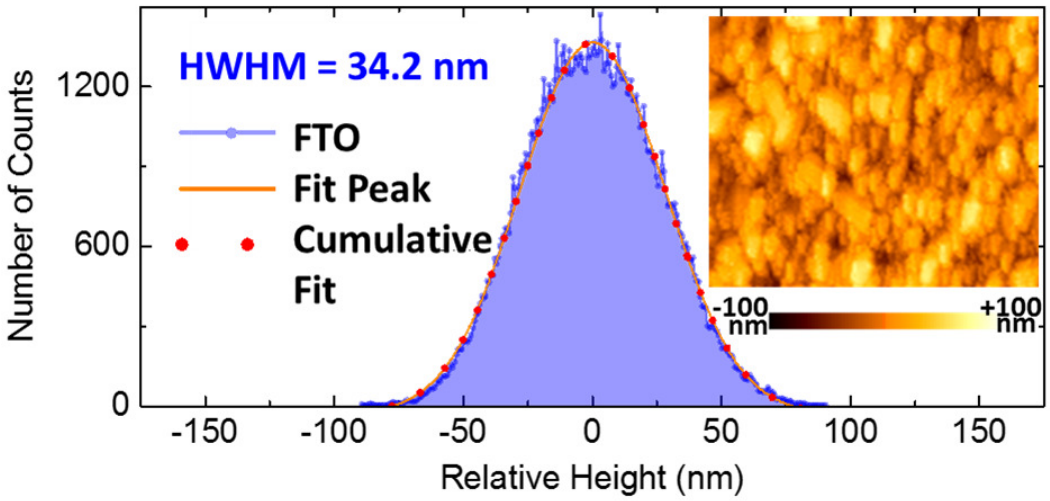


Figure 6.7: The Atomic Force Microscopy (AFM) image of FTO substrate, where the estimated half-width at half-maximum (HWHM) height distribution is 34 nm.

6.4 Optoelectronic Properties

We now investigate if the structural improvements in the Al^{3+}-doped polycrystalline films translate to enhanced optoelectronic properties. To understand the influence of Al^{3+} doping upon the photo-physical properties of the perovskite films we performed absorption and photoluminescence measurements, which we show in fig. 6.8. We observe little change in the absorption spectra for the films, but we do observe an increase in steady-state photoluminescence (PL) intensity with a maximum for the 0.15 mol% Al^{3+}-doped samples, and a subsequent fall off of in intensity upon further increase in doping concentration.

6.4.1 Photoluminescence Behaviour

In fig. 6.9 we compare the PL properties of the control films and those doped with 0.15 mol% Al^{3+}. In fig. 6.9a and b we observe that the Al^{3+}-doped perovskite films

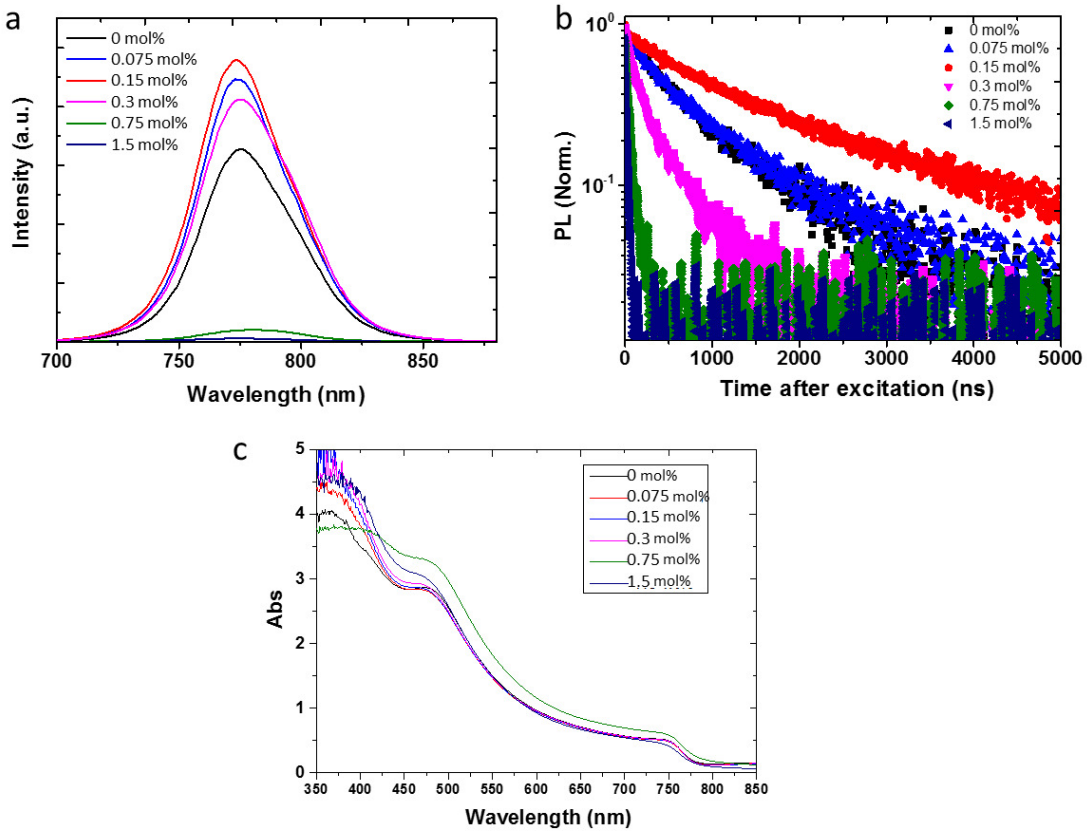


Figure 6.8: Characterizations of different Al^{3+} doping concentration of perovskite samples with (a) steady-state photoluminescence, (b) Time-resolved Photoluminescence decay, and (c) UV-vis absorption spectra.

have higher steady state PL intensity and an almost two-fold increase in PL life time compared to the control.

To further quantify the influence of the Al^{3+} doping upon the radiative and non-radiative recombination rates, we performed photoluminescence quantum efficiency (PLQE) measurements as a function of excitation power, which we show in fig. 6.9c. For both doped and control samples, the PLQE rises with increasing excitation power, a behaviour attributed to the filling of trap states and increasingly favourable competition of radiative bimolecular recombination over non-radiative trap assisted recombination.[30, 31, 32] Notably, the PLQE is higher for the Al^{3+}-doped samples at all light intensities, which, along with the increase we observe in the PL lifetime, is consistent with fewer fast non-

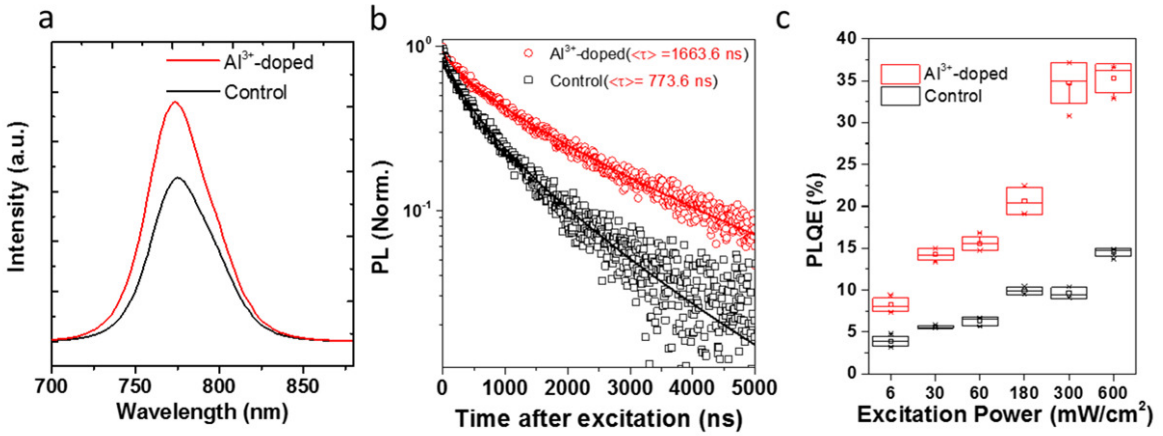


Figure 6.9: Photoluminescence spectroscopy of control (non-doped) and 0.15 mol% Al^{3+}-doped perovskite thin films deposited on glass substrate with (a) steady-state spectra (300 mW/cm^2, 507 nm), (b) time-resolved photoluminescence decay after excitation at 507 nm with pulsed (200 kHz) and a fluence of 30 nJ/cm^2/pulse, and (c) photoluminescence quantum efficiency (PLQE) as a function of excitation power.

radiative decay channels in the Al^{3+}-doped samples. We fit the bulk time-resolved PL data in fig. 6.9b with a stretched exponential function and extract the average lifetimes, $<\tau>$, as previously described.[9] We use these low-fluence PL lifetime values along with the low excitation power (6 mW/cm^2) PLQE values, where in both cases we expect the carrier recombination to be dominated by pseudo first-order kinetics,[9, 32] to estimate the radiative and non-radiative decay rates in the films using,

$$PLQE = \frac{k_{rad}}{k_{rad} + k_{non-rad}} \tag{6.4.1}$$

where k_{rad} is the radiative decay rate $k_{non-rad}$ is the non-radiative decay rate and $k_{rad}+k_{non-rad} = 1/ <\tau>$. For the control and Al^{3+}-doped films, the k_{rad} we determine are similar for the two films at 5.04x10 s^{-4} and 4.96x10 s^{-4}, while we observe there is a reduction in $k_{non-rad}$ from 1.24x10 s^{-6}to 5.52x10 s^{-5} for the control and Al^{3+}-doped films. This indicates that the substantive change in the photophysical properties of the perovskite films with 0.15 mol% Al^{3+} is approximately a two-fold reduction in the non-

radiative recombination rate. We note that both the radiative and non-radiative decay rates are relatively low for a crystalline semiconductor. The slow recombination in metal halide perovskites is a highly fortuitous property for PV devices, but the origin of the phenomenon remains to be elucidated.[33] The above analysis gives an indication of the macroscopic changes occurring within the perovskite films. However, we know that severe photophysical heterogeneity can occur within the polycrystalline films, and hence to clarify which microscopic regions of the film are responsible for the reduced non-radiative decay, we employ confocal fluorescence microscopy. In fig. 6.10a and b we show a 10 x 10 μm confocal fluorescence image of a control and 0.15 mol% Al^{3+}-doped perovskite film. We show the image histograms of occurrence versus PL (counts) in fig. 6.10c and d. In both films there exists heterogeneity in the PL emission with both bright and dark grains, and generally lower levels of PL in the regions near the grain boundaries. From the histograms it is apparent that the average number of PL counts (solid lines) of the Al^{3+}-doped films have shifted to higher levels, but the distribution is similarly broad to that seen in the control. In fact, the distribution has slightly broadened indicating no preferential spatial homogenisation of the PL, but simply an overall reduction in the non-radiative decay, both on or in the grains and at the grain boundaries.

6.4.2 Surface Potential & Trap states

In fig. 6.11 we performed Kelvin probe measurement in the dark and under illumination with perovskite films on FTO, and find a reduction in the surface photovoltage for Al^{3+}-doped films compared to control films, consistent with the removal of electronic traps in the former. In order to understand the effect of Al^{3+} on the energetics of the film surface which comes in contact with the charge transporting layer during the device fabrication, we performed Kelvin probe measurement of perovskite films on FTO in the dark and under illumination.[11] The difference in the work function in the dark and under illu-

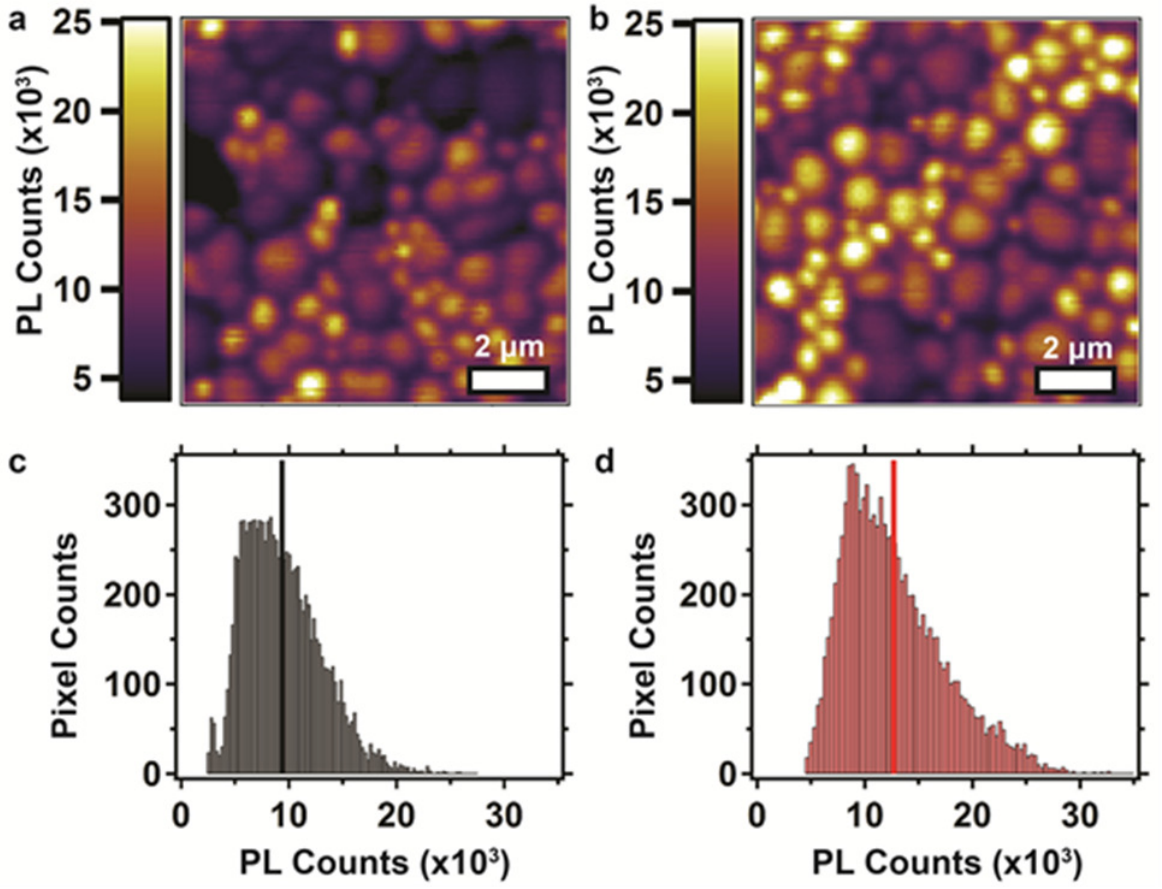


Figure 6.10: Fluorescence microscopy of a, control and b, Al^{3+}-doped (0.15 mol%) perovskite films with 10 x 10 μm area mapping excited with a pulsed 470 nm laser (40 MHz, 117 ps pulse width, 300 nJ/cm^2/pulse). c and d are the image histograms (10,000 pixels) showing the fluorescence emission distribution with solid lines indicate the average number of PL counts. The Al^{3+}-doped perovskite has more pixel counts falling under "bright" regions as compared to the control.

mination provides surface photo-voltage, which indicates the degree of band bending at the surface. The band bending at the surface depends on the density of trap states on that surface.[34] We observe in the dark, that the surface work function of a 0.15 mol% Al^{3+}-doped film is higher than that of the control films and the surface photovoltage of the Al^{3+}-doped films is lower than that of the control. Both measurements in dark and in exposure of light suggest that there is a shift in the surface potential caused by the Al^{3+} doping, and that the band bending at the surface of Al^{3+}-doped perovskite is lower than that of the control samples. This is consistent with fewer electronic trap sites on

surface of the Al^{3+}-doped films.

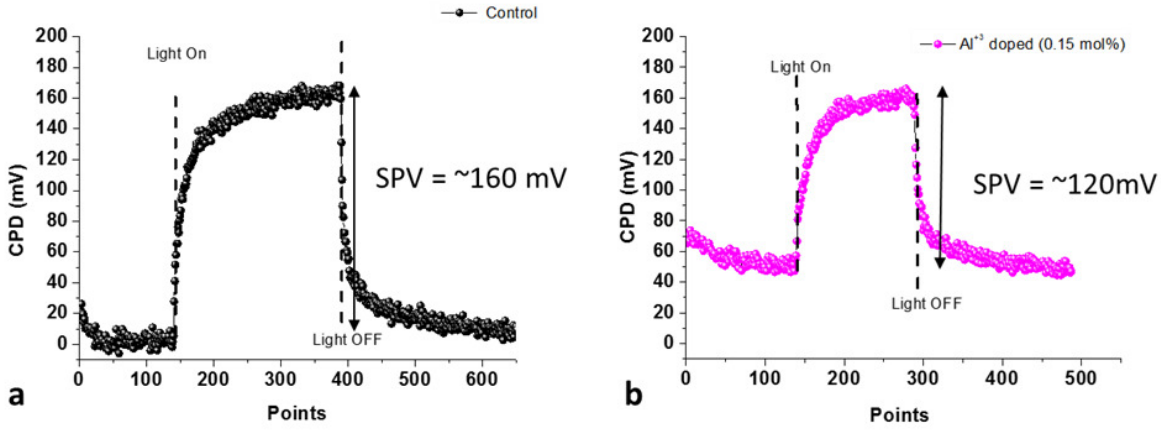


Figure 6.11: Kelvin probe measurement of control and doped perovskite films. The dark CPD (contact potential difference) value of the control sample is presented as the reference where the surface work function is 4.80 eV The SPV (surface photo voltage) for the doped samples are lower than that of the control sample.

6.4.3 Electronic Disorder

A direct method to probe the sub band gap absorption in a photovoltaic device is to make very sensitive measure of the spectral response of the photocurrent via Fourier Transform Photocurrent Spectroscopy (FTPS) on complete solar cells. In an approximation, a shallow slope in the rise in the external quantum efficiency (EQE) below the band gap indicates a large density of sub band gap states, and in contrast a steep rise in the EQE below the band gap indicates a lower density of sub band gap states. We can quantify this steepness, by fitting the exponential rise in the EQE spectra below the band gap, known as the Urbach tail, to derive the Urbach energy (E_U).[35, 36]

In order to quantify the electronic disorder in the films, we estimate the E_U of perovskite films from Fourier transform photocurrent spectroscopy (FTPS), which we show in fig. 6.12. We estimate the E_U for the control and 0.15 mol% Al^{3+}-doped samples to be 13.09±0.05 and 12.64±0.04 meV respectively.

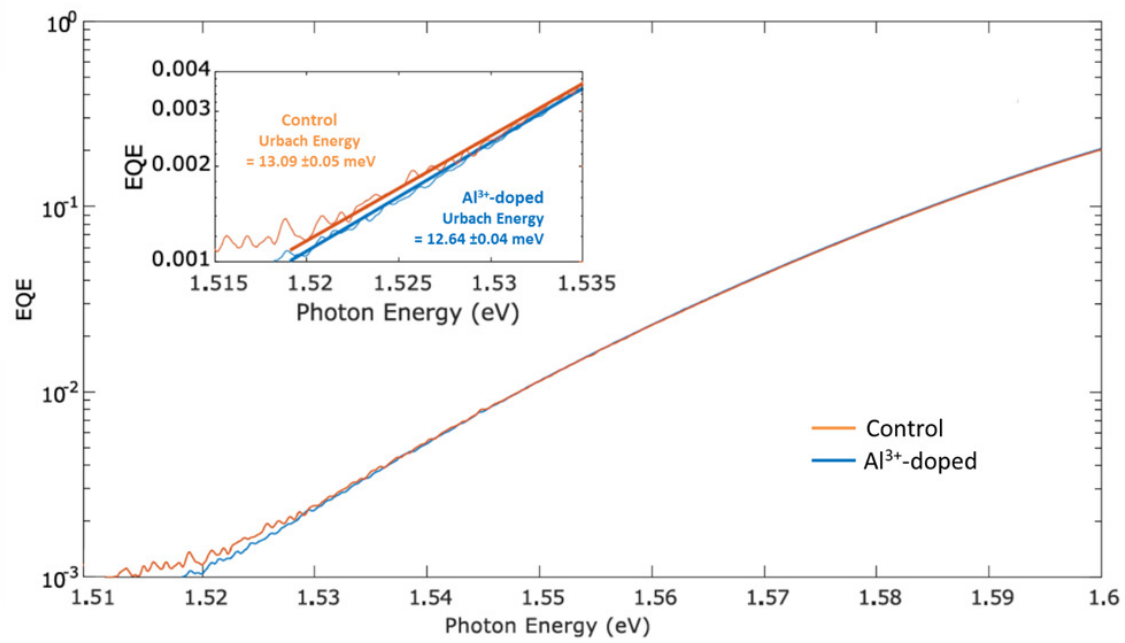


Figure 6.12: Fourier transform photocurrent spectroscopy of control and Al^{3+}-doped (0.15 mol%) perovskite devices and their estimated Urbach energies fitting the slope at low energy (fits are between 1.519 to 1.55 eV shown in the inlet figure).

This decrease in E_U is direct evidence for an enhancement of the electronic quality of the perovskite films by Al^{3+} doping. Notably, this is the first time an E_U has been determined to be less than 13 meV in a metal halide perovskite film, indicating the high electronic quality of the perovskite film[11, 35] and suggesting an improved crystalline order in the polycrystalline thin film. The reason why the steepness of the absorption onset, and ultimately EQE spectra is important, is that this governs the maximum open-circuit voltage a solar cell can achieve in the "radiative limit", where all non-radiative recombination is switched off.[37] The operational-loss, defined as E_G-qV_{oc}, where E_G is the band gap of the absorber, has been observed to approximately half when the Urbach energy reduces from 23 meV, for copper indium gallium selenide (CIGS), to 7.5 meV for GaAs.[35, 38] Therefore, although the Urbach energy which we estimate here for our best perovskite solar cells is significantly lower than kT (∼25 meV at room temperature, where k is Boltzmann constant), it remains an important factor to improve in the goal of developing a near-perfect solar absorber material.

By interpreting the photo-physical and electronic impact of the Al^{3+} doping, it is apparent that the optimally doped films possess fewer non-radiative decay sites and are of superior electronic quality as compared with the control films. This is consistent with the enhanced structural quality we observed in fig. 6.2, resulting in improved optoelectronic performance.

6.5 Photovoltaic Behaviour

6.5.1 Device Architecture

To assess if these enhanced film properties translate into enhancements in solar cell performance, we now integrate the perovskite films into "inverted" (p-i-n) planar heterojunction perovskite solar cells with a p-type organic hole transporting material (HTM), a solid 'intrinsic' (i) perovskite film and an n-type organic electron transporting material.[39] We show a high angle annular dark field STEM (HAADF-STEM) cross-sectional micrograph of an optimized device in fig. 6.14a, an illustration of the energy levels of the materials employed in fig. 6.13b and a schematic of the full device architecture in fig. 6.13c. We note that the energy levels we illustrate are for the individual isolated materials, and upon doping and contact with each other there is likely to be a relative shift in the absolute energy at the interfaces.[40]

6.5.2 Device Performance

In fig. 6.14 and in Table 6.1 we show the mean solar cell performance parameters for a batch of solar cells with a range of Al^{3+} doping concentrations, extracted from J-V curves measured under simulated AM 1.5, 100 mW/cm^2 irradiance. We observe a

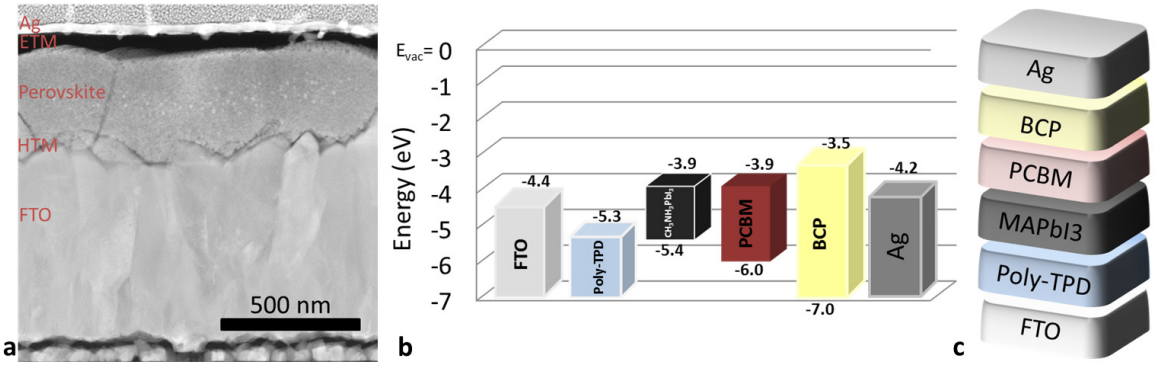


Figure 6.13: (a) High angle annular dark field STEM (HAADF-STEM) cross-sectional micrograph of optimized device with the structure of Ag/BCP/ETM (PCBM)/perovskite/HTM (poly-TPD)/FTO. (b) Diagram of the energy levels of the materials used, and (c) an illustration of the structure of the solar cells.

clear trend of enhancement in device performance produced by the introduction of Al^{3+} dopant in the perovskite precursor solution up to concentrations of around 0.15 to 0.3 mol%. For devices fabricated from the control precursor solution, i.e. pristine $MAPbI_3$, the average short-circuit current density (J_{sc}) and open circuit voltage (V_{oc}) are around 19.0±1.7mA/cm^2 and 1.01±0.04V, respectively. With the incorporation of the Al^{3+} dopant in the perovskite, both the J_{sc} and V_{oc} increase up to average values of 21.2±1.1 mA/cm^2 and 1.06±0.03 V, respectively, peaking at 0.15 mol%, while we observe that the average fill factor (FF) increases to 0.72±0.08with the addition of Al^{3+} up to 0.3 mol%, after which the FF begins to decrease. Hence, we observe the power conversion efficiency (PCE) to reach a maximum at 0.15 mol% of Al^{3+} doping with an average PCE of the solar cells fabricated with this doping concentration of 15.8±2.4%. Notably, the optimised Al^{3+} doping not only improves all of the performance parameters (i.e. FF, V_{oc}, J_{sc}, and PCE) as compared with the control devices, but also enhances device reproducibility, as we show in fig. 6.15.

In fig. 6.16a we show the current-density voltage (JV) curves for the most efficient control and Al^{3+}-doped devices, where the latter exhibits a J_{sc} of 22.4 mA/cm^2, a FF of 0.78, and a V_{oc} of 1.10 V yielding a PCE of 19.1%. When we compare this with the control

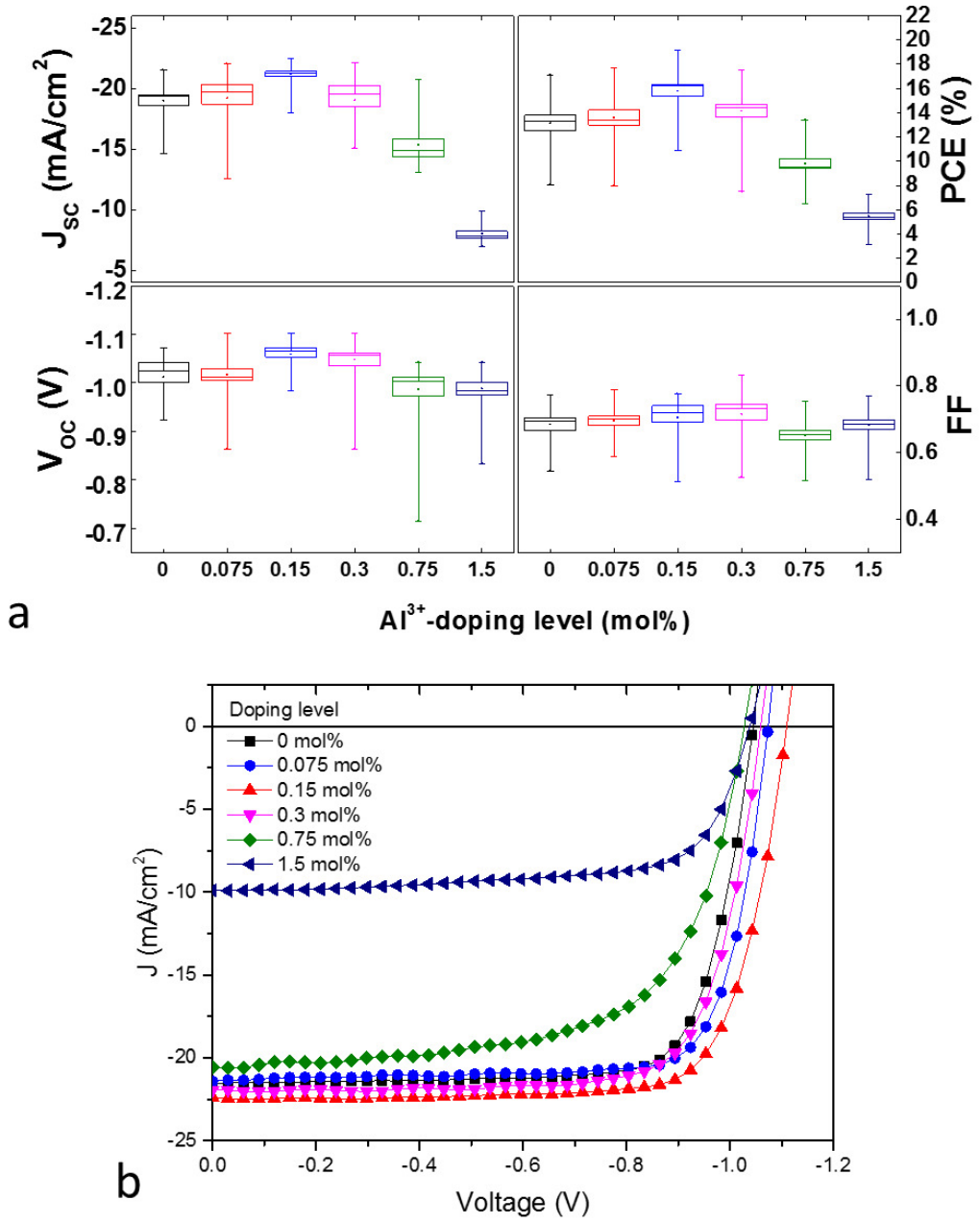


Figure 6.14: Devices performance characteristics with different doping levels of Al^{3+} perovskite under simulated AM 1.5, 100 mW/cm^2 irradiance in air. (a) Device performance parameters extracted from a batch of current-voltage measurements. (b) The current density-voltage curves of the best devices.

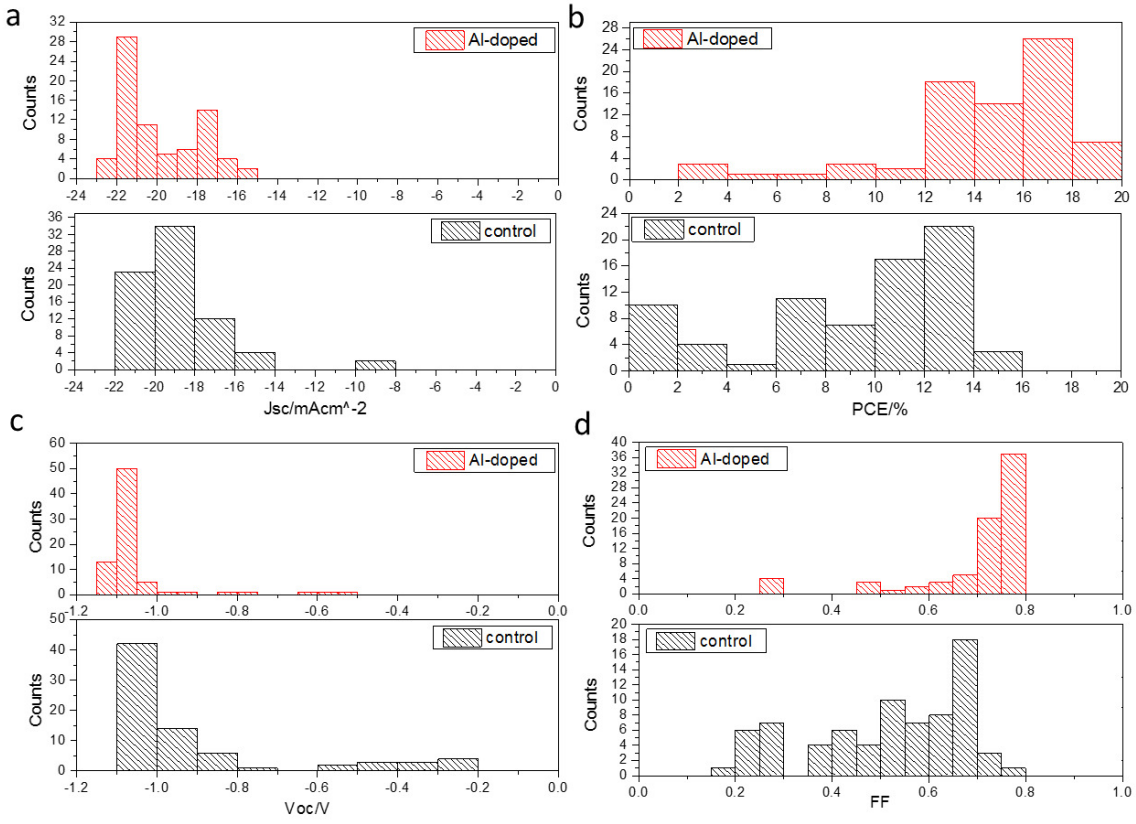


Figure 6.15: Histograms of the solar cell performance parameters for the optimally doped (0.15 mol%) and control devices.

Table 6.1: Mean solar cell performance parameters with different Al^{3+} doping concentration under simulated AM 1.5, 100 mW/cm^2 solar irradiation

Doping level (mol%)	J_{sc} (mA/ cm2)	V_{oc} (V)	FF	PCE (%)
0	19.0±1.7	1.01±0.04	0.68±0.08	13.2±2.6
0.075	19.2±2.4	1.02±0.05	0.70±0.06	13.6±2.8
0.15	21.2±1.1	1.06±0.03	0.71±0.07	15.8±2.4
0.3	19.0±2.4	1.05±0.06	0.72±0.08	14.2±2.4
0.75	15.3±2.4	0.99±0.08	0.65±0.07	9.8±1.9
1.5	8.0±1.0	0.99±0.06	0.68±0.07	5.5±1.2

device, we can see that the major improvement is coming from the increases in V_{oc} and J_{sc} . The external quantum efficiency (EQE) spectra for typical cells of each type, which we show in fig. 6.16b, exhibit the same trend as the measured JV curves, consistent with the enhanced photocurrent from the Al^{3+}-doped samples. Integrating the EQE over the AM1.5 solar spectrum at 100 mW/cm^2 irradiance gives an estimated J_{sc} of 20 and 18 mA/cm^2 for the Al^{3+}-doped and control devices, respectively. The measured J_{sc} under the solar simulator for these precise cells was 22.0 and 17.3 mA/cm^2 respectively, which gives an indication of an accuracy of between -10 and + 4%, comparing the current estimated from the EQE to the JV measurements under simulated sun light. This difference may be within the measurement accuracy since we use two different rigs with two different calibration diodes. The cells are masked in the same manner for both measurements, however, the spatial uniformity of the EQE measurement is not as controlled as it is for the JV measurements, which may contribute to the errors. Additionally, we note that we test these cells in air without encapsulation, and there is usually a little degradation in performance for these p-i-n inverted cells following testing.

The J-V curves for both control and Al^{3+}-doped perovskite solar cells exhibit very low levels of hysteresis. We illustrate this in fig. 6.16c showing the numerically averaged J-V curves measured at different voltage sweep directions in a selection of 20 high performance devices with their performance parameters in the inset table. As an aside, this observation further strengthens our understanding that the main source of such hystere-

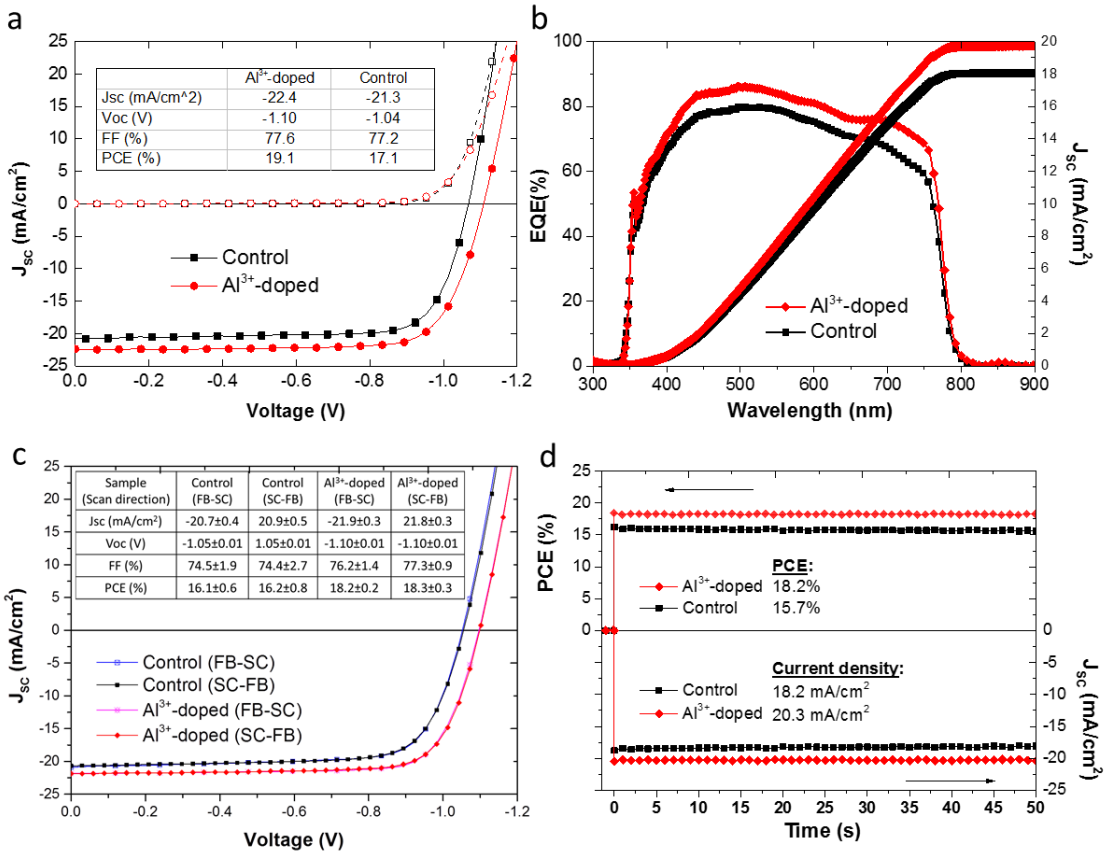


Figure 6.16: Photovoltaic performance of control and Al^{3+}-doped (0.15 mol%) perovskite solar cells under simulated AM 1.5, 100 mW/cm^2 solar irradiation (solid line), and in the dark (dotted line) at a scan rate of 0.38 Vs^{-1}.(a) the current density-voltage characteristics of the best cells. (b) external quantum efficiency (EQE) spectrum measured at short-circuit, along with the expected photocurrent integrated over the AM1.5 solar spectrum of 100 mW/cm^2. (c) Numerically averaged JV curves measured from forward bias (FB) to short-circuit (SC) and back again without observable hysteresis in a selection of 20 high performance control and Al^{3+}-doped devices. (d) Stabilized maximum power output measurement of the best cells with bias at their maximum power points.

sis originates at the interface between the perovskite film and the semiconducting metal oxide such as TiO_2 or ZnO in regular device structures, probably due to the generation of a large density of electronic defects at the surface of the perovskite when the films are crystallised on these metal oxide surfaces.[41] Here, these cells using only organic p and n-type charge collection layers exhibit very well behaved current voltage characteristics. Notably, we have recently identified that the presence of electronic defects through which trap assisted recombination occurs, are central to the mechanism governing JV hysteresis

in perovskite solar cells (combined with mobile ionic species).[41] This is consistent with the cells processed on the organic semiconductors containing fewer electronic defects.

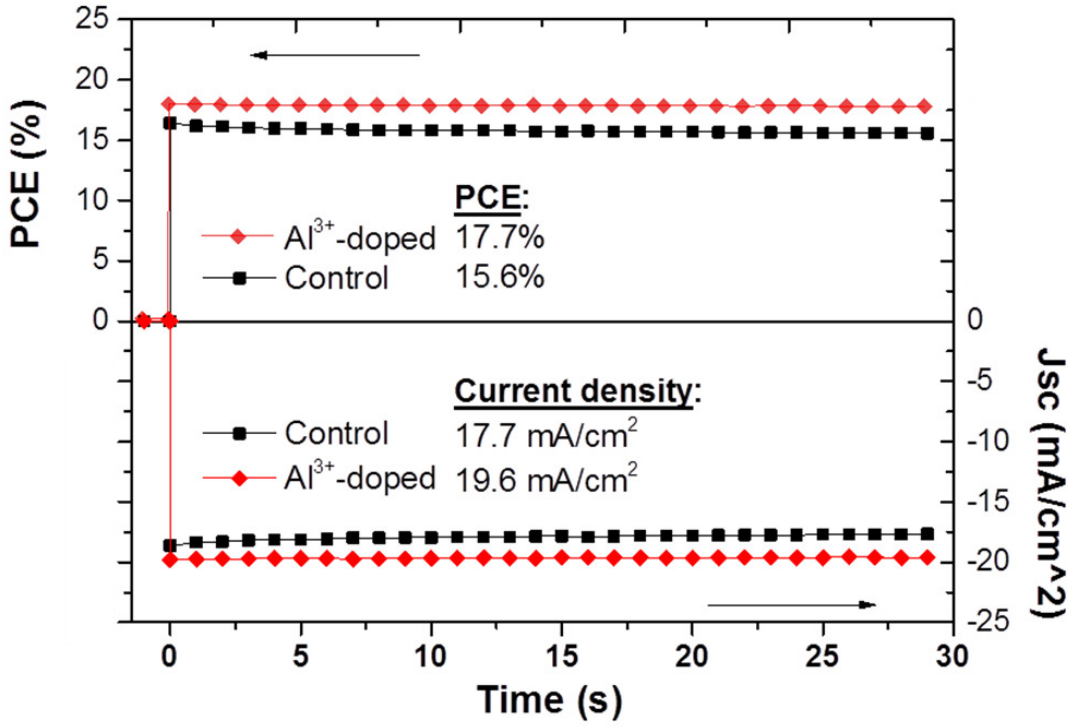


Figure 6.17: Numerically averaged stabilized power output and photocurrent in a batch of 20 high performing devices of the control and Al^{3+}-doped (0.15 mol%) cells.

In fig. 6.16d, we show the stabilised power output (SPO) of the best performing control and Al^{3+}-doped cells when holding the applied bias fixed at its maximum power point voltage under simulated AM 1.5 (100 mW/cm^2) sun light, and measuring the photocurrent as a function of time. Both devices reach their stabilised photocurrent within the first measurement window, indicative of negligible hysteresis.[42] For the Al^{3+}-doped device, we measure a stabilized photocurrent at 20.3 mA/cm^2 and PCE at 18.2%, which is superior to the control device for which we measure a stabilised photocurrent and SPO of 18.2 mA/cm^2 and 15.7%, respectively. We note that despite the negligible hysteresis in the JV curves, we still have slightly lower SPOs than the PCE determined from the

JV curves. This emphasises that SPO measurements remain important even in cells appearing to exhibit negligible hysteresis. In fig. 6.17, we further show the average-SPO in a selection of 20 high performance devices at 17.7% and 15.6% for the Al^{3+}-doped and control devices, respectively.

To confirm that the positive effects we observe here are due to the addition of Al^{3+}, as opposed to the acac ion, we also replaced the Al-$acac_3$ dopant with Aluminum iodide (AlI_3). These films exhibit enhanced luminescent properties, and subsequently deliver improved solar cells in comparison to the control devices. We show these results in fig. 6.18 where we observe that the addition of AlI_3 into perovskite precursor solution also delivers optimum performance with a doping level of around 0.15 mol%.

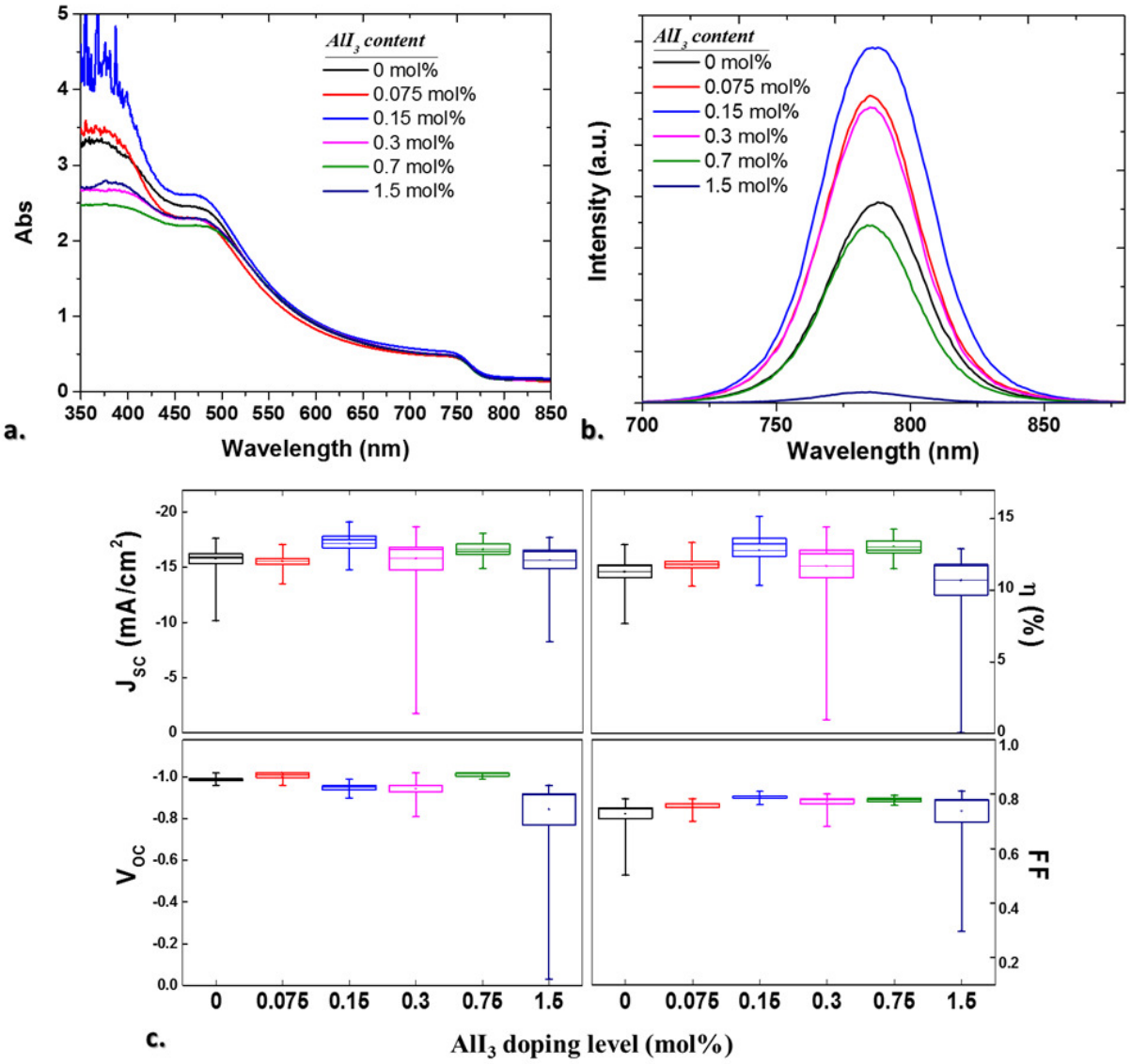


Figure 6.18: Characterizations of different Al^{3+} doping (AlI_3 as dopant) concentration of perovskite samples with (a) UV-vis absorption, (b) spectra Steady-state photoluminescence, and (c) Device performance parameters (with the structure of Ag/BCP/PCBM/$CH_3NH_3PbI_3$/PEDOT AI4083/FTO) extracted from a batch of current-voltage measurements under simulated AM 1.5, 100 mW/cm^2 irradiance in air. Note: Here we replaced the source of Al^{3+} from Al-acac$_3$ ($Al(C_5H_7O_2)_3$) to Aluminum iodide (AlI_3), in this case we substitute the methylammonium iodide for the corresponding different concentrations of AlI_3 to achieve Al^{3+} doping, while the amount of iodide in the $MAPbI_3$ remains constant.

6.6 Summary

To summarize our findings, we have discovered that the electronic quality of the $MAPbI_3$ films can be substantially enhanced by low levels of doping with the small metal cation Al^{3+} (Note: by "doping", we mean "adding the foreign ions into the precursor solution" here). We have proposed the mechanism by which Al^{3+}-doping enhances the quality of the films, and revealed a simple property of the material, microstrain, which can be studied, tuned and minimised to deliver even higher quality perovskite films for opto-electronics. With the presence of Al^{3+} during the perovskite crystallization, we observe reduced microstrain in the perovskite crystal, which we infer to indicate a reduction in the density of crystal defects. From these same films we observe enhanced luminescent properties and reduced electronic disorder, which we infer to suggest that the same defects responsible for microstrain in the crystal, are also responsible for losses in luminescence and the solar cell operation. In addition, the remaining Al^{3+} ions present, most concentrated in the regions near the grain boundaries, may also act to alter the energy of these defect sites making them more benign. However, this latter consideration is not necessary to explain our results and is only a postulation. We have demonstrated improved JV measured PCE of up to 19.1% with negligible hysteresis for these Al^{3+}-doped films, when integrated into planar heterojunction solar cells. We attribute the improved operation to the reduced non-radiative trap assisted recombination in the thin films and devices. Our work therefore highlights the possibility for considerable further improvement of the electronic quality of perovskite thin films, and subsequent devices by understanding the role of dopant impurities upon crystallisation, and crystal and electronic defects in perovskite thin films.

References

[1] Michael M. Lee, Joël Teuscher, Tsutomu Miyasaka, Takurou N. Murakami, and Henry J. Snaith. Efficient Hybrid Solar Cells Based on Meso-Superstructured Organometal Halide Perovskites. *Science*, 338(6107):643–647, nov 2012.

[2] Mingzhen Liu, Michael B Johnston, and Henry J Snaith. Efficient planar heterojunction perovskite solar cells by vapour deposition. *Nature*, 501(7467):395–398, sep 2013.

[3] Jin Hyuck Heo, Sang Hyuk Im, Jun Hong Noh, Tarak N Mandal, Choong-Sun Lim, Jeong Ah Chang, Yong Hui Lee, Hi-jung Kim, Arpita Sarkar, Md. K Nazeeruddin, Michael Grätzel, and Sang Il Seok. Efficient inorganic–organic hybrid heterojunction solar cells containing perovskite compound and polymeric hole conductors. *Nature Photonics*, 7(6):486–491, may 2013.

[4] Nam Joong Jeon, Jun Hong Noh, Young Chan Kim, Woon Seok Yang, Seungchan Ryu, and Sang Il Seok. Solvent engineering for high-performance inorganic-organic hybrid perovskite solar cells. *Nature materials*, 13(July):1–7, 2014.

[5] Michael Saliba, Taisuke Matsui, Ji-Youn Seo, Konrad Domanski, Juan-Pablo Correa-Baena, Mohammad Khaja Nazeeruddin, Shaik M Zakeeruddin, Wolfgang Tress, Antonio Abate, Anders Hagfeldt, and Michael Grä Tzel. Cesium-containing triple cation perovskite solar cells: improved stability, reproducibility and high efficiency. *Energy Environ. Sci.*, 9(6):1989–1997, mar 2016.

[6] James M. Ball, Michael M. Lee, Andrew Hey, and Henry J. Snaith. Low-temperature processed meso-superstructured to thin-film perovskite solar cells. *Energy & Environmental Science*, 6(6):1739–1743, 2013.

[7] Wan-Jian Yin, Tingting Shi, and Yanfa Yan. Unusual defect physics in CH3NH3PbI3 perovskite solar cell absorber. *Applied Physics Letters*, 104(6):063903, feb 2014.

[8] Michael L Agiorgousis, Yi-Yang Sun, Hao Zeng, and Shengbai Zhang. Strong covalency-induced recombination centers in perovskite solar cell material CH3NH3PbI3. *Journal of the American Chemical Society*, 136(41):14570–14575, oct 2014.

[9] D. W. DeQuilettes, S. M. Vorpahl, S. D. Stranks, H. Nagaoka, G. E. Eperon, M. E. Ziffer, H. J. Snaith, and D. S. Ginger. Impact of microstructure on local carrier lifetime in perovskite solar cells. *science*, 348(6235):683–686, apr 2015.

[10] Nakita Kimberly Noel, Antonio Abate, Samuel David Stranks, Elizabeth Parrott, Victor Burlakov, Alain Goriely, and Henry J. Snaith. Enhanced Photoluminescence and Cell Performance via Lewis Base Passivation of Organic-Inorganic Lead Halide Perovskites. *ACS Nano*, 8(10):9815–9821, aug 2014.

[11] Wei Zhang, Sandeep Pathak, Nobuya Sakai, Thomas Stergiopoulos, Pabitra K. Nayak, Nakita K. Noel, Amir A. Haghighirad, Victor M. Burlakov, Dane W. DeQuilettes, Aditya Sadhanala, Wenzhe Li, Liduo Wang, David S. Ginger, Richard H. Friend, and Henry J. Snaith. Enhanced optoelectronic quality of perovskite thin films with hypophosphorous acid for planar heterojunction solar cells. *Nature Communications*, 6:10030, nov 2015.

[12] Jixian Xu, Andrei Buin, Alexander H. Ip, Wei Li, Oleksandr Voznyy, Riccardo Comin, Mingjian Yuan, Seokmin Jeon, Zhijun Ning, Jeffrey J. McDowell, Pongsakorn Kanjanaboos, Jon-Paul Sun, Xinzheng Lan, Li Na Quan, Dong Ha Kim, Ian G. Hill, Peter Maksymovych, and Edward H. Sargent. Perovskite–fullerene hybrid materials suppress hysteresis in planar diodes. *Nature Communications*, 6:7081, may 2015.

[13] Yuchuan Shao, Zhengguo Xiao, Cheng Bi, Yongbo Yuan, and Jinsong Huang. Origin and elimination of photocurrent hysteresis by fullerene passivation in CH3NH3PbI3 planar heterojunction solar cells. *Nature Communications*, 5:5784, dec 2014.

[14] Wei Zhang, Michael Saliba, David T. Moore, Sandeep K. Pathak, Maximilian T. Hörantner, Thomas Stergiopoulos, Samuel D. Stranks, Giles E. Eperon, Jack A. Alexander-Webber, Antonio Abate, Aditya Sadhanala, Shuhua Yao, Yulin Chen, Richard H. Friend, Lara A. Estroff, Ulrich Wiesner, and Henry J. Snaith. Ultrasmooth organic–inorganic perovskite thin-film formation and crystallization for efficient planar heterojunction solar cells. *Nature Communications*, 6:6142, jan 2015.

[15] Gregor Kieslich, Shijing Sun, and Tony Cheetham. Solid-State Principles Applied to Organic-Inorganic Perovskites: New Tricks for an Old Dog. *Chemical Science*, 5:4712–4715, aug 2014.

[16] Ian Robinson and Ross Harder. Coherent X-ray diffraction imaging of strain at the nanoscale. *Nature materials*, 8(4):291 – 298, apr 2009.

[17] A. Pramanick, X. P. Wang, C. Hoffmann, S. O. Diallo, M. R. V. Jørgensen, and X.-L. Wang. Microdomain dynamics in single-crystal BaTi O 3 during paraelectric-ferroelectric phase transition measured with time-of-flight neutron scattering. *Physical Review B*, 92(17):174103, nov 2015.

[18] G.K Williamson and W.H Hall. X-ray line broadening from filed aluminium and wolfram. *Acta Metallurgica*, 1(1):22–31, jan 1953.

[19] Yusheng Zhao and Jianzhong Zhang. Microstrain and grain-size analysis from diffraction peak width and graphical derivation of high-pressure thermomechanics. *Journal of Applied Crystallography*, 41(6):1095–1108, nov 2008.

[20] David T. Moore, Kwan W. Tan, Hiroaki Sai, Katherine P. Barteau, Ulrich Wiesner, and Lara A. Estroff. Direct Crystallization Route to Methylammonium Lead Iodide Perovskite from an Ionic Liquid. *Chemistry of Materials*, page 150420110646007, apr 2015.

[21] Gregor Kieslich, Shijing Sun, and Anthony K. Cheetham. An extended Tolerance Factor approach for organic–inorganic perovskites. *Chem. Sci.*, 6(6):3430–3433, may 2015.

[22] Robert A. Meyers, editor. *Encyclopedia of Analytical Chemistry*. John Wiley & Sons, Ltd, Chichester, UK, sep 2006.

[23] James R. Lindsay, Harry J. Rose, William E. Swartz, Plato H. Watts, and Kenneth A. Rayburn. X-ray Photoelectron Spectra of Aluminum Oxides: Structural Effects on the "Chemical Shift". *Applied Spectroscopy*, 27(1):1–5, jan 1973.

[24] A. Hess, E. Kemnitz, A. Lippitz, W.E.S. Unger, and D.H. Menz. ESCA, XRD, and IR Characterization of Aluminum Oxide, Hydroxyfluoride, and Fluoride Surfaces in Correlation with Their Catalytic Activity in Heterogeneous Halogen Exchange Reactions. *Journal of Catalysis*, 148(1):270–280, jul 1994.

[25] Alexander G. Shard. Detection limits in XPS for more than 6000 binary systems using Al and Mg Kα X-rays. *Surface and Interface Analysis*, 46(3):175–185, mar 2014.

[26] R.A. Berner. The role of magnesium in the crystal growth of calcite and aragonite from sea water. *Geochimica et Cosmochimica Acta*, 39(4):489–504, apr 1975.

[27] Noriaki Kubota and J.W. Mullin. A kinetic model for crystal growth from aqueous solution in the presence of impurity. *Journal of Crystal Growth*, 152(3):203–208, jul 1995.

[28] Keshra Sangwal. Growth kinetics and surface morphology of crystals grown from solutions: Recent observations and their interpretations. *Progress in Crystal Growth and Characterization of Materials*, 36(3):163–248, jan 1998.

[29] J. J. De Yoreo, P. U. P. A. Gilbert, N. A. J. M. Sommerdijk, R. L. Penn, S. Whitelam, D. Joester, H. Zhang, J. D. Rimer, A. Navrotsky, J. F. Banfield, A. F. Wallace, F. M. Michel, F. C. Meldrum, H. Colfen, and P. M. Dove. Crystallization by particle attachment in synthetic, biogenic, and geologic environments. *Science*, 349(6247):67601–67609, jul 2015.

[30] Nakita K. Noel, Samuel D. Stranks, Antonio Abate, Christian Wehrenfennig, Simone Guarnera, Amir-Abbas Haghighirad, Aditya Sadhanala, Giles E. Eperon, Sandeep K. Pathak, Michael B. Johnston, Annamaria Petrozza, Laura M. Herz, and Henry J. Snaith. Lead-Free Organic-Inorganic Tin Halide Perovskites for Photovoltaic Applications. *Energy & Environmental Science*, 7:3061–3068, may 2014.

[31] Felix Deschler, Michael Price, Sandeep Pathak, Lina E Klintberg, David-Dominik Jarausch, Ruben Higler, Sven Hüttner, Tomas Leijtens, Samuel D Stranks, Henry J Snaith, Mete Atatüre, Richard T Phillips, and Richard H Friend. High Photoluminescence Efficiency and Optically Pumped Lasing in Solution-Processed Mixed Halide Perovskite Semiconductors. *The journal of physical chemistry letters*, 5(8):1421–1426, apr 2014.

[32] Samuel D. Stranks, Victor M. Burlakov, Tomas Leijtens, James M. Ball, Alain Goriely, and Henry J. Snaith. Recombination Kinetics in Organic-Inorganic Perovskites: Excitons, Free Charge, and Subgap States. *Physical Review Applied*, 2(3):034007, sep 2014.

[33] Michael B. Johnston and Laura M. Herz. Hybrid Perovskites for Photovoltaics: Charge-Carrier Recombination, Diffusion, and Radiative Efficiencies. *Accounts of Chemical Research*, 49(1):146–154, dec 2015.

[34] S. K. Vasheghani Farahani, T. D. Veal, J. J. Mudd, D. O. Scanlon, G. W. Watson, O. Bierwagen, M. E. White, J. S. Speck, and C. F. McConville. Valence-band density of states and surface electron accumulation in epitaxial SnO 2 films. *Physical Review B*, 90(15):155413, oct 2014.

[35] Stefaan De Wolf, Jakub Holovsky, Soo-Jin Moon, Philipp Löper, Bjoern Niesen, Martin Ledinsky, Franz-Josef Haug, Jun-Ho Yum, and Christophe Ballif. Organometallic Halide Perovskites: Sharp Optical Absorption Edge and Its Relation to Photovoltaic Performance. *The Journal of Physical Chemistry Letters*, 5(6):1035–1039, mar 2014.

[36] Aditya Sadhanala, Felix Deschler, Tudor H Thomas, Siân E. Dutton, Karl C Goedel, Fabian Cornelius Hanusch, May Ling Lai, Ullrich Steiner, Thomas Bein, Pablo Docampo, David Cahen, and Richard H. Friend. Preparation of Single Phase Films of CH3NH3Pb(I1-xBrx)3 with Sharp Optical Band Edges. *The Journal of Physical Chemistry Letters*, 5(15):2501–2505, jul 2014.

[37] Kristofer Tvingstedt, Olga Malinkiewicz, Andreas Baumann, Carsten Deibel, Henry J. Snaith, Vladimir Dyakonov, and Henk J. Bolink. Radiative efficiency of lead iodide based perovskite solar cells. *Scientific Reports*, 4:6071, aug 2014.

[38] S. R. Johnson and T. Tiedje. Temperature dependence of the Urbach edge in GaAs. *Journal of Applied Physics*, 78(9):5609, 1995.

[39] Pablo Docampo, James M Ball, Mariam Darwich, Giles E Eperon, and Henry J Snaith. Efficient organometal trihalide perovskite planar-heterojunction solar cells on flexible polymer substrates. *Nature communications*, 4:2761, jan 2013.

[40] Chu-Chen Chueh, Chang-Zhi Li, and Alex K.-Y. Jen. Recent progress and perspective in solution-processed Interfacial materials for efficient and stable polymer and organometal perovskite solar cells. *Energy Environ. Sci.*, 8(4):1160–1189, apr 2015.

[41] Stephan van Reenen, Martijn Kemerink, and Henry J. Snaith. Modeling Anomalous Hysteresis in Perovskite Solar Cells. *The Journal of Physical Chemistry Letters*, 6(19):3808–3814, sep 2015.

[42] Henry J. Snaith, Antonio Abate, James M. Ball, Giles E. Eperon, Tomas Leijtens, Nakita K. Noel, Samuel D. Stranks, Jacob Tse Wei Wang, Konrad Wojciechowski, and Wei Zhang. Anomalous hysteresis in perovskite solar cells. *Journal of Physical Chemistry Letters*, 5(9):1511–1515, mar 2014.

Chapter 7

Conclusion and Outlook

7.1 Conclusion and Outlook

7.1.1 Conclusion

With the vast concerns about climate change and the use of fossil fuels, finding alternative renewable energy sources is of great interest. Perovskite solar cells are currently the only solution-processed photovoltaic technology to surpass 20% power conversion efficiency, and capable of delivering the lowest cost with the highest efficiency, making them a promising candidate for the new generation of photovoltaic devices. In this thesis, we put emphasis on the development of interlayers, which plays the most critical role in promoting the device performance.

The main research achievements are as follows: in chapter 4, we report a significant breakthrough in the development of all low-temperature processed (entirely below 150 °C) thin film solar cells with a decent PCE of 15.6% on $CH_3NH_3PbI_{3-x}Cl_x$ perovskite-based MSSCs. This was the best-recorded efficiency for all low-temperature processed solar cells while the result published, which was also slightly higher than the high-temperature (500 °C) sintered devices due to the superior properties of the Gaphene-TiO_2 nanocomposites. By exploiting the nanocomposites of high-quality graphene nanoflakes and pre-synthesized TiO_2 nanoparticles in perovskite solar cells as a low-temperature processed electron-transporting layer, we have observed reduced series resistance and

unexpectedly reduced recombination losses with the low-temperature nanocomposite via the technique of impedance spectroscopy. In addition, the advantage of the large aspect ratio of graphene also enables better connection between TiO_2 nanoparticles, and functions as a 2D framework for the nanoparticles to anchor upon, thus improving the electron transfer rate (reduced series resistance), and reducing charge recombination (increased charge recombination resistance). This is reflected in a 40% IQE and 20% FF improvement, and also gives enhanced values for the rest device performance parameters, J_{sc} and V_{oc}. These findings indicate that high-efficiency PSCs may no longer need a high-temperature sintering process for TiO_2 as the electron-transporting layer sintering process at up to 500 °C is unfavourable for low-cost production and precludes applications on plastic substrates, and the fabrication of multi-junction device architectures for even higher efficiencies. Our results demonstrate the successful combination of two emerging materials, graphene and organic-inorganic perovskites, showing a great promise for developing high-efficiency graphene-based thin film solar cells, also enabling the use of fast printing deposition methods. To the best of our knowledge, this work also set a milestone for the graphene-incorporated photovoltaics.

In chapter 5, to explore the underlying mechanism of inverted perovskite solar cells, where we have deconstructed the device layer by layer. Our works highlight the importance of understanding and controlling the solar cell fabrication process from the very beginning. Starting with substrate work-function and wetting management, followed by thickness influenced device performance from the hole-transporting layer. We also modified the perovskite surface morphology by hot-solution casting, with improved interface and surface morphology observed. By creating a more uniform surface, minimising light reflection and pinholes, and reducing the shunting paths; subsequently, the thickness of electron-transporting layer was also being optimised. Furthermore, we carefully choose the organic solvent for the buffer layer, demonstrating the first orthogonal solution-deposition buffer layer, which enables the inverted PSCs devices to be

processed under ambient condition; putting all these efforts together, has led to the production of highly efficient inverted perovskite solar cells. Compared with the regular structure employing fullerene as ETL, we found the existence of hysteresis might not simply be eliminated with the help fullerene, thus emphasising the important role of the interface. Lastly, we introduced a Poly-TPD-based hole-transporting layer, with the addition of F6-TCNNQ as the dopant, which not only improves the surface wetting to give a much better interface, but also improve the hole transporting properties, leading to a reduced series resistance within the HTLs. The best inverted PSCs consist of F6-TCNNQ/Poly-TPD as HTL, which demonstrate an increased V_{oc} up to 1.07 V compared to the PEDOT:PSS-based devices. The careful optimisations throughout the entire carrier pathways have facilitated the charge transport, minimised the unfavourable recombination, and enabled efficient and hysteresis-free inverted devices to be produced. These combined efforts represent a leap forward in producing highly efficient perovskite solar cells.

In chapter 6, we focus on improving the electronic quality of the $CH_3NH_3PbI_3$ perovskite for solar cells. One of the main challenges for polycrystalline perovskite-based photovoltaics is to eliminate the presence of charge recombination centres throughout the bulk material. Here, we have found that heterovalent doping with the small metal cation Al^{3+}, delivered films with much higher photoluminescence efficiency, improved optoelectronic homogeneity, and the ensuing planar heterojunction perovskite solar cells delivered an improved PCE of up to 19% with negligible hysteresis. This is among the highest reported efficiencies for "inverted" planar heterojunction perovskite solar cells while the manuscript was being prepared. To investigate the mechanism behind this result, we first performed a microstrain study of the X-ray diffraction patterns of our perovskite films, according to the modified Williamson-Hall method. The origin of microstrain can be attributed to crystal imperfections/structural defects, and we observe a 30% reduction of microstrain in the Al^{3+}-doped films. This gives clear evidence that

the introduction of a small amount of Al^{3+} dopant has resulted in the decreased number of crystal defects in the perovskite films. We back this up with atomic force microscopy, which directly shows "flattening" of the surface of the perovskite films. Hence, this is direct evidence that the density of crystal defects, which could be terraces, steps, dislocations etc, is reduced when the perovskite is crystallised with the addition of Al^{3+}. Secondly, to highlight the existence of Al ions in the polycrystalline perovskite thin film, we present a study of nanoscale secondary ion mass spectrometry (NanoSIMS), which shows the Al ions are preferentially situated around the grain boundaries. Furthermore, we have performed a surface photovoltage study, from which we infer that the electronic band bending at the surface of Al^{3+}-doped perovskite film is lower than that of the undoped samples. Combined with the PL and sub-bandgap photocurrent spectroscopy, this corroborates the observation of fewer electronic trap sites on the surface of the Al^{3+}- doped films, via reducing the density of crystal defects. Finally, we speculated on the mechanism of how the Al^{3+} doping influences the crystallisation and crystalline quality of the films. Here, the foreign ions (Al^{3+}) are probably accelerating both nucleation and growth by adsorbing to crystal surfaces and changing the surface energy of the crystal growth front making it more favourable for rapid crystallisation. Via the photospectroscopy study, we observed these same films exhibit enhanced luminescent properties and reduced electronic disorder, which suggests that the same defects responsible for microstrain in the crystal, are also responsible for losses in luminescence and the solar cell operation. Interestingly, this is the first time, a report has shown a clear correlation between reduced structural crystal defects and enhanced optoelectronic properties, rather than simply inferring a reduction in electronic defects of unknown origin. This work is hence an important step forward via the discovery of a new route for performance enhancement of perovskite semiconductors, also opening a new avenue for investigation on understanding of the role of dopant impurities upon crystallisation and defect generation.

7.1.2 Outlook

A number of contributions have been made to advance the understanding of charge transportation within the interfaces. With careful experimental design, we have successfully utilised the interface engineering to demonstrates the continuing importance of improving the electronic quality of the heterojunctions and the nature of the perovskite absorber to further improve the solar cell performance. Despite the concerns raised in achieving long-term stability with its sensitivity to humidity, oxygen, and sunlight, which may be the biggest hurdle for this technology to overcome before it is ready for commercial deployment. But the manipulation of the composition of perovskite and the interlayers have appeared led to substantial improvement in this regard, and may be able to resolve these questions with further efforts made in this direction. In addition, to prolong the lifetime of the solar cell, encapsulation may also be a straightforward route to answer the environment-induced degradation. However, there are very few studies have been investigated in this perspective, as the use of orthogonal solvent is necessary to prevent the dissolution of underlying layers when the encapsulant apply, therefore the development of compatible encapsulant is urgently calling. On the other hand, the immobile and thermally-stable dopants or even dopant-free interlayers are also preferred choices to achieve durable solar cells. Taking all the advantages of perovskite solar cells possess, the next step is apparently to make flexible device with roll-to-roll process. Last but not least, a much deeper understanding of the fundamental mechanisms of efficient charge extraction in perovskite device is still needed, but as we have clearly identified the challenge need to be resolved for future research, and with the unprecedented efficiency growing speed in the short research history; It would not be too surprising, we soon can see perovskite solar cells widely adopted in the lives of human being to answer the oncoming energy crisis.

Abbreviations

2D two-dimensional

AM 1.5 Air mass 1.5

AFM Atomic Force Microscopy

Al-acac$_3$ aluminium acetylacetonate, $Al(C_5H_7O_2)_3$

ALD atomic layer deposition

BPhen bathophenanthroline

BCP bathocuproine

$CaTiO_3$ calcium titanium oxide

CB conduction band

CB Chlorobenzene

Cs_2CO_3 cesium carbonate

CO_2 carbon dioxide

CVD Chemical Vapor Deposition

$CH_3NH_3PbI_{3-x}Cl_x$ Methylammonium Lead Mix-Halide Perovskite

CH_3NH^{+3}, MA^+ Methylammonium

$CH_3NH_3PbI_3$ methylammonium lead iodide

CH_4 methane

DMF dimethylformamide

DOS Density of states

DSSCs dye-sensitized solar cells

$\mathbf{d}_{obs}$ observed d-space broadening

$\mathbf{d}_{ins}$ instrument response

$\mathbf{d}_{size}$ grain size

e elementary charge

ϵ dielectric constant

ε_d microstrain

$\mathbf{E}_b$ exciton binding energy

$\mathbf{E}_F$ Fermi level

EQE External Quantum Efficiency

$\mathbf{E}_{Fn}$ electron-quasi-Fermi levels

$\mathbf{E}_{Fp}$ hole-quasi-Fermi levels

$\mathbf{E}_G$ band gap

ETM electron-transporting material

ETL Electron-Transporting Layer

$\mathbf{E}_u$ Urbach energy

η_{cc} Charge-collection efficiency

η_{sep} Charge-separation efficiency

F4-TCNQ 2,3,5,6-(tetrafluoro-7,7,8,8-tetracyanoquino)dimethane

F6-TCNNQ 2,2'-(perfluoronaphthalene-2,6-diylidene)dimalononitrile

FF fill factor

FTPS Fourier transform photocurrent spectroscopy

FB forward bias

FB-SC forward bias toward the short-circuit

FTO Fluorine doped Tin Oxide

FTPS Fourier Transform Photocurrent Spectroscopy

GO Graphene Oxide

H_2NCNH^{2+}, FA^+ Formamidinium

HOMO Highest Occupied Molecular Orbitals

HTM hole-transporting material

HTL Hole-Transporting Layer

H_2SO_4 sulphuric acid

H_2O_2 hydrogen peroxide

HWHM half-width at half-maximum

HAADF-STEM High Angle Annular Dark Field-Scanning Transmission Electron Microscopy

HNO_3 Nitric Acid

ITO Indium tin oxide

ICP-OES Inductively Coupled Plasma Optical Emission Spectrometry

IQE internal quantum efficiency

IS Impedance Spectroscopy

IPA isopropanol

IPCE Incident Photon to Converted Electron Measurement

J_{dark} dark current

J_{Light} photocurrent

J_{Tot} total current

J-V current density-voltage measurement

J_{sc} short-circuit current density

k_B Boltzmann constant

LUMO Lowest Unoccupied Molecular Orbitals

L_D Diffusion length

LiF lithium fluoride

LPE Liquid-Phase Exfoliation

LHE Light Harvesting Efficiency

Li-TFSI lithium bis(trifluoromethanesulfonyl)imide

μ carrier mobility

MAI Methylammonium iodide

MBE Molecular Beam Epitaxy

MSSCs Meso-Superstructured Solar Cells

MoO_3 molybdenum trioxide

MPD Micro Photon Devices

NaCl sodium chloride

NREL National Renewable Energy Laboratories

Ω resistivity

OPV organic photovoltaics

OSCs organic solar cells

$PbCl_2$ lead chloride

$PbAc_2*(3H_2O)$ lead acetate trihydrate

PSCs perovskite solar cells

PCE power conversion efficiency

PCBM [6,6]-Phenyl C61 butyric acid methyl ester

P$_{MPP}$ maximum power point

PL photoluminescence

PLQE photoluminescence quantum efficiency

PTAA Poly(tertiary arylamine)

PHJ planar heterojunction

PLQE Photolumnincense Quantum Efficiency

Φ_h hole-tranporting barrier

$\Phi_{h'}$ reduced hole-tranporting barrier

QDSCs quantum dot solar cells

R$_{total}$ total recombination rate

R$_{series}$ series resistance

R$_{shunt}$ shunt resistance

RGO reduced graphene oxide

σ conductivity

SC short-circuit

SC-FB short-circuit toward forward bias

SEM scanning electron microscopy

spiro-oMeTAD 2,2,7,7-tetrakis-(N,N-di-p-methoxyphenyl amine) 9,9-spirobifluorene

SPO stabilised power output

ssDSSCs solid-state dye-sensitised solar cells

SPV Surface Photo Voltage

τ average lifetime

T temperature

TW terawatts

TF tolerance factor

TS Terahertz spectroscopy

tBP tert-butylpyridine

TEM Transmission Electron Microscopy

UPS Ultra-Violet Photoemission Spectroscopy

VB valence band

$\mathbf{V}_{oc}$ open-circuit voltages

XRD X-ray diffraction

XPS X-ray photoelectron spectroscopy